Investigation of a Novel Self-Healing Cementitious Composite Material System

PhD Thesis

2015

Tobias Hazelwood

Acknowledgements

I would like to thank both the BRE and ESPRC for the funding provided throughout this project, their financial support is gratefully acknowledged.

Special thanks are due to my supervisor Tony Jefferson; his support, guidance, and advice have been an immeasurable help, and it has been a pleasure working with him over the course of the project.

I would also like to thank my other two supervisors, Bob Lark and Diane Gardner, their input, support, and interest in the work has been invaluable.

I am grateful to my numerous office mates over the last few years; Iulia, Rob, Adriana, Chuansan, Waleed, Ollie, and Badorul have all been good friends and helped to create an enjoyable working environment.

I would also like to thank the laboratory technical staff for their help with the experimental aspects of the work; Harry, Des, Steff, and Carl were a great help whether they were building me a new piece of equipment or simply pointing me in the direction of a tool I needed.

I am very grateful for Simon's help and support over the course of the last number of years; lifts to and from Cardiff with car loads of stuff, and of course letting me move in and clutter up his living room for the last couple of months genuinely made finishing this project possible.

Finally I have to say thank you to my Mum; beyond the basics of lifts and accommodation mentioned above she may think that her input has been small, but whenever I have needed something she has always been there; I cannot thank her enough.

Abstract

This thesis describes a portion of the ongoing development of a novel self-healing cementitious material system named LatConX originally proposed by a group of researchers at Cardiff University. The research reported was undertaken with the aim of furthering understanding of the system's long-term behaviour, ultimately with a view to providing predictions for the performance of the system over a structure's working life. This aim is accomplished through a combination of experimental and numerical research.

An experimental series is presented which investigates the stress relaxation behaviour of polyethylene terephthalate in order to establish how the stress induced by heat-activated restrained shrinkage varies with time. Results of these experiments displayed very little stress reduction from the peak stress, with less than a 5 % loss observed over a 124 day period.

The development of a new one dimensional transient thermomechanical model for viscoelastic behaviour of pre-drawn polyethylene terephthalate is then described. This model is shown to be able to reproduce the observed experimental behaviour with good accuracy.

The polymer model is coupled with a number of other constitutive models for the behaviour of steel and concrete, thus forming a model for the material system as a whole. This coupling is undertaken within the framework of an idealised simply supported beam with a strong discontinuity for the simulation of a central crack hinge. The model is validated against experimental data and design code predictions.

Design considerations for the LatConX system are discussed and modified design equations derived. Parametric studies are presented investigating the structural performance and material costs of beams incorporating the LatConX system compared with that of standard reinforced concrete beams.

Encouraging results are reported suggesting that the LatConX system has the potential to simultaneously improve long-term durability and structural performance of reinforced concrete structures and reduce the initial material costs by replacing a percentage of the reinforcing steel with shape memory polymer.

Table of Contents

List of Tables

List of Figures

List of Symbols and Abbreviations

ACI	American Concrete Institute
BHET	Bis-hydroxyethyl-terephthalate
BSI	British Standards Institute
CDHM	Continuum Damage Healing Mechanics
CDM	Continuum Damage Mechanics
CMOD	Crack Mouth Opening Displacement
CoV	Coefficient of Variation
CSH	Calcium Silicate Hydrate
DMT	Dimethyl ester of terephthalic acid
EC2	Eurocode 2
ECC	Engineered Cementitious Composite
FPZ	Fracture Process Zone
FRC	Fibre Reinforced Concrete
FRP	Fibre Reinforced Polymer
GGBFS	Ground Granulated Blast Furnace Slag
HDPE	High Density Polyethylene
IEA	International Energy Agency
LDPE	Low Density Polyethylene
LTMx1	Constitutive model with one long term Maxwell Arm
LTMx2	Constitutive model with two long term Maxwell Arms
NAPCOR	National Association for PET Container Resources
OPC	Ordinary Portland Cement
OPEC	Organisation of the Petroleum Exporting Countries
PC	Polymer Concrete
PET	Polyethylene Terephthalate
PIC	Polymer Impregnated Concrete
PMC	Polymer Modified Concrete
RILEM	Réunion Internationale des Laboratories d'Essais et de Recherches sur les Matériaux et les Constructions
RVE	Representative Volume Element
SIFCON	Slurry Infused Fibrous Concrete
SLS	Serviceability Limit State

SLS	Standard Linear Solid
SMA	Shape Memory Alloy
SME	Shape Memory Effect
SMP	Shape Memory Polymer
TPA	Terephthalic Acid
UDL	Uniformly Distributed Load
ULS	Ultimate Limit State
UNEP	United Nations Environment Programme
WBCSD	World Business Council for Sustainable Development
WLF	Williams-Landel-Ferry

A, B, C	Coefficients for solving quadratic formula
$A_{c,eff}$	Effective tension area of concrete
A_{ef}	Effective concrete area
A_p	Cross-sectional area of polymer tendon
$A_{p,max}$	Maximum permissible polymer area
$A_{p,min}$	Minimum permissible polymer area
A_s	Cross-sectional area of reinforcing steel
A_s'	Cross-sectional area of compression steel
b	Beam width
b, c, d, f	Material parameters
d	Effective depth of beam
D_e	Elasticity Tensor
E	Young's Modulus
E_1, E_{TH}	Temperature independent Young's modulus
E_2	Temperature dependent Young's modulus
E_c	Compressive Young's modulus of concrete
E_{cef}	Effective concrete Young's modulus
E_d	Design value of actions
E_s	Young's modulus of steel
E_{TOT}	Low temperature Young's modulus
F	Force vector
f_c	Compressive strength

f_{ck}	Characteristic compressive strength of concrete
$F_{p0.1}$	Characteristic 0.1 % proof force
f_t	Tensile strength
f_{yk}	Characteristic steel yield stress
f_{yk2}	Characteristic stress marking the onset of perfect plasticity
G	Shear Modulus
G_f	Fracture energy
G_k	Permanent actions
h	Total depth of beam
H	Healing parameter
I_{cr}	Cracked second moment of area
I_{int}	Second moment of area of concrete beam
I_{un}	Uncracked second moment of area
k	Boltzmann Constant
L	Beam span
L_e	Length of elastic beam elements
L_{pmin}	Length of polymer tendon before drawing
L_R	Length at which polymer tendon is restrained
M	Internal moment
M_{ap}	Applied moment
M_{bal}	Limiting value for moment resistance to ensure an under-reinforced section
M_{cr}	Cracking moment
M_d	Design moment
M_{max}	Maximum historically applied moment
M_p	Moment due to polymer tendon
M_R	Moment of resistance
N	Internal axial force
N_e	Number of entanglements per unit volume
n_{lay}	Number of layers in beam model
P	Point load
Q_k	Variable actions
RH	Relative Humidity

S	First moment of area of reinforcing steel
s	Depth of concrete stress block
$S_{r,max}$	Maximum crack spacing
T	Absolute temperature
T_0	Ambient temperature
T_1	Short-term fall in temperature from hydration peak to ambient conditions
T_2	Long-term fall in temperature from ambient to the seasonal minimum
t_e	Time elapsed since thermal quench
T_g	Glass transition temperature
T_H	Transition end temperature
t_H	Time of healing
T_L	Transition start temperature
T_m	Melt temperature
u	Displacement vector
u_0	Crack mouth opening displacement at the end of stress opening curve
w_c	Fracture Process Zone Width
x_{lim}	Limiting value for neutral axis depth
x_u	Neutral axis depth
y_t	Lever arm from neutral axis to tension face
z	lever arm within section
z_p	Position of polymer tendon
α	Coefficient of thermal expansion
α_{cc}	Factor for long-term effects in concrete
β	Weighting factor
β_c	Creep weighting factor
γ_c	Partial factor for concrete
γ_p	Partial factor for polymer
$\gamma_{p,unfav}$	Eurocode factor for unfavourable prestressing
γ_s	Partial factor for steel
ΔL	Change in length of beam at level of polymer tendon
ΔL_{FPZ}	Change in length of fracture process zone at level of polymer tendon
ΔL_{nle}	Change in length of elastic beam elements at level of polymer tendon

Δz	Layer depth
ε	Strain
ε_0	Strain at the end of stress opening curve
$\bar{\varepsilon}$	Strain at reference height
ε_c	Strain at compressive strength limit
ε_{cm}	Mean concrete strain
ε_{cr}	Creep strain
ε_{cu2}	Maximum compressive strain
ε_E	Elastic strain
ε_{efc}	Effective creep strain
ε_{efm}	Effective mechanical strain
ε_{fr}	Strain parameter accounting for tensile damage in creep strain calculation
ε_H	Strain at time of healing
ε_{p0}	Drawing strain used in polymer manufacturing process
ε_R	Equivalent restrained strain
ε_{sh}	Shrinkage strain
ε_{sm}	Mean reinforcement strain
ε_t	Strain at tensile strength limit
ε_{TH}	Thermal strain
ε_{ve}	Viscoelastic strain
ε_{vec}	Viscoelastic creep strain
ε_{yk}	Characteristic steel yield strain
ε_{yk2}	Characteristic strain marking onset of perfect plasticity
ε_θ	Mid interval strain
ζ	Maximum strain parameter
η	Viscosity
η_1	Temperature independent viscosity
η_2	Temperature dependent viscosity
η_{2H}	Viscosity at low temperature
η_{2L}	Viscosity at high temperature
θ_2	Mid span beam rotation
λ	Retardation time

ρ	Reinforcement ratio
$\rho_{p,eff}$	Effective reinforcement ratio
σ	Stress
σ_H	Stress in healed material
σ_M	Maxwell arm stress
σ_p	Stress in polymer tendon
σ_{res}	Drawing stress
τ	Relaxation time
τ_c	Creep relaxation time
ϕ	Bar diameter
ϕ_c	Creep factor
Ψ_2	Quasi-permanent load factor
Ω	Stiffness matrix for beam system
ω	Damage parameter
ω_H	Damage parameter at time of healing

Chapter 1 - Introduction

1.1 Cementitious Materials

The use of cementitious materials for construction dates back to ancient times making them one of the oldest construction materials; early examples include the first true mortars which were used in Egypt, Greece, and Crete, and concrete's first use as a bulk construction material which is credited to Roman engineers (Hendrik 2005). The cementitious binder used in modern concrete, Ordinary Portland Cement (OPC), was discovered by Joseph Aspidin in 1824 (Hendrik 2005). In the almost two centuries since this discovery the cement and concrete industries have grown to a point where twice as much concrete is used annually as all other construction materials combined (McLeod 2005), and concrete is second only to water in terms of annual consumption by society (IEA and WBCSD 2009).

1.2 Major Problems with Concrete

1.2.1 Durability

Despite concrete's strength and versatility as a construction material, there are also significant drawbacks to its use, not least its durability issues. These issues stem from its susceptibility to cracking which is the result of its brittle nature and low tensile strength; properties that cause particular problems if concrete is loaded in tension or flexure. This inherent propensity for cracking is a problem that is known to jeopardise the strength, stiffness, durability and service life of concrete structures (van Breugel 2007).

Cracking is generally initiated through the formation of microcracks, which may later merge and develop into macrocracks. Cracks often allow the ingress of moisture and harmful chemicals which leads to issues such as freeze thaw damage and corrosion of the reinforcement; corrosion is particularly severe in saline environments such as marine applications or structures exposed to de-icing salts. This damage to the concrete and steel can lead to reduced capacity and potentially complete structural failure.

As cracking in reinforced concrete is effectively unavoidable, design is undertaken on the basis of limitation rather than prevention. Design codes such as the Eurocodes (BSI 2004) set maximum permissible crack widths which depend on the structure’s application. There are then three fundamental ways in which crack widths can be reduced (Mosley et al. 2012):

a) Reduce reinforcement stress
b) Reduce bar diameters thus reducing bar spacing
c) Increase the effective reinforcement ratio

Despite these design criteria, durability issues resulting from cracking are still common (Richardson 2002). The effects of cracking are of particular importance in fluid retaining and nuclear structures.

1.2.2 Sustainability

In addition to the problem of durability just described, there are major sustainability issues facing the cement and concrete industry, both in economic and environmental terms. The sustainability issues described below are intrinsically linked with the durability issues outlined above as any improvement in concrete’s durability will reduce the need for inspection, maintenance, repair, and eventually the replacement of a structure thus impacting positively on the sustainability of the material.

1.2.2.1 Environmental

It is estimated that for every tonne of OPC produced, approximately 1 tonne of CO_2 is released into the atmosphere (Davidovits 1994); when this is considered in conjunction with an annual global cement demand of approximately 4×10^9 tonnes the scale of the environmental issue facing the industry is clear (European Cement Association 2013). Global cement production is reported to account for 7-10 % of total global CO_2 emissions (McLeod 2005), placing it third behind the energy and transportation sectors (Pearce 1997).

1.2.2.2 Economic

As a result of the durability issues described above, concrete structures require frequent inspection, maintenance, and repair work; these ongoing works plus a structure's initial build cost are termed the whole life cost of a structure. The ongoing cost of a structure often accounts for a significant portion of the total, for example 38 % and 33 % of the UK and The Netherlands respective annual construction budgets are spent on these ongoing works (van Breugel 2009).

1.3 Existing Solutions

Solutions to the inherent durability and sustainability problems described so far can be categorised as either addressing the sustainability issue directly, or addressing the durability issue and thus to some extent indirectly improving sustainability. Although a number of solutions for improved sustainability are discussed in Section 2.3.2 the focus of this thesis is the durability of cementitious materials thus it is the second category of existing solutions that will be introduced here.

A common material design philosophy for improved durability is to create stronger materials which oppose the formation or extension of microcracks (RILEM 2013), an approach termed the "paradigm of damage prevention" (van der Zwaag 2007). When considering increased durability of a structure this damage prevention may be achieved either through the use of a stronger material, or appropriate structural design. In the case of concrete structures, appropriate design either means the use of prestressed concrete, or the provision of appropriate reinforcement and cover. Prestressed concrete is generally designed to be uncracked whereas in reinforced structures crack widths are restricted to a specified limit; typically 0.3 mm (BSI 2004). Despite carefully researched design criteria for both types of concrete structure, cracking still occurs in prestressed concrete and still exceeds the specified limit in reinforced concrete; highlighting that durability still poses a significant problem and that the damage prevention paradigm is not currently an entirely successful philosophy for concrete structures. This durability issue is generally managed through policies of regular inspection and maintenance; however these are not always possible and can be dangerous to the inspector and/or disruptive to the user. The maintenance of these structures upon the appearance of cracking can be achieved through a number of repair techniques including the use of mortar patch repairs, and the injection of resin or grout into macrocracks.

In recent years, with increasing focus from engineers and materials scientists on smarter materials, an alternate approach to the paradigm of damage prevention has been extensively investigated; that of self-healing cementitious materials. The progress of this rapidly increasing interest is presented in terms of the number of research publications in the field in Figure 1.1.

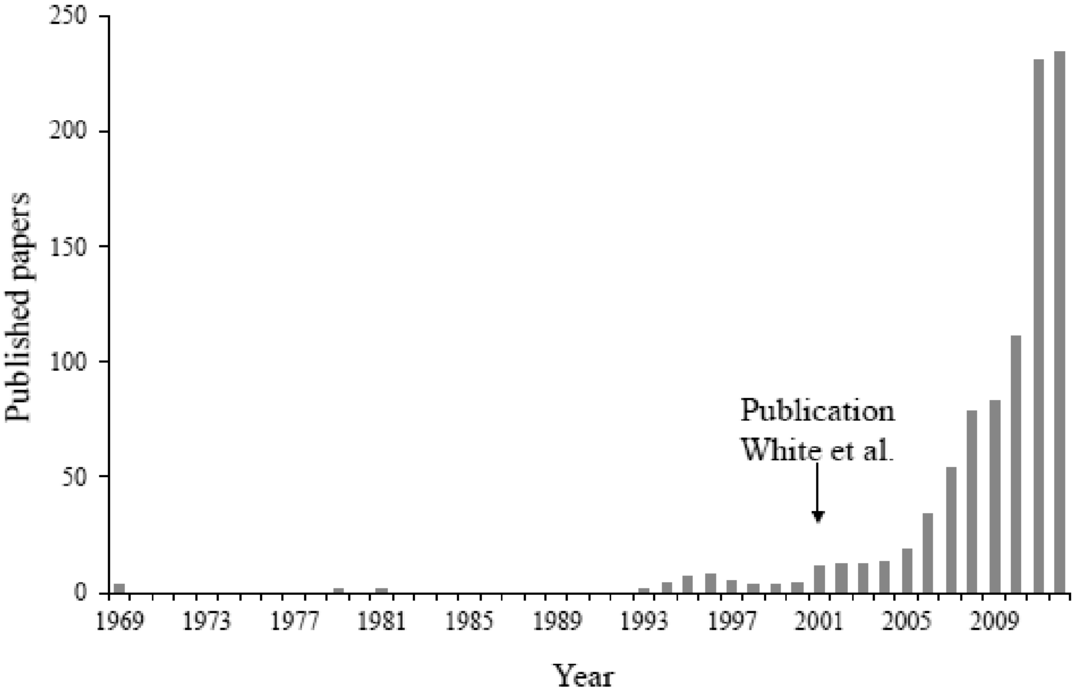

Figure 1.1 – Number of papers published on self-healing materials by year (Van Tittelboom and De Belie 2013)

This exciting new class of materials have the ability to respond to the onset of damage and repair themselves, thus durability is expected to be achieved through damage management as opposed to prevention (van der Zwaag 2007).

1.4 Motivation for Research

The research contained in this thesis is motivated by the requirement for improved sustainability within the construction industry, particularly the cement and concrete industries. Improving the durability of concrete structures will reduce the requirement for maintenance and new build structures to replace old, reducing the demand for cement and concrete and improving overall economic and environmental sustainability. Self-healing cementitious materials are a potential solution to this durability issue. A new self-healing cementitious material system called LatConX has been developed at Cardiff University and proven to be a viable concept by this research group (Jefferson et al. 2010); (Isaacs et al. 2013). This thesis will investigate the system further, focusing particularly on long-term performance and the potential for improved structural performance compared to current reinforced concrete practice.

1.4.1 The LatConX System

The LatConX system comprises shape memory polymer (SMP) tendons embedded within a cementitious matrix along with the required reinforcing steel. The SMP tendons are completely debonded from the concrete along their full lengths except for at their end anchorages. Upon activation, the SMP tendons shrink; this shrinkage is restrained by the concrete and thus induces a compressive force which closes any cracks present. Schematic diagrams of the system are shown in Figure 1.2 and Figure 1.3.

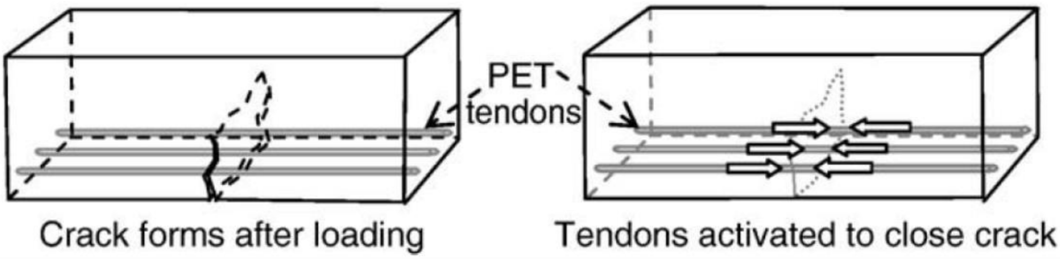

Figure 1.2 – Schematic representation of the LatConX system

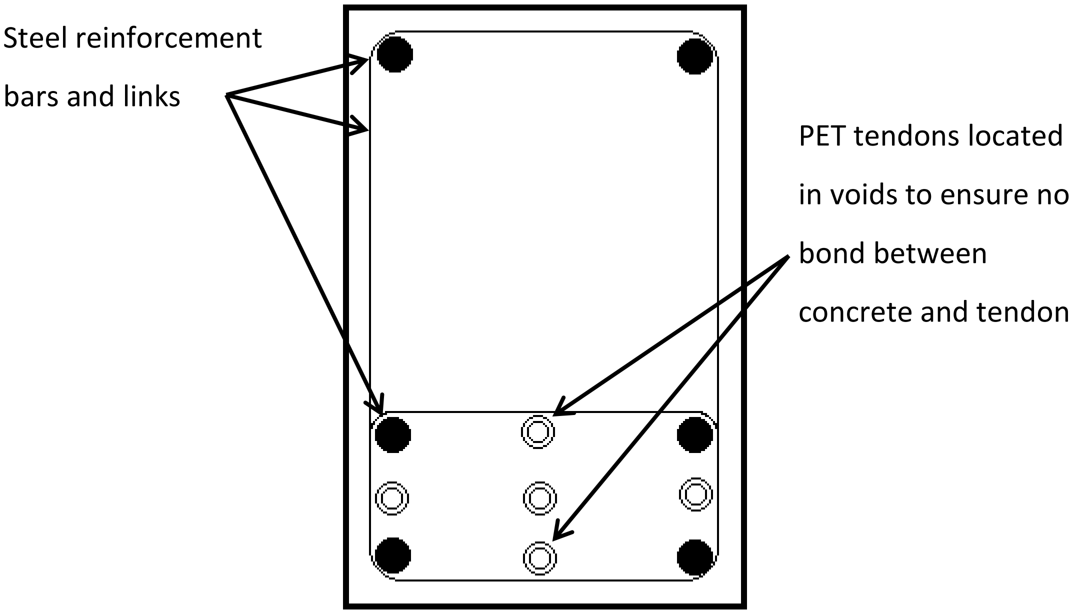

Figure 1.3 – Cross section through a mid span location of a beam containing the LatConX system

A paper published by members of the Cardiff University research group in 2010 demonstrated the concept to be viable both as a method of crack closure and low level prestressing. This publication also included screening tests which determined that pre-drawn PET was the most suitable SMP material for use in the system (Jefferson et al. 2010). In this paper the system is summarised by the following sequence:

1. Cracking occurs in the cementitious material due to early age shrinkage, thermal effects and/or mechanical loading.

2. The shrinkage mechanism in the anchored embedded polymer tendon (or tendons) is activated by heating, which results in crack closure and compressive stresses being developed across the closed crack faces.

Improved autogenous healing in laboratory specimens employing the LatConX system has also been observed, with strength recovery of between 80 and 200 % depending on curing conditions during healing (Isaacs et al. 2013).

Finally, in-depth studies of the restrained shrinkage behaviour of the suggested pre-drawn PET material were presented by Dunn et al. (2011), this is the same SMP material used in Chapter 3 of this thesis.

1.5 Scope and Objectives

The overriding aim of the research undertaken for this thesis was to further the knowledge and understanding of the proposed LatConX system for the closure and/or prevention of cracks in cementitious materials. Within this broad aim, the research focused on the following key objectives:

a) Determine the magnitude of any long-term stress relaxation processes of the proposed pre-drawn PET SMP material.
b) Develop a constitutive model for the restrained shrinkage behaviour and subsequent long-term stress relaxation of SMPs.
c) Develop a numerical model for the full LatConX system
d) Develop a design procedure for reinforced concrete beams incorporating the LatConX system
e) Investigate the long-term structural performance of beams designed to include the LatConX system compared with beams designed according to existing reinforced concrete principles.
f) Analyse and compare the material costs of standard reinforced concrete beams with LatConX beams.

1.6 Outline of Thesis

This thesis is divided into 7 chapters and there are also 3 appendices.

Chapter 2 is a review of the existing literature relating to all aspects of the proposed LatConX self-healing system and the research efforts presented within this thesis. The first section of this review introduces the concept of smart and intelligent materials and systems. It then moves on to discuss the sustainability issues facing the cement and concrete industry and potential solutions, including an in-depth discussion of self-healing cementitious materials as a potential durability solution. Polymers are introduced and some key properties and behaviours considered including shrinkage and the shape memory effect; other shape memory materials are also discussed. Finally numerical modelling techniques for the relevant materials and behaviours are discussed.

In Chapter 3 an experimental study of the long-term stress relaxation behaviour of polyethylene terephthalate (PET) is presented. Two methods of stress application were investigated with the stress relaxation considered over periods of time up to 280 days.

Two new transient thermomechanical constitutive models for the shrinkage and stress relaxation behaviour of SMP tendons are presented in Chapter 4. The models are validated and their capabilities compared using experimental data from Chapter 3. Some of the work from this Chapter and the experimental work of Chapter 3 are the subject of a publication in “Applied Polymer Science” (Hazelwood et al. 2014).

Chapter 5 presents the development of a layered beam model for the LatConX system. The preferred polymer model from Chapter 4 is combined with constitutive models for the relevant aspects of concrete and steel behaviour to allow transient mechanical simulations of a reinforced concrete beam including the LatConX system to be carried out. The beam model is validated by comparison with experimental data previously published by other authors (Jefferson et al. 2010); (Gilbert 2013) and Eurocode (BSI 2004) predictions. Some of the work from this Chapter is the subject of a publication submitted to the journal “Engineering Structures” upon which the authors are awaiting feedback.

In Chapter 6, the design implications of the LatConX system are discussed leading to the development of a suitable design procedure; including a proposed construction sequence and the derivation of design equations. Building on this, three parametric studies are presented comparing the structural performance and material cost of reinforced concrete elements designed with and without the LatConX system.

Finally, Chapter 7 collates the key conclusions from Chapters 3-6, and some recommendations for further work are given.

Chapter 2 - Literature Review

This Chapter presents a review of the existing literature relevant to the LatConX system, and the research techniques adopted throughout this thesis; the aim is to place the work into appropriate context within the civil engineering and material science field. There are four core topics covered in this review although there is inevitably an overlap in places, the topics are:

- Introduction to terms – The concept of smart and intelligent materials is introduced in conjunction with definitions of these terms and relevant others.
- Cement and Concrete – The state of the industry is discussed including the issue of sustainability. Existing solutions to improve sustainability and durability are presented, as well as an in-depth discussion of the potential solution that self-healing cementitious materials may provide. Alternative materials to steel for the reinforcement or prestressing of concrete are also reviewed.
- Polymers – Relevant properties of polymeric materials are introduced with a particular focus on thermal and mechanical behaviour. The shrinkage and shape memory properties of polymers and some other interesting materials are discussed. Finally, PET, the material selected for use in the LatConX system is described.
- Numerical material modelling – Relevant numerical modelling techniques for concrete and polymer are discussed.

2.1 An Introduction to Terms

The large number of specialist terms used within the literature to describe the wide and varied field of advanced material science naturally leads to a certain amount of ambiguity. For this reason the first section of this literature review will attempt to define the most important of these terms and subsequently define the LatConX material system’s position within their spectrum.

2.1.1 Self-healing vs Repair

In a thesis, which focuses on the development of a self-healing system, an initial definition of precisely what constitutes self-healing seems logical. According to a recent RILEM report, a material should be considered as self-healing if its recovery capability stems from the material design concept itself; in contrast, recovery due to some material replacement requiring human intervention is defined as repair (RILEM 2013).

2.1.2 Levels of Intelligence

To a large extent a material's ability to self-heal will be influenced by its level of intelligence. A hierarchy of intelligence has been proposed by the RILEM report which is shown in Figure 2.1. This hierarchy builds on the work of Mihashi et al. (2000) and Sharp and Clemeña (2004).

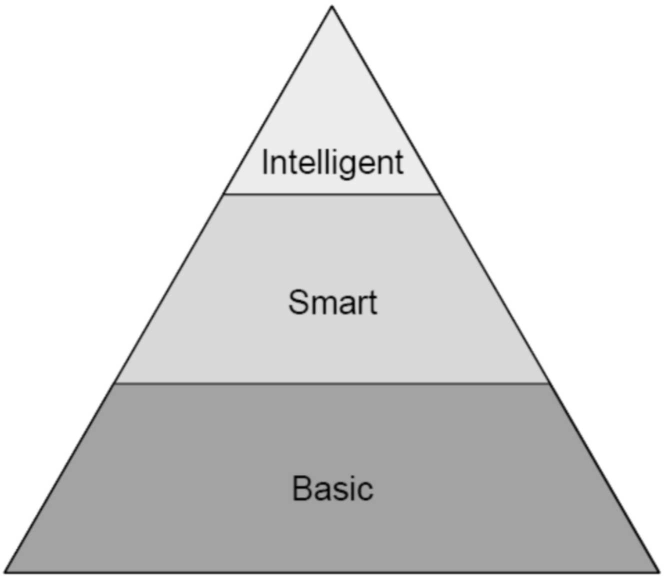

Figure 2.1 – Hierarchy of materials based on different levels of intelligence (RILEM 2013)

The basic class encompasses the vast majority of materials, these possess no intelligence and are therefore incapable of responding to environmental stimuli (RILEM 2013).

2.1.2.1 Intelligent Materials

Mihashi et al. (2000) define intelligent materials as those that “incorporate the notion of information as well as physical indexes such strength and durability”. This allows intelligent materials a self-control capability, meaning that their responses to external stimuli are conducted in a regulated manner (Joseph 2008). Many natural materials; including biological tissues such as bone, skin, and tendons; can be categorized as intelligent. Schmets (2004) attributes this intrinsic intelligence of natural materials, and subsequent adaptability, to their highly organised hierarchal structure, which is present at all levels (length scales) of the material. Schmets (2004) also remarks on the highly complex nature of these hierarchies, and the resulting complexity in incorporating them into man-made engineering materials. It is due to this complexity that the existence of these materials is currently largely limited to the early design and concept stage; particularly in the fields of medicine, bionics, and aeronautics/astronautics (Joseph 2008).

2.1.2.2 Smart Materials

These are materials that have been engineered to respond in a unique beneficial manner to certain changes in their surrounding environment (Sharp and Clemeña 2004). Examples of these include shape memory materials, piezoelectric materials, temperature responsive polymers which change colour with temperature, and smart gels which can shrink or swell by large factors in response to chemical or physical stimuli. Considering these definitions, Joseph (2008) states the key distinction between intelligent and smart materials as the degree to which they can gather and process information, and react accordingly.

2.1.2.3 Smart Structures

These differ from smart materials as they are engineered composites composed of basic materials. The combined properties of these basic materials result in the smart structure exhibiting sensing and actuation properties (Joseph 2008). This class of materials are not included on the intelligence hierarchy shown in Figure 2.1, however can probably be considered as equal in intelligence to smart materials.

2.1.2.4 Sensory Structures

Joseph (2008) introduces sensory structures as the fourth and least intelligent category of advanced materials. These are defined by their ability to sense the conditions of their environment, and inability to actuate any sort of intelligent response to those conditions. Examples include: smart bricks, smart optical fibres, and smart paints; which can all monitor different relevant environmental aspects. Logically this category seems to lie in a sub-category of materials between the basic and smart levels in Figure 2.1.

2.1.2.5 Intelligence in the Context of Self-healing Cementitious Materials

The RILEM report (2013) gives a good explanation as to how these definitions of material intelligence apply to self-healing cementitious materials. The closure of cracks in ordinary concrete materials through processes such as mechanical blocking and carbonation would be a basic intelligence process. A smart material would require the addition of some encapsulated healing agent, thus the healing process is activated by release of the agent through cracking of the material. Finally an intelligent cementitious material would require a sensor and feedback mechanism of some kind to trigger and control the self-healing mechanism.

2.2 Self-healing Materials

The majority of self-healing materials are classed as smart and not intelligent as they rely on previous knowledge of the nature of the damage they are likely to be subject to (Joseph 2008); for example self-healing polymers, coatings and composites, none of which are capable of moderating their response to the relevant stimuli.

Further to this, many are considered to be smart structures and not materials as the healing mechanism is often the release of encapsulated healing agents by the onset of damage, this agent heals the damage, thus increasing the materials' life (Joseph 2008). It is for this reason that self-healing materials are displayed as a subclass of smart structures in Figure 2.2, which introduces four new terms to the self-healing vocabulary; autonomic healing, autogenous healing, and the passive and active modes of healing.

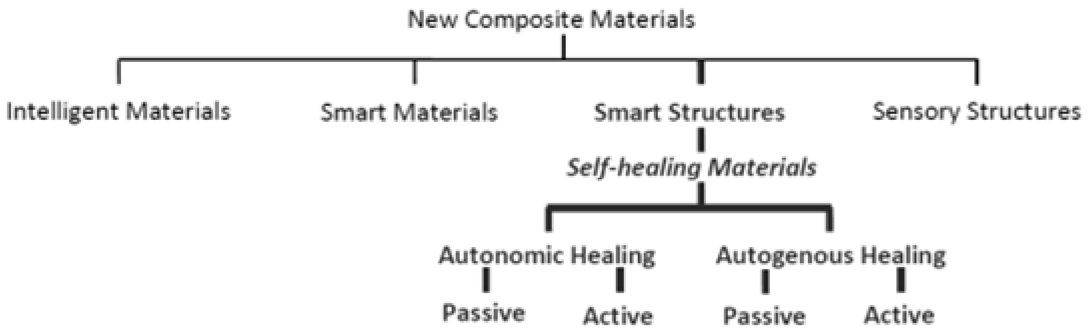

Figure 2.2 – Tree diagram highlighting new advanced composite materials (Dunn 2010)

2.2.1 Autonomic and Autogenous Healing

The RILEM report (2013) defines two distinct types of self-healing mechanism, namely autogenous and autonomic. The mechanism is considered autogenous if it solely depends on components of the material that could still be expected to be present when not specifically designed to self-heal. Conversely, the mechanism is considered autonomic if it relies on components of the material that would not usually be present.

The best examples of autogenous healing mechanisms come from cementitious materials. Their autogenous healing mechanisms include hydration of unhydrated cement within the matrix, mechanical blocking of cracks, and the formation of calcite.

An example of an autonomic healing mechanism is the system developed for the self-healing of polymers by the group at University of Illinois (White et al. 2001); the system is displayed in Figure 2.3. A microencapsulated healing agent and a catalytic trigger are incorporated within an epoxy matrix; cracking of the epoxy resin causes the microcapsules to rupture and release the healing agent, which polymerises upon contact with the catalyst and bonds the crack faces.

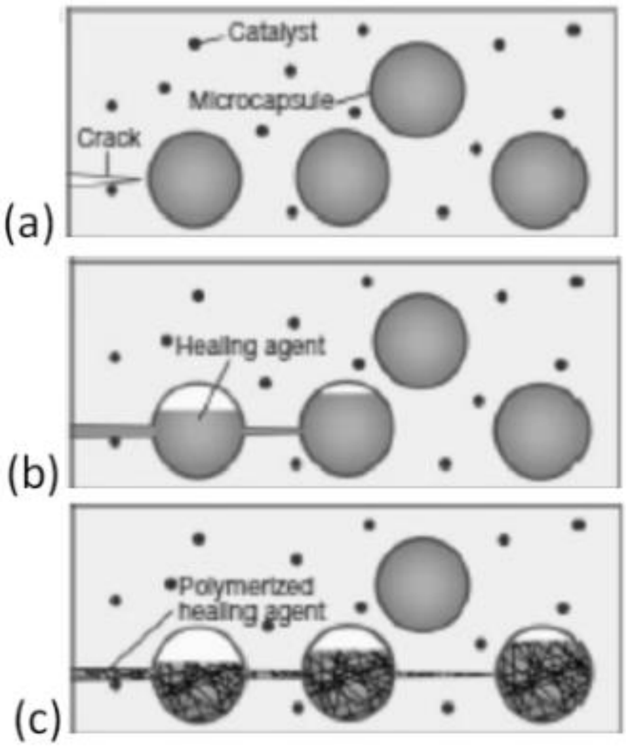

Figure 2.3 – Autonomic self-healing polymer system (White et al. 2001)

2.2.2 Passive and Active Modes

These two healing modes are differentiated by their requirements for human intervention; a passive mode process does not require any, whereas an active mode process does (RILEM 2013). Their respective benefits are summed up by the RILEM report (2013); a fully passive system does not require any inspection, repair or maintenance; whereas in an active system, the requirement for human intervention allows a larger degree of control, and is therefore likely to inspire greater confidence in the end user.

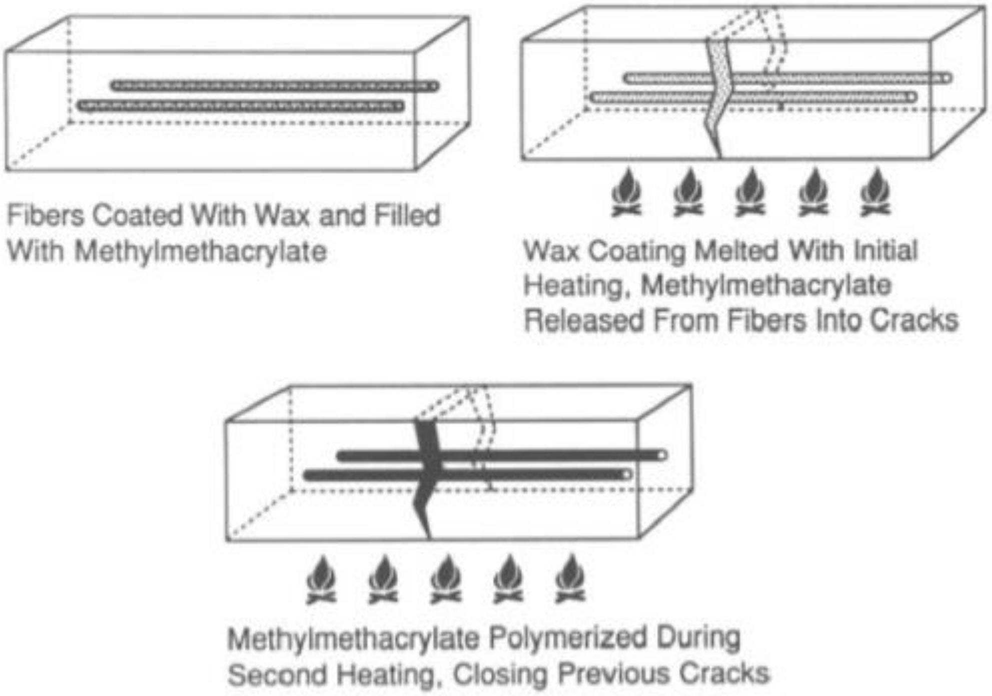

Figure 2.4 – Example of active mode in which healing agent is released through melting of wax coating (Dry 1994)

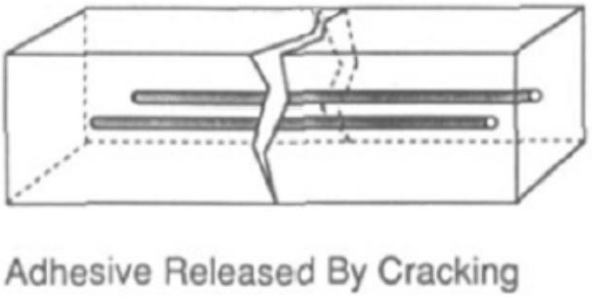

Figure 2.5 – Example of passive mode in which healing agent is released through cracking of the matrix (Dry 1994)

The distinction between these two modes is well clarified by consideration of the healing tests carried out on concrete by Dry (1994), the active and passive modes are displayed in Figure 2.4 and Figure 2.5 respectively.

The vision for a fully developed LatConX system involves a combination of SMP tendons for crack closure/limitation, and a healing agent with associated delivery system. Thus, according to the definitions laid out thus far, the LatConX system is a smart structure incorporating a smart material (SMP tendons). Activation of the SMP tendons is likely to rely on human intervention, thus the system cannot be considered completely passive. There is potential for further development into an entirely passive intelligent material system, this would be require the inclusion of sensors able to identify damage and moderate the appropriate response i.e. activation of the polymer tendons, and/or application of the healing agent. This is however beyond the scope of the current research.

2.3 Cement and Concrete Industry

The use of cementitious materials in construction is an ancient practise dating back as far as the Ancient Egyptian and Greek times, the first use of pozzolanic cements is usually credited to the Ancient Romans (Hendrik 2005). The Romans used these pozzolanic cements for a range of construction purposes, including the waterproof lining of aqueducts, and the construction of sea walls.

The ordinary portland cement (OPC) used in the production of concrete today was not discovered until 1824, when Joseph Aspidin filed a patent for it, the patent was called: “An improvement in the modes of producing an artificial stone” (Hendrik 2005).

As is well known, concrete is a relatively strong material in compression with the strength of traditional concrete varying between 20 MPa and 60 MPa, high strength concretes have strengths between 150 and 200 MPa, and very high strength cement based composites have been produced with compressive strengths up to 800 MPa (RILEM 2013). However, in tension, concrete is relatively weak with a typical tensile strength being 10 % or less of the compressive strength (Neville 1996). It is this low tensile strength combined with its brittle nature that renders concrete susceptible to cracking (van Breugel 2009), the need to control this cracking is the reason that concrete elements are usually reinforced in the tension zone. Reinforced concrete structures are designed according to relevant design codes such as the Eurocodes (BSI 2004), with maximum crack widths limited to between 0.1 and 0.4 mm depending on the application. Requirements laid out in these design codes often require increases in section dimensions, reinforcement areas, or concrete cover to ensure that crack widths remain satisfactorily small; this can leave structures overdesigned in some respects. In contrast, van Breugel (2009) reports that around 90 % of durability problems in concrete structures stem from failure of the concrete cover and subsequent corrosion of the reinforcement, suggesting that the current design procedures may be inadequate.

Despite concrete's shortcoming in its ability to resist tensile forces, it is the most used construction material on earth, and second only to water in terms of the total volume used annually by society (IEA and WBCSD 2009). To put this in other terms, twice as much concrete is used in construction every year as all other building materials combined (McLeod 2005).

2.3.1 Current Issues

There are several inherent sustainability issues linked to the use of concrete, these will be discussed in detail in the following sections. These issues are only exacerbated by concrete's propensity for cracking and the subsequent reduction in the durability and life of a structure. Thus any means of reducing cracking and improving durability will have an immediate positive effect on concrete's sustainability.

2.3.1.1 Environmental Sustainability

Concrete's greatest impact on the environment comes from the production of cement which has been reported to account for 7-10 % of total global CO_2 emissions (McLeod 2005); this ranks cement production as the third largest contributor, behind the transportation and energy sectors, and ahead of the aviation industry (Pearce 1997). Global cement production in 2013 has been estimated at 4×10^9 tonnes (European Cement Association 2013).

Considering that 60 – 130 kg of fuel oil, and 110kWh of electricity are required to produce each tonne of cement (UNEP 2010); which equates to emissions totalling almost 1 tonne of CO_2 for every tonne of cement produced, it is no surprise that the cement industry is responsible for such high emissions. The 1 tonne of CO_2 produced for every tonne of cement is the total of approximately 0.55 tonnes of emitted through the reaction process, and approximately 0.4 tonnes from the fossil fuel required to heat the process (Davidovits 1994).

2.3.1.2 Economic Sustainability

Wherever one looks, the maintenance of concrete structures has a major economic impact. In the UK, £ 47 billion (38 % of the annual construction spend) is spent on the maintenance of existing infrastructure (Department of Trade and Industry 2014). In the Netherlands one third of the annual budget for large civil engineering works is spent on inspection, monitoring, maintenance and repair (van Breugel 2009). Finally, the average annual maintenance spend for bridges in the US has been estimated at $ 5.2 billion (RILEM 2013). In addition to this, it is estimated that indirect costs to the infrastructure users as a result of traffic jams and loss of productivity can be as high as 10 times the direct maintenance costs (Freyermuth 2001).

2.3.1.3 Social Issues

Social issues surrounding the sustainability of concrete materials include public nuisance due to maintenance and inspection work, as well as reduced road safety stemming from a poorly maintained highway infrastructure (Dunn 2010). For example, in the USA in 2000, the cause of 30 % of all traffic fatalities was considered to be inadequate road conditions (Li et al. 2004).

2.3.1.4 Future Projections

Review of previous Activity Reports from the European Cement Association shows a year on year increase in cement production which can be observed in Figure 2.6. According to Taylor et al. (2005) there has been a relatively stable relationship between cement consumption and the size of the global economy since the 1970s, with every 1000 US$ of GDP equating to approximately 40 kg of cement. However, Taylor et al. go on to say that the stable trend at a global level masks a large range of trends across different regions. Specifically, the cement demand in Europe and North America has shown little change, whereas China alone has accounted for around two-thirds of the global growth in demand (Taylor et al. 2005). The upshot of this continued increase in cement demand according to the RILEM report (2013) is that unless the current production techniques can become less carbon intensive, cement production's contribution to global CO_2 emissions will only continue to grow. This prediction appears to be confirmed by the increase in cement's contribution to global emissions from the 5 % stated by Worrell et al. (2001) in 2001, to 7-10 % in 2005 (McLeod 2005).

Contrastingly, Duxson et al. (2007) see the large demand and production levels of the expanding markets of China and India as a potential opportunity for an improvement in sustainability, suggesting that these markets may be more open to adopting newer, less carbon intensive solutions.

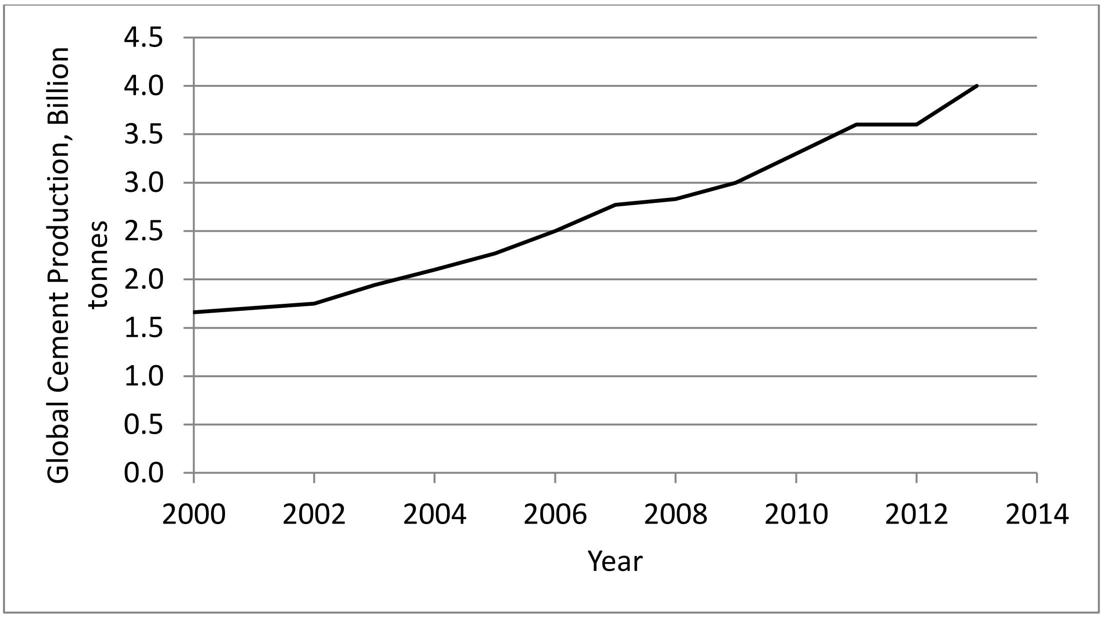

Figure 2.6 - Global cement production year on year (European Cement Association 2013)

The Cement Technology Roadmap in 2009 (IEA and WBCSD 2009) set out projected targets for global annual cement consumption of between 3.7 and 4.4 x 10^9 tonnes by 2050, along with an intermediate projected target of between 3.4 and 3.5 x 10^9

tonnes in 2015 (See Figure 2.7). Comparing these projections with the figure of 4 x 10^9 tonnes for 2013 (European Cement Association 2013) given above suggests that the cement industry is very unlikely to meet the 2015 target, and significant progress will be required to meet the 2050 target.

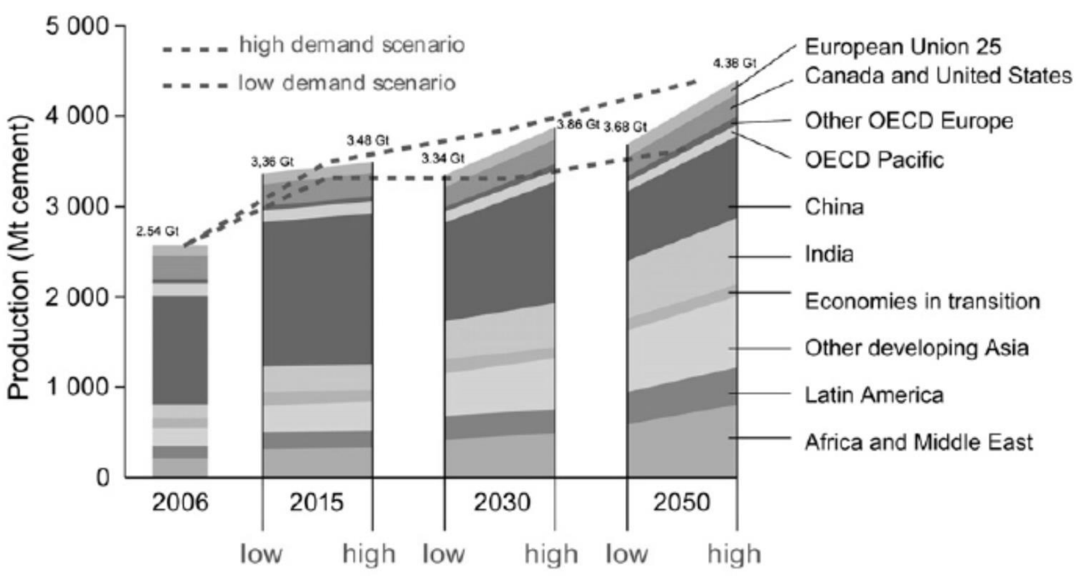

Figure 2.7 - Projected global cement production (IEA and WBCSD 2009)

2.3.2 Existing Sustainability Solutions

Hendrik (2005) offers four main strategies to reduce the CO_2 emissions from the cement industry, these can be summarised as:

1. The use of lower carbon fuels.
2. More fuel efficient kilns.
3. Reduced CO_2 emissions from the calcination process by using raw materials that will contribute CaO for clinker from a source other than $CaCO_3$ (limestone).
4. Reduced clinker content for the final cement product through the use of supplementary materials.

The initial impetus for a more sustainable cement industry was the OPEC oil embargo of 1973. This lead to less of a dependence on oil, along with an improvement in fuel efficiency throughout the manufacturing processes (Gartner

2004); thus addressing points 1 and 2 above. Indeed, the average specific kiln fuel energy requirement for clinker manufacture reduced by approximately 40 % in the two decades following 1973. Gartner also points out that as there is already a high level of energy efficiency any further research lead gains are likely to be minor, in fact the biggest barrier to a continued improvement in energy efficiency is most probably the need for both time and capital to allow all cement producers to introduce the most energy efficient technologies (Gartner 2004).

Blended cements are those in which the proportion of clinker in the cement is reduced and replaced with an alternative pozzolanic material such as GGBFS, fly ash, silica fume, or a natural pozzolan i.e. volcanic material. These blended alternatives to OPC are capable of achieving the same performance levels while reducing associated emissions as the materials used are either by-products of other industries or naturally occurring (Hendrik 2005). The reduction in clinker to cement ratio in blended cements can be as much as 60 % (Worrell et al. 2001). Potential drawbacks to these blended cements are a lack of availability of the replacement materials compared to the highly abundant limestone used to produce clinker (Gartner 2004), the resulting potentially large transportation distances involved will cause large cost variation and undermine the potential environmental gains (Worrell et al. 2001). Lothenbach et al. (2011) provide a good summary of the underlying science governing the behaviour of a number of these blended cements.

A potential solution that completely removes the need for OPC is geopolymeric cement, a cementitious binder that can offer emissions reductions of up to 80 %. Geopolymers are based on aluminosilicates either from natural sources such as Kaolin, or waste materials such as fly ash. The curing of geopolymer cements occurs through a process called polycondensaton activated by a highly alkaline environment instead of the hydration required by OPC (Schneider et al. 2011). This polycondensation process removes any reliance on calcination, reducing their carbon output; further to this they do not require the same extreme kiln temperatures thus reducing fossil fuel emissions; finally the required raw materials are available on all continents so costs and emissions due to transport are expected to be acceptable (Davidovits 2010). Other benefits of this technology include rapid strength gain, good resistance to heat, acids and salt solutions, low shrinkage and thermal conductivity, and inherent protection of steel reinforcing due to high residual pH and low chloride diffusion rate (Duxson et al. 2007).

Ceratech, a company based in the USA, have developed a cementitious binder consisting of 90-95 % fly ash combined with chemical actuators (Vander Werf 2012). Although similar in composition to some geopolymeric binders the chemical actuators required are in fact quite different and much less caustic and therefore safer (Patel et al. 2012). The result is a binder with strong cementitious properties; concrete from a typical mix can achieve a 28 day strength of 55 MPa and is reported to be considerably more resistant to chemical and heat exposure owing to its dense nature and lack of interconnected capillaries found in more conventional concrete (Vander Werf 2012).

A group of researchers from Imperial College in London have developed a novel cement that does not emit any CO_2 during the reaction process for its production; moreover the cement actually absorbs a considerable amount of CO_2 from the atmosphere as it cures. The cement is produced from magnesium oxide, which is obtained from the abundantly available magnesium silicate; there are two advantages to this, the reaction happens at approximately half the temperature of that for OPC so less fuel is required and no CO_2 is given off during the reaction, resulting in total CO_2 emissions of approximately 0.4 tonnes per tonne of cement produced. In addition to this, the new cement absorbs roughly 1.1 tonnes of CO_2 from the atmosphere as it hardens giving a net absorption of 0.7 tonnes per tonne; OPC does this too, however only in relatively small quantities (between 0.2 and 0.5 tonnes) (Kennett 2009).

It is clear that all material solutions described above have the potential to address the sustainability issues surrounding OPC to a differing extents; however any success will rely on their ability to overcome the significant challenge of achieving widespread implementation within the construction industry. Major obstacles to this goal include the lack of certification of potential raw material sources, the lack of appropriate design codes as all are currently based on the use of at least a minimum amount of OPC, and finally a lack of long-term durability data. The difficulty imposed by these obstacles is compounded by the conservative nature of the construction industry (Duxson et al. 2007). This conservatism in relation to new technologies is understandable, considering the potentially catastrophic consequences of a material failure. These potential consequences are exemplified by the issues surrounding High Alumina Cement Concrete, a novel material concept which caused a number of collapses in the 1970s (Currie and Crammond 1994).

Despite the obstacles outlined above, realising real-world adoption of new construction materials is not impossible. This is well demonstrated by the example of Van Deventer et al. (2012) who describe their success in implementing the geopolymeric cement E-crete in real-world construction projects. They highlight the “vast regulatory, asset management, liability and industry stakeholder engagement process” that was necessary for the technology’s commercialisation. It is anticipated that the process of industrial implementation and commercialisation of the LatConX system will face similar challenges, thus this success is encouraging for the future development of the system.

A more common method of crack prevention in concrete structures, resulting in improved durability, is the use of prestressed concrete which is designed to be uncracked at the serviceability limit state. However there are some problems with these systems; firstly, the steel tendons, anchors, and jacking equipment are expensive; secondly, there are a number of health and safety issues related to their use (Dunn 2010). Attempts have been made to overcome the cost and safety issues by using shape memory alloys (SMA) as a post-tensioning mechanism thus eliminating the need for the jacking process. This system will be discussed in more detail in a more relevant later section; relevant examples in the literature include, but are not limited to, the works of Maji and Negret (1998), El-Tawil and Ortega-Rosales (2004), Deng et al. (2006), Saiidi et al. (2007), and Li et al. (2007).

2.3.3 Self-healing Cementitious Materials

In recent years a large amount of literature has been generated relating to improved durability of concrete through the development of self-healing cementitious composites, in this Section some of the key developments and techniques in this field are introduced and discussed.

As described in Section 2.2.1, the RILEM report into Self-healing Phenomena in Cement-based Materials (RILEM 2013) introduced two distinct types of healing mechanism within cementitious materials, autogenous healing and autonomic healing. Both of these healing mechanisms have received significant attention from researchers aiming to develop materials with better healing capabilities and thus improved durability.

2.3.3.1 Autogenous Healing

Autogenous healing refers to the ability of concrete mixes with no special additives to fill and seal cracks throughout the material's life (RILEM 2013).

2.3.3.1.1 Intrinsic Autogenous Healing

The natural healing ability of concrete was first recognised by the French Academy of Science in 1836 (Hearn 1998), however it was not studied in detail until near the end of the 19th century (Hyde and Smith 1889). A more systematic study was subsequently carried out by Glanville (1931) who introduced the distinction between self-sealing, where cracks close but no strength is regained, and self-healing, where the crack closure is accompanied by strength regain. According to Wu et al. (2012) there are several potential causes of the self-healing/sealing phenomena:

- Formation of calcium carbonate or calcium hydroxide
- Blocking of cracks by impurities in the water and loose concrete particles as a result of crack spalling
- Hydration of previously unhydrated cementitious materials
- Expansion of the hydrated cementitious matrix in the crack flanks

Most researchers are in agreement that the two primary mechanisms of crack healing are the formation of calcium carbonate (carbonation), and the hydration of unhydrated cement particles (Edvardsen 1999); (Ramm and Biscoping 1998).

The contribution of these mechanisms to the healing process is not entirely clear. Neville (2002) maintains that the relative contributions depend on the concrete age; if cracking occurs at a young age, the relatively large amount of unhydrated cement causes ongoing hydration to be the more significant of the two, whereas if cracking occurs at a later age, carbonation is the more likely major mechanism. Neville and the majority of other researchers agree that the presence of water is essential for both mechanisms(Ramm and Biscoping 1998); (Edvardsen 1999); (Neville 2002); (Reinhardt and Jooss 2003); (Clear 1985). ter Heide and Schlangen (2007) found that the age of a specimen at cracking has a significant effect on the strength regained through healing (see Figure 2.8) with specimens cracked at a younger age (less than 24 hours) regaining the most strength, and specimens cracked at 72 hours displaying little, if any, strength regain. This suggests that carbonation is useful as a self-sealing mechanism but does not result in any significant self-healing.

Van Tittelboom et al. (2012) suggest that the finer cement grains produced by modern techniques have led to a reduction in the capacity of modern structures for autogenous self-healing; this reduction is the result of the increased efficiency of the hydration reactions due to the increase in the cement’s relative surface area. Granger et al. (2007) propose that a reduced water/cement ratio will counteract this trend by increasing the proportion of unreacted cement. Similarly, van Breugel (2007) suggests a return to the use of coarser cement to improve a material’s capacity for autogenous healing, however the issue of increased initial reaction times is raised.

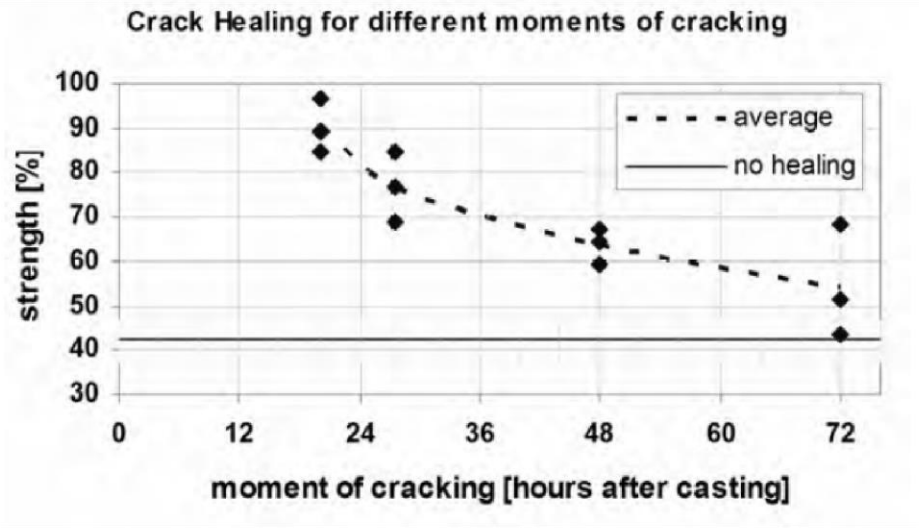

Figure 2.8 – Effect of specimen age at cracking on strength regain during healing (ter Heide and Schlangen 2007)

An important factor to consider is the maximum crack size that can be healed by these intrinsic mechanisms. There is no clear answer to this question at the present time and different results have been observed by several different authors. A range of these reported results and their origins are displayed in Table 2.1.

Table 2.1 – Maximum healable crack widths

Maximum healed crack width (µm)	100	200	205	300
Reference	(Reinhardt and Jooss 2003)	(Edvardsen 1999)	(Aldea et al. 2000)	(Clear 1985)

The general finding throughout the references in Table 2.1 is that the quality and degree of crack healing improved with decreasing initial crack width, and the smaller the initial crack the more likely the occurrence of complete healing.

ter Heide and Schlangen (2007) took their investigation into the effect of crack width on healing efficiency a step further by comparing healing between specimens in which the cracks were left open at a width of 50 µm, and those in which cracks were closed and held shut by a compressive force. The results of this investigation in Figure 2.9 clearly show that closure of a crack by a compressive force has a beneficial effect on the strength regained during healing; however, the magnitude of the force does not seem important as long as it is sufficient to bring the cracked faces into contact.

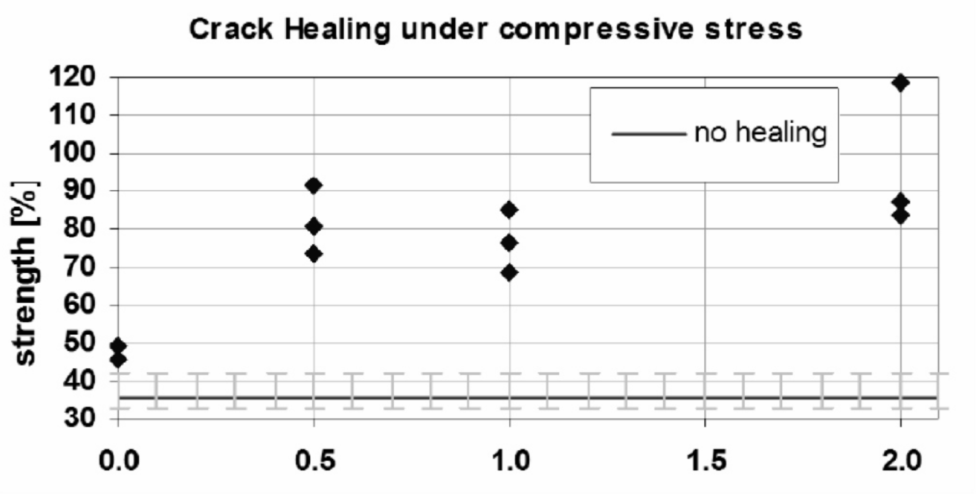

Figure 2.9 – Effect of compressive stress across cracked faces on strength regain during healing (ter Heide and Schlangen 2007)

The slowed reaction times of some alternative binders relative to that of OPC prompted some researchers to investigate the self-healing capabilities of mixes containing different levels of blast furnace slag, fly ash, and limestone. The conclusion of this was that healing capability is most improved by the use of blast furnace slag as the alternative binder, a reduced water/binder ratio was also found to increase healing capability (Van Tittelboom et al. 2012).

Qian et al. (2009) compared the effects of air curing with water curing on the self-healing behaviour of engineered cementitious composites. The key finding was that water curing gave significantly enhanced healing with a 65-105 % recovery of strength compared to 40-60 % for air curing.

Reinhardt and Jooss (2003) considered the effect of temperature on autogenous healing and concluded that higher temperatures yield a faster healing process.

2.3.3.1.2 Improved Autogenous Healing

Improved autogenous healing has elements of both autogenous and autonomic healing. The healing mechanism itself relies solely on the standard constituents of a concrete mix, however non-standard additions are included with the aim of enhancing the effectiveness of the autogenous healing mechanism. If no further healing agent is added then the LatConX system would be included in this category.

One of the simplest yet most effective methods of improving concrete's autogenous healing capability is to limit crack widths; as noted above, researchers are in agreement that healing improves considerably as the crack width decreases. Li et al. (1998) first suggested the use of polyethylene fibres distributed throughout the matrix to minimise crack widths in self-healing cementitious materials in the late 1990s before proving the effectiveness of the system in relation to autogenous healing some years later (Yang et al. 2009); (Yang et al. 2011). This system was named an engineered cementitious composite (ECC). ECC are characterised by their high ductility, and unique cracking properties; instead of forming one macrocrack in regions of tensile strain, multiple microcracks form with the maximum width remaining below 60 µm.

An alternative approach for limiting crack widths is that reported in two papers by Kuang and Ou which takes advantage of the unique superelastic behaviour phenomenon of SMA wires (Kuang and Ou 2008a); (Kuang and Ou 2008b); this behaviour is described in more detail in Sections 2.4.3.1, and 2.6.1. The experiments undertaken showed this to be a highly effective method for ensuring the post-damage closure of cracks (see Figure 2.10), however the improvement in autogenous healing as a result cannot be judged as the SMA wires were employed in conjunction with a healing agent rendering the healing mechanism autonomic.

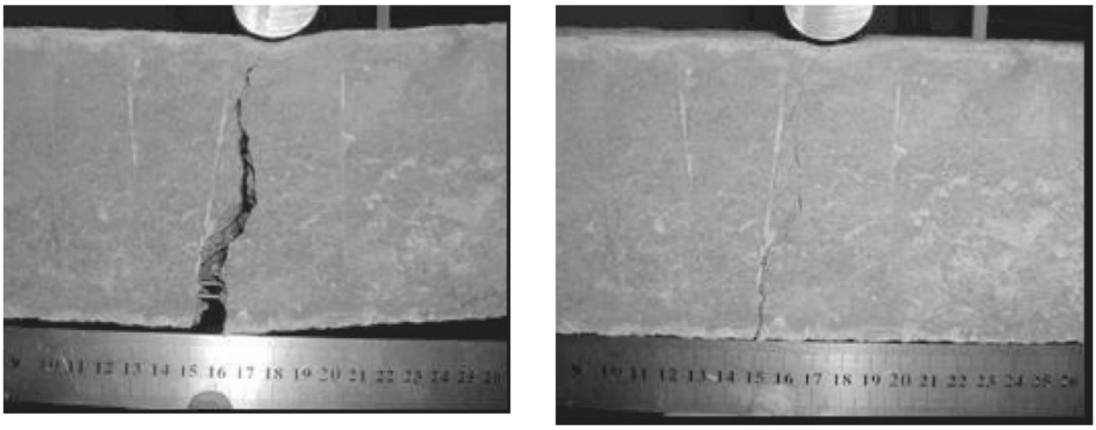

a) At maximum deflection b) After unloading: the crack almost disappeared

Figure 2.10 - Crack closure using superelastic shape memory alloys (Kuang and Ou 2008a)

Another method for assisting the autogenous healing mechanism is to provide an internal water supply for improved hydration upon cracking. One such recent technique involves the inclusion of superabsorbent polymers in the concrete mix (Lee et al 2010); (Kim and Schlangen 2011); (Dejonghe et al 2011); (Snoeck et al. 2012). This technique was found to improve the self-healing effect resulting in greater crack closure and greater regain of mechanical properties; perhaps more importantly, these specimens were also confirmed as able to partially heal without water curing (Snoeck et al. 2012). A similar method was studied by Qian et al. (2010) who exploited the water retaining properties of nanoclay concluding that this approach allowed the internal curing and healing of microcracks.

The use of expansive additives within the matrix has also seen some success. Sisomphon and Copuroglu (2011) trialled the inclusion of calcium aluminate based agents; water ingress triggered crack sealing through the formation of ettringite crystals, however the expansive properties of the additive caused microcracking in the interfacial transition zone. Encapsulation was proposed as a solution to prevent the problem of uncontrolled expansion.

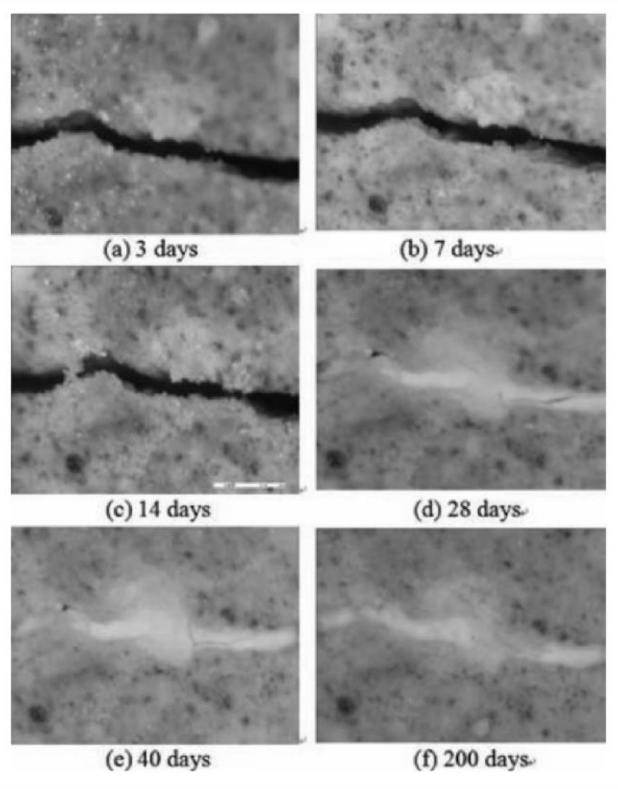

Figure 2.11 – Time evolution of improved autogenous healing for a cementitious material incorporating geo-materials (Ahn and Kishi 2009)

Ahn and Kishi (2009) demonstrated impressive crack sealing results (Figure 2.11) by replacing 10 % of the cement content with a combination of geo-materials and expansive agents, however no mechanical tests were undertaken so the healing capability of the mix is not clear.

Abd-Elmoaty (2011) investigated the self-healing effect in polymer modified concrete (PMC) in which organic polymers are distributed throughout the matrix. Cement hydration causes these polymers to coalesce into a co-matrix of hydrated cement and polymer film (Van Tittelboom and De Belie 2013).The healing mechanism still relies on the presence of unhydrated cement, however it was enhanced because a greater amount of this unhydrated material was available due to the encapsulating effect of the polymer membranes.

Considering the above observations from the existing research it seems that, for the LatConX system to be most effective at encouraging autogenous healing, activation should take place at an early age, cracks should be reduced to a minimum, and if possible the healing process should be aided by warm water curing. A specific concrete mix designed to improve autogenous healing should also be considered.

2.3.3.2 Autonomic Healing

Autonomic healing is a very wide term encompassing any healing mechanism that relies on the presence of a healing agent not normally found in a cementitious material, these healing agents are generally supplied to the damaged areas in one of two ways; microencapsulation, or through vascular networks.

2.3.3.2.1 Healing Agents

The properties of the healing agent are obviously going to be of significance to the final healing result. Joseph (2008) states that the effectiveness of an agent-aided healing process depends on both the capillary force (which increases with decreasing crack width) and the viscosity of the healing agent (a reduction in viscosity increases the repaired area). Another requirement is that the bond formed by the healing agent must have sufficient strength to prevent reopening of the crack, thus forcing new cracks to open and increasing the specimen’s total fracture energy for failure. Finally Joseph discusses the economic factors that must be considered, noting that for application in bulk construction products like concrete, any healing agent must be low cost and readily available off the shelf.

Van Tittelboom and De Belie (2013) categorise healing agents used in conjunction with cementitious materials according to their activation mechanism.

The first category are agents cured by contact with moisture, air, or the action of heat, examples include methyl methacrylate (Dry 1994), cyanoacrylate (Li et al. 1998); (Joseph et al. 2010), and one part epoxies (Thao et al. 2009). (Li et al. 1998) noted that the very reactive cyanoacrylate sometimes hardened earlier than required, reducing its effectiveness as a healing agent, this was not a problem with the less reactive one part epoxy agent (Thao et al. 2009).

A second category of healing agents includes those activated by contact with the cementitious matrix. Huang (2011) and Pelletier (2014) both used an encapsulated sodium silicate solution which forms calcium silicate hydrate (CSH) upon contact and subsequent reaction with the calcium hydroxide naturally present in the matrix. A benefit of this agent is that it avoids any premature hardening of the agent as activation can only occur when it is brought into contact with the cementitious matrix, something most likely caused by the onset of damage (Van Tittelboom and De Belie 2013).

Finally there are two-part healing agents that require both parts to come into contact with each other for the healing mechanism to be triggered. The two parts can either both be encapsulated or one encapsulated and one free within the matrix (Van Tittelboom and De Belie 2013). One potential problem with these two part healing agents is their reliance on sufficient mixing upon their release which is difficult to guarantee (Van Tittelboom et al. 2011). Dry and McMillan (1996) suggest that the increased shelf life of multiple part healing agents is a key benefit. Yang et al. (2011) and Wang et al. (2013) both trialled the use of methylmethacrylate monomer and triethylborane as the healing agent and catalyst respectively, finding that the agent and catalyst pairing led to a decrease in permeability of the specimens and an increase in crack resistance and toughness. Van Tittelboom et al. (2011) trialled the use of a two-part polyurethane expanding foam with the two-parts separately encapsulated and reported good results. The two capsules were connected in an attempt to ensure improved mixing of the separate parts; an approach that found success. The expansive reaction was beneficial for two reasons, firstly as it forced any remaining healing agent out of the capsules, and secondly as the additional volume in the matrix was more efficiently filled by the healed material.

A full review of all aspects of the performance of the large variety of healing agents trialled by researchers around the world is beyond the scope of this thesis, however detailed information on these topics can be found in the review by Van Tittelboom and De Belie (2013).

2.3.3.2.2 Healing Agent Encapsulation

A common method for implementing some of the above healing agents into a cementitious matrix is through microencapsulation. This often renders the material system a smart structure as the onset of damage ruptures the microcapsules, releasing the healing agents, and triggering the healing mechanism.

Dry (1994) presented the first instance of a microencapsulated self-healing cementitious material. Both active and passive versions of the system were developed using methyl methacrylate encapsulated within polypropylene and glass fibres respectively, both were found to be workable methods for self-healing. Other researchers to use brittle capillary tubes for agent encapsulation include Li et al. (1998), Mihashi et al. (2000), Joseph et al. (2010), and Van Tittelboom et al. (2011). The size of tube used has ranged from 0.8 mm to 4 mm (Van Tittelboom et al. 2011).

Joseph et al. (2010) noticed that large quantities of the microencapsulated cyanoacrylate used in his tests remained inside the broken capillary tubes even after complete fracture of the specimens. This release failure was attributed to the capillary forces from the cracks not being sufficient to overcome the capillary forces in the tubes because of their sealed ends. Joseph solved this by using longer capillary tubes extended beyond the boundary of the specimen allowing them to be open to the atmosphere and thus reducing the resisting capillary force. It is of note that in experiments on their ECC Li, Lim, and Chan (1998) did not experience the same problem, this is assumed to be due to the narrower crack widths resulting in higher capillary action within the cracks.

Van Tittelboom et al. (2011) compared the use of glass and ceramic tubes for microencapsulation and found that more healing agent was released by the ceramic tubes; the difference is attributed to the differing surface tensions of the two materials.

The potential of spherical microcapsules formed from several different materials has also been investigated. Wang et al. (2013) used urea formaldehyde to produce their microcapsules, whereas and Yang et al. (2011) used silica gel. Wang et al. (2013) found that if the amount of microcapsules increased above 3 % of the cement content (by weight) then both the flexural and compressive strengths of the specimens were seen to decrease significantly, this was attributed to the microcapsules performing as effective defects within the matrix.

Joseph (2008) provides a convenient summary as to the relative merits of spherical and tubular encapsulation; stating that spherical capsules enhance the healing agent release as well as reducing the stress concentrations around the resulting void. On the other hand tubular capsules have a larger internal area of influence for the same volume of healing agent; however this increased area of influence is hindered somewhat by the inferior release, particularly in the occurrence of multiple cracks around one capsule. Further important criteria for encapsulation media are sufficient brittleness, limited extensibility, and good adhesion to the matrix to ensure efficient rupture upon concrete cracking (Van Tittelboom et al. 2011).

2.3.3.2.3 Vascular Healing Systems

A potential problem with microencapsulation is the limited volume of healing agent that can be included and the resulting finite nature of the healing response; this also limits the size of the maximum healable damage event. The development of vascular networks within a cementitious matrix has the potential to counteract this issue as they can be externally fed with additional healing agent potentially allowing the healing of an infinite number of damage events of a much larger size. A further benefit is that the type of healing agent applied can be varied (Joseph 2008).

Vascular networks can be split into two categories; those formed by some additional tubular material within the matrix, and those formed by tubes or voids composed of the matrix material itself.

Dry (1994) proposed the first example of a vascular network for convenient agent replenishment, stating that in circumstances where additional healing agent is required “vehicles for outside replenishment would be useful”. The proposed system, which can be seen in Figure 2.12, comprises a reservoir of healing agent drawn through porous fibres by a vacuum pump.

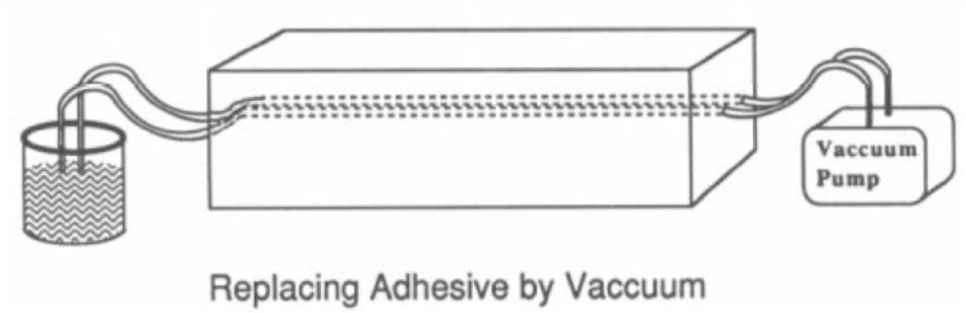

Figure 2.12 – Method for external replenishment of healing agent (Dry 1994)

Joseph et al. (2010) investigated the effectiveness of a vascular network carrying the adhesive healing agent cyanoacrylate. Their network comprised four glass capillary tubes (internal diameter 3 mm) cast longitudinally into a reinforced concrete beam. The experimental setup is displayed in Figure 2.13.

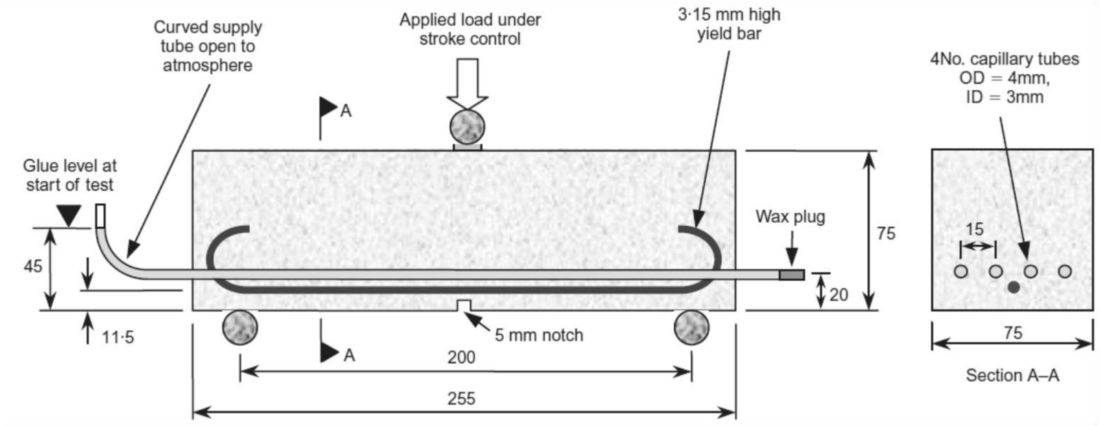

Figure 2.13 – Experimental setup for continuous flow system trialled by (Joseph et al. 2010)

Tests followed a three-stage process; specimens were first cracked to produce a 0.3 mm crack, rupturing the capillary tubes and releasing the healing agent, this was followed by a 24 hour healing period, finally in the third stage the specimens were reloaded to a central deflection of 3 mm i.e. to failure.

Joseph et al. (2010) concluded that the cyanoacrylate delivery network yielded both a primary and secondary healing response, with the secondary response actually showing increased strength beyond that of the original material.

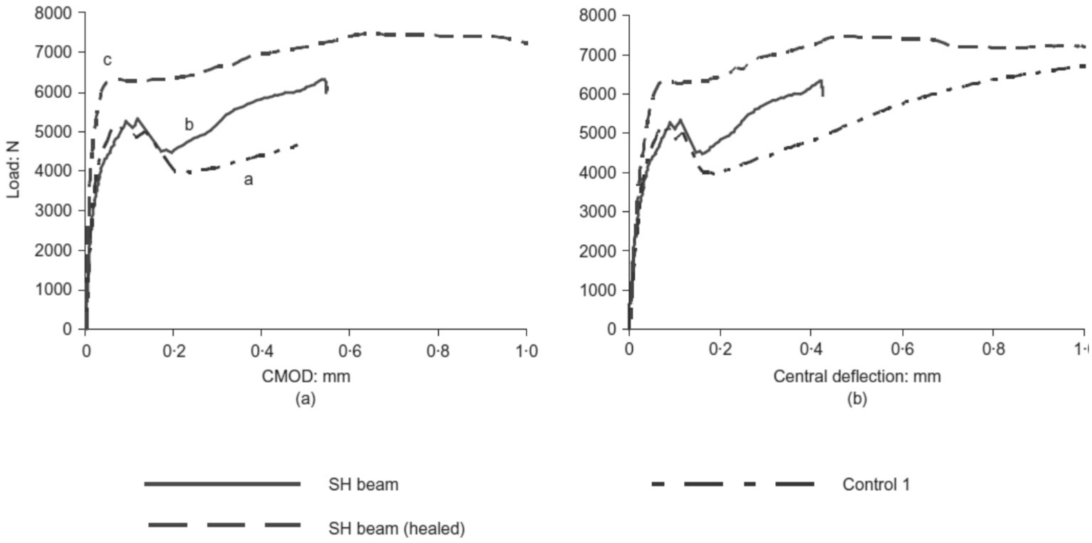

Figure 2.14 – Results of continuous flow self-healing system trialled by (Joseph et al. 2010)

an innovative method for creating vascular transport networks within concrete specimens was inspired by the healing process of bones (Sangadji and Schlangen 2013). A schematic diagram of the proposed healing agent transport system is displayed in Figure 2.15; the system consists of a core of porous concrete within a regular concrete matrix which allows the transport of healing agent to any damage sites.

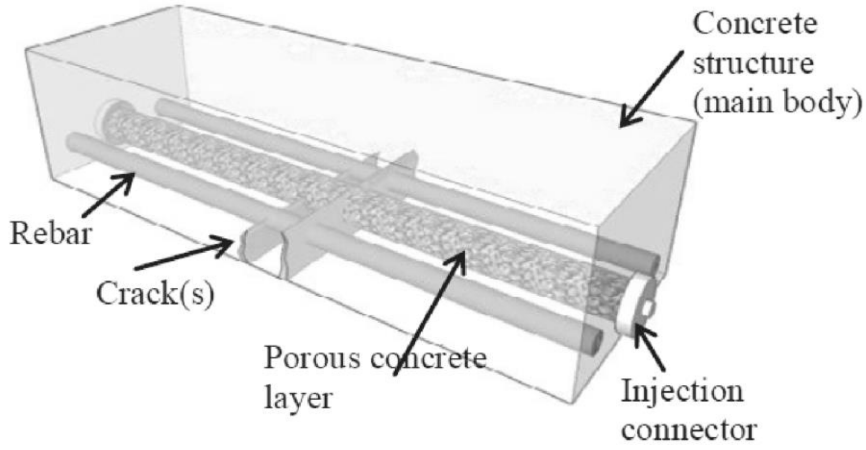

Figure 2.15 Schematic diagram of porous network concrete (Sangadji and Schlangen 2013)

Dry and McMillan (1996) created a two-channel vascular system by casting round steel rods into concrete beams and then pulling them out after 24 hours of curing. The resulting channels were coated with a brittle sealant to ensure sufficiently low permeability. A three-part methylmethacrylate adhesive system was used, with two parts contained in one channel and one in another channel. Upon cracking the three parts all mixed successfully and bonded the crack, with the retested post-healing beams showing an increase in mechanical strength of 30 % or more.

2.3.3.2.4 Bacterial Healing

A final healing agent and encapsulation technique is the use of calcium carbonate precipitating bacteria to develop a sustainable self-healing concrete. This method has been set apart from the others due to the unique challenges involved as a result of the living nature of the healing agent.

The capability of specific bacteria to fill pores and cracks in concrete was first noted by Ramachandran et al. (2001) before Jonkers (2007) suggested their potential for use in a self-healing concrete. In the first trials bacterial spores and nutrients were mixed directly into the concrete batch (Jonkers 2007). Water Ingress to any cracks dissolves the spores and nutrients, triggering the bacteria to produce both calcium carbonate and carbon dioxide. The calcium carbonate directly contributes to filling of the crack, while the additional carbon dioxide leads to indirect filling through its reaction with calcium hydroxide present in the matrix forming further calcium carbonate (Jonkers and Schlangen 2009). The biggest problem with this approach is that the spores' life-time in the matrix is reduced to a matter of months; this was addressed by loading the spores into expanded clay particles up to 4 mm in size. This approach saw no loss of viability of the spores after 6 months, however the addition of what are essentially lightweight aggregates caused a 50 % loss of compressive strength for the specimens (Jonkers 2011). Alternative methods for implementing bacteria as a self-healing agent are their inclusion within a silica gel, or polyurethane microencapsulation (Wang et al. 2012), Wang et al (2012) discovered that the polyurethane encapsulated bacteria yielded greater strength regain than the silica gel. In later work the use of polyurethane encapsulated bacteria allowed cracks of up to 970 μm to be closed.

As the bacterial healing mechanism relies on calcium carbonate precipitation and not hydration of unhydrated cement, and thus does not generally lead to any strength regain it should be considered as a self-sealing mechanism not self-healing (Schlangen and Sangadji 2013).

2.3.3.3 Self-healing Cementitious Materials in the Real World

Owing to the emergent nature of the technology described throughout this section, there are very few examples of self-healing cementitious materials currently being used in the real world at this time.

Reportedly, the first application of a self-healing technology in the real world was the use of the ECC developed by Li et al. (1998) for the creation of durable bridge expansion joints in Michigan ("'Bendable Concrete' Replaces Bridge Expansion Joints" 2014). As previously described the technology relies on the use of polymer fibres distributed throughout the matrix, this results in widespread microcracking as opposed to discrete macrocracking of the concrete. As the crack widths are limited to 60 μm autogenous healing is improved (Yang et al. 2009), healing can also be enhanced by the application of an autonomic additive such as cyanoacrylate (Li et al. 1998).

In 2012 it was reported that the bacterial concrete developed by Jonkers and Schlangen (2009) was ready for full scale outside testing, and that discussions were being held with several construction firms (*BBC* 2012); no further information is yet available on this.

Although not a concrete material system, the self-healing asphalt developed by Garcia et al. (2010) is a third example of a self-healing construction material that has been implemented in the real world. The system comprises both passive and active modes to assist with asphalt natural healing properties. Passively, embedded encapsulated chemicals are released upon cracking, encouraging the natural repair process; actively, conductive steel fibres are included in the binder mix, these can be induction heated which contributes to the repairing effect on the binder. A test section has been paved on the Dutch A58 highway, it will be interesting to see how its performance progresses (Liu et al. 2012).

All of these are trials as opposed to full scale implementations, their success will be key to the further implementation of self-healing technologies in real world concrete applications.

2.3.3.4 Economic and Environmental Potential

As was described in Section 2.3.1 there are a number of significant environmental and economic drivers for the development of more durable cementitious materials. Increased durability would be expected to reduce the need for maintenance throughout the life of a structure, while at the same time extending its overall life expectancy (van Breugel 2007). The reduction in maintenance needs would result in significant economic benefits as well as improving health and safety by reducing the need for human intervention in the upkeep of potentially dangerous structures. Potential environmental benefits include a reduction in global cement demand due to the increased life expectancy (van Breugel 2007).

The RILEM report (2013) presents a qualitative comparison of performance and costs between 'normal' structures and those made with self-healing materials which can be seen in Figure 2.16; this provides a good introduction to the concept of whole life-costs, a topic expected to be of significant importance for self-healing materials within the construction industry.

Figure 2.16 shows that the implementation of a self-healing structure is likely to have a sizeable associated increase in initial costs; however as a result of maintenance and repair costs throughout the life of a 'normal' structure the whole life costs are actually expected to be smaller for a self-healing structure. As demonstrated in Section 2.3.1.2, maintenance costs to the construction industry are very significant. As well as this direct saving on maintenance costs, there is likely to be a secondary cost benefit due to not needing to close the structure for these maintenance events and thus not impacting on the structure's use. These indirect secondary savings are often the more welcomed of the two by owners (van Breugel 2007). It should be noted that the situation illustrated in Figure 2.16 assumes a perfect self-healing structure and thus ignores all maintenance and associated inspection and monitoring costs, this is not a realistic expectation. However given the huge scale of worldwide concrete construction, a gradual incremental increase in self-healing capabilities is expected to yield considerable economic returns (van Breugel 2007).

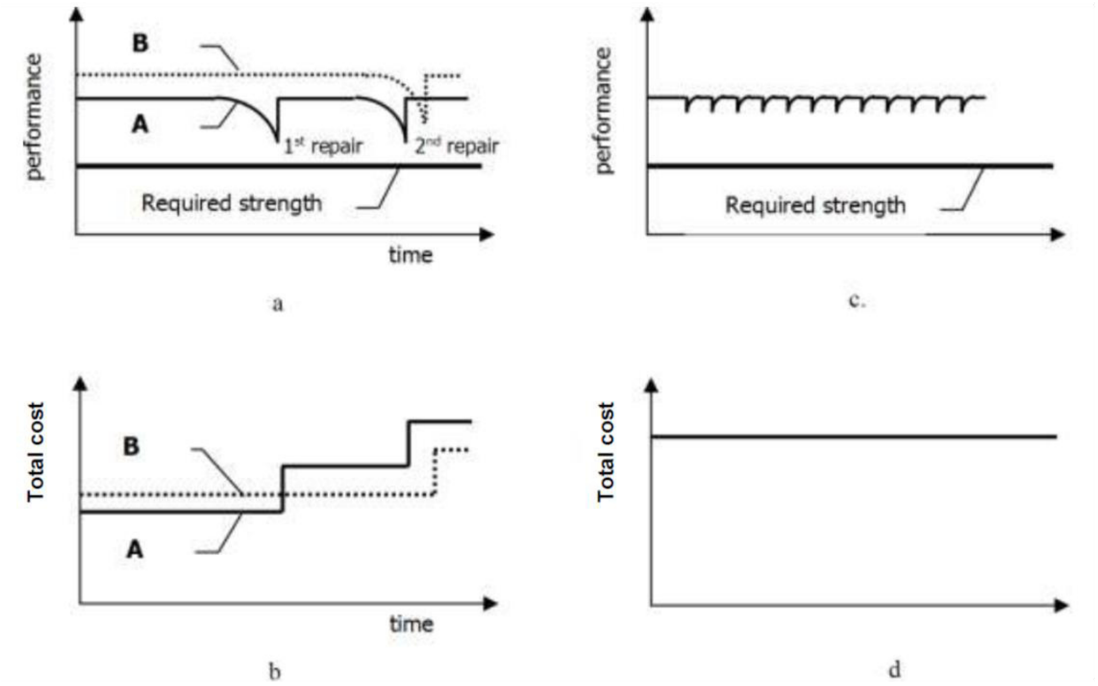

Figure 2.16 – Performance (a) and costs (b) with elapse of time for normal (A) and high quality (B) structures, and performance (c) and cost (d) of a self-healing structure. Direct repair costs included, no consideration of inflation or interest. (RILEM 2013)

A final advantage of more durable concrete structures is linked to the increase in life-expectancy. The associated reduction in cement demand from this has already been discussed, however there will also be a considerable environmental and economic benefit from the reduced need for demolition and disposal of rubble from old structures (van Breugel 2007).

Despite the numerous economic and environmental benefits outlined, persuading the wider construction industry to begin introducing these new technologies may not be straightforward. It is likely that owners will be reluctant to outlay the large initial costs for these technologies in a sector with a historically frugal culture. This is not helped by the fact that the expected savings through reduced maintenance are unlikely to materialise for some years after construction, and ownership of a civil structure is likely to change throughout its life (Foresight Smart Materials Taskforce 2004). A further barrier to uptake is the lack of long-term durability data to support researchers claims (Duxson et al. 2007).

2.3.3.5 Potential Barriers to Real World Application

There are a number of practical barriers that must be overcome before self-healing systems can be fully implemented in the construction industry.

The first and perhaps most significant of these is the need for any new materials to comply with regulatory standards which at the moment do not exist for these new materials. Once again the lack of long-term data makes the development of these standards problematic; if implementation within the construction industry is to be achieved then the appropriate research to produce the relevant data and the development of appropriate standards must be a priority (Duxson et al. 2007). A further complication to this barrier is the need to development these standards in conjunction with the companies responsible for the supply of OPC, there are clearly a number of commercial reasons why this group may be averse to the introduction of more durable concrete materials (Dunn 2010).

Another significant barrier is the need to ensure that the materials can fulfil the requirements of implementation in a construction environment, this barrier to their introduction is two-fold. Firstly the self-healing capability must be maintained throughout the life of the structure, 50 years for buildings and 120 years for highway structures (Dunn 2010). Secondly their construction must be feasible beyond the sterile environment of a laboratory, for example the use of brittle glass tubes or microcapsules may not be realistic as they may not survive the industrial compaction processes. The healing system must also be practical throughout its life, i.e. if a structure requires soaking with water every 6 months throughout its life for the healing to be effective then a lot if not all of the financial and environmental benefits are likely to evaporate very quickly (Dunn 2010).

Despite these barriers there does seem to be substantial potential for these systems and technologies to provide multiple significant benefits to the construction industry, and there is a definite drive for their introduction from some influential quarters. A government led programme (Department of Trade and Industry 2001) has stated the “promotion of ‘smart’ buildings and infrastructure” as the first of its major recommendations, and encouraged industry to “accelerate the introduction of new technologies, ‘intelligent’ products, standardised pre-assembled components and advanced materials into every level of the built environment”.

2.4 Current Alternatives to Standard Reinforced Concrete

Owing to the proposed use of SMP as an alternative reinforcing material in the LatConX system, a brief review of other research into the use of non-steel materials for the reinforcement of concrete elements would seem appropriate. Several alternatives to steel have been investigated including various forms of plastic, glass, carbon, alternative metallic materials, and natural materials. These materials have been included within the cementitious matrix in a number of ways; most commonly either formed into bars intended to act similarly to standard reinforcement, or as individual fibres distributed throughout the matrix. The properties, and thus advantages and disadvantages, of the resulting structural element can vary greatly as a result of the type and form of the materials used.

2.4.1 Fibre Reinforced Concrete

Fibre reinforced concrete is defined as concrete containing dispersed randomly oriented fibres (Zollo 1997), the fibres can be of many different materials including steel, glass, synthetic, carbon, and others (Brandt 2008). The concept was first proposed for concrete by Romualdi and coworkers (Romualdi and Mandel 1964); (Romualdi and Batson 1963), in the fifty years since thousands of papers have been published on the subject, therefore only a brief summary is provided here. The main benefit of fibre reinforced concrete is the increased crack width and propagation control offered by the dispersal of the fibres (Brandt 2008). The fibres used can vary in material, diameter, and length; and the form of the fibres chosen will affect the final properties of the cured concrete. As a general rule shorter, finer fibres control microcracking; whereas longer thicker fibres are more effective in controlling larger cracks and improving the overall strength properties of the concrete (Brandt 2008).

As mentioned originally, several different materials have been used since the original material was developed using steel fibres, a few of these different materials and their most appropriate applications are outlined now.

A first example of a non-steel FRC material is the previously discussed ECC developed by (Li et al. 1998) which used high modulus polyethylene to significantly limit crack widths.

Ochi et al. (2007) trialled the use of monofilaments extruded from recycled PET bottles in FRC with considerable success. They report comparable bending strength to steel FRC, as well as improved mixability. The material has undergone successful site trials at Hishikari mine, Japan; reports after one year of service were that the product was entirely crack free. The authors recommend that the product is suitable for wider use within the construction industry, and predict particular benefits in harsh underground, coastal, or underwater environments.

Low modulus polypropylene fibres have been used for two different beneficial reasons. Ramakrishnan et al. (2007) found the material was effective in controlling cracks caused by plastic shrinkage. Alternatively they have been used in concrete mixes for apartment buildings' walls as a means of improving fire resistance; upon heating the fibres melt, providing channels for the release of internal pressure without damage to the concrete, prolonging its life when exposed to extreme heat.

Natural fibres including wood pulp, banana, coconut, sisal, and others have been trialled with researchers reporting similar composite properties when compared with the use of synthetic fibres; however the biggest problem generally found with natural fibres is their propensity for degradation in the highly alkaline environment of OPC concrete (Pacheco-Torgal and Jalali 2011). Attempts have been made to improve the durability performance of natural fibre reinforced concretes by replacing a portion of the OPC with GGBFS, thus reducing the alkalinity of the matrix environment. This approach has allowed the successful development of a natural fibre reinforced building material using coir fibres. This research is of particular interest in developing countries such as Brazil where the fibres are widely available (Agopyan et al. 2005).

In 2006 the British Standards Institute released two standards to allow the use of FRC in construction; EN 14889-1 & 2, for steel and polymer fibres respectively (BSI 2006a); (BSI 2006b).

2.4.2 Fibre Reinforced Polymer Composites as Reinforcement

The term fibre reinforced polymer (FRP) composites refers to a set of materials that consist of brittle high strength fibres (usually glass, carbon, aramid, or basalt) embedded in a thermosetting polymer matrix (Bank 2013). Their superior resistance to corrosion, thermomechanical properties, and high strength to weight ratio have led some to herald FRP composites as “the materials of the 21^{st} century” (Hota and Liang 2011). Accordingly there has been a great deal of interest in their potential application in the construction industry including as an alternate reinforcing material for concrete. It is their resistance to corrosion in particular that makes them such an appealing alternative due to the high maintenance and repair costs related to the corrosion of steel reinforcement; in Europe it has been estimated to cost as much as £ 1000 million per year (Clarke 2003). The use of FRP composites for the reinforcement of concrete structural members has three categories: bars/grids for reinforced concrete, tendons for prestressed concrete, and permanent formwork for reinforced concrete (Bank 2006).

Potentially the most significant barrier to the widespread application of FRP composites as an alternative reinforcement is the brittle nature of the material resulting in a typical non-ductile failure mode which would provide little warning in a structural element (Bank 2013). Several different attempts have been made to increase their ductility over the last twenty years.

Harris et al. (1998) trialled a method of braiding several fibres together within the polymer matrix to produce a ductile response, the bars produced displayed a bilinear stress-strain curve similar to that of steel albeit with a lower ultimate strength. A similar method for producing pseudo-ductility is that proposed by Bakis et al. (2001) who combined carbon fibres with a low maximum strain with others with a larger maximum strain capability, the pseudo-ductility stems from the carbon fibres breaking at a lower strain than the other fibres, thus reducing the overall Young's modulus of the rods and resulting in a somewhat ductile stress-strain relationship.

Lees and Burgoyne undertook experimental (Lees and Burgoyne 1999), and numerical studies (Lees and Burgoyne 2000) into the effect of bond on the failure behaviour of concrete beams prestressed with aramid FRP tendons. Their approach aims to maximise the rotational capacity of a beam as it approaches failure, thus allowing a warning of failure in a non-ductile system. Beams with fully bonded, partially bonded, and unbonded tendons were all considered, with the partial bond the result of either alternating bonded and unbonded lengths of tendon, or a full length resin based bond of a lower strength than a bond directly with the concrete. As hypothesised, beams with the fully bonded tendons displayed high ultimate capacity, but limited deflection at failure which occurred through rupturing of the tendon. Conversely, the beams with unbonded tendons experienced much larger deflections but the ultimate load was 25 % lower, with failure occurring through crushing of the concrete. Finally the beams with partially bonded tendons generally behaved in between those that were fully bonded and unbonded, displaying higher deflections than the fully bonded beams and higher ultimate capacities than the unbonded beams. Thus utilisation of a progressively failing partial bond seems a potentially workable solution to the problem posed by FRP composite materials' limited ductility.

A very common "solution" is to simply over-reinforce FRP composite reinforced beams, inducing a failure through crushing of the concrete. Although this does not result in a similar moment-curvature relationship to that of a beam under-reinforced using steel, it does provide a less brittle failure than one initiated by the tensile failure of the FRP bar, and a relatively large deflection at failure (Bank 2013). Wu et al. (2010) improved upon this less than ideal regular crushing failure by including perforated slurry-infiltrated fibrous concrete (SIFCON) blocks in the compression zones; these SIFCON blocks result in a more stable crushing failure and a moment-curvature plateau similar to that of a steel under-reinforced beam.

A final set of potential solutions involves the use of progressively failing two and three- dimensional cages formed of FRP composites, failure is initiated by local bearing pressure at the member junctions, giving a pseudo-ductile response (Bank 2013).

2.4.3 Shape Memory Alloys

As briefly mentioned earlier shape memory alloys (SMA) have also been used as a means to reinforce tension zones of concrete structures. The most commonly used SMA is Nitinol due to its superior thermomechanical and thermoelectrical properties. Nitinol has two important properties that make it potentially very useful in certain concrete reinforcement applications; namely, the shape memory effect (SME), and superelasticity (Song et al. 2006). Both of these effects occur as a result of the different crystalline phases that exist in SMAs; stronger austenite phase and weaker martensite phase. In SMAs exhibiting a SME, the transition between the two phases is triggered by temperature variation (Song et al. 2006), whereas in SMAs exhibiting superelastic behaviour the transition is caused by an increase in externally applied stress (Alam et al. 2008). As well as the advantages offered by these two unique effects, SMAs perform well in resisting degradation due to corrosion (Otsuka and Kakeshita 2002), and have a coefficient of thermal expansion close to that of concrete (Saiidi et al. 2007); both properties making them suitable for use in concrete reinforcement applications. There are also some inevitable drawbacks to the use of SMA materials in the construction industry, including their high cost which is quoted at approximately 250 US$ per pound by Liu et al. (2007); this high cost means that SMA can never be considered a suitable alternative to steel for widespread application, instead their use will need to be limited to specialist applications where their unique properties can provide the most benefit. A further drawback is their poor fatigue performance, found to be as much as two orders of magnitude lower than other metals (Patoor et al. 2006).

2.4.3.1 Shape Memory Effect

The shape memory effect exhibited by SMA materials has been trialled as an alternative method of applying prestress by several research groups (Maji and Negret 1998); (El-Tawil and Ortega-Rosales 2004); (Deng et al. 2006); (Saiidi et al. 2007); (Li et al. 2007). This prestress effect is achieved by eccentrically embedding prestrained SMA wires within a concrete beam and subsequently activating them, the concrete matrix restrains any shrinkage causing a prestress force in the beam; this concept is almost identical to the LatConX system. Restrained shrinkage of this nature in SMAs has been found to cause a prestress of up to 600 MPa (Deng et al. 2006). The advantage of this over conventional prestressing is the elimination of the need for expensive and potentially dangerous jacking operations (Dunn 2010).

The use of the shape memory effect of SMAs in a fibre reinforcing system for concrete has also been trialled (Moser et al. 2005), with internal compressive stresses of up to 7 MPa reached in the concrete specimens upon activation. This technology is envisioned as being useful in reducing shrinkage cracking of repair mortars for the patching of concrete structures.

A final potential application of the shape memory effect of SMAs in civil structures is for the concept of natural frequency tuning; this relies on the use of embedded SMA wires to increase a structure’s stiffness, resulting in a change in its natural frequency. McGavin and Guerin (2002) reported natural frequency changes of up to 32 % through this method.

2.4.3.2 Superelasticity

In recent years the use of the superelastic properties of SMAs has been regularly proposed as a method for mitigating the problem of permanent large deformations induced by seismic activity (Alam et al. 2008); (Shrestha et al. 2013). This solution would involve the use of superelastic SMA materials instead of regular steel reinforcement in the plastic hinge regions of beam-column elements, potentially allowing recovery of a structure to its original shape after significant deformation as the result of a seismic event (Alam et al. 2008).

Shrestha et al. (2013) compared post unloading recovery behaviour of steel reinforced and superelastic SMA reinforced concrete specimens. All specimens were loaded to form a 6 mm crack and then unloaded and allowed to recover. The specimens reinforced with SMA wires performed significantly better, recovering to a final crack width of 0.3 mm compared to 5.7 mm in the steel reinforced specimens.

2.5 Polymers

2.5.1 History

The first man-made polymer was developed in 1862 and was named Parkesine for its creator, Alexander Parkes, however Parkes' manufacturing techniques involved the use of large quantities of expensive solvent and so were not commercially viable. In 1863 John Hyatt experimented with reducing the quantity of solvent and supplementing it with heat and pressure, this approach yielded the first commercially viable process for plastic manufacturing and with it Celluloid. Celluloid remained the only commercially viable plastic for 40 years until the arrival of Bakelite (McCrum et al. 1997). The next big step forwards in the development and understanding of polymeric materials came with Hermann Staudinger's ground breaking explanation of the structure of polymers, "The Macromolecular Hypothesis", which included the controversial assertion that all plastics and rubbers are polymers. Ultimately Staudinger's initiation of a more scientific approach to polymer science lead to the commercialisation of nylon and polyethylene, and hence to the vitally important role played by polymeric materials in modern life. Polymer uses now range from packaging and children's toys, to medical, automotive, and aerospace applications (McCrum et al. 1997).

2.5.2 Chemical Structure

The word polymer literally means "many parts", from the Greek poly meaning many, and meros meaning parts; accordingly, polymers are long molecules consisting of many small units (monomers) joined end to end. An example is the molecules that make up polyethylene which generally consist of between 10^3 and

10^6 individual ethylene monomers (McCrum et al. 1997). This high number of monomers results in polymer chains having very high molecular weight and often being described as macromolecules. The material properties of polymers, including physical, mechanical, and thermal properties, are the result of this long chain formation, and the resulting molecular weight, structure, and organisation down the chains. The degree of crystallinity and interactions between chains (which are both ultimately the result of chain length) also play a large part in determining the material properties (Sperling 2005). Using the polyethylene series, the progression of the resulting material state and properties at room temperature with chain length is shown in Table 2.2.

Table 2.2 – Progression of state and material properties at room temperature with chain length for polyethylene (Sperling 2005)

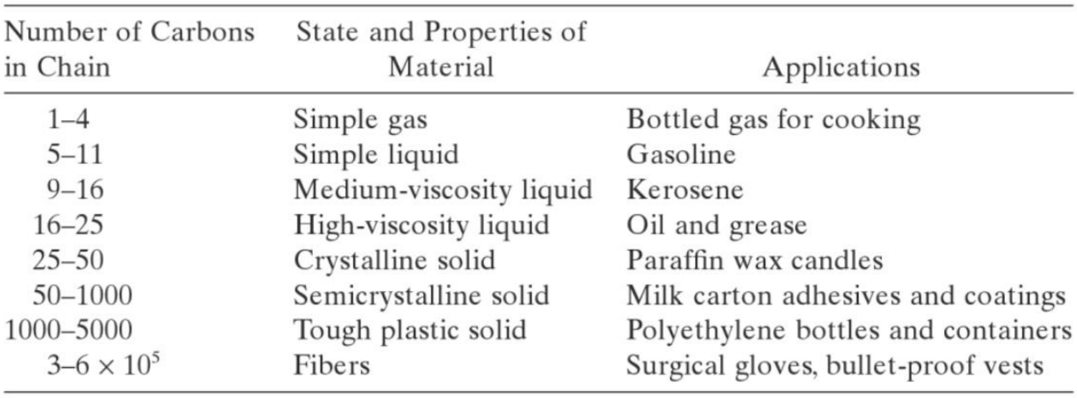

Number of Carbons in Chain	State and Properties of Material	Applications
1–4	Simple gas	Bottled gas for cooking
5–11	Simple liquid	Gasoline
9–16	Medium-viscosity liquid	Kerosene
16–25	High-viscosity liquid	Oil and grease
25–50	Crystalline solid	Paraffin wax candles
50–1000	Semicrystalline solid	Milk carton adhesives and coatings
1000–5000	Tough plastic solid	Polyethylene bottles and containers
$3–6 \times 10^5$	Fibers	Surgical gloves, bullet-proof vests

2.5.3 Mechanical Properties

On a microscale, the mechanical behaviour of polymers is fundamentally dependent on the ability of the constituent chains to adjust their conformations at a molecular level by rotation about the chain bonds. Rotations are inter- and intra-molecularly restrained by chain-stiffness and inter-chain interactions respectively (Klompen 2005). There are two molecular factors that influence the level of this molecular restraint; the chain length which is proportional to the molecular mass, and the molecular shape i.e. the nature of any side branches (McCrum et al. 1997).

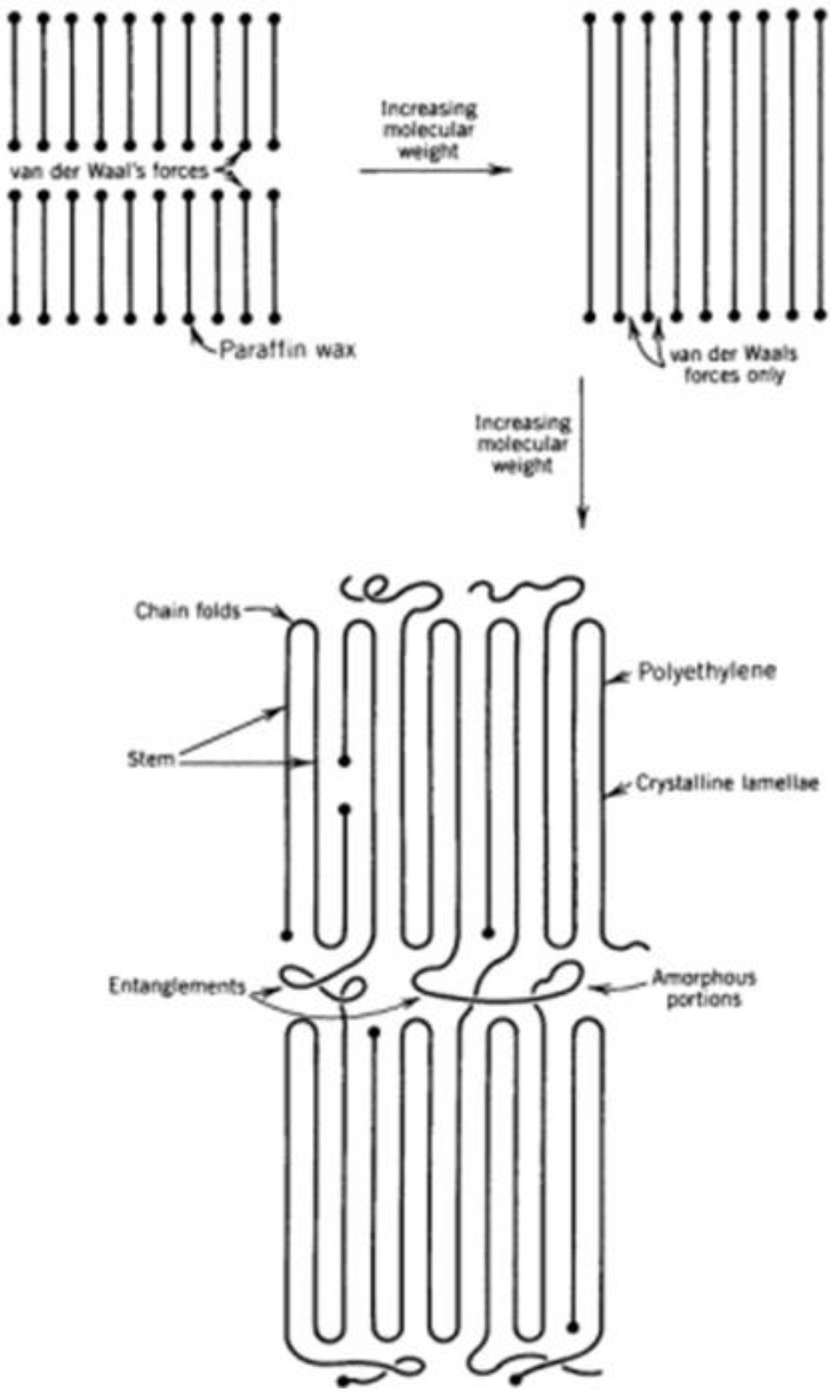

Figure 2.17 - Effect of chain length on polymer structure and morphology (Sperling 2005)

An increased chain length impacts on the microstructure and morphology of a polymeric material, as shown in Figure 2.17. The increased chain length leads to stems becoming interconnected in lamellar crystallite structures, these structures are connected to each other through strong covalent bonds which forms extended crystalline regions. These regions are separated by rubbery amorphous regions giving the material flexibility. Finally the long chains lead to entanglements which hold the material together under stress. In contrast, short chains form entirely crystal structures with only weak van der Waals forces to hold them together, and no chain entanglement (Sperling 2005). As an example of the importance of molecular weight on a polymer's physical properties, its effect on tensile strength is shown in Figure 2.18.

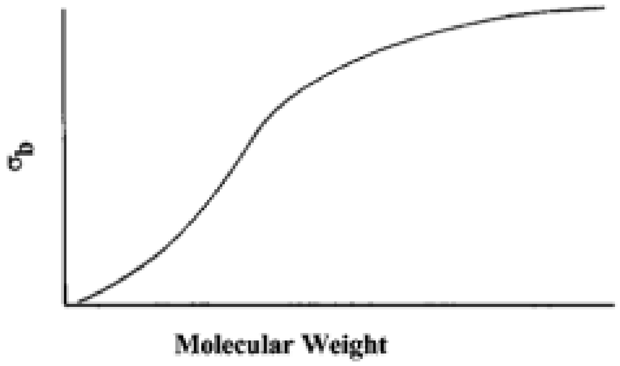

Figure 2.18 – Relationship between molecular weight and tensile strength (Sperling 2005)

The second molecular factor mentioned above was the shape of polymer molecules; this refers to whether a chain is linear, in which all monomers are joined end to end in a single line, or contains side branches that can be one or more monomers in length. The presence and number of any side branches depends on the polymerisation conditions and can cause significant changes in material properties including elastic modulus, creep resistance, and toughness (McCrum et al. 1997). High density polyethylene (HDPE) and low density polyethylene (LDPE) are examples of linear and chain-branched polymers respectively (Ward and Sweeney 2004).

All molecular structures and behaviour discussed up to this point are relevant to individual discrete chains with no permanent bonds to other chains, whether the chains are linear or side-branched they form materials that fall into the category of thermoplastic polymers. This means that they have a temperature above which they flow like any other liquid. The alternate category is that of the thermosetting polymers which do not flow upon heating. In a thermosetting polymer the chains are joined together by chemical cross-links throughout the molecular structure, creating a single cross-linked network with a fixed shape. These cross-links cannot be broken by heating (unless the whole material is degraded – burned), this gives the thermosetting behaviour whereby melt does not occur. Generally the presence of these physical cross-links leads to a polymer with properties typical of rubber (McCrum et al. 1997). Indeed, the vulcanisation of rubber from natural rubber is a cross-linking process in which sulphur atoms are added to connect the long C_5H_8 natural rubber molecules together; these cross-links give rubber its characteristic feature of rapid recovery from large extensions. The chain entanglements mentioned earlier perform a similar function to chemical cross-links, however they must be considered as strictly temporary in contrast to the permanent nature of chemical cross-links (Ward and Sweeney 2004).

2.5.4 Orientation and Crystallinity

As mentioned above the degree of crystallinity and orientation will also have an effect on the physical properties of a polymer. Synthetic polymers are never 100 % crystalline as a consequence of their long chain nature and resulting entanglements (Sperling 2005), the term crystalline polymer implies a partially crystalline or semicrystalline material (McCrum et al. 1997). Generally, higher degrees of crystallinity give stiffer, denser, stronger, less ductile materials (Dusunceli and Colak 2008).

The key molecular characteristic that distinguishes crystalline polymers from non-crystalline is molecular regularity; in amorphous polymers it is the irregular chain structure that prevents regular packing (McCrum et al. 1997). According to (Ward and Sweeney 2004) there are three key criteria to be fulfilled for a polymer to crystallise:

- The molecular chains must have a regular structure
- The temperature must be below the crystal melting point
- Sufficient time must be available for the molecules to become ordered in the solid state

In crystallisation from the melt, crystal growth radiates out in three-dimensions from individual nucleation sites, this often forms spherulitic structures (Dusunceli and Colak 2008). In this case, the polymer is said to be crystalline but unoriented; these materials are unoriented on a macroscopic scale as evidenced by their isotropic mechanical properties, however on a microscopic scale they are not homogenous due to the spherulitic structures. As alluded to in the third criterion above, the rate of cooling is of great importance to the crystal (or non-crystal) structures that form, rapid cooling i.e. quenching in water will form disordered amorphous states. In contrast to the spherulitic crystals formed from melt, crystallisation from a dilute solution tends to form lamellar-shaped single crystals, the structure of which varies depending on the concentration of the solution (Cheremisinoff 1989).

It is not only crystalline regions that show orientation though; the interconnecting amorphous regions are not arranged entirely randomly. In contrast to crystalline regions which when solid display a high degree of structural regularity, amorphous structures are described as having greater or lesser amounts of disorder (Sperling 2005). Stretching of an amorphous polymer tends to align the molecules along the stretch direction; this is detected through optical methods by small differences between the refractive index in directions parallel and perpendicular to the stretch direction (Ward and Sweeney 2004). For orientation to occur, the stretching stress must be applied at or above the glass transition temperature (T_g) but below the melt temperature (T_m) (Abdel-Bary 2003).

There are two common mechanisms that reduce crystallinity; namely plastic deformation, and melting. Plastic deformation results in decreasing crystallinity with increasing strain; the final degree of crystallinity is determined by the initial degree of crystallinity and the amount of plastic strain applied. Heating above T_m which will result in complete destruction of the crystalline structure and the formation of an amorphous melt (Sperling 2005).

2.5.5 Thermal Behaviour

It was stated earlier that the mechanical behaviour of a polymer is fundamentally governed by the chains' ability to undergo conformational changes. The potential restrictions placed on this ability for conformational change by molecular structure have been introduced in the preceding sections; thermal dependence and its effects will now be introduced.

Klompen stated that the inter- and intra-molecular interactions discussed so far result in an energy barrier which restricts conformational changes of the polymer chains. The rate of conformational changes or "molecular mobility" for any system is purely governed by the available thermal energy; an increase in thermal energy, or temperature, will increase the rate of conformational changes, in turn allowing larger molecular rearrangements in a fixed time. Ultimately it is this relationship that gives rise to the pronounced temperature dependency of polymer behaviour (Klompen 2005).

2.5.5.1 Transition Regions

There are two transitions relevant to semicrystalline polymers; melt/crystallisation, applicable to the crystal phase; and glass transition, applicable to the amorphous phase (Sperling 2005).

Melt/crystallisation is a first order transition; as such the transition is accompanied by a discontinuity in the volume-temperature relationship, and a heat of transition. On the other hand, the glass transition is a second order transition and thus is a less familiar concept. Instead of a discontinuity in the volume-temperature relationship there is a change in slope and corresponding change in heat capacity (Sperling 2005). According to Debenedetti and Stillinger (2001) the glass transition cannot be classed as a phase transition as there are no associated discontinuous changes in material properties.

The increase in molecular mobility with increasing thermal energy is the cause of the glass-transition behaviour. At temperatures below the glass transition only vibrational chain movements are possible due to the reduced molecular mobility resulting in a hard glassy material (Figure 2.19 - region 1). As the temperature increases through the glass transition (region 2), the modulus drops significantly and molecular mobility increases, giving polymers the rubbery behaviour often observed at higher temperatures. Regions 3, 4, and 5 are the rubbery plateau, rubbery flow, and viscous flow regions respectively (Sperling 2005).

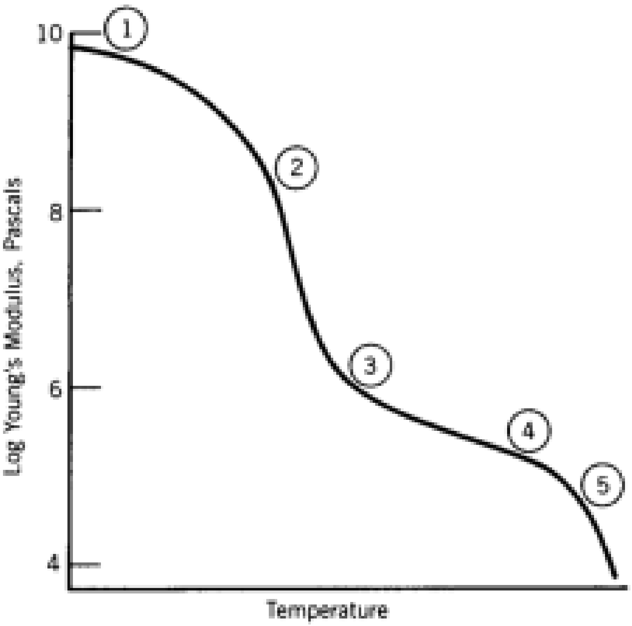

Figure 2.19 – Idealised modulus-temperature relationships for an amorphous polymer showing transition regions (Sperling 2005)

As stated, crystalline regions of polymers do not undergo a glass transition; however as no synthetic polymers are 100 % crystalline they will all display some level of glass transitional behaviour as a result of the amorphous phases. The resulting macroscopic effects on the material properties are slightly altered as a result of the two-phase structure. If the amorphous region is above T_g then the overall modulus is likely to be between rubbery and glassy, if below T_g the overall modulus is likely to be slightly stiffer than that of a totally amorphous glassy polymer. In semicrystalline polymers the melt/crystallisation-transition always takes place at a higher temperature than the glass-transition (Sperling 2005).

2.5.5.1.1 Factors Affecting Glass Transition Temperature

The glass transition is only effected by changes to the amorphous regions in a semicrystalline polymer because, as noted previously, the crystalline regions are not subject to glass-transition behaviour (Daniels 1989). Logically it can be predicted that changes that reduce molecular mobility will increase the thermal energy required for transition and thus the transition temperature, accordingly any increase in molecular weight is likely to increase the transition temperature (Fox and Flory 1950). Lightly cross-linking the molecules would also be expected to increase the transition temperature (Daniels 1989), this cross-linking brings chains closer together and reduces the free volume of the polymer (Ward and Sweeney 2004). T_g also increases at increased pressure as this also brings chains closer together, reducing the free volume and as a result the molecular mobility (Daniels 1989).

As a general rule, any changes in the material or environmental conditions that reduce the molecular mobility at a fixed temperature will increase T_g.

2.5.5.2 Thermal Expansion and Contraction

The magnitude of any thermal expansion or contraction is a final important aspect of thermal behaviour to consider. Baschek and Hartwig (1998) investigated the effects of several parameters on the coefficient of thermal expansion; including annealing, thermal cycling, mechanical preloading, and the geometrical shape. Their key conclusions were that manufacturing parameters and water content variations had a small influence on the coefficient of thermal expansion, whereas thermal cycling and geometrical shape had a significantly larger influence. However as the tests in this publication were carried out on anisotropic carbon fibre reinforced polymers further work is required to generalise the conclusions drawn to non-fibre reinforced polymers.

Bhushan (2000) notes that increasing orientation of oriented PET causes a concurrent decrease and increase in the coefficient of thermal expansion in the stretch direction and transverse direction respectively.

2.5.6 Deformation Behaviour

A typical stress-strain curve for a polymer is displayed in Figure 2.20. Any strains below yield are entirely recoverable, as annotated this behaviour is viscoelastic i.e. stress-strain relationships are time-dependent and not instantaneous. Any strains above yield are irrecoverable as a result of stress induced plastic flow which initially reduces the material’s resistance to plastic flow (strain softening). Finally at very large deformations, the molecules become increasingly oriented, which results in an increase in modulus and therefore stress (strain hardening) (Klompen 2005).

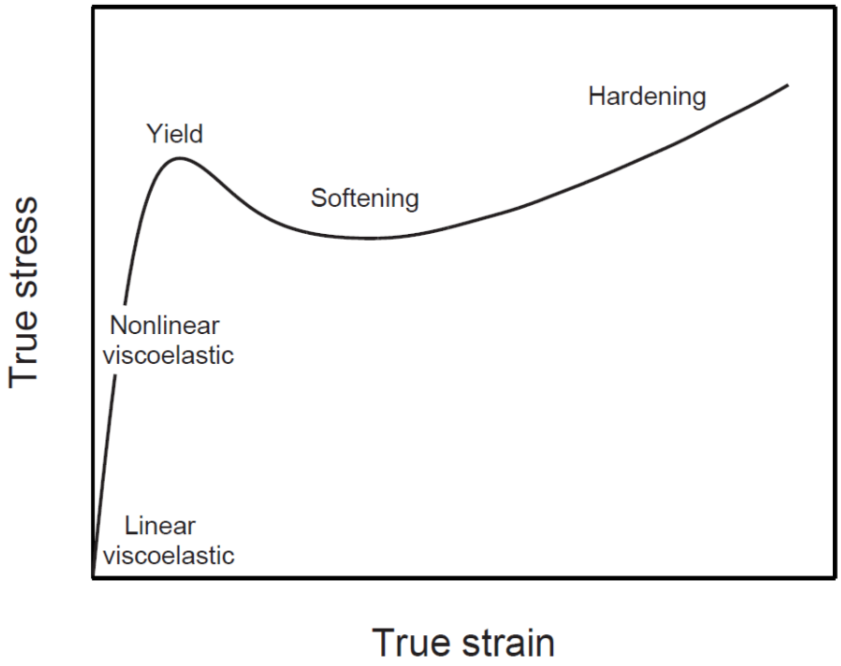

Figure 2.20 – Intrinsic deformation behaviour of a polymeric material (Klompen 2005)

2.5.6.1 Time-temperature Correspondence

Stress and temperature both have a significant influence on the polymer's molecular mobility which as described previously is the fundamental driver for conformational change and thus deformational behaviour. Further to this, any fixed molecular mobility for a given set of stress and temperature conditions will determine the time-dependence of any deformational behaviour i.e. the nature of creep and stress relaxation behaviour. For relatively short time-scales the response to an applied stress or strain is solid-like because of the limit placed on the potential for conformational changes. A logarithmically increasing time-scale increases the potential for conformational change, as it is a rate-dependent property, resulting in larger deformations and rubber-like behaviour, although the presence of entanglements acting as temporary cross-links still limits very large scale chain motions. Finally, at very long time-scales main chain diffusion dissolves these entanglements and the polymer behaves like a fluid (Klompen 2005). A review of the previous statements reveals that longer time-scales have the same effect on mechanical properties and deformational behaviour as increased temperature, this effect is called time-temperature correspondence. Time-temperature correspondence can be used in a superposition procedure to construct master curves for the full time-dependency of a polymer’s behaviour based on the observation of a single time-scale at a range of temperatures (Figure 2.21).

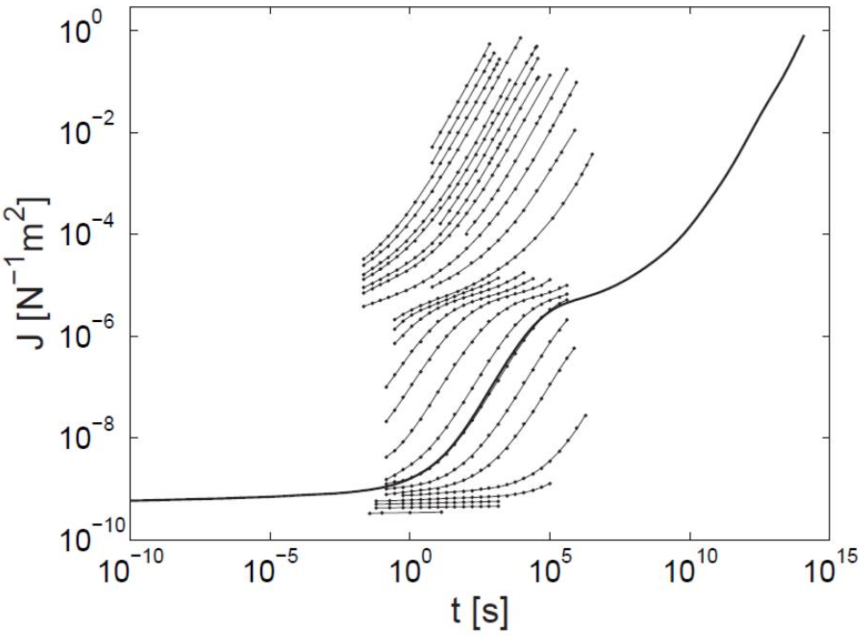

Figure 2.21 – Master curve for creep compliance of polystyrene constructed using time-temperature superposition (Klompen 2005)

Time-temperature superposition cannot always be undertaken, and its applicability depends on the magnitude and position of the shift, and the polymer considered; polymers to which it does apply are termed “thermo-rheologically simple” (Klompen 2005).

Conversely, if a polymer’s thermomechanical behaviour cannot be superimposed in this way then it is termed thermo-rheologically complex. This complexity arises from secondary glass transitions for the molecular mobility of the chains’ side branches, resulting in a second spectrum of relaxation times with an alternate temperature dependency (Klompen 2005).

2.5.6.2 Physical Ageing

A further complication to the deformational behaviour is the phenomenon of physical ageing, first observed by Struik (1976). This is the effect that the period of elapsed time (t_e) after a thermal quench from above T_g has on molecular mobility, as the elapsed time increases the mobility decreases. This is the result of a non-equilibrium thermodynamic state upon initial cooling due to the reduced molecular mobility and subsequent increase in time required for equilibrium to be reached. Thus physical ageing is the gradual progression from the initial non-equilibrium state towards equilibrium, which is accompanied by reducing molecular mobility (Klompen 2005). The effect that this ageing phenomenon has on creep compliance, volume, and deformation behaviour is displayed in Figure 2.22 a, b, and c respectively.

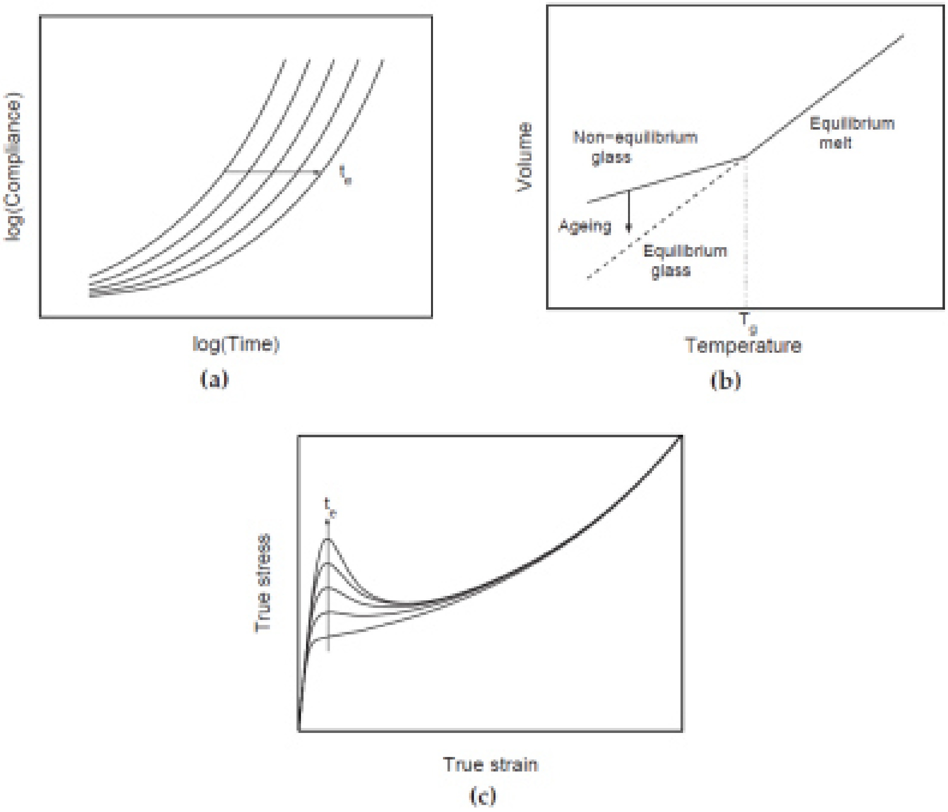

Figure 2.22 - Effect of physical ageing on polymer properties (Klompen 2005)

2.5.7 Shrinkage Behaviour

Certain polymers can be programmed to return to a pre-programmed permanent shape upon heating, these are termed either heat-shrinkable or SMPs. There are many potential applications for these materials, including insulation tubes for electronics, shrink film for packaging, and self-deployable sun sails in spacecraft, among many others (Behl and Lendlein 2007).

The manufacture of these materials requires two steps. The first step is to form the specimen into the required shape and cross-link it making the shape permanent, this is called pre-forming. The second step is called shape memory induction or programming and involves heating the specimen above T_g, stretching or deforming it to the required temporary shape, and quenching to below T_g while restrained in this shape. This “freezes in” the oriented molecules and resulting internal elastic stress, allowing the external deforming stress to be removed while the specimen holds the temporary shape. Upon reheating the material softens, releasing the locked in internal stress and causing the specimen to return to the permanent shape. This softening is the result of the melting of the crystalline regions (Morshedian et al. 2005); (Khonakdar et al. 2003). Temporary shape programming can also be applied through drawing the sample without heating (cold drawing) (Lendlein and Kelch 2002).

The ability of drawn polymers to generate shrinkage stresses in this manner is the product of two basic properties; the tendency of the long chain molecules to become oriented in the drawing direction (Ward and Sweeney 2004), and their entropic preference to assume more coiled and random conformations (Mody et al. 2001). Various more precise descriptions of the mechanisms responsible for the shrinkage behaviour have been proposed by a number of researchers; these include the formation of taut tie molecules during drawing (Peterlin 1971), adoption of a folded conformation under heating in nylon 66 fibres (Dismore and Statton 1964), or the presence of two different amorphous domains which have differing stress- and temperature-dependent responses (Prevorsek et al. 1974).

It is widely believed that shrinkage behaviour is mainly related to the properties of the amorphous phases, the upshot of this is that observations regarding amorphous polymers can be considered equally applicable to semi-crystalline polymers (Pakula and Trznadel 1985). However, the dependency of shrinkage behaviour on the amorphous phase properties means that resistance to shrinkage increases with increasing crystallinity (Mody et al. 2001).

The amount of shrinkage, and activation temperature for the shrinkage mechanism are largely dependent on the previous stretching and thermal history of the polymer; this is due to the effects of this history on the conformations of the crystalline and amorphous regions (Mody et al. 2001). A series of papers written by Chandran and Jabarin discussed the varied crystallisation and orientation behaviour of PET as a result of different stretching and temperature conditions, finding that higher strain rates or lower temperatures during the stretching process cause a higher degree of crystallinity (Chandran and Jabarin 1993a; Chandran and Jabarin 1993b; Chandran and Jabarin 1993c).

Sharma and Misra (1987) found that the amount of shrinkage was reduced in specimens drawn at a higher ratio, however several other authors have reported findings that contravene this observation including Khonakdar et al. (2003) in their series of tests on HDPE, and several test series by other authors on PET (Haworth et al. 1993); (Gupta et al. 1994). Khonakdar et al. (2003) also found that an increase in the temperature during stretching caused an increase in the activation temperature. Finally, Morshedian et al. (2005) reported that any increase in the time held at extension, or the cooling time allowed an increase in the amount of relaxation of the internal stress and hence reduced the shrinkage potential of the specimen.

Further information on the shape memory effect in polymers and other materials is given in Section 2.6.

2.5.8 Polymers as Cementitious Binders

The application of polymers in combination with concrete to form construction materials can be divided into two categories; the use of either bars or fibres to provide a reinforcing effect, and their use as a part, or the whole, of the binder. The first of these two categories was discussed in Section 2.4.

The idea of combining polymeric and cementitious materials for improved binder properties is not a new one, the earliest record of this dates back to the clay brick walls of ancient Babylon which used natural polymer asphalt in the mortar (Kardon 1997).

There are several forms that this polymer/cement binder can take. Polymer impregnated concrete (PIC) is a technique mainly used for repairs; monomers are infused into cracks and voids where they are polymerised by a chemical hardener or heat. Polymer concrete (PC) consists of just polymer and aggregate, there is no OPC. The bind achieved by the polymer is very good and there is no transition zone.

The space between particles is minimised by using evenly graded aggregate, this reduces the spaces to be filled by the binder which is more expensive than OPC and undergoes greater shrinkage during curing. PC is often used for connecting precast elements, and overlaying concrete repairs. Finally polymer-modified concrete (PMC) involves a combination of OPC and a polymer admixture, which produces two intermingled binder matrices (Kardon 1997).

A recent method for the production of more sustainable concrete uses recycled PET from existing waste sources i.e. plastic bottles. The PET can be chemically modified to produce unsaturated polyester which in turn can be used in polymer concrete. The resulting concrete was found to achieve high strength relatively quickly, although poor performance at elevated temperatures or under large sustained loads as a result of the viscoelastic nature of the resin deformation was noted (Rebeiz 1995); (Jo et al. 2008).

The American Concrete Institute undertook a comprehensive overview of the state of the art of polymers in concrete in 2009 which can be referred to for further information (ACI Committee 548 2009).

2.5.9 Polyethylene Terephthalate (PET)

PET, the most common thermoplastic polyester, was discovered and patented in England in 1941. It is formed from two monomers; modified ethylene glycol and purified terephthalic acid. The combined monomer is shown in Figure 2.23 (National Association for PET Container Resources (NAPCOR) 2014).

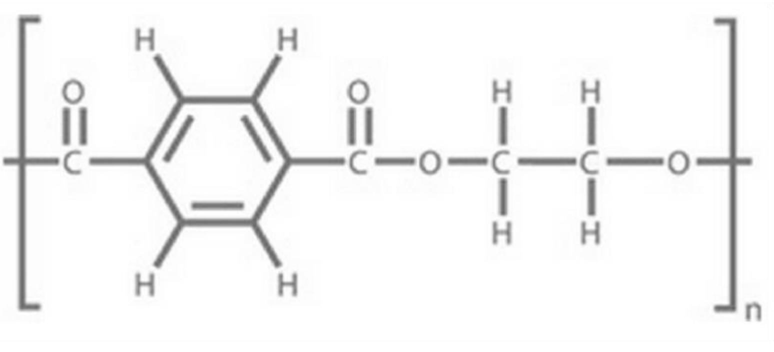

Figure 2.23 – Chemical structure of PET monomer

At room temperature PET is a hard, stiff, strong, dimensionally stable material, with good gas barrier properties, good chemical resistance, and very low water absorption (AZOM 2003). The crystallinity of PET varies from amorphous to highly crystalline depending on the manufacturing process (Goodfellow 2014). PET absorbs very little water, and has generally good chemical resistance properties except for against alkalis (AZOM 2003); further investigation into the material's resistance to alkalis will be required before its successful application in the LatConX system.

There are a number of common uses for PET, including applications in the fabrics/textiles industries, beverage bottles, photographic film, and magnetic recording tape (Encyclopedia Britannica 2014).

2.5.9.1 Manufacture

PET is manufactured from two intermediate components, pure terephthalic acid (TPA) and ethylene glycol, both of which are derived from crude oil. The reaction of these components takes place in two stages; first a mixture of bis-hydroxyethyl-terephthalate (BHET) and some other short chain polymers is formed, upon further reaction excess ethylene glycol is distilled out and the PET is formed. The PET is initially a viscous molten liquid which is then extruded and quenched in water yielding a glass-like amorphous material (ILSI Europe, Packaging Material Task Force, and ILSI Europe 2000). Heating above 72 °C and stretching leads to chain alignment; rapid cooling from this stretched state freezes the chains with their orientation intact yielding the properties typically seen in a PET drinks bottle. Alternatively slow cooling from 72 °C increases the degree of crystallisation, the material becomes opaque and less flexible and is more resistant to the application of high temperatures. The degree of crystallisation can be manipulated between the two extremes to produce a range of materials with varied properties, all with the same chemical formula. Chemical modifiers are sometimes added to facilitate the manipulation of these properties (ILSI Europe 2000).

An alternative process uses dimethyl ester of terephthalic acid (DMT) instead of BHET, this is often preferred for film applications (Independent Chemical Information Service 2014). Fibres and films are formed by drawing the amorphous solid at an elevated temperature (above T_g) (Global Association of Manufacturers of Polyester Film 2014); uni-directional stretching is used for fibre production, or bi-directional stretching for films and bottles (ILSI Europe 2000).

An attractive property of PET is that it is fully recyclable. Used PET materials are washed, granulated into flakes, and remanufactured by heating and following the processes described above (Kenplas Industry Limited 2014).

2.5.9.2 Applications

PET applications are wide and varied, a selection of uses for its different forms are outlined below.

Rigid PET is used in many applications, including for the production of plastic drinks bottles and heat-resistant food trays suitable for use in ovens (ILSI Europe 2000).

PET films are often used for food packaging, release films, adhesive tapes, insulation films, flexible printed circuit films, x-ray films, magnetic recording tape, as well as a multitude of other uses (Global Association of Manufacturers of Polyester Film 2014).

PET fibres are commonly used in the textiles industry where its strength, and temperature and wear resistance, make it an ideal replacement for natural fibres (Kenplas Industry Limited 2014).

Recycled PET is often used for clothing, carpet fibres, fibre stuffing, bottles for non-food products, industrial strapping, and automotive parts (National Association for PET Container Resources (NAPCOR) 2014). Recycled PET can be used for food and beverage containers however it must pass certain approved process requirements relating to contaminants and material properties (Kenplas Industry Limited 2014).

2.6 Shape Memory Materials

Shape memory materials have the ability to memorise a permanent shape, be fixed into a temporary shape, and finally under some thermal, electrical or environmental trigger return to the permanent shape (Liu et al. 2007). This shape memory effect (SME) has been observed in ceramics, metals, and polymers, and each is the result of a different molecular mechanism. In metals and ceramics this is a well-defined crystalline phase change at a specific stress or temperature, in polymers the effect is the result of a variety of molecular interactions with less well-defined activation temperatures/stresses (Abrahamson et al. 2003).

2.6.1 Shape Memory Alloys

Shape memory alloys (SMA) have historically been the most widely used shape memory materials; their behaviour has been investigated extensively over the last 50 years with commercialisation following in a number of fields (Liu et al. 2007). SMA were initially discovered by Chang and Read in 1932 when they observed the reversible phase transformation of gold-cadmium alloy. The observations of the shape memory effect in nickel titanium alloy by Buechler and colleagues in 1962 were the catalyst for more in-depth research into these materials. The shape memory effect in this alloy was initially observed at the Naval Ordnance Laboratory and it is after this which the most common SMA material, Nitinol, is named (Song et al. 2006).

SMAs have been used in a wide range of applications including as pipe couplings, actuators in electrical appliances, the automotive industry, mobile phone antennae, and medical implants (Wayman and Ōtsuka 1999). Their use has also been trialled in certain civil engineering applications as discussed in Section 2.4.3.

The properties of SMAs are the result of the reversible phase transformations between two crystal phases. The two phases are the stronger austenite which is stable at high temperature, and weaker martensite which is stable at low temperature. This phase change can either occur due to a change in temperature as in alloys exhibiting the shape memory effect, or the application of an external stress as in superelastic alloys (Song et al. 2006).

2.6.2 Shape Memory Polymers

SMPs were actually discovered earlier than SMAs, however they received less initial attention; their first commercialisation was in the 1960s with the development of heat shrinkable polyethylene tubing, although consistent research efforts did not begin until the late 1980s (Liu et al. 2007). Current applications are varied, ranging from relatively low technology shrinkable packaging, up to high technology industries such as their use in aviation for the creation of wings that can adjust their surface area based on flying conditions, and aerospace applications including satellites and other space vehicles (Volk and Whitley 2005).

SMPs have a number of key advantages over SMAs in that they exhibit shorter recovery times upon activation, and allow a higher rate of deformation between the permanent and temporary shapes (Behl and Lendlein 2007). They are also significantly cheaper as mentioned earlier. One potential drawback of SMPs, particularly in the context of the LatConX system, is the relatively low shrinkage stress that they can generate (Dunn 2010), roughly 80 MPa compared to 600 MPa for SMA (Long and Ward 1991); (Deng et al. 2006).

On the macroscale, a typical shape memory cycle is as depicted in Figure 2.24. First the polymer is deformed at an elevated temperature and subsequently cooled while held in the deformed shape, this process is called programming and fixes in the temporary shape and associated latent strain energy; the polymer will remain stable in this temporary fixed shape for long times. Reheating above the relevant transition temperature releases the stored strain energy and returns the polymer to its permanent "memorised" shape (Liu et al. 2007).

Observation of Figure 2.24 reveals very different responses to this shape memory cycle for the SMPs and the natural rubber; the SMP does not recover from the applied deformation until it is reheated, in contrast unloading of the natural rubber at low temperature returns it to its equilibrium state without any temporary shape fixing (Liu et al. 2007).

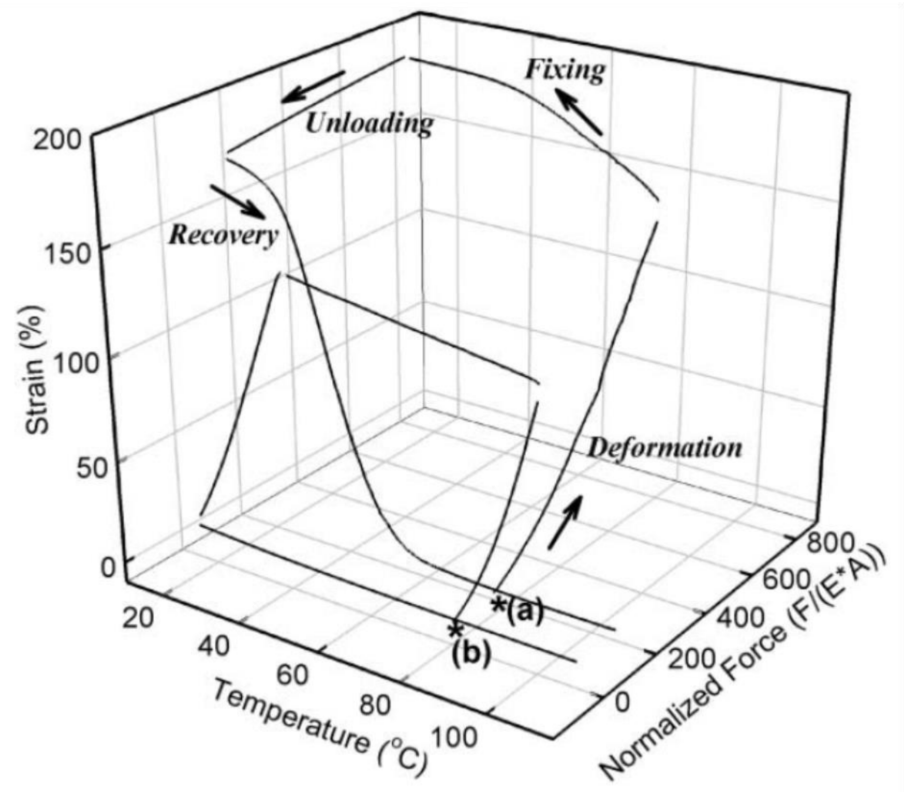

Figure 2.24 – Response to the shape memory cycle for a) a shape memory polymer, and b) natural rubber (Liu et al. 2007)

A polymer will be capable of this shape memory behaviour if the polymer network can be temporarily fixed in a deformed shape through the presence of certain environmental conditions. This requires the deformed chain network to be reversibly prevented from recoiling by the introduction of environmentally dependent “netpoints” within the network. These netpoints determine a network’s shape when free from external stress under a given set of environmental conditions. The network’s permanent shape is determined by another group of netpoints which are either permanent or require a higher activation energy to be broken down such as crystalline melt. Netpoints can take a range of forms, they are generally categorised as chemical (covalent bonds) or physical (intermolecular interactions) (Behl and Lendlein 2007).

The nature of these temporary netpoints was used to differentiate between SMPs by (Liu et al. 2007) who designated 4 categories: 1) Covalently cross-linked glassy thermoset networks, 2) Covalently cross-linked semi-crystalline networks, 3) Physically cross-linked glassy copolymers, and 4) Physically cross-linked semi-crystalline block copolymers.

There are three key features which determine the quality of a polymer’s shape memory performance: 1) the sharpness of the transition used to fix the temporary shape or trigger recovery, 2) the degree of superelasticity displayed above the transition temperature, and 3) rapidity of temporary shape fixing, thus minimising internal strain/stress loss to creep/relaxation (Liu et al. 2007).

One significant benefit of SMPs is that T_g can be conveniently adjusted and can be set to fall anywhere between -40 °C and 120 °C by controlling the molecular structure, weight, and composition. One example of the advantage offered by this adjustable transition is in medical applications where T_g is set to body temperature in the production of self-retaining needles for catheters and drips (Hayashi et al. 2004).

Shape memory research initially focused on the thermally induced shape memory effect, more recently this has been extended to allow the use of alternative stimuli. These can be split into two groups. The first relies on indirect activation of the thermally induced effect; examples of this include indirect heating through irradiation, or the use of infrared light and conducting particles within the polymer. Other examples in this group include activation by water immersion in which a reduced T_g allows water to act as a plasticiser and trigger shape recovery, or the application of an alternating magnetic field (this approach is discussed in more detail below). The second group does not rely on any thermal effect whether directly or indirectly actuated. The most prominent example of this is light induction in which photoreactive molecular switches are incorporated into the material; the bonds created by these molecular switches are formed and broken by light of different wavelengths. All the activation methods described here are discussed in more detail in the review by (Behl and Lendlein 2007).

One activation method that is potentially of particular interest for the LatConX system is that of induction heating through the application of an alternating magnetic field to magnetic nanoparticles included in the material (Behl and Lendlein 2007). This technology would likely improve the energy efficiency, and ease of activation of the LatConX system by eliminating the need to heat the entire polymer environment above T_g. However the inclusion of magnetic nanoparticles within the polymer may be too expensive on the scale required in the construction industry.

2.6.3 Other Shape Memory Materials

Certain ceramic materials known as martensitic ceramics have a martensitic transition between structural phases which results in a thermoresponsive shape memory effect. Polymer gels have the ability to swell or shrink by a considerable amount as a reaction to changes in their environment. As well as the common environmental triggers for SMPs such as temperature, light, and electric fields; pH variation, ionic strength, and solvent quality can also be used to activate the shape memory effect in these gels. A significant drawback is their poor mechanical properties (Lendlein and Kelch 2002).

2.7 Numerical Material Modelling

2.7.1 Concrete Modelling

2.7.1.1 Mechanical Constitutive Modelling

Numerical simulation of the mechanical, and particularly the cracking, behaviour of concrete is of great importance to the accurate analysis of concrete structures; this has led to the development of a large number of material models in the last 50 years. These constitutive models fit into one of two categories; macroscopic models which generally employ a phenomenological approach and micromechanical models which attempt to simulate the microstructure of the material and resulting physical mechanisms governing the evolution of microcracking (Mihai 2012). The set of phenomenological models are most commonly based on plasticity and/or damage theories, each applied to tensile and compressive regions respectively (Jefferson 2010); it is this group of phenomenological models that are focused on in the following discussion.

Two classic methods, widely regarded as the earliest non-linear concrete models and thus marking the beginning of numerical modelling of concrete, are the discrete crack (Ngo and Scordelis 1967), and smeared crack (Rashid 1968) approaches; the behaviour of both of these early models was limited to the cracking of concrete in tension. Discrete crack models, sometimes referred to as cohesive crack models rely on the “incorporation of discontinuous displacement fields to properly capture the strong discontinuity kinematics of a discrete crack”; this requires the introduction of a discontinuity interface, the behaviour of which is governed by a traction-separation law. Contrastingly, smeared crack models are based on the concept of spreading “the dissipated energy along the (finite) width of the localisation band”. The width of this band is set by relating the dissipated energy to the fracture energy (Feist and Hofstetter 2006).

2.7.1.1.1 Plasticity

Plasticity theory and thus models based on it require a yield surface and one or more evolutions functions; further to these an elastic constitutive relationship may be required for example in small strain applications in which the total strain is split into elastic and plastic (Mihai 2012).

Yield surfaces for concrete are generally derived from a biaxial (Kupfer and Gerstle 1973) or triaxial (William and Warnke 1975); (Chen and Chen 1975) failure envelopes which have been obtained experimentally.

Effective plasticity models developed to simulate the nonlinear behaviour of concrete include those of Etse and Willam (1994), Feenstra and De Borst (1995), Grassl et al. (2002), and Chen (2007); a universal weakness of models based solely on plasticity theory lies in their inability to simulate the material degradation that occurs with microcracking.

2.7.1.1.2 Continuum Damage Mechanics

The key damage theory concepts were originally defined by Kachanov in 1958 with the introduction of a scalar damage variable, however the term “continuum damage mechanics” (CDM) was not brought into common usage until its introduction by Hult in 1972 (Lemaître 2005).

Damage mechanics provides a convenient framework able to account for the progressive effects of the propagation of microvoids and microcracks on the strength and stiffness of a material; this is based on a set of kinematic variables which reflect the damage in a smoothed sense instead of any attempt to describe the actual evolution of the microcrack pattern (Krajcinovic and Fonseka 1981). A damage parameter is used to represent the degree of material degradation; this can be a scalar, a family of vectors (Krajcinovic and Fonseka 1981), or in its most general form a fourth-order tensor (Lemaitre and Chaboche 1990). The initiation and evolution of the damage parameter is governed by a damage function most commonly expressed in terms of stresses (Giry et al. 2011), strains (Häussler-Combe and Hartig 2008), or an-energy based variable derived within a thermodynamic framework (Nguyen 2008).

The basic form of an isotropic damage model is that given by Equation (2.1).

$$\boldsymbol{\sigma} = (1 - \omega)\boldsymbol{D_e} : \boldsymbol{\varepsilon} \tag{2.1}$$

in which is ω the damage parameter ($\omega \in [0,1]$), D_e is the elasticity tensor, and ε is the strain tensor. In this model it is assumed that Poisson's ratio is unaffected by damage allowing the use of a single scalar as a damage parameter.

One substantial limitation of such a simple formulation is its inability to differentiate between compressive and tensile behaviour of the simulated material. Mazars (1986) addressed this by introducing a damage parameter that consists of two individual damage components, one each for tension (ω_t) and compression (ω_c), with each governed by a separate evolution function. This approach yields the following expression for the damage parameter.

$$\omega = \alpha_t \omega_t + \alpha_c \omega_c \tag{2.2}$$

in which α_t and α_c are parameters that depend on the amount of tension and compression respectively in a multiaxial loading case.

Other isotropic models employing a similar dual damage parameter approach include the work of Faria et al. (1998), Comi and Perego (2001), Comi (2001), Marfia et al. (2004), and Tao and Phillips (2005).

However in a material such as concrete in which damage is not an isotropic process these isotropic models exhibit a number of limitations; these include an inability to capture the associated volumetric expansion, and an unrealistic loss of strength in lateral directions to a uniaxially applied stress (Mihai 2012). Several anisotropic damage models have been formulated over the last thirty years to attempt to overcome these drawbacks, including the works of Papa and Taliercio (1996), Dragon, Halm, and Désoyer (2000), Sellier and Bary (2002), and Desmorat et al. (2007). However these models are often significantly more complicated than their isotropic equivalents as they tend to require second, or sometimes fourth order tensors for the damage parameter. Convergence issues are also common upon their implementation within finite element codes (Contrafatto and Cuomo 2006), this has been cited by several authors as the reason for making the unrealistic assumption of isotropic damage (Jirásek and Zimmermann 1998); (Salari et al. 2004).

2.7.1.1.3 Plastic-Damage Models

The respective shortcomings of plasticity theory and damage mechanics in simulating all characteristics of the mechanical behaviour of concrete has led to the development of several models based on a combination of the two methods. These plastic-damage models are able to capture both the onset of irreversible deformation, and progressive material degradation characteristics of concrete behaviour through the plastic and damage theory components respectively (Contrafatto and Cuomo 2006). Plasticity theory based on isotropic hardening is usually combined with either isotropic or anisotropic damage (Grassl and Jirásek 2006); examples of the former include the work of Lubliner et al. (1989), J. Lee and Fenves (1998), and Salari et al. (2004); and the latter include Ortiz (1985), Cicekli, Voyiadjis, and Abu Al-Rub (2007), and Voyiadjis, Taqieddin, and Kattan (2008).

2.7.1.1.4 Healing

The development of material models for self-healing behaviour has received significant attention over the past two decades. Some models have been developed in relation to specific materials; for example, Miao et al. (1995) presented a model for rock salt, while Mergheim and Steinmann (2013) considered the behaviour of self-healing polymers. Further to these, models have also been developed by other authors in a more general setting, and thus with correct calibration are applicable to a range of materials (Barbero et al. 2005); (Schimmel and Remmers 2006); (Voyiadjis et al. 2011); (Darabi et al 2012); (Abu Al-Rub and Darabi 2012).

The behaviour simulated by these models results from the healing of any microcracks (or macrocracks) and microvoids present, a process which has been considered to be the opposite of that simulated by continuum damage mechanics.

Thus the healing is often accounted for by considering it as negative damage (Miao et al. 1995); (Barbero et al. 2005); (Schimmel and Remmers 2006). This approach is frequently termed continuum damage healing mechanics (CDHM), a term originally coined by Barbero et al (2005). Furthering this concept, Voyiadjis et al. (2011) developed a combined plasticity and CDHM model, including kinematic and isotropic hardening functions for plasticity, damage, and healing. Mergheim and Steinmann (2013) developed a phenomenological model for self-healing polymers based on the assumption that healing is identical to negative damage. Their model is capable of simulating damage and healing processes simultaneously, and accounting for healing at non-zero strain. A related approach to the modelling of self-healing behaviour is the framework described by Darabi et al. (2012) and Abu Al-Rub and Darabi (2012); in their derivations they consider a cylinder under uniaxial tension splitting the cross-sectional area into three parts to represent the intact area, the unhealed damaged area, and damaged area that have undergone healing thus regaining their strength. This yields an extended version of CDM by introducing the healing configuration alongside the effective configuration in which damage and healing are accounted for by separate internal state variables. A simple one-dimensional form of a healing model was presented by Schimmel and Remmers (2006). Their model is described in relation to discrete damage models however it can also be conveniently applied to the healing of continuum damage. The model allows a proportion of any damage present to be recovered due to healing at one time only; the progress of healing at this time is governed by a healing function, the form of which is chosen depending on the precise healing agent or process under consideration.

2.7.1.2 Transient Behaviour

The time-dependent phenomena of creep and shrinkage in concrete were discovered over a century ago, however despite major successes and significant interest from many researchers the behaviour remains far from fully understood (Bažant 2001). Research in the area was particularly intense during the 70s and 80s due to the importance of understanding the long-term deformation behaviour of nuclear containment structures (Idiart 2009).

The two phenomena of creep and shrinkage are closely linked and share a number of common features (Idiart 2009):

- Both originate in the hardened cement paste
- Strains are partially reversible
- The evolution of the deformations is similar
- They are affected by similar factors, and in similar ways

A full review of the literature on the mechanisms and modelling of creep and shrinkage behaviour of concrete is beyond the scope of this thesis; as such this section only includes an introduction to the most relevant models. For a more comprehensive review of these phenomena the author refers the reader to the works of Bažant (2001) and Idiart (2009).

According to Bažant (2001), there are two main model types for predicting the creep and shrinkage behaviour of concrete; true constitutive equations that deal with a small representative volume element (RVE), and models that approximate the mean cross sectional behaviour of larger elements. Bažant compares the relative merits of the two types, stating that the cross-sectional models are "inevitably much more complicated in their form, because they must also characterise the solution to the boundary value problem of evolution of humidity distributions, residual stresses, and cracking"; while the former set of models are "much more difficult to identify from test data because their fitting to data involves an inverse boundary layer problem".

The design models that appear in concrete codes of practice are generally of the cross-sectional type, examples include the ACI-209R-82 model (American Concrete Institute (ACI) 1982), the B3 (Bažant and Baweja 1995) and B4 (Wendner et al. 2013) models, the CEB-FIP 1990 (CEB-FIP 1994) models, GL2000 model (Gardner and Lockman 2002), and Eurocode 2 (BSI 2004). Goel et al (2007) presented a comparative study of five of these creep and shrinkage models in which they summarised the merits, and shortcomings of the models reviewed.

A notable RVE model for predicting creep is the method termed solidification theory developed by Bažant and coworkers (Bažant and Prasannan 1989); (Bažant et al. 1997). Ageing of the concrete is considered to result in an increase in the volume fraction of the load-bearing solidified material i.e. hydrated cement; this solid material is then treated as a non-ageing viscoelastic material. Thus the total creep strain can be defined as the total of the ageing and non-ageing viscoelastic strains, and the ageing viscous strain. A schematic diagram for the resulting rheological model is shown in Figure 2.25.

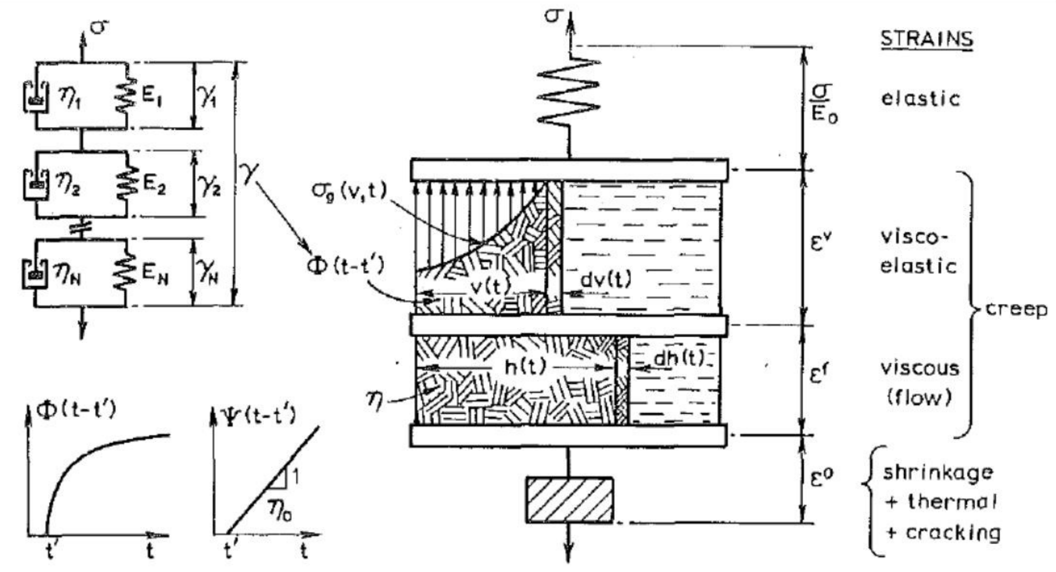

Figure 2.25 – Schematic diagram of rheological model for creep proposed by Bažant and Prasannan (1989)

In a later publication, Bažant et al. (1997) state that the above described solidification is insufficient for a full description of creep behaviour as it cannot account for long-term ageing due to the volume growth of the hydration products being too short-lived. This is addressed by extending the theory to what is termed “microprestress-solidification” in which the viscosity of the flow term is a function of a tensile microprestress carried by the bonds and bridges between micropores in the hardened cement gel. Long-term relaxation of this microprestress results in long-term ageing of the flow term.

2.7.2 Polymer Modelling

In this section a number of methods for the modelling of polymer material behaviour are introduced. Numerical techniques for quantifying the deformation and temperature dependent behaviour of polymers in isolation are initially introduced, before the more recent use of these theories in combination for the simulation of more complex behaviour such as the shape memory effect is discussed.

2.7.2.1 Deformational Behaviour

The formulation of a constitutive model capable of simulating the full range of deformation behaviour discussed in Section 2.5.6 and observed in Figure 2.20 poses a considerable problem to polymer scientists. A complete polymer model would need to account for the time, temperature, and stress dependent behaviour throughout the full strain range, as well as the effects of physical ageing and a number of other phenomenon; these requirements are summarised well in the context of uncross-linked amorphous polymers by Buckley and Jones (1995). Numerical models in this field can be classified into two distinct sets; macroscale rheological models, and microscale molecular models, a number of these will now be introduced.

The earliest attempts to model the deformational behaviour of polymers focused on specific aspects in isolation and often relied on single integral or differential equations (Buckley and Jones 1995). Rheological models used to model linear viscoelastic behaviour are examples of this approach, these are mechanical models made up of combinations of spring and dashpot elements, representing the elastic and viscous characteristics respectively. Basic examples are the Maxwell and Kelvin-Voigt models show in Figure 2.26 which are capable of representing stress relaxation and creep behaviour respectively (Aflaki and Hajikarimi 2012).

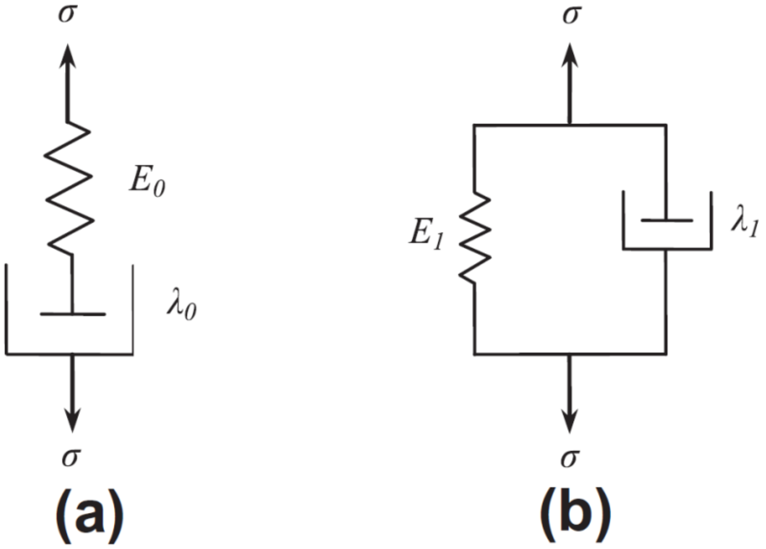

Figure 2.26 – Basic rheological models for viscoelastic behaviour: a) Maxwell model, b) Kelvin-Voigt model (Aflaki and Hajikarimi 2012)

The Zener or standard linear solid (SLS) model consists of an elastic spring either in parallel with a Maxwell element, or in series with a Kelvin-Voigt element, this provides a more comprehensive model capable of simulating both stress relaxation and creep behaviour. The use of SLS models for this purpose has been demonstrated by Wang et al. (1995) and Almagableh, Raju Mantena, and Alostaz (2010). A further example of a rheological model is the Burgers model which is composed of a Kelvin-Voigt model and a Maxwell model in series; Aflaki and Hajikarimi (2012) used this configuration to represent the viscoelastic properties of asphalt binders.

Another common method for describing behaviour in the linear viscoelastic region is the Boltzmann single integral representation, which for short timescales reduces to Hookean elasticity (Klompen 2005).

There are a plethora of constitutive relations for the nonlinear viscoelastic range, with the most common approach being to generalise the linear Boltzmann interval (Klompen 2005). One example of a generalised Boltzmann interval involves the inclusion of higher order stress or strain terms (Findley and Onaran 1976). A comprehensive discussion on nonlinear viscoelastic theories is available in the book by Ward (1983).

The strong strain-rate and temperature dependence of polymers prohibits the description of their yield stress through conventional yield criteria; instead molecular flow theories are usually applied. These models which include the Eyring theory (Eyring 1936) and Argon theory (Argon 1973) consider polymers to be high-viscosity stress activated fluids (Klompen 2005).

Halsey et al. (1945) observed that for almost all applications the dashpot appears to be non-Newtonian, and suggested that in cases of model inadequacy the appropriate solution is the use of more complicated laws for the element behaviour instead of simply increasing the number of simple elements used. This approach led to the development of the Eyring model in which the Newtonian dashpot of an SLS model is replaced with a dashpot governed by the Eyring equation (Halsey et al. 1945); the macroscopic deformation of such an Eyring dashpot is assumed to be the result of fundamental processes, such as chain sliding or conformational chain changes (Ward and Sweeney 2004). The stress dependent flow process is attributed to the applied stress altering the potential energy barrier, resulting in unequal flow in each direction (see Figure 2.27) (Halsey et al. 1945).

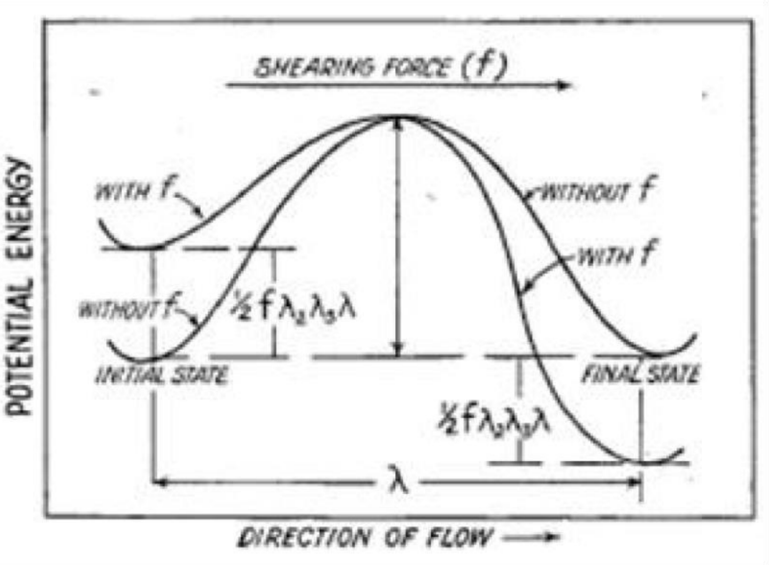

Figure 2.27 – Effect of applied stress on potential energy barrier (Halsey et al. 1945)

Adaptations of the Eyring equation have been used to model several aspects of viscoelastic behaviour including creep (Sherby and Dorn 1958), stress relaxation (Guiu and Pratt 1964), and yield behaviour (Sweeney et al. 1999).

One drawback of molecular flow theories such as Eyring and the Argon models is that they do not account for strain softening or hardening behaviour in the post-yield strain range (Klompen 2005). The majority of approaches applicable to this range of behaviour are based on the work of Haward and Thackray (1968) who proposed a model incorporating a finite extendable rubber spring in parallel with an Eyring dashpot to account for strain hardening.

2.7.2.2 Thermal Behaviour

One of the simpler methods of accounting for the temperature dependence of polymer properties is the “Gaussian Network” in which the shear modulus (G) varies with temperature according to the relationship shown in Equation (2.3).

$$G = N_e k T \tag{2.3}$$

in which N_e is the number of entanglements per unit volume, k is Boltzmann's constant, and T the absolute temperature.

Williams et al. (1955) built on the work of Doolittle (1951) in developing another widely used relationship for temperature dependence; the WLF Equation. The equation describes the behaviour of polymers near and above T_g as they soften and flow.

The Arrhenius Equation is an empirically derived relationship for the thermal dependency of viscosity (Tobushi et al. 2001). The equation describes the influence of temperature on the rate of chemical reactions, and thus the frequency of molecular conformational changes (Ward and Sweeney 2004). Tobushi et al. (2001) used a similar exponential relationship to the Arrhenius equation to describe the temperature dependence of Young's modulus and several other temperature dependent material parameters. Other authors using Arrhenius related temperature dependence include Buckley and Jones (1995), Brandt (1959), and O'Connell and McKenna (1999).

Tobushi et al. (1997) discuss the requirement for a polymer constitutive equation to take account of thermal expansion/contraction of the material. They propose that the coefficient of expansion should be independent of mechanical behaviour.

2.7.2.3 Shape Memory Effect

Recent constitutive modelling work undertaken in the area of SMPs has focused on the programming of the shape memory effect and the material's behaviour immediately before and after activation.

An early approach developed by Pakula and Trznadel (1985) accounted for the temperature dependence of amorphous polymers by use of a four-state model based on the Burgers model but with the dashpots replaced with two-site elements. The model consists of two elastic springs and two two-site elements as shown in Figure 2.28. The left-hand spring accounts for chain elasticity, while the right hand spring accounts for the elastic junction between the matrix and subunit.

The extension/contraction of both springs is governed by the behaviour of the two-site elements which act as barriers to molecular movement at low temperature. This allows shrinkage stress to be locked in until the applied temperature is raised sufficiently for the barrier to be overcome. The barrier heights are defined by the Helmholtz free energy difference, with the probability of movement between sites defined by the height of the barrier and the stresses in the springs.

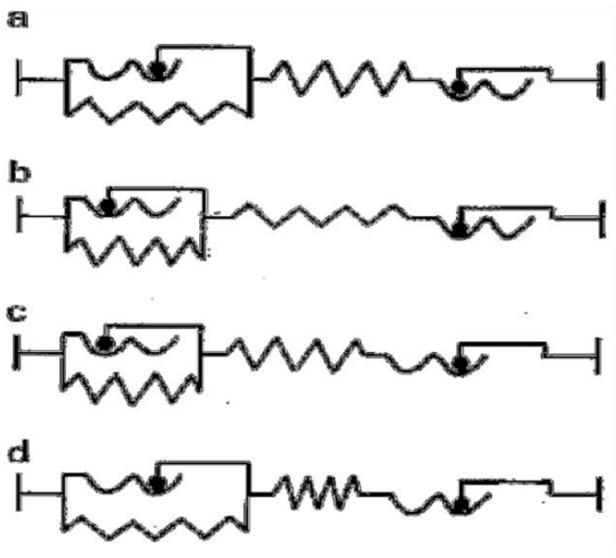

Figure 2.28 – Four possible states of four element model by Pakula and Trznadel (1985)

A modified SLS model for the shape memory behaviour of polyurethane was developed through a series of papers by Tobushi and coworkers (Tobushi et al. 1997); (Bhattacharyya and Tobushi 2000); (Tobushi et al. 2001). A frictional element was added in series with the elastic element of an SLS (see Figure 2.29) to account for the change in mechanical properties either side of T_g; it is this frictional element that fixes in the temporary shape and accounts for the varying levels of irrecoverable creep strain at different temperatures (Tobushi et al. 2001).

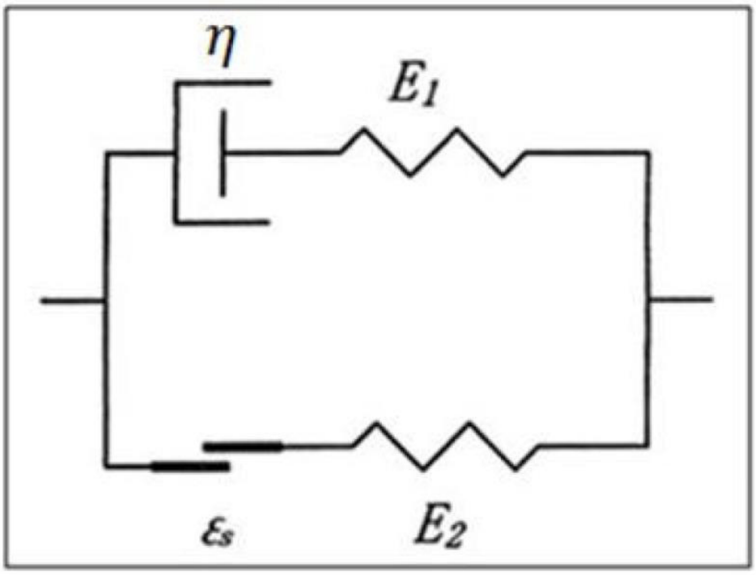

Figure 2.29 – Four element model of Tobushi et al. (1997)

The constitutive equations governing the model’s behaviour are initially developed in a linear form as shown in Equation (2.4) (Tobushi et al. 1997), before being extended to the nonlinear form shown in Equation (2.5) (Tobushi et al. 2001).

$$\dot{\varepsilon} = \frac{\dot{\sigma}}{E} + \frac{\sigma}{\mu} - \frac{\varepsilon - \varepsilon_s}{\lambda} + \alpha\dot{T} \tag{2.4}$$

$$\dot{\varepsilon} = \frac{\dot{\sigma}}{E} + m\left(\frac{\sigma - \sigma_y}{k}\right)^{m-1}\frac{\dot{\sigma}}{k} + \frac{\sigma}{\mu} + \frac{1}{b}\left(\frac{\sigma}{\sigma_c} - 1\right)^{n} - \frac{\varepsilon - \varepsilon_s}{\lambda} + \alpha\dot{T} \tag{2.5}$$

In both of the above equations σ, ε, T, E, μ, λ, and α are stress, strain, temperature, modulus of elasticity, viscosity, retardation time, and the coefficient of thermal expansion respectively. ε_s is the irrecoverable strain, given by $\varepsilon_s = S\varepsilon_c$ in Equation (2.4) and $\varepsilon_s = S(\varepsilon_c + \varepsilon_p)$ in Equation (2.5), in which S is a proportionality coefficient, ε_c is the time-dependent creep strain, and ε_p is the time-independent plastic strain. In the nonlinear equation σ_y and σ_c are proportional limits of stress for the time-independent and the viscous terms respectively.

The mechanical properties of the four element model are assumed to be constant above and below the glass transition (T_g ± 15 K) and to vary according to Equation (2.6) through the transition. Equation (2.6) is an exponential function of a similar form to the Arrhenius and Eyring Equations.

$$x = x_g exp\left[a\left(\frac{T_g}{T} - 1\right)\right] \tag{2.6}$$

In Equation (2.6), x is the material property under consideration, T is the temperature under consideration, x_g is the value of x at T_g, and a is a constant.

The model is used to recreate a range of thermomechanical material behaviour including shape fixity, shape recovery, and recovery stress with good accuracy (Tobushi et al. 2001).

Morshedian et al. (2005) developed a rheological model comprising a Kelvin-Voigt element in series with another dashpot as seen in Figure 2.30. Both dashpot viscosities are temperature dependent allowing the model to simulate the four stages of the shape memory effect shown in Figure 2.30 with good accuracy.

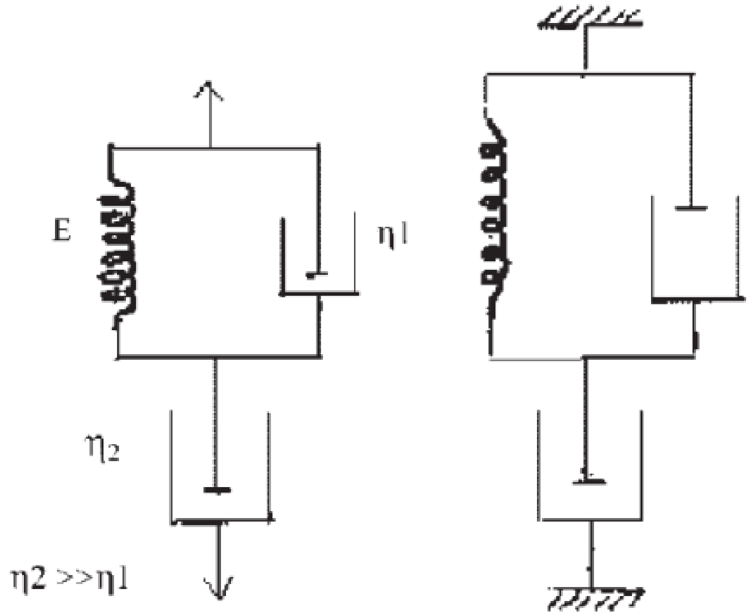

a) Proposed model

b) Stretched by a fixed strain and cooled

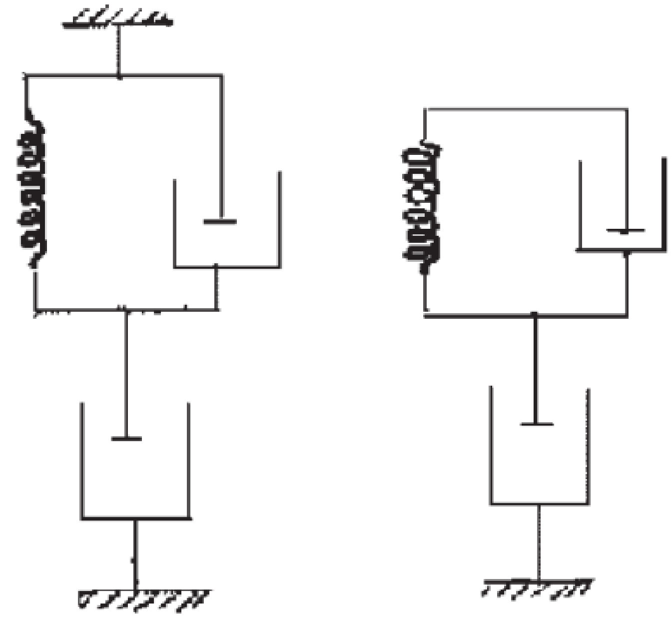

c) Stress relaxation followed by orientation freeze-up to produce a heat shrinkable system

d) Heat shrunk model without full recovery

Figure 2.30 – Three element model and shape memory induction and recovery process proposed by Morshedian et al. (2005)

Examination of the model’s behaviour allowed Morshedian et al. (2005) to attribute the incomplete strain recovery observed in the experimental aspect of the work to "the occurrence of some stress relaxation during molecular orientation freeze-up in the stretch holding-cooling time-step".

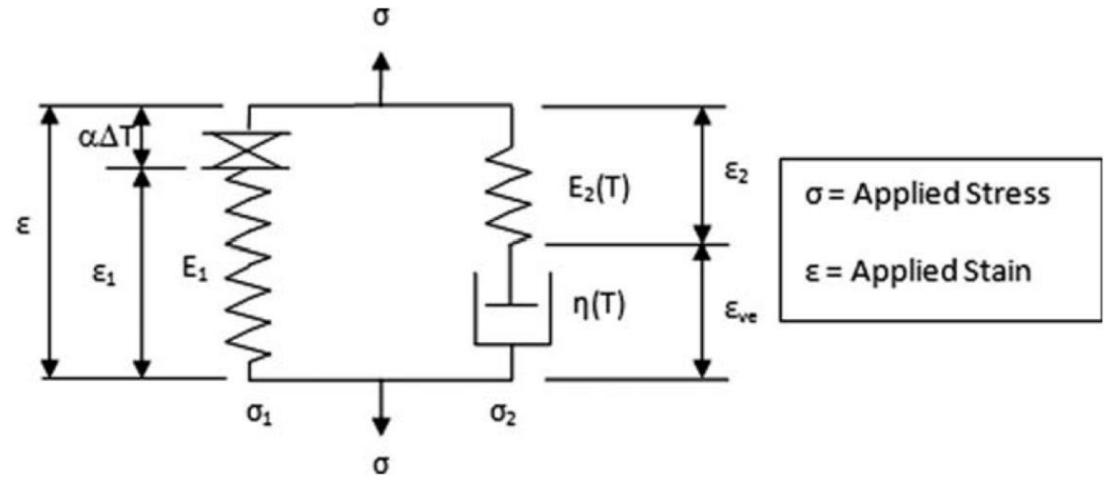

Figure 2.31 – Modified SLS model proposed by Dunn et al. (2011)

A final rheological approach is that of Dunn et al. (2011) who developed a modified SLS model as shown in Figure 2.31. The viscosity and Young's modulus of the Maxwell arm were represented by modified tanh functions with good agreement demonstrated between these numerical idealisations and the measured material properties (see Figure 2.32). Validation was achieved with good accuracy by comparing the model predictions for restrained shrinkage stress build up against experimental findings; both the time and temperature dependent behaviour was validated.

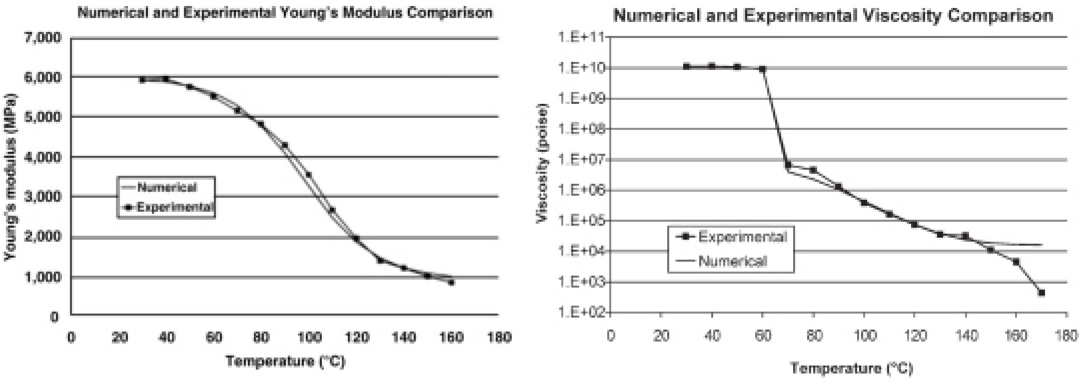

Figure 2.32 – Numerical idealisations vs measured experimental values for temperature dependent material properties (Dunn et al. 2011)

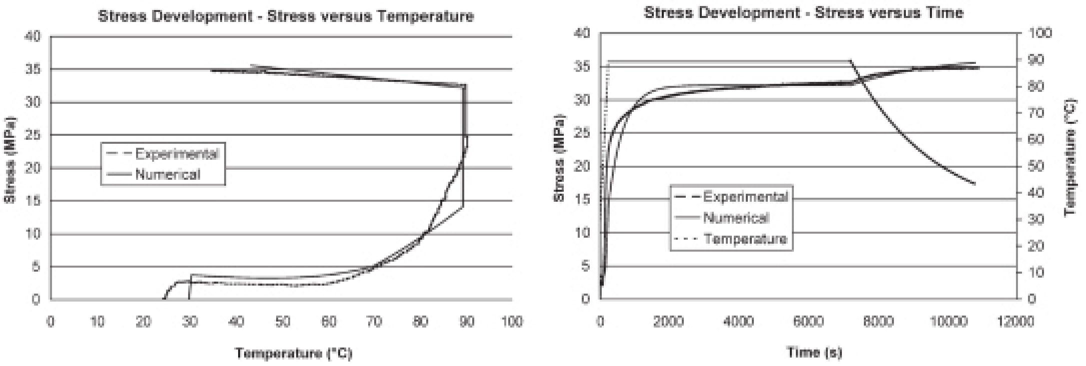

Figure 2.33 – Model simulations compared to experimental data for restrained shrinkage induced stress development vs temperature and time (Dunn 2010)

A different approach to the modelling of the shape memory phenomenon is to consider the polymer as consisting of a number of distinct extreme phases each with its own material properties and constitutive relationship. An example of this type of model is the work of Liu et al. (2006), the model consists of active and frozen phases which account for the differences in state either side of the glass transition. In the frozen phase the conformational rotations corresponding to high temperature deformation are completely disabled which means that deformation is only possible through stretching and small rotations. Contrastingly in the active phase free conformational motion can take place. The ratio of these two phases varies through the glass transition as a function of temperature resulting in a glassy response at low temperatures and a rubbery response at high temperatures

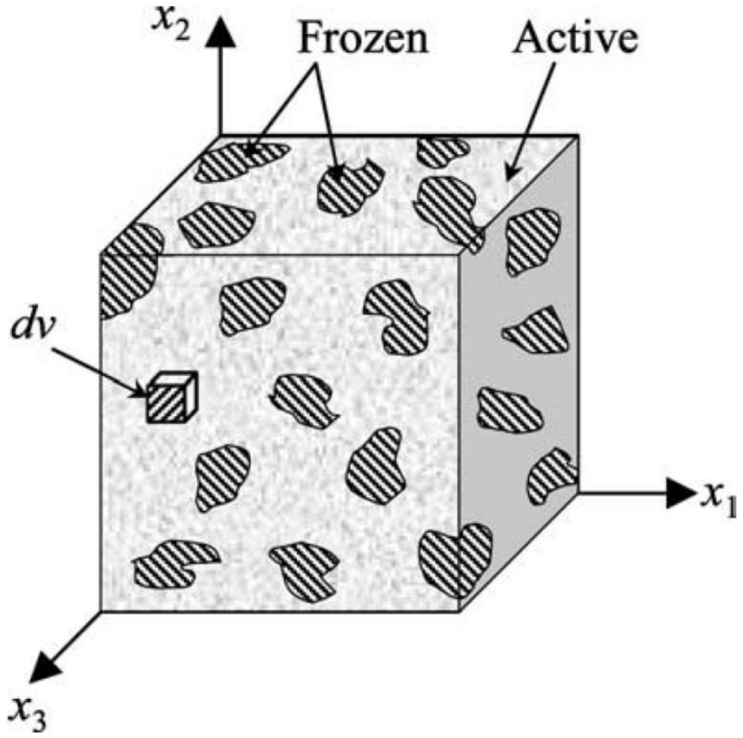

Figure 2.34 – Two phase model of Liu et al. (2006)

The model is demonstrated to be capable of simulating uniaxial strain and constrained stress recovery behaviour with suitable accuracy.

Qi et al. (2008) take these concepts further in the development of a three-dimensional model in which the glassy phase considered by Liu et al. (2006) is divided into a frozen glassy phase and an initial glassy phase in order to account for the glassy phase’s deformation history.

Barot et al. (2008) have developed a model based on similar principles to the model of Liu et al. (2006) discussed above for the shape memory effect in crystallisable SMPs. Two phases are used to represent the different material states, namely rubbery amorphous and rigid semi-crystalline, with the crystallising and melting processes governed by prescribed rate equations (Barot and Rao 2006); (Barot et al 2008).

Chapter 3 - Shape Memory Polymer – Experimental Studies

An experimental test series was carried out to investigate the long-term viscoelastic behaviour of the shape memory polymer (SMP) material intended for use in the LatConX system. The primary aim of this was to gain an understanding of the stress relaxation behaviour of the material subsequent to heat-activated restrained shrinkage. A secondary aim was to gain a better general understanding of the material's long-term viscoelastic behaviour in order to inform the development of the numerical model presented in Chapter 4.

Clearly for the intended purpose within the LatConX system a thorough understanding of these viscoelastic processes is vital as any reduction in the polymer stress will reduce the applied crack closure force.

Selected findings from this experimental work are presented in the publication by Hazelwood et al. (2014).

3.1 General Testing Information

Two types of stress relaxation test were carried out on the polymer specimens, namely heat-activated stress, and manually applied stress tests; details of these tests are given in full in the relevant sections below. Stress relaxation is defined as the reduction in stress in a specimen held at constant strain.

All tests were carried out on the same material, and similarly constructed specimens. Specific details of these are given in the relevant sections below.

3.1.1 Material Specifications

All experiments were carried out using the pre-drawn polyethylene terephthalate (PET) material Aerovac ShrinkTite, in 32 mm × 0.046 mm tape form. This was obtained from Aerovac (http://www.aerovac.com/), however the company has since changed name to Umeco (http://www.umeco.com). This was the material identified as the best suited for this application during screening tests carried out by Jefferson et al. (2010). The criteria outlined by Jefferson et al for a suitable material were fourfold:

1. Minimum restrained shrinkage stress of 20 MPa, this value was determined by Jefferson et al. (2010) as being the required stress to result in an extreme fibre compression of 1 MPa – twice that required for enhancement of autogenous self-healing (ter Heide and Schlangen 2007).
2. Shrinkage activation temperature between 60 – 100 °C. Activation within this range is necessary firstly to avoid unintended activation by either heat of hydration or warmth from the environmental conditions; and secondly to avoid potential damage to the cementitious matrix from excessive application of heat during activation.
3. Good resistance to the alkaline environment of a cementitious matrix.
4. Maximum stress relaxation losses of 30 % over the working life of the structure.

The first two of these criteria were satisfied in full during the screening tests, and it is suggested that further long-term tests are required to satisfy the third criterion (Jefferson et al. 2010). Investigation of the fourth criterion is the key aim of this Chapter.

Satisfaction of this criterion would be beneficial for two reasons; firstly it would mean that an adequate stress will be applied to the cracked faces of the cementitious material for an extended period of time giving continuous aid to autogenous healing of the crack (ter Heide and Schlangen 2007); (Isaacs et al. 2013). Secondly the polymer tendons could be considered to act as an effective long-term prestressing system improving the performance of the cementitious structure.

3.1.2 Test Specimen Preparation

All test specimens were composed of a number of strips of the polymer tape 400 mm long (±2 mm), held by a grip at each end consisting of two flat metal plates measuring 60 mm × 23 mm × 2 mm as shown in Figure 3.1, each pair of flat plates was held together by two bolts which were tightened to hold the specimen in place. The number of strips varied from 8 to 25 depending on the exact conditions required for the test i.e. the stress required in the specimen.

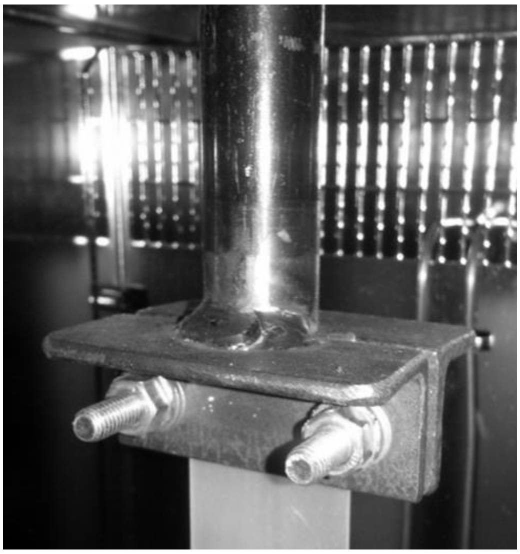

Figure 3.1 – Grip used to hold ends of test specimens

It was important to ensure that the strips making up each specimen were all the same length between the two grips so that when any strain was applied the stress would be effectively equal in each strip. This was achieved by using a timber jig (see Figure 3.2) to hold the strips together along their full length while the end grips were attached.

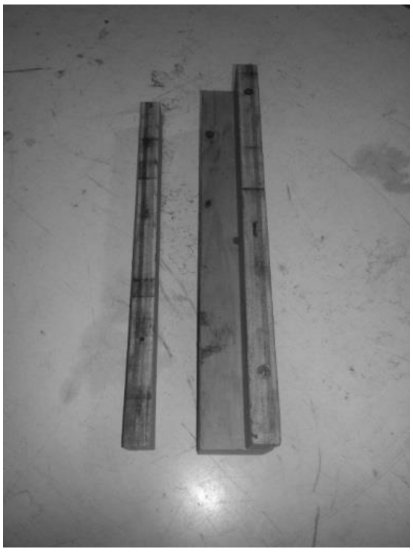

Figure 3.2 – Timber jig used to hold strips while grips were attached

When similar tests to these have been carried out by Dunn in the past, a major issue encountered was slipping of the specimen between the grips (Dunn 2011). Dunn addressed the issue by melting the ends of the polymer specimen to form a mechanical plug behind the grip, thus removing the specimen's propensity to slip. In the experiments presented here an alternative method was preferred which used larger grip plates and screws, allowing a greater frictional force to be applied to the specimens by the grips. In order to detect any slip, a line was drawn (in pen) on the specimen parallel to the bottom of the grip at both ends. The grips, specimens' ends, and marked lines were monitored closely throughout all experiments to ensure that no slippage took place.

In all tests the data recording equipment was turned on before any load or temperature was applied to the specimens thus ensuring that any immediate relaxation behaviour was captured.

3.2 Manually Applied Stress Relaxation Tests

The first stage of the investigation involved a series of simple one-dimensional stress relaxation tests carried out on un-activated specimens; a custom built rig was constructed for this purpose, which may be seen in Figure 3.3 and Figure 3.4. A screw tightening system was used to manually apply stress to a polymer specimen.

Once the desired initial stress was reached, the screw tightening system was locked off to ensure a constant strain within the specimen. The force was monitored at 10 minute intervals using a 0.5 kN load cell for the duration of the test, which varied from 11 – 20 days. This was carried out for initial stresses ranging from 4 MPa up to 20 MPa. During the 4 MPa test there was an error with the thermocouple that led to the ambient temperature only being recorded every 12 hours instead of every 10 minutes.

Figure 3.3 – Experimental setup for manually applied stress relaxation tests

The results for the five tests are shown in Figure 3.5. Due to the large quantity of data, and minor short term stress and temperature fluctuations, the data points have been time averaged, yielding bi-daily values; this provides much improved clarity when plotting the data. This method of time averaging has been applied to all manually applied stress relaxation data unless stated otherwise.

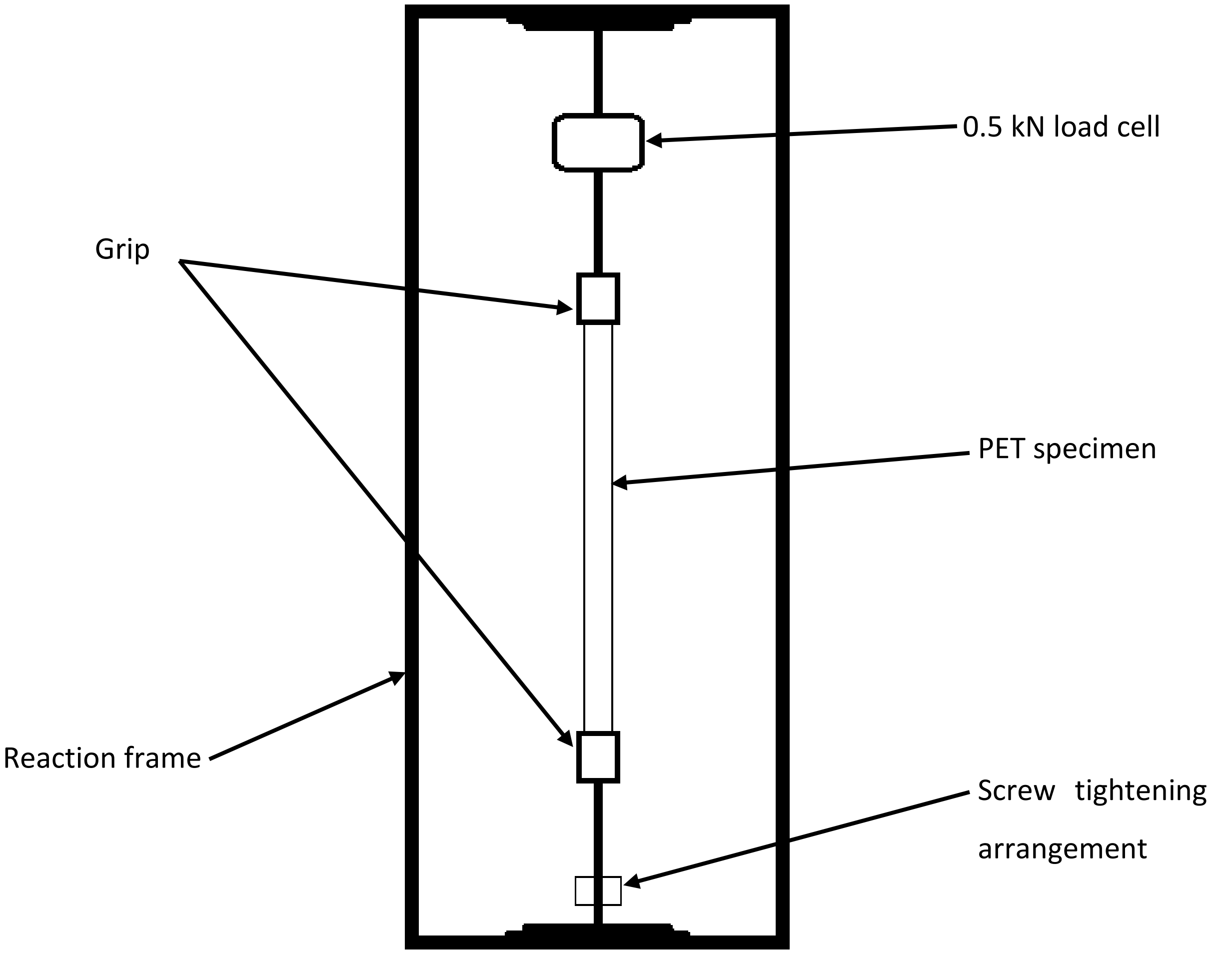

Figure 3.4 – Diagram of experimental setup for manually applied stress relaxation tests

The stress on the specimens fluctuates both above and below the initially applied stress by up to 0.5 MPa and 1.3 MPa respectively, there is also a clear pattern of the stress reducing when the temperature increases. This pattern is assumed to be due to thermal expansion or contraction of the specimens. An analysis of these trends gave Pearson's product-moment coefficients ranging from -0.27 to -0.73, with a mean value of -0.51. This means that there is a weak correlation between temperature increase and stress decrease, hence there must also be other factors causing further stress changes beyond those due to thermal movement. At this stage these further stress changes are assumed to be due to the viscoelastic relaxation of the material.

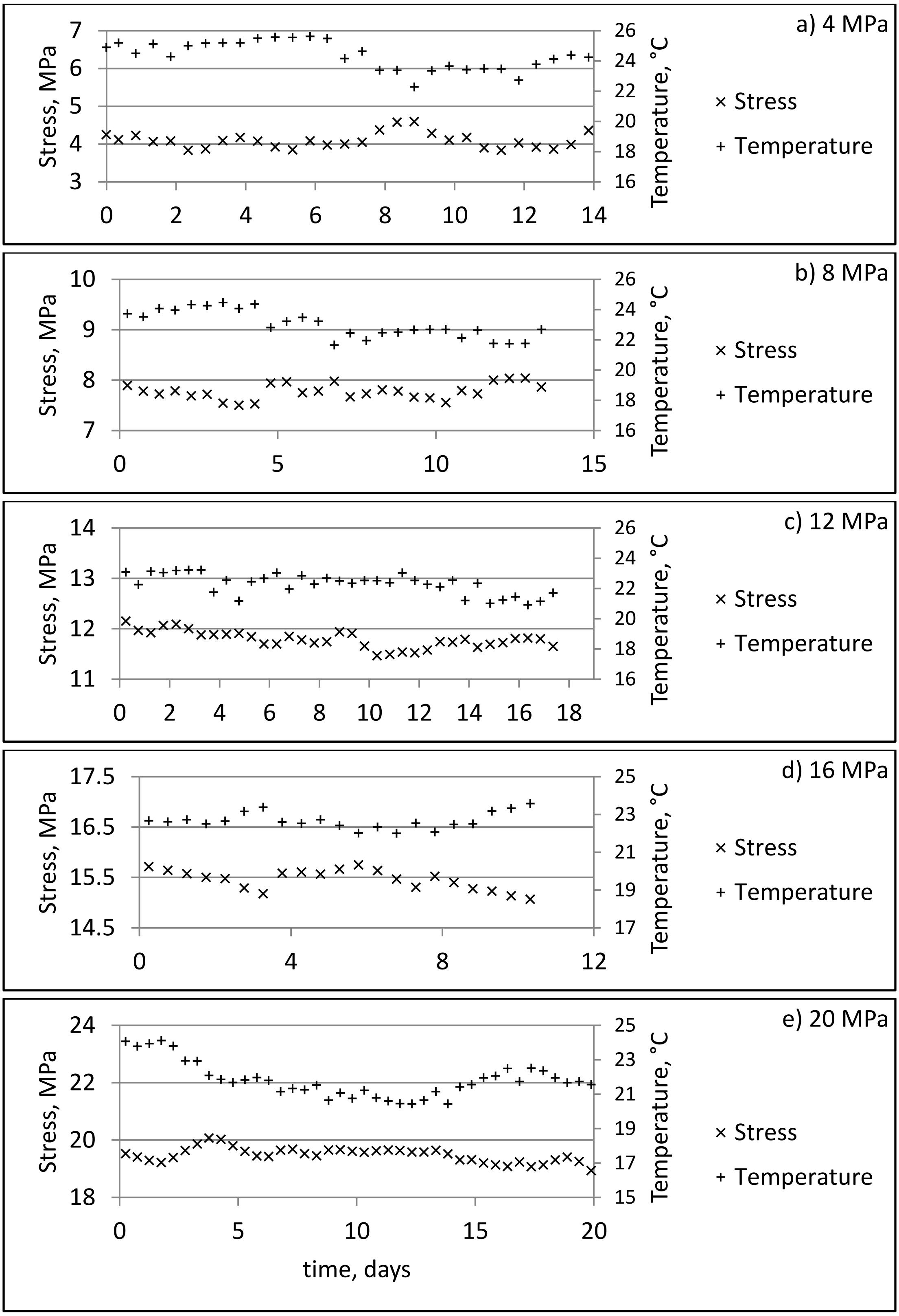

Figure 3.5 – Stress and ambient temperature vs time for manually applied stress relaxation tests

To investigate this assumption, the temperature change from the initial temperature was used to calculate the expected stress change due to thermal expansion or contraction of the specimen. This calculation was carried out based on the assumptions that the material behaves elastically and that the low temperature Young's modulus (6000 MPa) is applicable, the latter having been determined using the procedure described by Dunn et al. (2011). A value of 16 x 10^{-6} was measured for the coefficient of thermal expansion hence the stress change, $\Delta\sigma_T$, due to any change in temperature, ΔT, can be calculated from:

$$\Delta\sigma_T = \Delta T \cdot E_{TOT}\alpha_p \tag{3.1}$$

where $\Delta\mathrm{T}$ is the change in temperature, E_{TOT} is the low temperature Young's modulus, and α_p is the coefficient of thermal expansion.

The original results were then modified by removing this stress change to reveal any underlying trends. The stress values were also normalised to the initially applied stress to allow any losses to be easily observed as a percentage. These modified normalised results are shown in Figure 3.6.

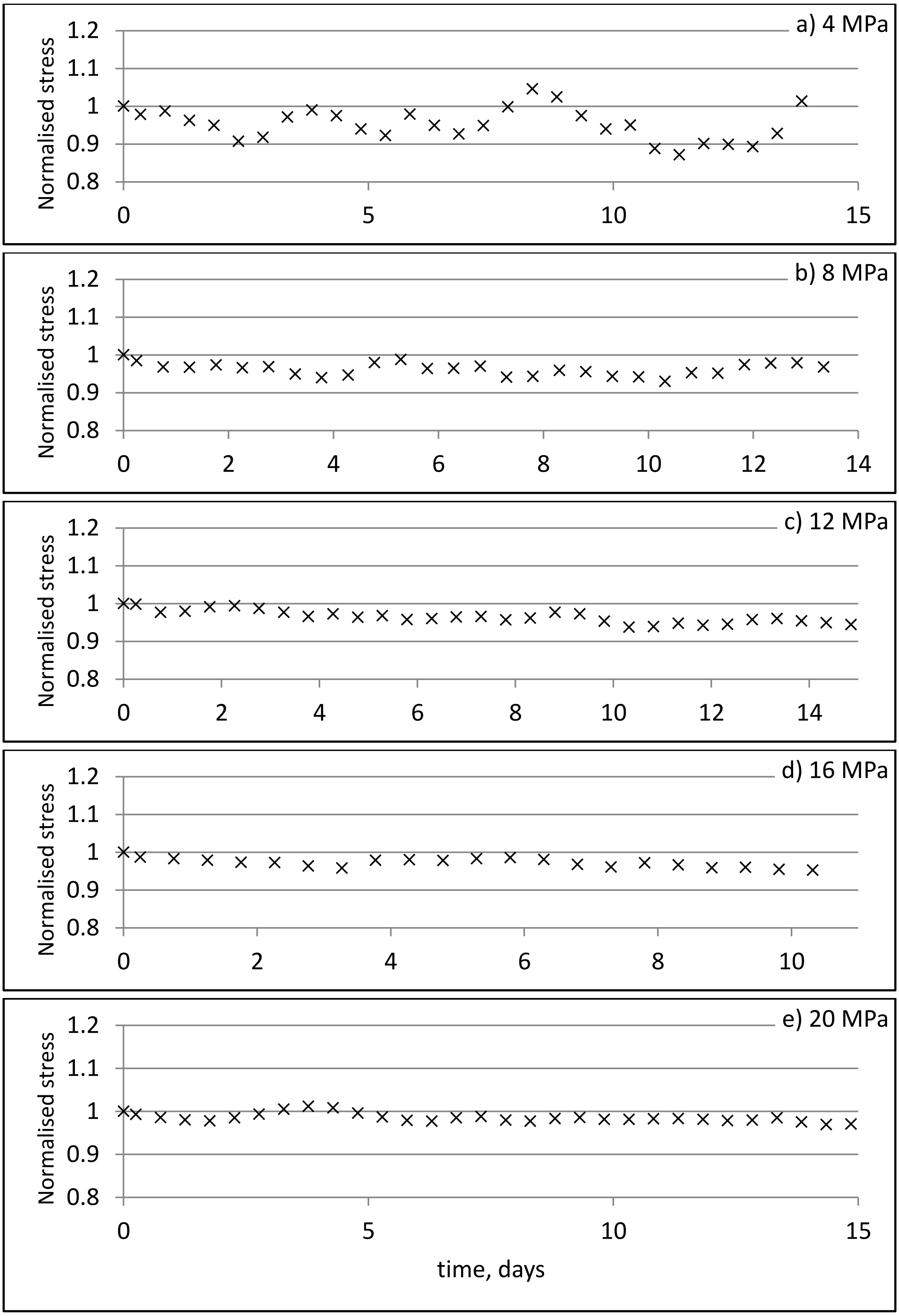

Figure 3.6 – Normalised temperature modified stress vs time plots for manually applied stress relaxation tests

At first observation, the 4 MPa Figure still shows relatively large stress fluctuations both above and below the initial stress, while fluctuations on the other plots are considerably reduced and are now primarily below the initial stress as would be expected. This disparity is considered to be a result of the lack of temperature data due to the thermocouple error mentioned earlier. The lack of temperature data meant that the results of the 4 MPa test could not be modified to account for temperature at all data points, thus the modified stress could not be time averaged, resulting in the large stress fluctuations. For this reason, discussions from here on will refer to the 8 – 20 MPa tests only. In the remaining four tests the stress appears to relax to a relatively steady primary plateau stress, although this plateau does still display fluctuations of as much as 1 %. These fluctuations make it hard to define a clear plateau value and time by pure observation; however more in depth analysis involving a series of averages taken at different points throughout the data has revealed that the time of plateau varies between 4 and 10 days, and the stress on this initial plateau varies between 95.7 and 98.5 % of the initially applied stress. At this point any remaining stress relaxation is too minor in magnitude to be clearly observed from tests at this time-scale.

A definitive cause for the stress fluctuations observed in Figure 3.6 has not been identified, however two possibilities seem most likely. The most likely seems to be the effect of further thermal effects that have not been accounted for, i.e. expansion/contraction of the reaction frame, grips, load cell, and connection fittings. The effects of vibrations caused by other activity in the laboratory environment, including the operations of nearby large machinery, and passing foot and small vehicle traffic may also have caused a certain amount of noise in the data.

Finally, the normalised stresses have been averaged across the four initial stress values, 8 – 20 MPa, thus taking all available data into account. The results of this are displayed in Figure 3.7. This plot confirms the trends described above, the average time taken to reach the primary stress plateau is approximately 9 days. The average plateau stress observed from Figure 3.7 is 96.4 %.

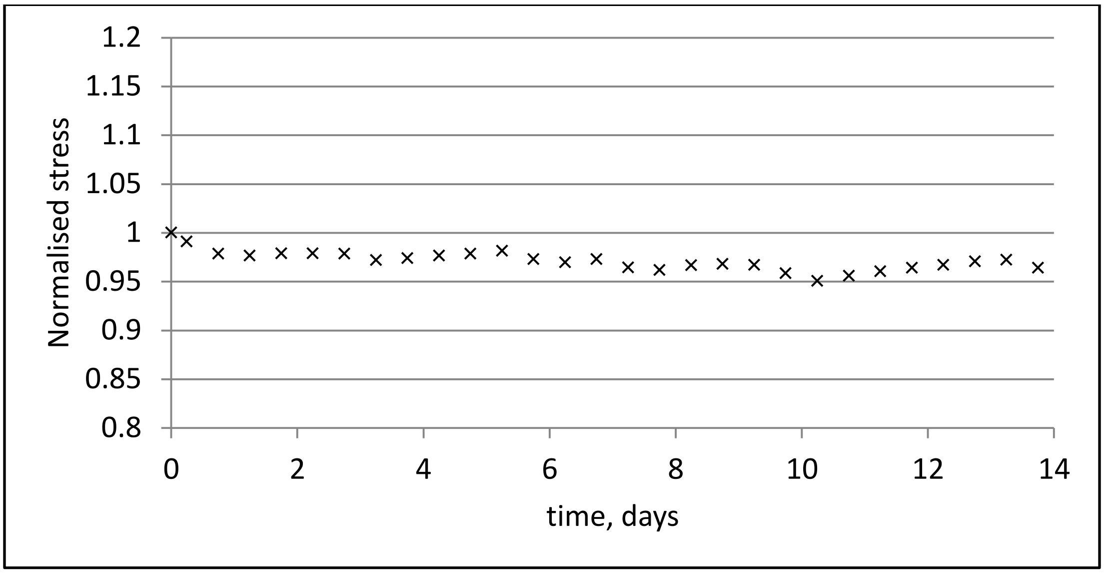

Figure 3.7 – Normalised modified stress vs time averaged across four manually applied relaxation tests

3.3 Heat-activated Stress Relaxation Tests

The second element of these long-term stress relaxation investigations considered the magnitude of any relaxation subsequent to heat-activated restrained shrinkage. As mentioned earlier, quantifying any reduction of this type of stress was vital for the further development of the LatConX material system. This issue was directly addressed by recreating the restrained conditions a polymer tendon would be subject to within the system.

In this series of tests, the specimen was held in the grips in a position so that it was just taut, a heat of 90 ^{o}C was then applied to the specimen for a period of ten minutes, thus activating the shrinkage behaviour of the drawn polymer, and thereby inducing a stress within the specimen. A soak time of ten minutes was chosen due to the finding of Dunn et al. (2011) that five minutes soak time is sufficient. This has been increased to 10 minutes to allow for the temperature rise time and thereby ensure application of a full five minutes at 90 ^{o}C. The stress in the specimen was monitored and logged over time as well as the ambient temperature of the surrounding environment.

Figure 3.8 – Experimental setup for heat-activated stress relaxation tests

The experimental setup for this test is shown in Figure 3.8. To enable these tests to be undertaken, an Instron oven was fixed within a Mechtric reaction frame, fixings were constructed to connect the grips holding the specimen to the top and bottom of the reaction frame with the specimen running through the middle of the oven. A load cell was incorporated into these fixings above the oven as can be seen in Figure 3.8. The force in the specimen, and the temperature at different locations both inside and outside the oven were monitored by a 2.5 kN load cell and 12 thermocouples respectively. These were all attached to a data logger; with readings initially taken at fifteen second intervals, increasing to 15 minute intervals and finally 12 hour intervals for the duration of the test. A diagram of the experimental setup for these tests can be seen in Figure 3.9.

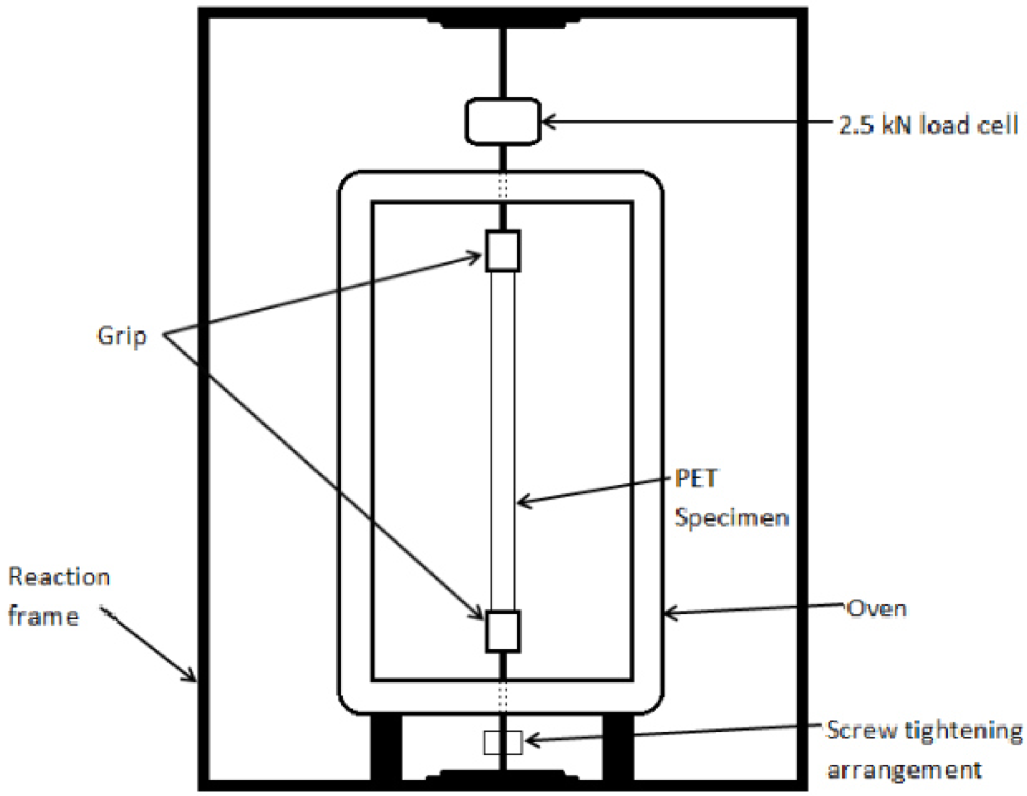

Figure 3.9 – Diagram of experimental setup for heat-activated stress relaxation tests

Five of these tests have been carried out with a typical set of results being as presented in Figure 3.10 and Figure 3.11. In this example the stress reaches a peak of 26.7 MPa approximately 2.5 hours into the test before reducing over a period of approximately 150 days to an average plateau stress of 25.6 MPa. This value is an average since the stress continues to fluctuate between 25.2 MPa and 25.9 MPa once the plateau is reached.

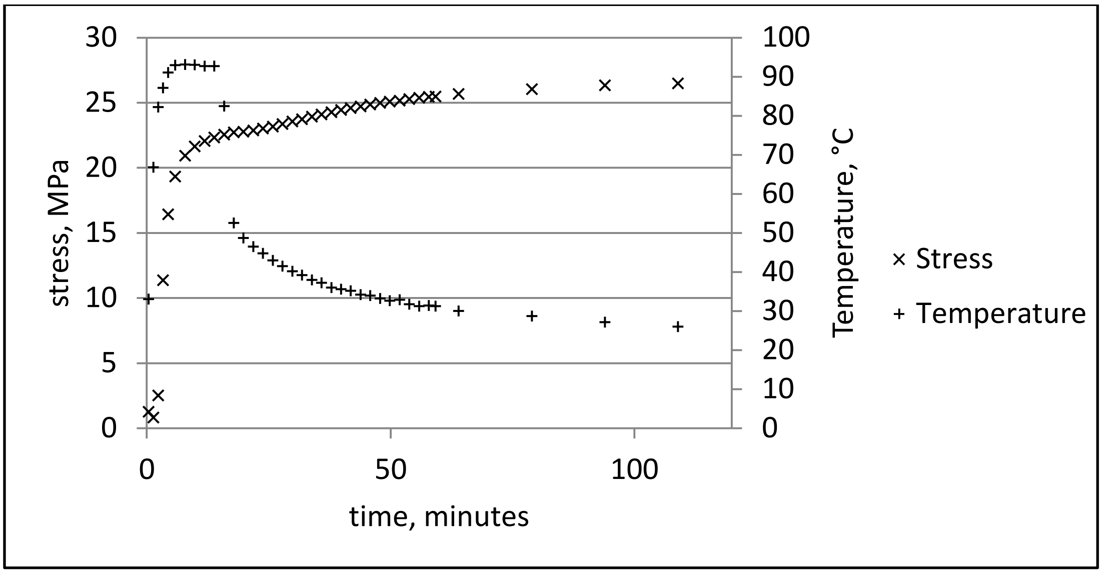

Figure 3.10 - Early stress build up in typical heat-activated stress relaxation test

Figure 3.10 shows the stress build up behaviour observed over the first 120 minutes of testing in more detail; an initial stress decrease due to thermal expansion is observed followed by a sharp stress increase as the applied temperature enters the transition zone in which the drawn shrinkage process is activated. As the locked in stress is released, the rate of stress increase decreases and the stress begins to plateau. When the applied temperature is removed the rate of stress development increases again, due to thermal contraction of the specimen. Finally, as the temperature reaches ambient, the stress increase due to thermal contraction halts, and the stress again plateaus as all available locked in stress has been released. The peak stress varied from a minimum of 26.0 MPa to a maximum of 32.8 MPa and occurred between 2.5 and 3.4 hours into each test.

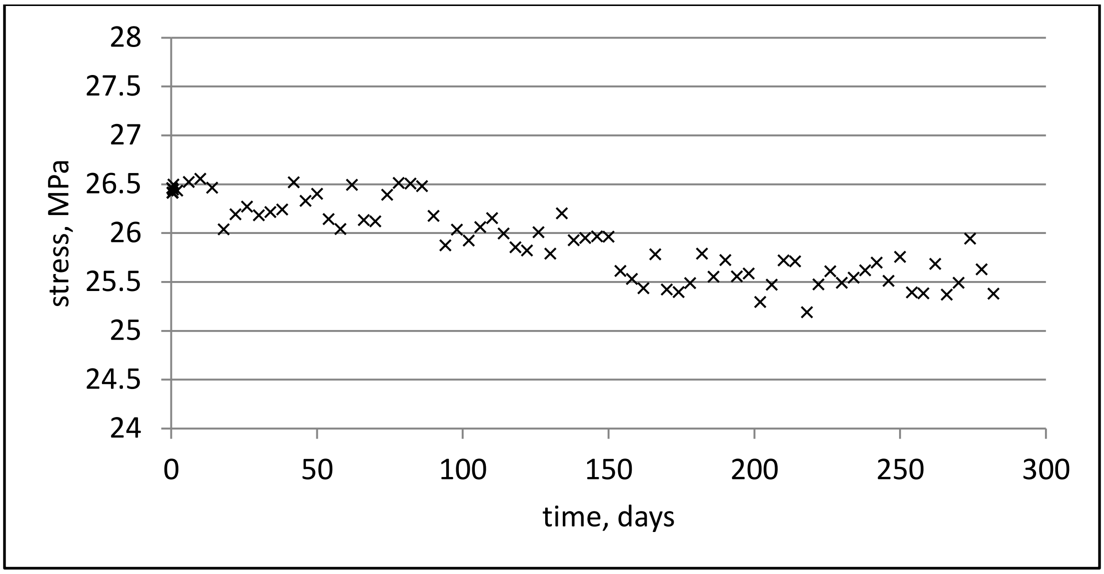

Figure 3.11 - Long-term stress relaxation in typical heat-activated stress relaxation test

The long-term stress relaxation behaviour from the peak stress can be seen in Figure 3.11. During the stress relaxation period, and subsequent plateau period, the stress displays large fluctuations that appear similar to those attributed to thermal expansion and contraction of the specimen in the manually applied stress relaxation tests. Thus based on the same assumptions and making use of Equation (3.1) the expected stress changes due to this effect were calculated and removed. These modified stresses were used to produce the post-peak stress relaxation plots displayed in Figure 3.12. In these plots the stress has also been normalised to the peak stress. Due to the long time period required to carry out a test such as the one above, it was not possible to continue every test for this period. As mentioned above, five tests were carried out, three of these were shorter-term tests, undertaken to confirm that a similar early trend was seen. The early behaviour in tests was found to show close agreement with that of the two longer-term tests.

The five modified normalised plots shown in Figure 3.12 show similar trends for the stress relaxation behaviour. The stress shows an initial rapid relaxation of between 2 and 5 % occurring in the first 2 to 5 days. The relaxation then slows or in some cases (d) appears to stop completely (however it is hard to discern slow relaxation processes in short term tests such as this one). In both long-term tests the stress continues to gradually relax until a plateau is reached after approximately 100 days, the average plateau stresses are 95 and 96 % of the peak stresses for (a) and (e) respectively. The magnitude and times of these plateaus have again been determined by considering a number of averages of large numbers of individual data points at different times throughout the tests. This approach allows the underlying trends, otherwise hidden by the stress fluctuations, to be observed.

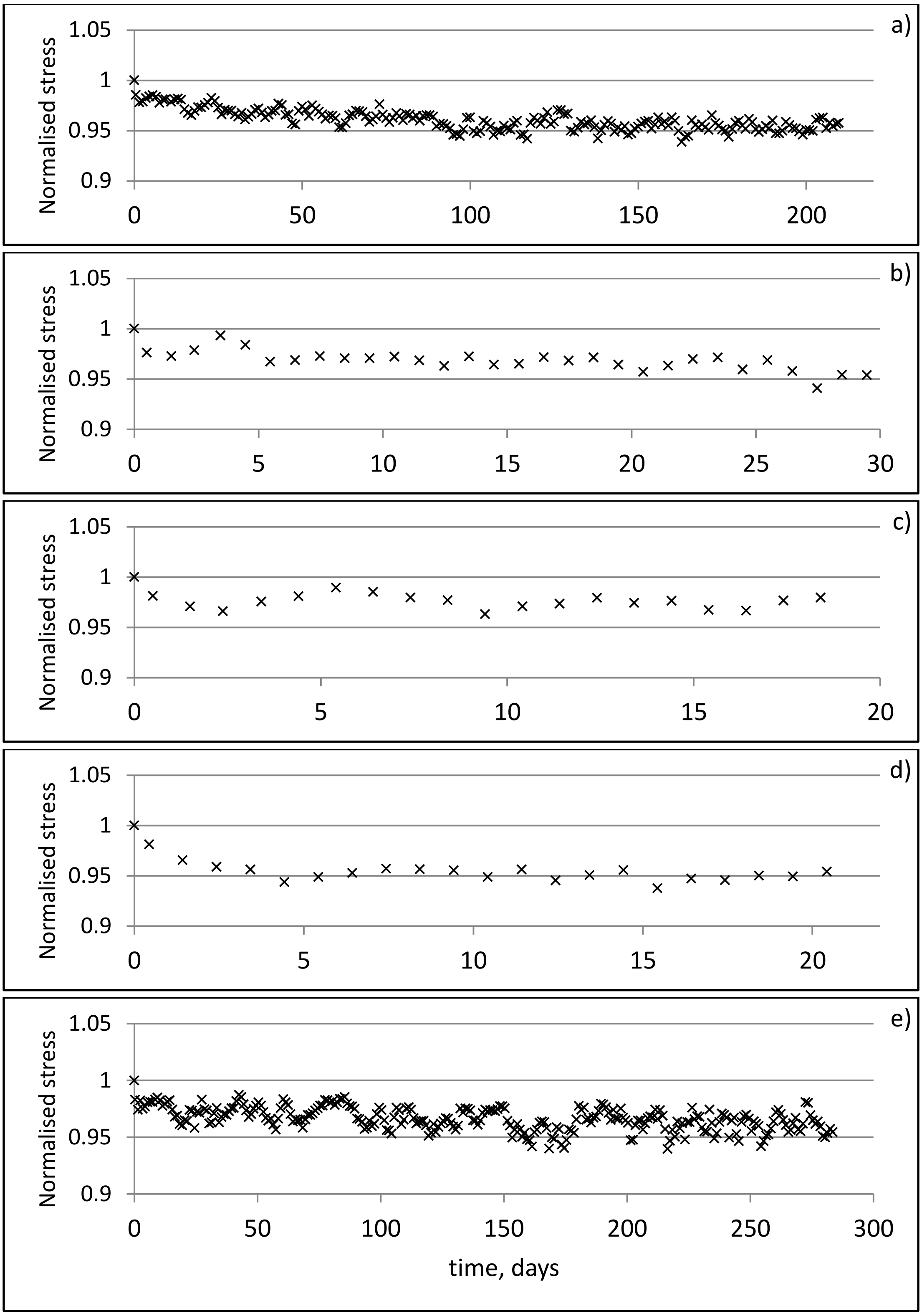

Figure 3.12 – Modified post-peak stress relaxation behaviour for five heat-activated stress relaxation tests

Finally these modified normalised stresses have been averaged across the five tests to produce a plot of the average long-term behaviour of the material. This is displayed in Figure 3.13 and Figure 3.14, and shows a smoother clearer view of the trends already described.

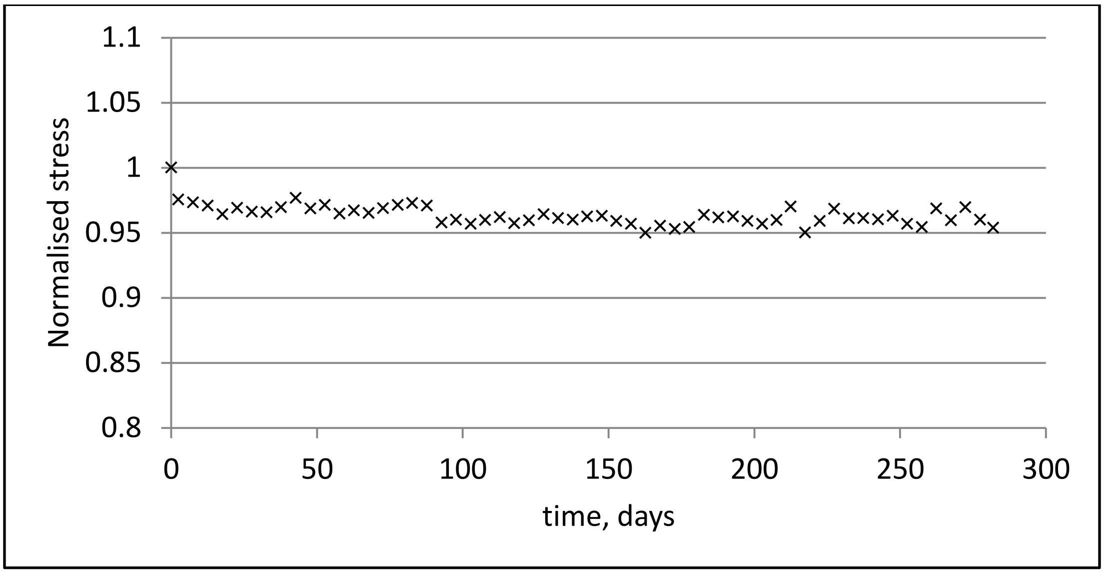

Figure 3.13 – Average long-term stress relaxation behaviour for heat-activated stress

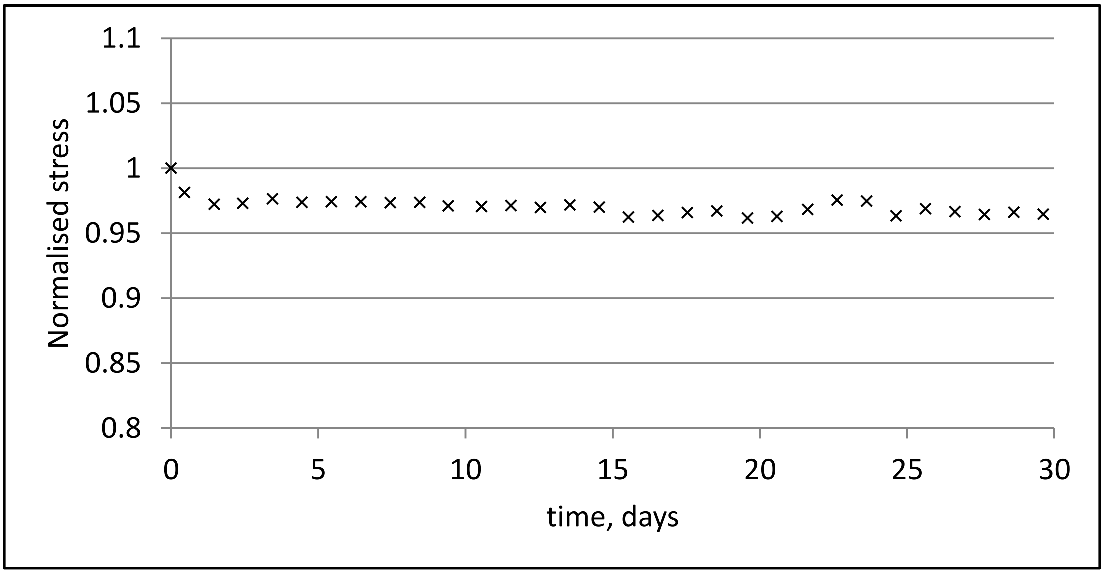

Figure 3.14 – Average short-term stress relaxation behaviour for heat-activated stress

The key values relating to the material behaviour observed in the five tests are summarised in Table 3.1.

Table 3.1 – Key values observed in heat-activated stress relaxation tests

	1	2	3	4	5	Average
Duration (days)	210	30	19	21	284	NA
Time of peak stress (hours)	3.0	2.6	2.8	3.4	2.5	2.8
Peak stress (MPa)	32.8	25.7	27.0	28.7	26.7	28.2
Relaxation time (Long-term tests only) (days)	95.0	NA	NA	NA	95.0	95.0
Plateau stress (Long-term tests only) (days)	31.2	NA	NA	NA	25.6	28.4
Unrelaxed percentage of peak stress (Long-term tests only) (%)	95.0	NA	NA	NA	96.0	95.5

Although the same specification of material was employed for all the tests, different rolls of material were used, and the slight differences in the values of Table 3.1, particularly the peak stress differences, are believed to relate to the variations in the supplied material. One theory is that the value of the peak stress is closely linked to the age of the material as the locked in stress is thought to gradually release over time. This process is similar in nature to the phenomenon of physical aging described in Section 2.5.6.2. The system is in a non-equilibrium thermodynamic state due to the long chain molecules' entropic preference to assume more coiled and random conformations (Mody et al 2001), this state combined with a small but non-zero molecular mobility causes a gradual progression towards thermodynamic equilibrium i.e. a gradual release of the locked in stress.

The limited stress relaxation, and the apparent stress plateaus in the longest term tests presented in this Chapter have good implications for the use of this material in the proposed LatConX system; these material properties are beneficial for the reasons mentioned earlier in the Chapter. However it is expected that in a longer term test (note: longer by an order of magnitude or more i.e. 10 or even 100 years) a degree of stress relaxation would continue. An understanding of this continued stress relaxation may be vital to the successful real world application of the LatConX system, however tests of this duration are impracticable and beyond the scope of this thesis. Alternatively, a method based on the principles of time-temperature superposition (Section 2.5.6.1) could be used to investigate any longer term stress relaxation behaviour. This would involve undertaking a series of tests similar to those presented above, however with the stress relaxation proceeding at a range of different, controlled temperatures. The results of these tests could then be combined to form a master curve for the material similar to that shown in Figure Figure 2.21.

3.4 Conclusions

- Two types of stress relaxation test have been presented, differentiated by the manner of stress applied to the specimen; namely manually applied stress, and heat-activated stress. The aim of these was to quantify and characterise any stress relaxation processes causing stress loss, and to inform the development of the numerical models presented in Chapter 3.
- In both test types limited stress loss to relaxation was observed.
- In the manually applied stress relaxation tests, between 1.5 and 4.3 % of the initially applied stress was lost to relatively early relaxation processes over the first 4 – 10 days. Across the five tests carried out the average early stress loss was 3.6 % over the first 9 days. Any longer term behaviour could not be quantified by observation of these tests.
- In the heat-activated stress relaxation tests, similar early stress relaxation behaviour to that described for the manually applied stress relaxation tests was observed. Further, less rapid stress relaxation continued for approximately 95 days to an average final plateau value of 95.5 % of the peak stress.
- These findings of limited loss of stress to long-term relaxation processes further confirm pre-drawn PET as a suitable material for use in the LatConX system. Particularly the observations of the longer-term heat-activated tests as these directly replicate the restrained shrinkage conditions anticipated in the LatConX system.
- An investigation of the material’s longer term behaviour (over durations of 10-100 years) should be undertaken on by utilising the principles of time-temperature superposition (see discussion above).

- Additional future work should focus on development of a pre-drawn polymer manufactured in a larger bar form making it more suitable for real-world civil engineering applications. A greater shrinkage stress would also be beneficial if possible.
- An investigation of the relationship between the material’s age since drawing and its shrinkage stress and relaxation time would aid understanding of the material’s ageing behaviour and the relaxation processes present, and be beneficial to the system’s future development. Knowledge of the initial drawing stress and age of the material from initial drawing would be required for this.

Chapter 4 – Shape Memory Polymer – Numerical Modelling

To enable accurate simulation of the long-term behaviour of the LatConX system a numerical model for the relevant behaviour of pre-drawn PET was required. Earlier work carried out by this research group had successfully developed a model capable of predicting the shrinkage behaviour of the material and thus the stress development under restrained conditions (Dunn et al. 2011). However, in order to be fully applicable to the LatConX system, a more comprehensive polymer model was required, capable of accurately simulating the long-term behaviour of the activated PET tendons subsequent to initial shrinkage. Further to this extension of the model to account for long-term behaviour of the material, a thermodynamic inconsistency with the model of Dunn et al. (2011) has also been addressed in the development of the new model. This inconsistency arises from the temperature dependence of the Young’s modulus of the polymer, which increases as the material’s temperature decreases.

In this chapter the development and calibration of two constitutive models designed with the above criteria in mind is described. The two models have been named long-term Maxwell x1 (LTMx1), and long-term Maxwell x2 (LTMx2) in reference to the number of Maxwell arms that are used to account for long-term behaviour, these abbreviations will be used for the remainder of this thesis. The capabilities of the two models are demonstrated through the accurate simulation of experimental data presented in Chapter 3. Finally due to its broader range of applicability without recalibration the LTMx2 model is deemed the more suitable model for use in the combined LatConX system model presented in Chapter 5.

The LTMx1 model described in this chapter is presented in the publication by Hazelwood et al. (2014).

4.1 Common Theory to Both LTMx1 and LTMx2

Due to the similarities between the two models much of the relevant theory will be covered here before the unique elements of the underlying theory for each model are discussed separately.

4.1.1 General Form of the Models

The models are modified versions of that originally proposed by Dunn et al. (2011). Modifications comprise the addition of either one or two Maxwell elements in parallel with the existing Hookean spring element; these new elements take account of the long-term relaxation (or creep) in the material. The thermal expansion element has also been applied to all parallel arms in the new models. Both new models are now able to predict the stress development under restrained shrinkage conditions in the same way as the model of Dunn et al. (2011), as well as predicting long-term creep or stress relaxation behaviour induced by an applied stress or strain path respectively, including stress relaxation occurring subsequent to restrained shrinkage. This key development of predicting long-term creep or stress relaxation is achieved by the additional Maxwell arms in series with the thermal expansion element.

4.1.2 Time Dependency

Any time dependency of the models developed in this Chapter arises from the behaviour of the Maxwell elements present. The generalised standard solution for the behaviour of a Maxwell element will now be derived.

From equilibrium the stress (σ_M) on a Maxwell arm is:

$$\sigma_M = E\varepsilon_E = \eta\dot{\varepsilon}_{ve} \tag{4.1}$$

where E is the Young's modulus of the elastic spring, ε_E is the elastic strain on the spring, η is the viscosity of the dashpot, and ε_{ve} is the viscous strain of the dashpot.

Given that $\varepsilon_E = \varepsilon - \varepsilon_{ve}$ and introducing a relaxation time parameter ($\tau = \eta/E$), Equation (4.1) can be rearranged to give the following differential equation:

$$\dot{\varepsilon}_{ve} + \frac{1}{\tau}\varepsilon_{ve} = \frac{1}{\tau}\varepsilon \tag{4.2}$$

Using the factor of integration $exp\ (t/\tau)$ as per the standard solution of (Simo and Hughes 1998), and differentiating by parts yields:

$$\frac{d}{dt}\left(e^{t/\tau} \cdot \varepsilon_{ve}\right) = \frac{1}{\tau} e^{t/\tau} \cdot \varepsilon \tag{4.3}$$

Integrating by parts and rearranging gives a convolution integral in the form of Equation (4.4), in which s is the free variable.

$$\varepsilon_{ve}(t) = \frac{1}{\tau}\int_{t_0}^{t} e^{-(t-s)/\tau} \cdot \varepsilon(s) \tag{4.4}$$

The solution to this integral is found by considering the interval $t \to t + \Delta t$, and assuming a value for the strain (ε_θ) that is constant and equal to the strain at $t + \theta\Delta t$, where $0 \leq \theta \leq 1$:

$$\varepsilon_{ve}(t + \Delta t) = \frac{1}{\tau}\int_{t}^{t+\Delta t} e^{-(t+\Delta t-s)/\tau} \cdot \varepsilon_\theta ds + \frac{1}{\tau}\int_{t_0}^{t} e^{-(t+\Delta t-s)/\tau} \cdot \varepsilon(s) ds \tag{4.5}$$

The solution to Equation (4.5) is attained by considering each of the two right hand side integrals in turn. The solution to the first integral is:

$$\varepsilon_\theta\left(1 - e^{-\Delta t/\tau}\right)$$

And the second is:

$$\varepsilon_{ve}(t)e^{-\Delta t/\tau}$$

From these two solutions, the updated visco-elastic strain (time t_j) for a time step (Δt), in terms of values at time t_{j-1} is found from:

$$\varepsilon_{ve_j} = \varepsilon_{\theta_j}\left(1 - e^{-\Delta t/\tau}\right) + \varepsilon_{ve_{j-1}}.e^{-\Delta t/\tau} \tag{4.6}$$

where Δt is equal to t_j-t_{j-1}, and θ is 0.5.

4.1.3 Temperature Dependency

In the temperature dependent Maxwell element, both the Young's modulus of the spring and the viscosity of the dashpot are functions of temperature. This temperature dependent arm acts identically to the temperature dependent arm in the model of Dunn et al. (2011) with the same temperature dependent functions for the material properties.

The 'low' and 'high' temperature Young's moduli and viscosities have been established following the basic approach described by Dunn et al. (2011) The Young's moduli are the values consistent with short term stress excursion tests in which the loading rate is rapid enough for viscous effects to be minimal. The idealised variation of each of these properties with temperature is illustrated in Figure 4.1. Although the material used for the current tests was nominally the same as that used by Dunn et al. (2011), the properties of this batch of material, given in Table 4.2, Table 4.3, and Table 4.4, were found to be slightly different from those quoted by Dunn et al. (2011).

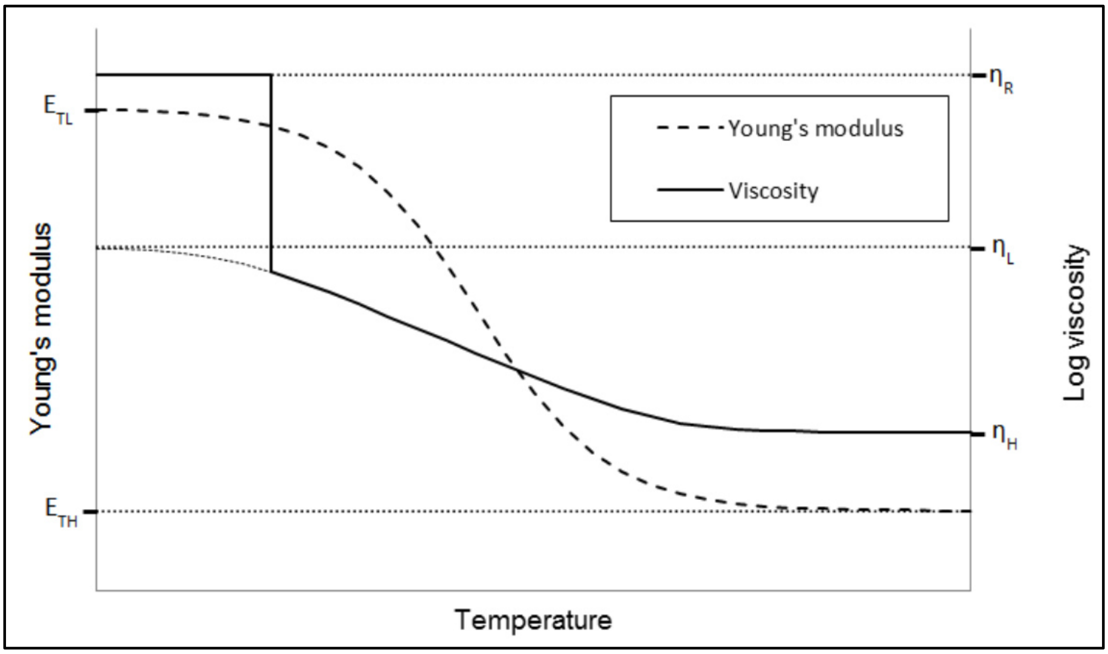

Figure 4.1 – Idealised Representation of Young's Modulus and Viscosity Versus the Temperature (Dunn et al. 2011)

4.1.4 Solution to Thermodynamic Issue

As mentioned in the introduction to this chapter, an issue with the thermodynamic validity of the model of Dunn et al. (2011) has been addressed in the two models presented here. The issue occurs when a decrease in the temperature applied causes an increase in the stress in the temperature dependent arm with no increase in the strain and no other energy source. This is due to the inversely proportional relationship between temperature and Young's modulus. The solution to this problem is outlined below.

The stress in the temperature dependent arm is that shown in Equation (4.7) (in which the contribution of thermal expansion has been removed for clarity):

$$\sigma_2 = E_2(T)(\varepsilon - \varepsilon_{ve2}) \tag{4.7}$$

In the absence of an associated thermodynamic source of energy, there should be no increase in stress due to the increase in stiffness alone i.e.:

$$\Delta\sigma_{\Delta E} = 0 \tag{4.8}$$

This is satisfied by the use of a small change in viscoelastic strain as follows:

$$\Delta\sigma_{\Delta T} = \Delta E_2(\varepsilon - \varepsilon_{ve2} - \Delta\varepsilon_{ve2}) + E_2(-\Delta\varepsilon_{ve2}) = 0 \tag{4.9}$$

where:

$$\Delta E_2 = E_2(T_j) - E_2(T_{j-1})\ but\ \Delta E_2 > 0 \tag{4.10}$$

Rearranging gives:

$$\Delta\varepsilon_{ve2} = \frac{\Delta E_2(\varepsilon - \varepsilon_{ve2})}{E_2 + \Delta E_2} \tag{4.11}$$

This value of $\Delta\varepsilon_{ve2}$ is then added to the current viscoelastic strain.

4.1.5 Summary of Model Parameters

A number of material parameters are used to produce the model predictions that follow (see Table 4.2, Table 4.3, and Table 4.4), Table 4.1 below provides a summary of these parameters including how they have been determined.

Table 4.1 – Summary of material parameters

Symbol	Description	Comments
T_0	Ambient temperature	Set as 20°C in all model simulations, this is used as a thermal datum thus its value is arbitrary.
α_p	Coefficient of thermal expansion	Measured in laboratory
E_{TH}	High temperature Young's modulus plateau value	Taken as the value measured by Dunn et al (2011)
E_{TOT}	Low temperature Young's modulus plateau value	Taken as the value measured by Dunn et al (2011)
T_{LE}	Transition start temperature (Young's modulus)	Taken as the value measured by Dunn et al (2011)
T_{HE}	Transition end temperature (Young's modulus)	Taken as the value measured by Dunn et al (2011)
T_{gE}	Temperature at the centre of the transition (Young's modulus)	Taken as the value measured by Dunn et al (2011)
b	Elastic modulus material parameter	Taken as the value measured by Dunn et al (2011)
d	Elastic modulus material parameter	Taken as the value measured by Dunn et al (2011)
σ_{res}	Stress at drawing	Peak stress reached in hot stress relaxation test
η_{2L}	High temperature viscosity	Taken as the value measured by Dunn et al (2011)
η_{2H}	Low temperature viscosity	Initially set to the value measured by Dunn et al (2011) however it was found that a small change was required to achieve good agreement with the data – this is considered acceptable due to the variability of predrawn PET behaviour
$T_{L\eta}$	Transition start temperature (viscosity)	Taken as the value measured by Dunn et al (2011)
$T_{H\eta}$	Transition end temperature (viscosity)	Initially set to the value measured by Dunn et al (2011) however it was found that a small change was required to achieve good agreement with the data – this is considered acceptable due to the variability of predrawn PET behaviour
$T_{g\eta}$	Temperature at the centre of the transition (Viscosity)	Initially set to the value measured by Dunn et al (2011) however it was found that a small change was required to achieve good agreement with the data – this is considered acceptable due to the variability of predrawn PET behaviour
c	Viscous material parameter	Taken as the value measured by Dunn et al (2011)
f	Viscous material parameter	Taken as the value measured by Dunn et al (2011)
β, β_{1a}, β_{1a}	Long-term Maxwell arm weighting factors	Calibrated by observation of experimental data presented in Chapter 3 – calibration methods are described in Section 4.2.2 and Section 4.3.2
τ_1, τ_{1a}, τ_{1b}	Relaxation time parameters for long-term Maxwell arms	Calibrated by observation of experimental data presented in Chapter 3 – calibration methods are described in Section 4.2.2 and Section 4.3.2

4.2 LTMx1

There are two key developments for the LTMx1 model, from the model of Dunn et al (2011). Firstly, a temperature independent Maxwell arm has been added in parallel with the previous two arms; secondly, the thermal expansion element has been extended to include all model arms.

Any stress on the temperature independent Maxwell arm will tend to zero over a period of time related to the relaxation time parameter. This means that its addition allows the model to recreate temperature independent stress relaxation processes such as both types of applied stress investigated in the experiments presented in Chapter 3. The proportion of the applied stress that will be able to relax is governed by the relative Young's moduli of the springs in arm 1a and 1b (see Figure 4.2).

No explanation is provided in the work of Dunn et al (2011) as to why the thermal expansion element is only applied to the permanent elastic spring. The implication of only considering thermal expansion and contraction on the permanent elastic spring is that only the permanent component of the polymer network is subject to this behaviour, this seemed hard to justify for such an elementary material behaviour. A brief study was undertaken comparing model behaviour with the thermal expansion element applied to just the permanent elastic spring, and to all arms of the model; simulations with this element applied to all arms were found to more closely represent the expansive behaviour, particularly in the regions of largest temperature change. As a result of this superior performance the model with the thermal expansion element applied to all arms in the model was used for all of the work presented in this chapter.

A representation of the first proposed rheological model, with a single Maxwell element for the simulation of long-term behaviour, is shown in Figure 4.2.

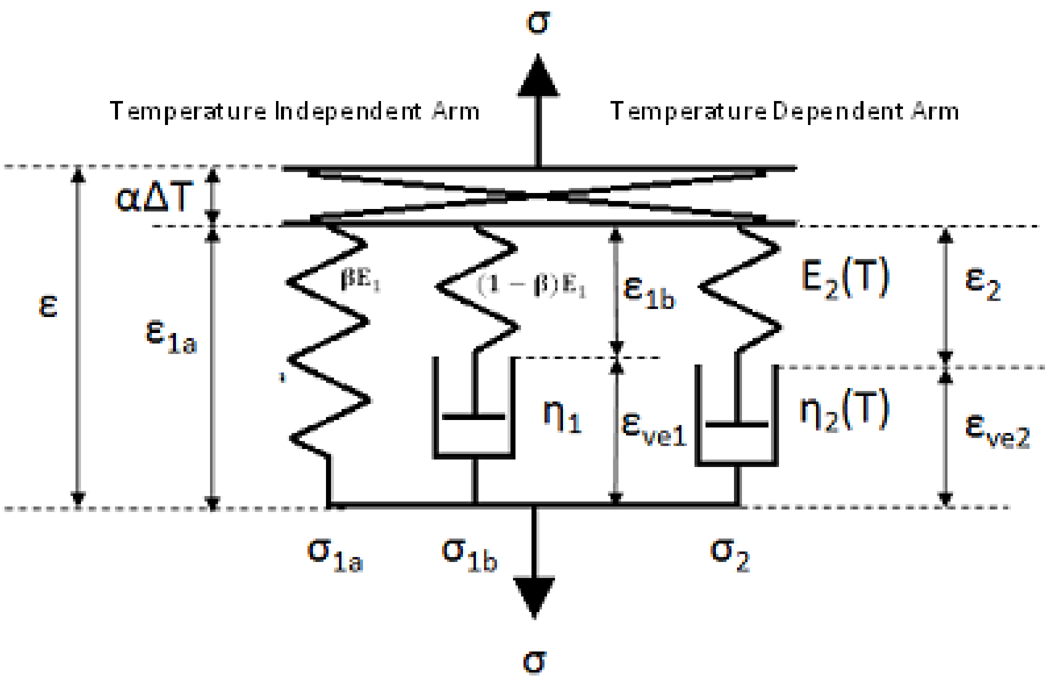

Figure 4.2 – Rheological Representation of Proposed LTMx1 Constitutive Model

4.2.1 Development of Governing Equations

The total Young's modulus of the temperature independent arm (E_1) is subdivided across the two elements that form it by using a weighting factor, β ($0 \leq \beta \leq 1$). The total stress is the sum of those in the arms:

$$\sigma_T = \sigma_{1a} + \sigma_{1b} + \sigma_2 \tag{4.12}$$

These stresses are given in the following equations:

$$\sigma_{1a} = \beta E_1 . \varepsilon_{1a} \tag{4.13}$$

$$\sigma_{1b} = (1 - \beta) E_1 . \varepsilon_{1b} = \eta_1 . \dot{\varepsilon}_{ve1} \tag{4.14}$$

$$\sigma_2 = E_2(T) . \varepsilon_2 = \eta_2 . \dot{\varepsilon}_{ve2} \tag{4.15}$$

where E is the Young's modulus of each spring, η is the viscosity of each dashpot, and each ε is the strain for the relevant element as displayed in Figure 4.2.

Making use of the Maxwell element solution derived in the Common Theory section of this Chapter (see Equations (4.1) - (4.8)), the stresses at any time increment (j) may be written in terms of the total and viscous strains as follows:

$$\sigma_{1a_j} = \beta E_1 . [\varepsilon_j - \alpha_p . (T_j - T_0)] \tag{4.16}$$

$$\sigma_{1b_j} = (1 - \beta) E_1 . \left[\varepsilon_j - \varepsilon_{ve1_j} - \alpha_p . (T_j - T_0)\right] \tag{4.17}$$

$$\sigma_{2_j} = E_2(T) . \left[\varepsilon_j - \varepsilon_{ve2_j} - \alpha_p . (T_j - T_0)\right] \tag{4.18}$$

where T_0 is the ambient temperature, α_p is the coefficient of thermal expansion, and T_j is the temperature at time increment j.

4.2.2 Calibration of Material Parameters

There are two new model parameters relating to the long-term Maxwell arm that need to be calibrated; the weighting factor β, and the relaxation time parameter τ_1 – from which the viscosity is calculated.

The permanent proportion of the locked in stress is controlled by β. The value of β can therefore be calculated from the relationship below:

$$\beta = \frac{\sigma_{plat\ exp}}{\sigma_{peak\ exp}} \tag{4.19}$$

where $\sigma_{plat\ exp}$ is the average plateau stress, and $\sigma_{peak\ exp}$ is the peak experimental stress, both modified to take account of temperature fluctuations as described in Chapter 3, using Equation (3.1). τ_1 is then found by calibration. This involves identifying the time at which the plateau stress is effectively first reached and then converting to a representative value for τ_1 using Equation (4.20).

$$\tau_1 = \frac{-t_{plat}}{ln\,0.01} \tag{4.20}$$

Equation (4.20) is derived on the basis that 99 % of the stress has relaxed at the observed plateau time.

Finally the viscosity of the long-term arm is given by:

$$\eta_1 = \tau_1(1-\beta)E_1 \tag{4.21}$$

4.2.3 Model Evaluation

The suitability of this model for recreating the relevant material was evaluated using two examples, both taken from the results presented in Chapter 3.

4.2.3.1 Heat-activated Restrained Stress

The results of data set 5 of the heat-activated stress relaxation test series are considered in the first example. As previously described, a specimen measuring 400 x 32 x 1.15 mm^3 was heated to 90°C, held at that temperature for a period of 10 minutes at which point the oven was turned off and the specimen's behaviour at ambient temperature monitored for a period of 284 days.

The above described temperature path was applied to the newly developed model, using the material parameters from Table 4.2, to simulate the experimental behaviour. A comparison of the resulting numerical prediction and the experimental data is shown in Figure 4.3, Figure 4.4, and Figure 4.5.

Table 4.2 – Numerical input values for simulation of heat-activated stress relaxation test 5

Model parameter	Value
T_0	20°C
α_p	$10^{-4.8}$
E_{TH}	845 MPa
E_{TOT}	6000 MPa
T_{LE}	70°C
T_{HE}	120°C
T_{gE}	95°C
b	3.3
d	1.2
σ_{res}	26.57 MPa
η_{2L}	1.575 x 10^4 P
η_{2H}	5.122 x 10^7 P
$T_{L\eta}$	30°C
$T_{H\eta}$	90°C
$T_{g\eta}$	60°C
c	5
f	0.1
τ_1	2.8 x 10^6 s
β	0.963

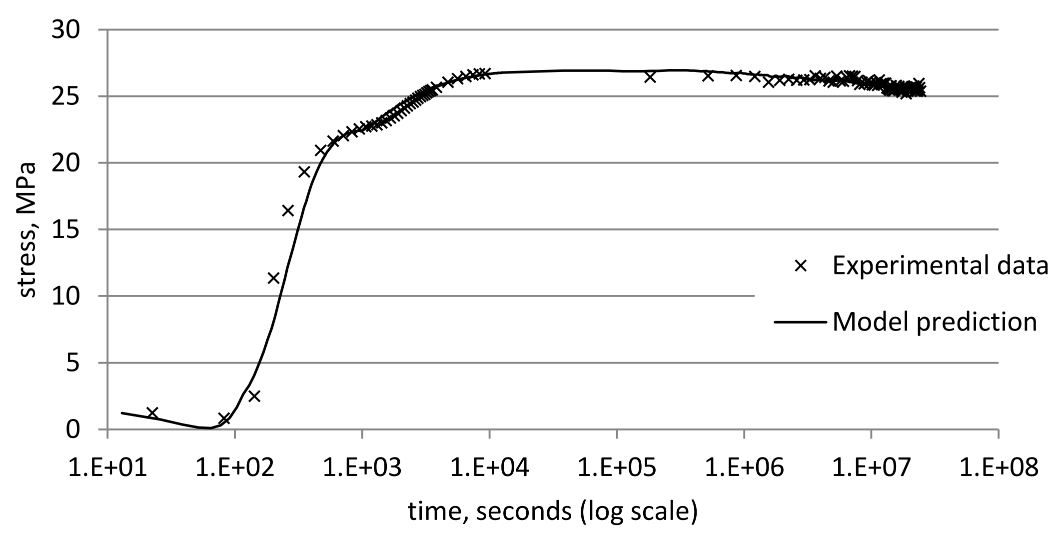

Figure 4.3 – Full model simulation compared to experimental data – Heat-activated stress relaxation test 5

From Figure 4.3 and Figure 4.4 it is clear that this numerical model is capable of reproducing the stress build up behaviour of this type with good accuracy in the same way as that of the original model of Dunn et al. (2011).

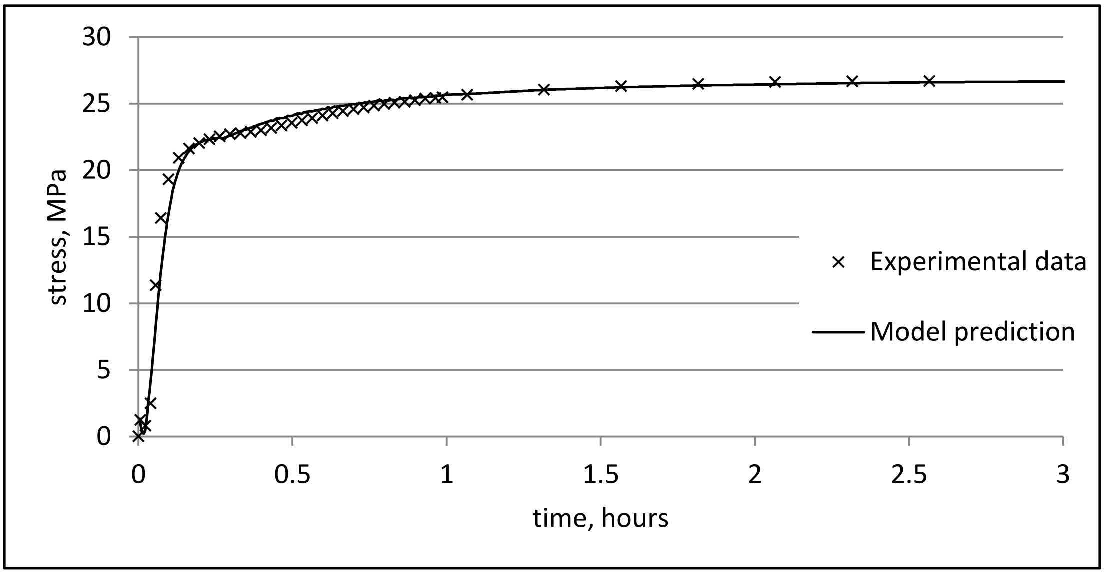

Figure 4.4 – Early stage model simulation compared to experimental data – Heat-activated stress relaxation test 5

The behaviour of the newly developed aspect of the model can be observed on both Figure 4.3 and Figure 4.5. There is good agreement between the model prediction and the experimental data, however the peak stress is maintained for too long as the initially rapid component of the relaxation behaviour cannot be captured entirely satisfactorily by the single Maxwell element.

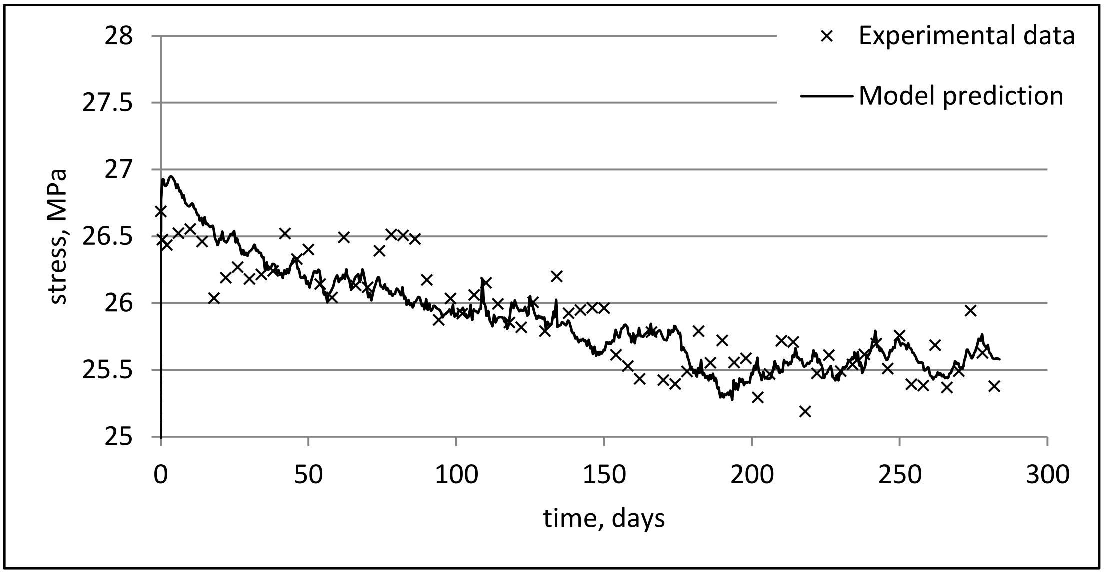

Figure 4.5 – Long-term relaxation model simulation compared to experimental data – Heat-activated stress relaxation test 5

4.2.3.2 Manually Applied Stress

The results of the manually applied 8 MPa stress relaxation test have also been simulated using this model. As described in Chapter 3, a specimen measuring 400 x 32 x 0.92 mm^3 was loaded until an initial stress of 8 MPa was reached. The specimen was then held under constant displacement (and strain) and the stress monitored at 10 minute intervals for a period of 14 days. The material parameters displayed in Table 4.3 were used for the numerical simulation of this test.

The values of the weighting factor (β), and the relaxation time of the long-term arm (τ_1) are different from those used to model the hot relaxation experiment, this was necessary to obtain a good fit to the experimental data. This apparent discrepancy will be discussed in more detail shortly.

Table 4.3 - Numerical input values for simulation of manually applied 8 MPa stress relaxation test

Model parameter	Value
T_0	20°C
α_p	$10^{-4.8}$
E_{TH}	845 MPa
E_{TOT}	6000 MPa
T_{LE}	70°C
T_{HE}	120°C
T_{gE}	95°C
b	3.3
d	1.2
σ_{res}	26.57 MPa
η_{2L}	1.575×10^4 P
η_{2H}	5.122×10^7 P
$T_{L\eta}$	30°C
$T_{H\eta}$	90°C
$T_{g\eta}$	60°C
c	5
f	0.1
τ_1	7.5×10^4 s
β	0.982

Figure 4.6 shows the comparison between the experimental data and model prediction for the case described above. Good agreement is observed between the experimental data and the model simulation. The model is capable of simulating both the stress decrease due to long-term relaxation of induced stress, and the pattern of stress fluctuations due to variation of the ambient temperature. There is some discrepancy between the magnitudes of the predicted and experimental stress fluctuations due to temperature changes but these are considered acceptable given the general level of variability of PET material behaviour.

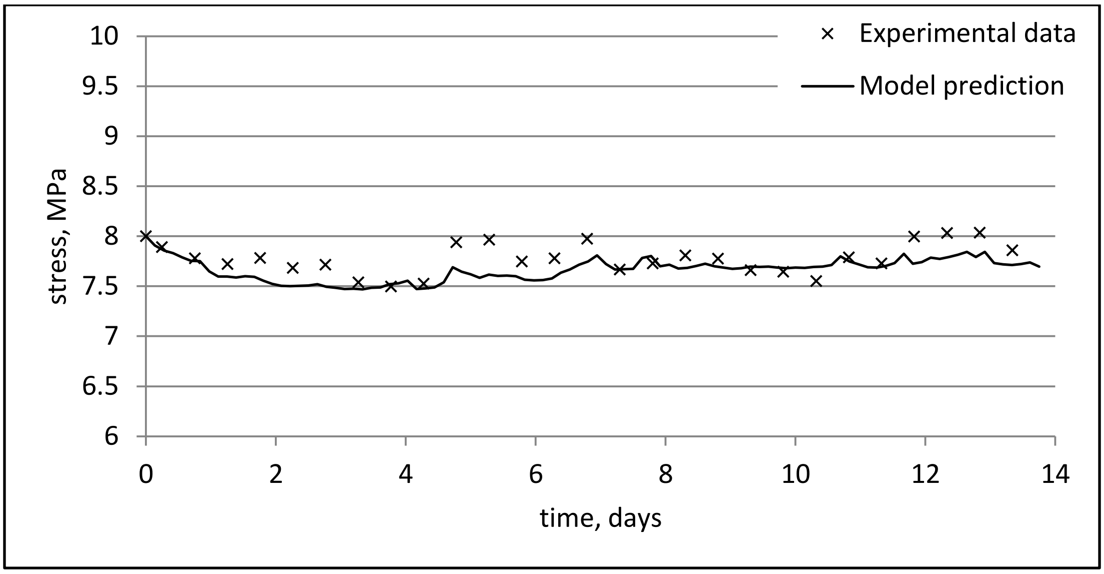

Figure 4.6 – Model simulation compared to experimental data for manually applied 8MPa stress relaxation test

4.3 LTMx2

In the previous section it was found that the LTMx1 model was only able to produce accurate simulations of both types of relaxation behaviour if significantly different values for the weighting factor (β), and the relaxation time (τ_1), of the long-term arm were used in each simulation. Another key observation relating to the predictions of the LTMx1 model was that in simulating the heat activated stress relaxation behaviour the peak stress was maintained for too long due to the single dashpot's inability to successfully capture both this initially rapid component of the relaxation behaviour (dominant in the manually applied stress tests) and the longer term relaxation behaviour (dominant in the heat-activated stress tests).

Representing a real material's stress relaxation behaviour with a single linear viscoelastic process, as the LTMx1 model attempts to do, results in a highly simplified solution. The predictions of the LTMx1 model presented in Section 4.2.3 and the fact that it requires recalibration for each specific dataset shows that it is insufficiently general for its intended purpose. The relaxation behaviour of a real material is more closely resembled by a spectrum of relaxation processes occurring simultaneously. This can be conveniently represented by a number of Maxwell elements arranged in parallel (Ward and Sweeney 2004); thus it seemed appropriate to investigate the behaviour of a model similar to the LTMx1 however with two temperature independent Maxwell arms. It was anticipated that with correct calibration this model would be able to accurately simulate both the initial rapid relaxation and the slower secondary relaxation, thus allowing both the manually applied stress tests and the heat activated stress tests to be recreated with a single set of material parameters.

A representation of the second proposed rheological model, with two Maxwell elements for the simulation of long-term behaviour, is shown in Figure 4.7.

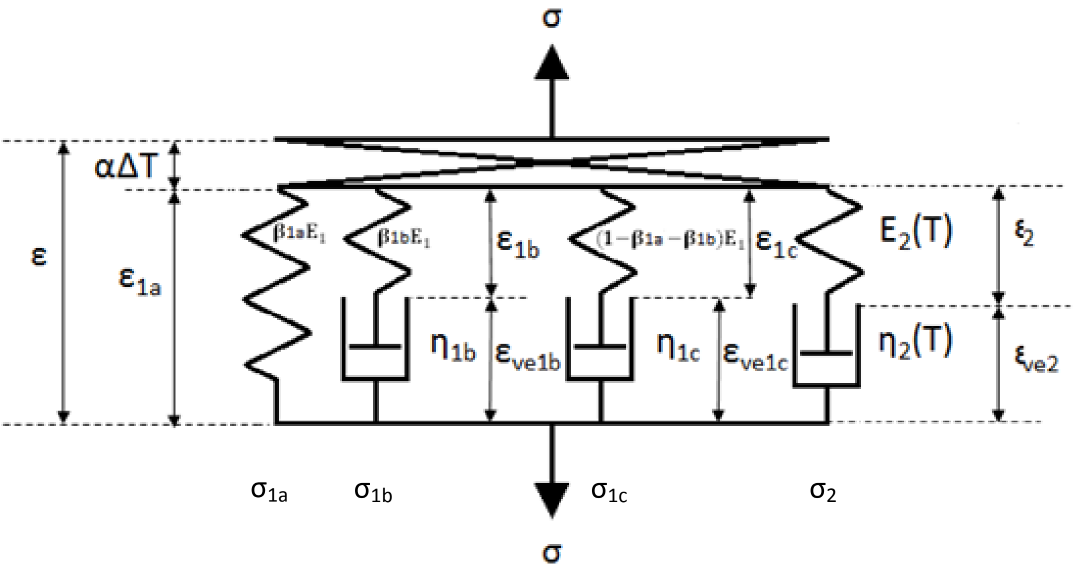

Figure 4.7 - Rheological representation of proposed LTMx2 constitutive model

4.3.1 Development of Governing Equations

As shown in Figure 4.7 the LTMx2 model is identical to the LTMx1 model except the rate and quantity of stress lost to relaxation is governed by two Maxwell elements instead of the single Maxwell element used in the LTMx1 model. Thus, the total Young's modulus of the temperature independent arm (E_1) is subdivided across three elements by using two weighting factors, β_{1a} ($0 \leq \beta_{1a} \leq 1$), and β_{1b} ($0 \leq \beta_{1b} \leq 1$). The total stress is the sum of those in the arms:

$$\sigma_T = \sigma_{1a} + \sigma_{1b} + \sigma_{1c} + \sigma_2 \tag{4.22}$$

These stresses are given in the following equations:

$$\sigma_{1a} = \beta_{1a} E_1 . \varepsilon_{1a} \tag{4.23}$$

$$\sigma_{1b} = \beta_{1b} E_1 . \varepsilon_{1b} = \eta_{1b} . \dot{\varepsilon}_{ve1b} \tag{4.24}$$

$$\sigma_{1c} = (1 - \beta_{1a} - \beta_{1b}) E_1 . \varepsilon_{1c} = \eta_{1c} . \dot{\varepsilon}_{ve1c} \tag{4.25}$$

$$\sigma_2 = E_2(T) . \varepsilon_2 = \eta_2 . \dot{\varepsilon}_{ve2} \tag{4.26}$$

where E is Young's modulus of each spring, η is the viscosity of each dashpot, and each ε is the strain for the relevant element as displayed in Figure 4.7.

Once again making use of the Maxwell element solution derived in the Common Theory section of this Chapter (see Equations (4.1) - (4.8)), the stresses at any time increment (j) may be written in terms of the total and viscous strains as follows:

$$\sigma_{1a_j} = \beta_{1a} E_1 . [\varepsilon_j - \alpha_p . (T_j - T_0)] \tag{4.27}$$

$$\sigma_{1b_j} = \beta_{1b} E_1 . \left[\varepsilon_j - \varepsilon_{ve1b_j} - \alpha_p . (T_j - T_0)\right] \tag{4.28}$$

$$\sigma_{1c_j} = (1 - \beta_{1a} - \beta_{1b}) E_1 . \left[\varepsilon_j - \varepsilon_{ve1c_j} - \alpha_p . (T_j - T_0)\right] \tag{4.29}$$

$$\sigma_{2_j} = E_2(T) . \left[\varepsilon_j - \varepsilon_{ve2_j} - \alpha_p . (T_j - T_0)\right] \tag{4.30}$$

4.3.2 Calibration of Material Parameters

There are now four model parameters to be calibrated; the two weighting factors, β_{1a} and β_{1b}, and the viscosities of the two long-term arms, τ_{1b} and τ_{1c}.

One Maxwell element now represents the faster early stress relaxation process observed in the manually applied stress relaxation, while the other represents the slower stress relaxation process observed in the heat activated stress relaxation test. This allows the four parameters for the LTMx2 model to be set using the four parameters calibrated above for the LTMx1 model (one β value and one τ value for each of the two simulations presented above):

β_{1a} represents the proportion of any stress applied to the temperature independent arm that is permanent, i.e. the final normalised average plateau value observed in the heat-activated stress relaxation test from approximately 150 days onwards. This parameter therefore takes the value of β from Table 4.2 (β_{1a} = 0.963).

β_{1b} represents the proportion of any of the non-permanent stress that is subject to the more rapid initial relaxation. This is the behaviour observed during the shorter term manually applied stress relaxation tests, and which was not adequately simulated at the early stages of the longer term heat-activated stress relaxation tests. This leads to a value of $\beta_{1b} = (1-\beta)$ where β is the weighting factor used in the manually applied stress relaxation simulation shown in Table 4.3 (β_{1b} = 1 - 0.982 = 0.018).

τ_{1b} and τ_{1c} are again found by identifying the time at which the plateau stress is effectively first reached, and using Equation (4.20). Finally the viscosity of the long-term arms is given by Equation (4.21).

4.3.3 Model Evaluation

This model's capability for simulating the long-term stress relaxation behaviour is now evaluated by recreating the same two examples considered in the previous evaluation section, however this time the simulations are carried out using the same single set of parameters for both examples. The model parameters are displayed in Table 4.4; the values of the four new parameters can be seen to correspond, as described in Section 4.3.2, with those calibrated for the two examples of the LTMx1 model presented in Sections 4.2.3.1 and 4.2.3.2.

Table 4.4 – Numerical input values for the LTMx2 model for simulation of both stress relaxation examples

Model parameter	Value
T_0	20°C
α_p	$10^{-4.8}$
E_{TH}	845 MPa
E_{TOT}	6000 MPa
T_{LE}	70°C
T_{HE}	120°C
T_{gE}	95°C
b	3.3
d	1.2
σ_{res}	26.57 MPa
η_{2L}	1.575 x 10^4 P
η_{2H}	5.122 x 10^7 P
$T_{L\eta}$	30°C
$T_{H\eta}$	90°C
$T_{g\eta}$	60°C
c	5
f	0.1
β_{1a}	0.963
τ_{1b}	7.5 x 10^4 s
β_{1b}	0.018
τ_{1c}	2.8 x 10^6 s

4.3.3.1 Heat-activated Restrained Stress

The accuracy of the simulations displayed in Figure 4.8 and Figure 4.9 appears almost identical to that of the LTMx1 model; however observation of Figure 4.10 shows an improved simulation, particularly in the early period from 0 to 40 days (3.5 x 10^6 seconds). The peak stress is now not maintained for an extended period of time, and the rapid early relaxation is accurately recreated.

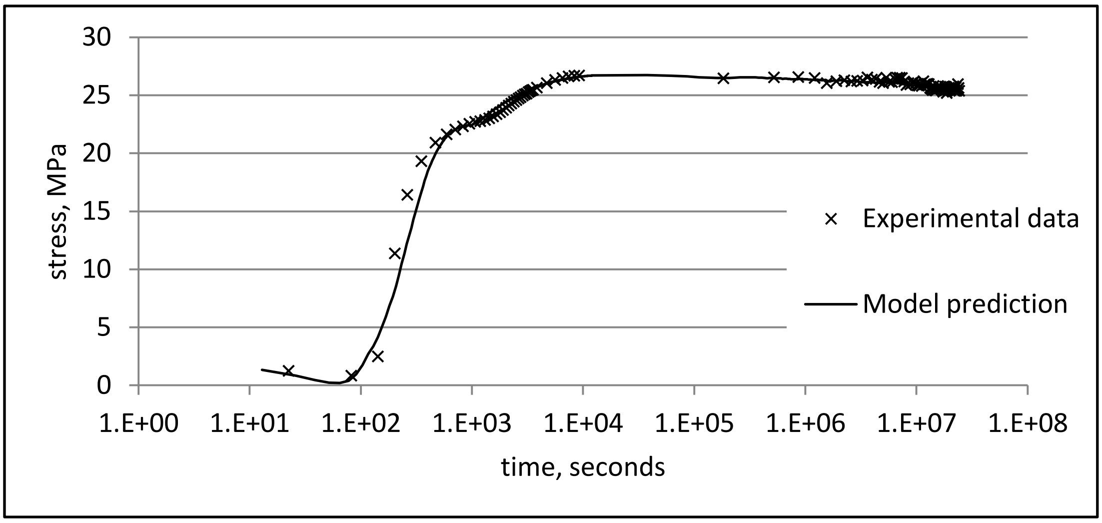

Figure 4.8 – Full model simulation compared to experimental data – Heat-activated stress relaxation test 5

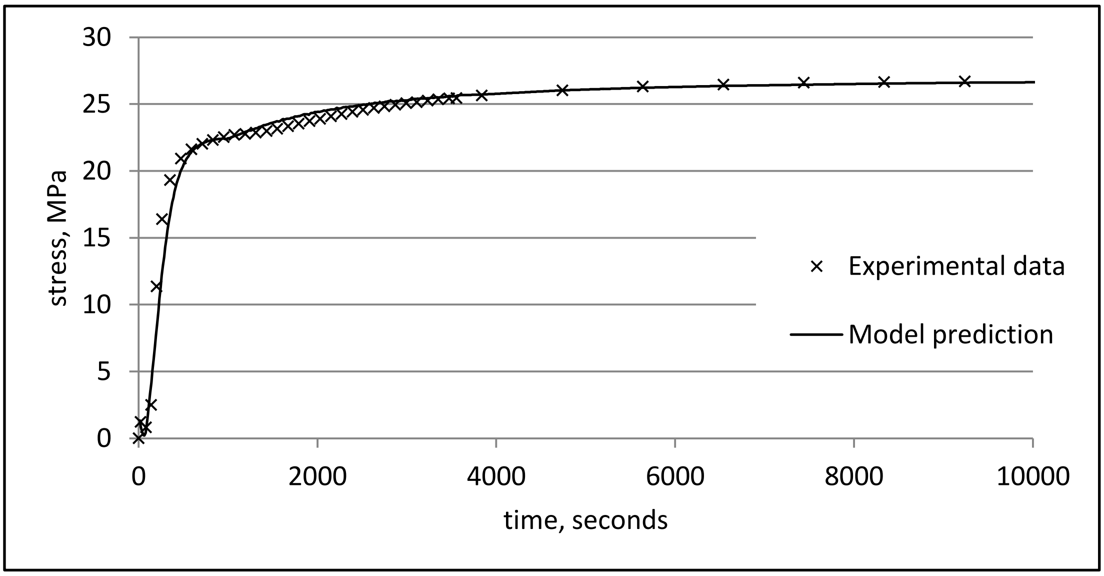

Figure 4.9 - Early stage model simulation compared to experimental data – Heat-activated stress relaxation test 5

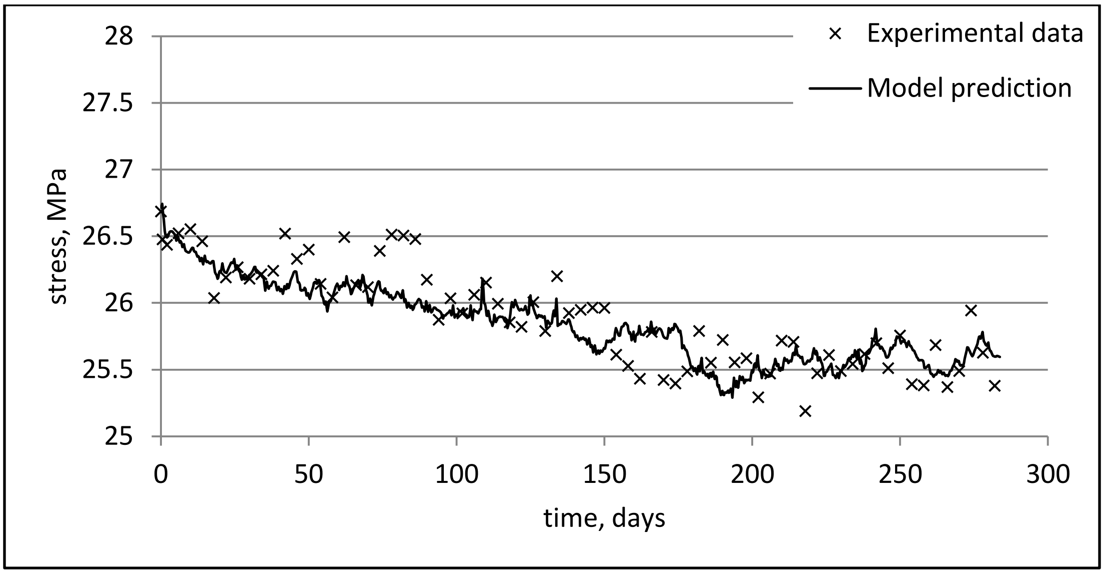

Figure 4.10 – Long-term model simulation compared to experimental data – Heat-activated stress relaxation test 5

4.3.3.2 Manually Applied Stress

The LTMx2 model results compared to experimental data for this example are displayed in Figure 4.11. The accuracy of the LTMx2 model in predicting this behaviour type is equal to that displayed by the LTMx1 model however it has now been achieved using the same set of material parameters as in the heat-activated model example.

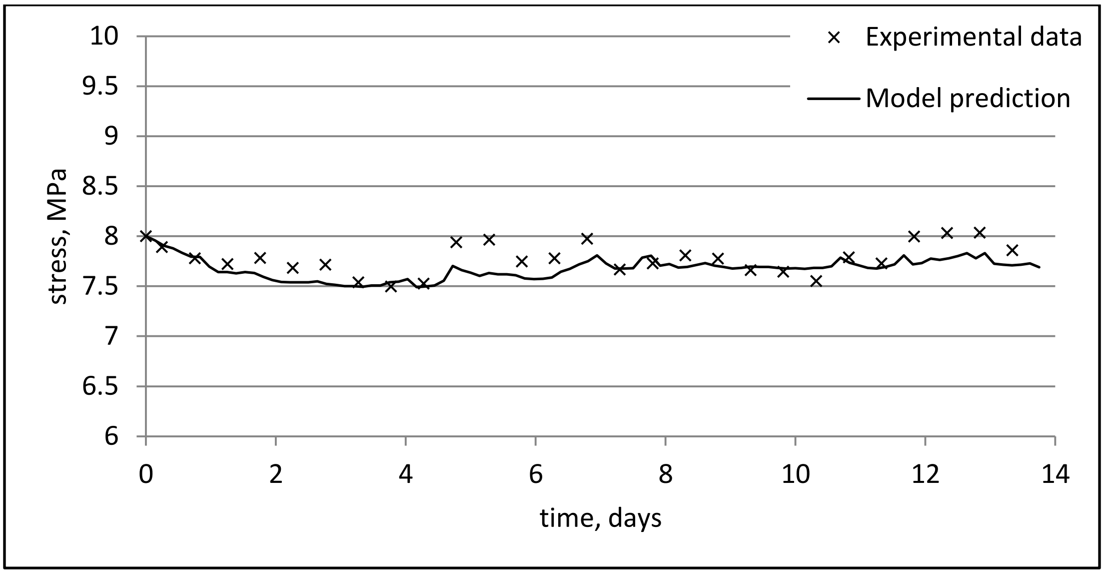

Figure 4.11 - Model simulation compared to experimental data for manually applied 8MPa stress relaxation test

4.4 Conclusions

- Two numerical models for the constitutive behaviour of pre-drawn PET have been presented; both are able to simulate the short- and long-term thermomechanical behaviour of the material.
- The new models have been shown to be able to accurately predict the stress relaxation behaviour of restrained PET specimens following heat-activation, as well as the stress variation in specimens loaded in the pre activated state.
- The LTMx1 model was able to accurately simulate both types of experiment accurately; a slight drawback of this model was that differing sets of material parameters were required for each case.
- The LTMx2 model was also able to accurately simulate both types of experiment however both simulations were carried out with a single set of material parameters. This will allow the LTMx2 model to simulate a larger range of SMP material behaviour without recalibration, something which will be useful for its intended application within a LatConX beam model.
- The LTMx2 simulation of the manually applied stress test appeared identical to that of the LTMx1 model, while the accuracy of the simulation of the

heat-activated stress relaxation test appeared improved, particularly in the early stages from approximately 0 – 40 days.

- In this study, the models have only been applied to pre-drawn PET however, if properly calibrated, they are considered suitable for use with other SMPs.
- In conjunction with the recommendation for further work of Chapter 3, the LTMx2 model could be extended and calibrated to take account of any ageing behaviour of the material prior to activation.

Chapter 5 – LatConX System – Numerical Model Development

In this Chapter a numerical model for the behaviour of the LatConX system is developed and its accuracy is validated by comparison with experimental data. The model takes the form of a nonlinear layered beam model with one major central crack. The work presented in this Chapter is the subject of an article submitted to the journal “Engineering Structures” for publication. Upon review, some minor revisions were recommended which have been implemented throughout the work presented herein. The journal article has also been amended and resubmitted to *Engineering Structures*.

5.1 Outline of LatConX System Model

The form of the non-linear layered beam model developed to simulate the required behaviour of the LatConX material system is illustrated in Figure 5.1.

The model is composed of a set of sub-models, each representative of a different aspect of a material’s behaviour, which are combined and thus able to simulate the transient thermomechanical behaviour of reinforced concrete beams with shrinkable SMP tendons included. The model accounts for all relevant material behaviours and their interactions; these include: mechanical damage, creep, shrinkage, thermal expansion/contraction, and self-healing of the cementitious matrix; mechanical behaviour of reinforcement; and transient thermomechanical behaviour of SMP tendons.

The model is composed of a number of elements; the exact configuration of which depends on the details of the LatConX structure being considered. There are four different element types; elastic beam elements, a fracture process zone (FPZ) element, SMP bar elements, and reinforcement bar elements. In all cases presented in this thesis the model consists of two elastic beam elements either side of a central fracture process zone; further to this, SMP and reinforcement elements are incorporated as required. In this configuration the model is applicable to situations in which it is assumed that all mortar/concrete fracture can be realistically expected to occur in a major central crack i.e. a beam with a significant central notch. If required, the model can be set up with multiple FPZ elements and used to model more complicated, realistic structural situations; however this was not considered necessary for the present work.

Ultimately, the model is capable of simulating the long-term behaviour of any concrete element of rectangular cross section with or without any reinforcement and/or SMP tendons.

The model setup considered for all applications presented in this article is shown in Figure 5.1. This is a simply supported beam of length L, with a significant central notch, subjected to a centrally applied point load, P. The total length of the beam comprises two continuum beam elements, each of length L_e, and a central FPZ of length w_c. Elements representing steel reinforcement and PET tendons are also shown in Figure 5.1.

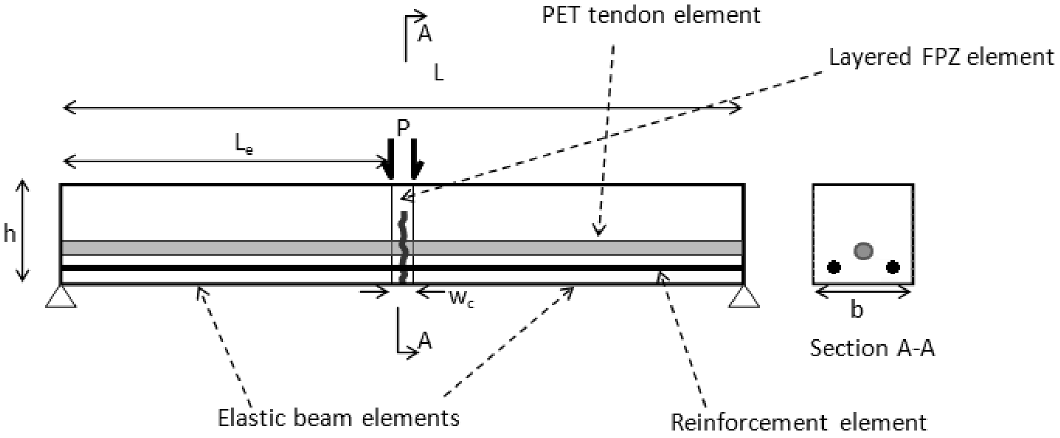

Figure 5.1 - Schematic diagram of numerical model

5.2 Theory

5.2.1 Nonlinear Fracture Process Zone

A summary of the behaviour and key assumptions governing the behaviour of the FPZ is shown in Figure 5.2.

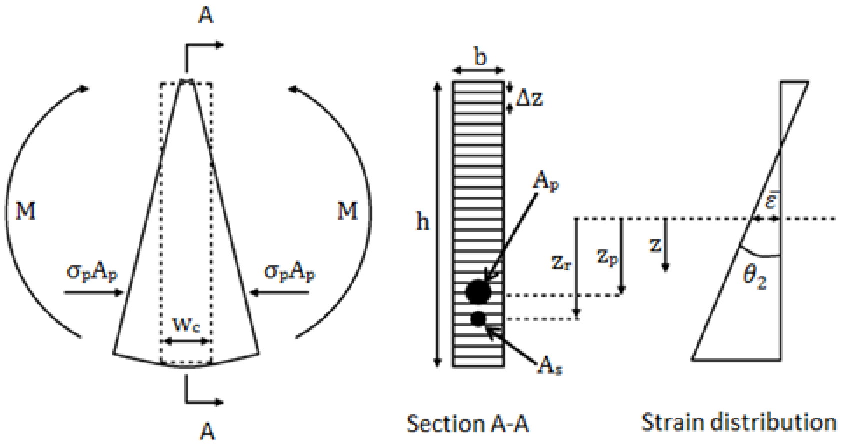

Relationships governing FPZ behaviour are derived assuming a constant moment and curvature across its width, w_c. In all cases considered in this Thesis the moment (M) across the FPZ is given by the following:

$$M = \frac{PL_e}{2} + \sigma_p A_p z_p$$

FPZ discretised into layers; each of depth Δz, width b, and located at a vertical distance z from the reference height.

The strain distribution through the depth of the FPZ is assumed to behave according to Equation 5.1 i.e. plane section remaining plane. This allows the uniaxial strains applicable to each concrete/mortar layer, reinforcing element, and PET tendon element to be determined.

Figure 5.2 – Schematic diagram describing the assumed behaviour of the FPZ element

From the information displayed in Figure 5.2, the total strain (ε) at any level (z) in a beam section may be derived to be:

$$\varepsilon = \bar{\varepsilon} - \frac{2}{w_c} z\theta_2 \tag{5.1}$$

where $\bar{\varepsilon}$ is the mid-level reference strain and θ_2 the angle of rotation. w_c is the width of the FPZ (see Figure 5.1 and Figure 5.2) which represents the physical zone over which micro-cracking occurs adjacent to a macro-crack and is normally assumed to be approximately three to five times the size of the coarse aggregate particles (Bažant and Oh 1983). However, since the post-peak stress-strain relationship used in the FPZ element is scaled to w_c, as in Bažant and Oh's Crack-

Band theory, the results are always highly insensitive to the value used for w_c (Bažant and Oh 1983).

The behaviour of the concrete, steel, and polymer in this model are each governed by separate constitutive models; the form of each of these is outlined below.

5.2.1.1 Mortar/concrete Constitutive Models

The constitutive behaviour of mortar or concrete is simulated with the one-dimensional model shown in Figure 5.3.

Tensile behaviour is governed by a uniaxial damage model, in which damage evolution is controlled by an exponential softening function. In the compression region, the behaviour is governed by a simple linear elastic relationship up to a compressive strain limit at which point behaviour is considered to enter a plastic region. This plastic region is not based on a full plasticity model, a simplification that is considered acceptable as plastic behaviour in the compression region would not be expected to have a significant impact on the overall model behaviour in the long-term simulations.

The constitutive model also accounts for healing, creep, shrinkage, and thermal behaviour; the theories and resulting models governing these aspects of behaviour, and their integration with the basic mortar constitutive model are described in the relevant sections below.

The effective mechanical strain ε_{efm}, taking account of shrinkage, creep, and thermal strain is given by:

$$\varepsilon_{efm} = \varepsilon - \varepsilon_{sh} - \varepsilon_{cr} - \varepsilon_{TH} \tag{5.2}$$

where; ε_{sh} is the shrinkage strain, ε_{cr} is the creep strain, and ε_{TH} is the thermal strain.

The constitutive equation for the tension zone is given by Equation (5.3).

$$\sigma = (1 - \omega) \cdot E \cdot \varepsilon_{efm} \tag{5.3}$$

in which σ is the axial stress, ω is the damage parameter given by Equation (5.4), E is Young's modulus of the mortar/concrete, and ε_{efm} is the effective mechanical axial strain taking into account creep, shrinkage and thermal effects.

$$\omega = 1 - \frac{\varepsilon_t}{\zeta} e^{-c\frac{\varepsilon_{efm}-\varepsilon_t}{\varepsilon_0-\varepsilon_t}} \tag{5.4}$$

in which ζ is the maximum strain parameter, ε_0 is the strain at the end of a stress opening curve ($\varepsilon_0 = \frac{u_0}{w_c}$), u_0 is the crack opening displacement at the end of a stress-opening curve ($u_0 \approx \frac{c \cdot G_f}{f_t}$), G_f is the fracture energy, and f_t is the tensile strength of the mortar. The constant c is set to a fixed value of 5, a value agreed upon by other authors (Jefferson 2003).

The constitutive equation for the compression zone is given by Equation (5.5).

$$\sigma = E_c \cdot \varepsilon_{efm} \tag{5.5}$$

where E_c is the nonlinear compressive Young's modulus of the mortar/concrete. E_c is taken as E until the compressive strain exceeds ε_c, the elastic compressive strain limit of mortar/concrete; upon exceeding this strain the 'secant' compressive Young's modulus is given by

$$E_c = \frac{f_c}{\varepsilon_{efm}} \tag{5.6}$$

in which f_c is the compressive strength of mortar/concrete.

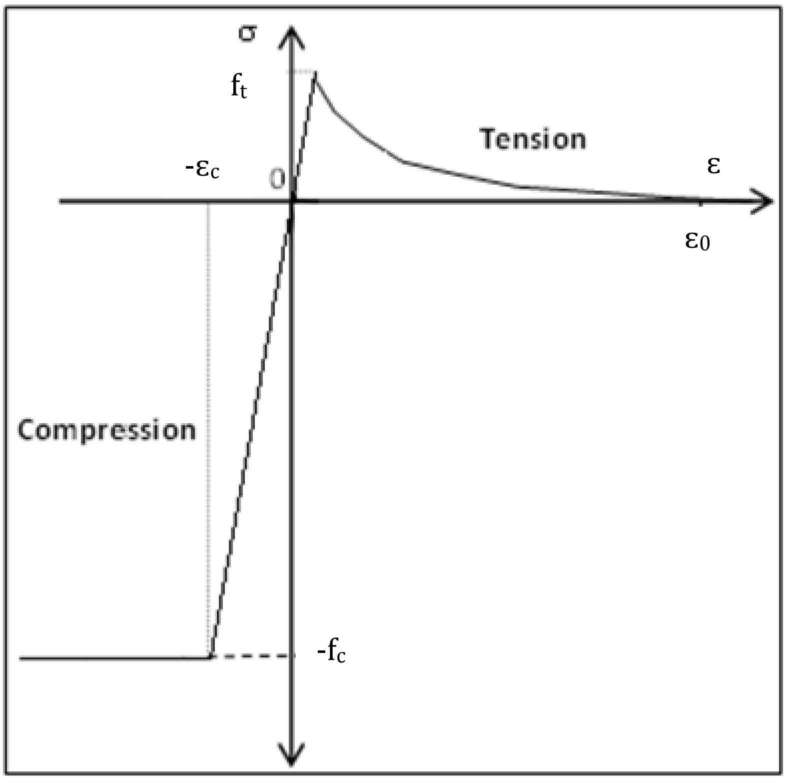

Figure 5.3 – Mortar/concrete constitutive model and primary variables

Post-damage strength regain in the form of self-healing is also accounted for in the mortar/concrete constitutive model. This strength regain could either be due to the action of healing additives or autogenous healing within the cementitious matrix. Hence its magnitude varies depending on the exact nature of the healing phenomenon considered.

The healing model is similar to that of Schimmel and Remmers (2006) however instead of the healing progressing according to a healing function it is assumed to occur instantaneously. Thus there are just two parameters to be set; the time of healing (t_H) and the percentage of current damage regained ($0 \leq H \leq 1$). Healed material is considered as forming in a stress free state and thus the strain given by Equation (5.2) at the instant healing is applied (ε_H) must be recorded and used as a reference position for any further applied strains. The level of damage at the time of healing (ω_H) is also recorded and included in the expression for the stress in the healed material (σ_H) given in Equation (5.7). This inclusion of ω_H results in the level of healing being proportional to the existing level of damage at the time of healing.

$$\sigma_H = H \cdot \omega_H \cdot E_H \cdot (\varepsilon - \varepsilon_H) \tag{5.7}$$

where the Young's modulus of the healed mortar/concrete, E_H, is a function of any strain applied to the material beyond the strain at healing i.e. ε-ε_H according to the constitutive model shown in Figure 5.3.

Combining Equations (5.3) or (5.5), and (5.7) gives the total stress strain relationship for the mortar shown in Equation (5.8).

$$\sigma_{total} = \sigma + \sigma_H \tag{5.8}$$

5.2.1.1.1 Shrinkage Strain

The shrinkage strain is taken from Eurocode 2 (BSI 2004). In this code the shrinkage curve is calculated as a function of the environment's relative humidity, the mean compressive 28 day strength of the concrete, and the notional member size. The key expressions are given in Appendix A for convenience.

5.2.1.1.2 Creep Strain

A simplified version of the creep model developed by Jefferson et al. (2014) has been implemented for this work. This simplified model comprises of an elastic spring and three Maxwell elements in parallel. As the concrete strain and therefore stress is likely to vary through its depth, the creep strain is calculated separately for each layer as a function of the effective creep strain (ε_{efc}) applied to that layer.

The solution for a Maxwell element was derived in Chapter 4, thus the viscoelastic strain at any time increment (j) is given by Equation (4.8), substituting ε_{efc} given by Equation (5.9) for ε_θ.

$$\varepsilon_{efc} = \varepsilon - \varepsilon_{sh} - \varepsilon_{TH} - \varepsilon_{fr} \tag{5.9}$$

where ε_{fr} is a strain parameter included to account for any damage due to tensile strains by reducing the effective strain used in for the creep computations. ε_{fr} is given by Equation (5.10).

$$\varepsilon_{fr} = \omega(\varepsilon - \varepsilon_{sh} - \varepsilon_{TH} - \varepsilon_{cr}) \qquad \text{if} \qquad \varepsilon - \varepsilon_{sh} - \varepsilon_{TH} - \varepsilon_{fr} > 0 \tag{5.10}$$

$$\varepsilon_{fr} = 0 \qquad \text{otherwise}$$

The above equations allow the viscoelastic strain for each Maxwell arm to be calculated, and these are combined into a single total creep strain. The contribution of each Maxwell arm to this total creep strain is controlled by a weighting factor, β_c; therefore the total creep strain, ε_{cr} is given by (5.11);

$$\varepsilon_{cr} = \sum_{i=2}^{4} \beta_{c_i} \varepsilon_{vec_i} \tag{5.11}$$

where β_{ci} are the weighting factors for each arm, and ε_{vec} is the viscoelastic strain for each arm. The values of β_{ci} and τ_{ci} for each arm were set by calibrating against the creep model presented in Eurocode 2 (BSI 2004) for the desired environmental conditions.

An example calibration curve and the relevant β_c and τ_c values can be seen in Figure 5.4 and Table 5.1.

Table 5.1 - β_c and τ_c values used for example creep calibration curve

Arm No	**1**	**2**	**3**	**4**
β_c	0.2	0.5	0.26	0.04
τ_c **(days)**	NA	0.6	50	2000

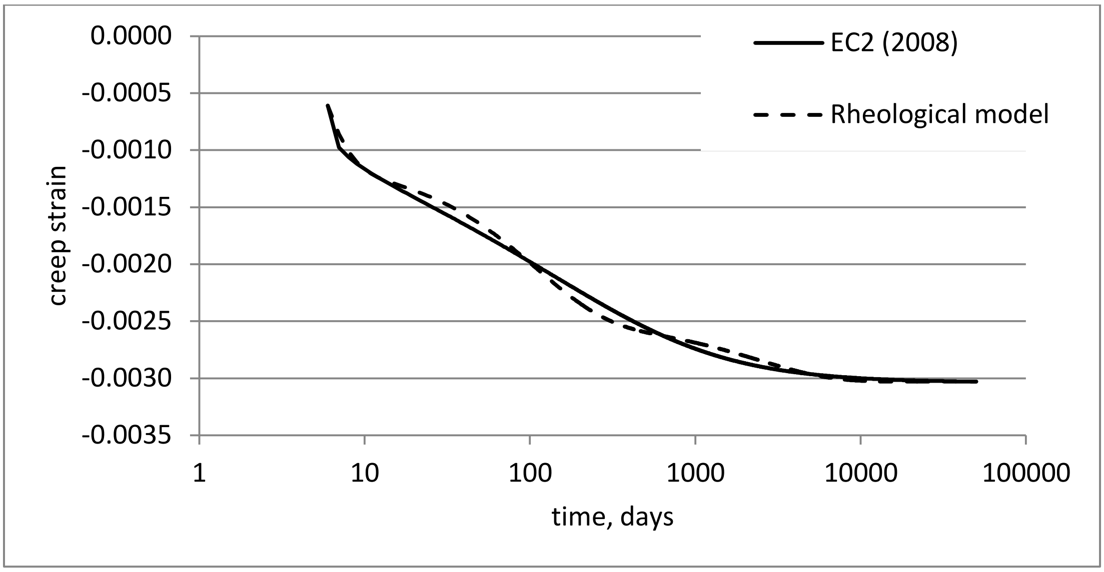

Figure 5.4 – Example calibration curve. Compressive strength = 30 N/mm^2, dimensions 300 x 450 mm, relative humidity 50 %, loaded at 7 days

5.2.1.1.3 Thermal Strain

The thermal strain due to cooling subsequent to the maximum heat of hydration occurring during the curing process is determined using Equation (5.12) taken from BD28/87 (The Highways Agency 1987).

$$\varepsilon_{TH} = -0.8\alpha_c(T_1 + T_2) \tag{5.12}$$

where α_c is the coefficient of thermal expansion for concrete, taken as 12 x 10^{-6}, and T_1 and T_2 are anticipated temperature decreases from the hydration peak. The values of T_1 and T_2 are determined in accordance with BD28/87 (Bamforth 2007). The thermal strain is applied as a single shrinkage episode at a time, t_{TH}, before any other creep, shrinkage, or applied load effects act on the beam. This approach has been adopted so as to avoid the necessity for detailed consideration of the hydration processes and associated early age behaviour.

5.2.1.2 Reinforcing Steel Constitutive Model

The trilinear constitutive model governing the behaviour of the reinforcing steel is displayed in Figure 5.5, the stress-strain relationships are simply interpolated between the different yield positions as a function of the strain level in this reinforcement.

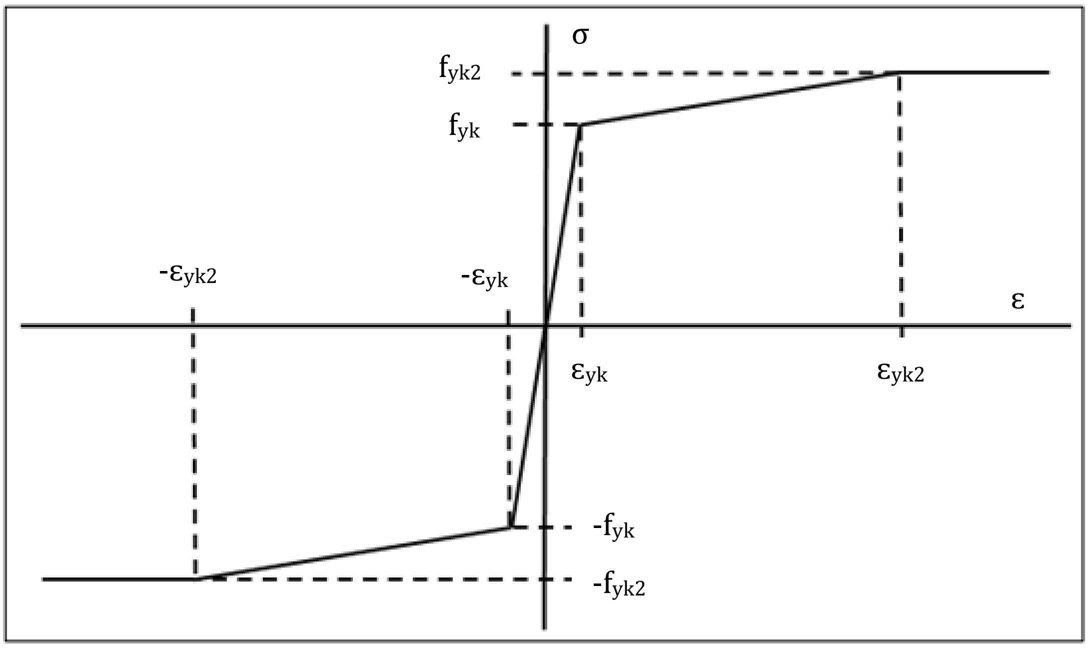

Figure 5.5 – Reinforcing steel constitutive model

It is assumed that there is no slip between the cementitious matrix and the reinforcing steel and therefore the strains applied to reinforcement elements are the total strains at the relevant level in the beam from Equation (5.1). This assumption is considered acceptable when a beam subjected to loads at the working load level is considered (Beeby and Scott 2005).

5.2.1.3 Polymer Tendons Constitutive Model

The constitutive behaviour of the SMP tendons is governed by the LTMx2 model described in Chapter 4; of the two models described LTMx2 was selected for its greater range of applicability with a single set of material parameters. The stress on a restrained polymer tendon is the sum of Equations (4.27) - (4.30).

5.2.1.3.1 Coupling of LTMx2 model with Nonlinear Layered Beam Model

For each time increment, the stress in any polymer tendon is computed on the assumption that it is restrained at a length equal to that of the beam at the level of the polymer tendon (z_p), this assumption is justified as the polymer tendons are intended to be completely debonded along their lengths (except for the end anchorages). This restraining length is denoted L_R and is calculated according to Equation (5.13).

$$L_R = L + \Delta L \tag{5.13}$$

in which L is the original length of the beam, and ΔL is the change in length of the beam at the level of the polymer tendon, contributed to by the displacements of both the elastic beam elements (ΔL_{nle}) and the FPZ (ΔL_{FPZ}). In the FPZ, the sum of all contributing strains at any level is given by Equation (5.1), thus the total displacement for the FPZ at the level of the polymer tendon is:

$$\Delta L_{FPZ} = \bar{\varepsilon} w_c - 2\theta_2 z_p \tag{5.14}$$

The displacement in the two elastic beam elements is that shown in (5.15) which accounts for axial and rotational displacements in the elements due to applied moment, stress in the polymer, shrinkage, creep, and thermal strains. The first set of terms account for strains due to applied axial and flexural loads from the polymer tendon and externally applied moment. The first sub-term of this set gives the strain required at the mid-height of the beam to maintain axial force equilibrium between the beam and tendon. The second sub-term gives the strain at the level of the polymer tendon due to the rotation required to maintain moment equilibrium. This is derived on the assumption of a linear moment distribution along the length of the elastic beam element from $A_p \sigma_p z_p$ at the end of the beam to $A_p \sigma_p z_p + M_{ap}$ at the central end of the elastic beam element. The second set of terms gives the strain at the level of the polymer tendon due to applied thermal and shrinkage strains of the mortar/concrete. As in the first set of terms, the first sub-term accounts for axial equilibrium between the steel and concrete, while the second sub-term accounts for rotational equilibrium.

$$\Delta L_{nle} = 2L_e \left[\frac{A_p\sigma_p}{AE_{cef}} + \frac{z_p}{E_{cef}I_{int}}\left[A_p\sigma_p z_p + \frac{M_{ap}}{2}\right] + [\varepsilon_{sh} + \varepsilon_{TH}]\left[\frac{AE_{cef}}{A_sE_s + AE_{cef}} + \frac{\alpha_e S z_p}{I_{int}}\right]\right] \quad (5.15)$$

In Equation (5.15) A_p is the cross sectional area of the polymer tendon, σ_p is the stress in the polymer tendon at the end of the previous time increment, A is the concrete area, E_{cef} is Young's modulus of the concrete as a function of time to account for creep in the elastic elements (see Equation (5.24)), z_p is the depth of the polymer tendon relative to the reference height, M_{ap} is the applied moment, and I_{int} is the second moment of area of the beam as a function of the applied moment to account for any cracking in the elastic elements (see Equation (5.23)), A_s is the total area of reinforcement, E_s is Young's modulus of the reinforcement, α_e is the modular ratio, and S is the first moment of area of the reinforcement.

Based on this restrained length (L_R), an equivalent strain (ε_R) applied to the polymer is given by Equation (5.16).

$$\varepsilon_R = \frac{L_R - L_{pmin}}{L_{pmin}} \quad (5.16)$$

in which L_{pmin} is the original length of the polymer before drawing given by:

$$L_{pmin} = \frac{L}{1 + \varepsilon_{p0}}$$

in which ε_{p0} is the drawing strain used in the polymer manufacturing process given by:

$$\varepsilon_{p0} = \frac{\sigma_{res}}{E_1}$$

ε_R from Equation (5.14) is then substituted for ε in Equations (4.27) - (4.30), the sum of which yields the polymer stress.

5.2.1.4 Assembly of Equilibrium Equations for FPZ

The FPZ behaviour is analysed by use of a layered approach, thus the beam is divided into a number of discrete layers (n_{lay}– usually 100) each layer with effective width b and depth Δz, and with material properties derived from the mortar/concrete constitutive model outlined above. The strain in each layer is given by Equation (5.1). The effect of any reinforcement is accounted for in the same manner by adding its contribution to the overall axial and bending stiffness as a function of the reinforcement's area, depth within the beam, and axial stiffness according to the constitutive model presented in Figure 5.5.

Thus the internal axial force, N, and moment, M, for a reinforced concrete section subjected to a total strain at a specified reference height ($\bar{\varepsilon}$) and rotation (θ_2) are represented by (5.17) and (5.18) respectively.

$$N = \sum_{i=1}^{nlay} (1-\omega)E\varepsilon_{efm_i} b_i \Delta z_i + \sum_{i=1}^{nlay} (1-\omega_2)\omega_H HE\left(\varepsilon_{efm_i} - \varepsilon_{H_i}\right) b_i \Delta z_i + \sum_{i=1}^{nrebar} E_s \varepsilon_i A_{s_i} \tag{5.17}$$

$$M = \sum_{i=1}^{nlay} (1-\omega)E\varepsilon_{efm_i} b_i z_i \Delta z_i + \sum_{i=1}^{nlay} (1-\omega_2)\omega_H HE\left(\varepsilon_{efm_i} - \varepsilon_{H_i}\right) b_i z_i \Delta z_i + \sum_{i=1}^{nrebar} E_s \varepsilon_i A_{s_i} z_{r_i} \tag{5.18}$$

in which z_i and z_{ri} are the depths for each mortar or reinforcement layer respectively relative to the reference height; the damage parameters ω and ω_2 for each layer are a function of ε_{efmi} and $\varepsilon_{efmi} - \varepsilon_{Hi}$ respectively; and A_{si} is the area of steel in each reinforcement layer.

ε_i, and ε_{efmi} are the strains at the centre of each layer given by Equations (5.19) and (5.20) which are discretised forms of Equations (5.1) and (5.2) in accordance with the form of the layered beam element.

$$\varepsilon_i = \bar{\varepsilon} - \frac{2}{w_c} z_i \theta_2 \tag{5.19}$$

$$\varepsilon_{efm_i} = \varepsilon_i - \varepsilon_{sh} - \varepsilon_{cr_i} - \varepsilon_{TH} \tag{5.20}$$

Combining Equations (5.17), (5.18), (5.19), and (5.20); equating (5.17) to the load from the polymer tendon, if present, and (5.24) to the externally applied moment leads to a system of equilibrium equations for the FPZ as shown in Equation (5.21).

$$\boldsymbol{F} = [\boldsymbol{\Omega}] \cdot [\boldsymbol{u}] \tag{5.21}$$

in which $\boldsymbol{F}$, $\boldsymbol{\Omega}$, and $\boldsymbol{u}$ are represented by the following:

$$\boldsymbol{F} = \begin{bmatrix} \sigma_p A_p + \sum_{i=1}^{nlay} b_i \Delta z_i E\left((1-\omega_i)(\varepsilon_{TH} + \varepsilon_{sh} + \varepsilon_{cr_i}) + (1-\omega_{2_i})\omega_{H_i} H(\varepsilon_{TH} + \varepsilon_{sh} + \varepsilon_{cr_i} + \varepsilon_{H_i})\right) \\ M_{ap} + \sigma_p A_p z_p + \sum_{i=1}^{nlay} b_i z_i \Delta z_i E\left((1-\omega_i)(\varepsilon_{TH} + \varepsilon_{sh} + \varepsilon_{cr_i}) + (1-\omega_{2_i})\omega_{H_i} H(\varepsilon_{TH} + \varepsilon_{sh} + \varepsilon_{cr_i} + \varepsilon_{H_i})\right) \end{bmatrix}$$

$$\Omega = \begin{matrix} \sum_{i=1}^{nlay} b_i \Delta z_i E\left((1-\omega_i) + (1-\omega_{2_i})\omega_{H_i} H\right) + \sum_{i=1}^{nrebar} E_s A_{s_i} & \frac{-2}{w_c}\left[\sum_{i=1}^{nlay} b_i z_i \Delta z_i E\left((1-\omega_i) + (1-\omega_{2_i})\omega_{H_i} H\right) + \sum_{i=1}^{nrebar} E_s A_{s_i} z_{r_i}\right] \\ \sum_{i=1}^{nlay} b_i z_i \Delta z_i E\left((1-\omega_i) + (1-\omega_{2_i})\omega_{H_i} H\right) + \sum_{i=1}^{nrebar} E_s A_{s_i} z_{r_i} & \frac{-2}{w_c}\left[\sum_{i=1}^{nlay} b_i {z_i}^2 \Delta z_i E\left((1-\omega_i) + (1-\omega_{2_i})\omega_{H_i} H\right) + \sum_{i=1}^{nrebar} E_s A_{s_i} {z_{r_i}}^2\right] \end{matrix}$$

$$\boldsymbol{u} = \begin{bmatrix} \bar{\varepsilon} \\ \theta_2 \end{bmatrix}$$

5.2.2 Elastic Beam Elements

A summary of the behaviour of the elastic beam elements and key assumptions governing it is shown in Figure 5.6.

The behaviour of the two sections of the simply supported beam on either side of the FPZ is simulated by two single elastic beam elements; one located on each side. Each of these elements has a length (L$_e$) given by: $L_e = \frac{L-w_c}{2}$.

The creep, shrinkage, and cracking behaviour of these element is governed by a set of nonlinear constitutive relationships taken from Eurocode 2 (BSI 2004), this is described in detail in Section 5.2.3.

The moment in each of these elements is assumed to vary linearly from $-\sigma_p A_p z_p$ at the supports, to $\frac{PL_e}{2} - \sigma_p A_p z_p$ at the edge of the FPZ as depicted below, thus ensuring moment compatibility with the boundary conditions imposed by the support and the FPZ element.

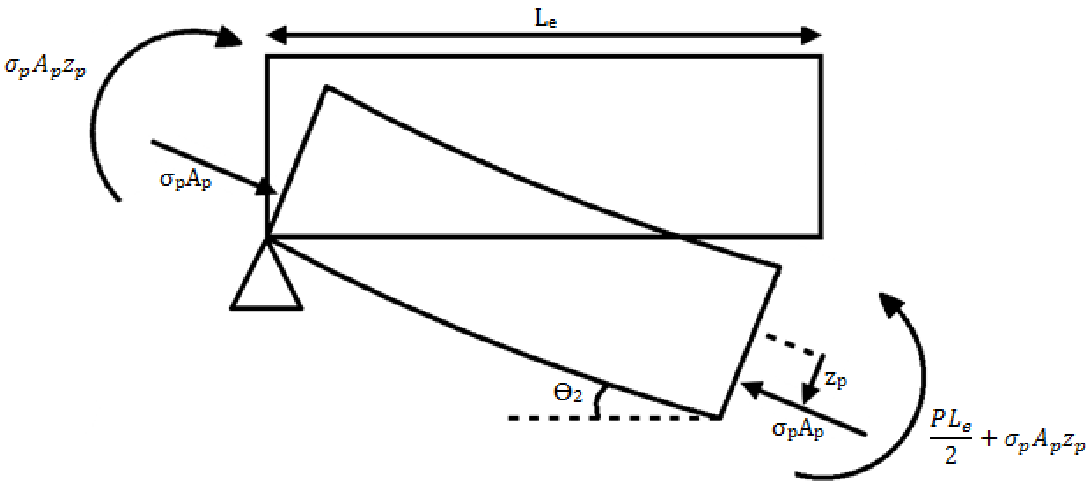

Figure 5.6 - Schematic diagram describing the assumed behaviour of the elastic beam elements

The elastic beam elements are Bernoulli-Euler beam elements with nonlinear constitutive relations that take account of cracking and creep. The secant relationship governing their behaviour is shown in Equation (5.22).

$$\begin{bmatrix} F_1 \\ M_1 \\ F_2 \\ M_2 \end{bmatrix} = \frac{E_{cef}(t) \cdot I_{int}(M_{max})}{L_e} \begin{bmatrix} {}^{12}/_{L_e{}^2} & {}^{6}/_{L_e} & -{}^{12}/_{L_e{}^2} & {}^{6}/_{L_e} \\ {}^{6}/_{L_e} & 4 & -{}^{6}/_{L_e} & 2 \\ -{}^{12}/_{L_e{}^2} & -{}^{6}/_{L_e} & {}^{12}/_{L_e{}^2} & -{}^{6}/_{L_e} \\ {}^{6}/_{L_e} & 2 & -{}^{6}/_{L_e} & 4 \end{bmatrix} \begin{bmatrix} w_1 \\ \theta_1 \\ w_2 \\ \theta_2 \end{bmatrix} \qquad (5.22)$$

The first nonlinear constitutive relationship concerns the effect of cracking of the concrete section. This is accounted for by a decrease in the second moment of area,

I, as a function of the maximum historically applied moment M_{max}. M_{max} is determined based on the assumption of a linear moment distribution along the length of the elastic beam element from $A_p\sigma_p z_p$ at the end of the beam to $A_p\sigma_p z_p + M_{ap}$ at the central end of the elastic beam element. If the maximum historically applied moment exceeds two times the cracking moment (M_{cr}), the value of I_{int} used in the stiffness matrix of Equation (5.22) is interpolated between those for the uncracked and fully cracked section according to Equation (5.23). The cracking moment is multiplied by two to account for the assumed linear distribution of cracking (and thus the resulting reduction in stiffness) between that corresponding to M_{max} at the edge of the FPZ, and zero at the support.

$$I_{int} = (1 - \kappa)\mathrm{I}_{un} + \kappa \cdot I_{cr} \tag{5.23}$$

where I_{un} and I_{cr} are the uncracked and cracked second moments of area respectively, and κ is a distribution factor used to take account of tension stiffening of a reinforced concrete section given by:

$$\kappa = 1 - \beta\left(\frac{2M_{cr}}{M_{max}}\right)^2$$

where β is a load duration factor taken as 0.5 for the case of sustained loading, and M_{cr} is the cracking moment given by:

$$M_{cr} = \frac{f_t \cdot I_{un}}{y_t}$$

where y_t is the lever *arm* from the neutral axis to the tension face.

The second nonlinear constitutive relationship within the elastic beam elements arises from the effects of creep. This is accounted for by obtaining a creep factor (φ_c) in accordance with Eurocode 2 (BSI 2004), the key expressions for this are summarised in Appendix A. The creep factor is then applied to the Young's modulus of concrete as shown in Equation (5.24) to give an effective Young's modulus, E_{cef}.

$$E_{cef} = \frac{E}{\varphi_c + 1} \tag{5.24}$$

This effective Young's modulus is then used in all calculations relating to the elastic elements.

5.3 Model Algorithms

Algorithms implemented in the model are outlined in the following section.

5.3.1 Main Algorithm Defining Details for Analysis

The overall algorithm for simulating the long-term behaviour of a structural element is outlined below.

Table 5.2 – Main algorithm defining details for model analysis

1	is, t, T, ε_{ve1}, ε_{ve2}, ε_R, M, $\overline{\varepsilon}$, θ_2, ε_L, ζ, ε_{sh}, ε_{cr}, ε_{vecr}, σ_p, ε_H, ω_H, ε_{LH}, ζ_H	*Initialise all variables and counters*
2	while t < t_{TH} is = is + 1, t = t + Δt (T, ε_{ve1}, ε_{ve2}, ε_R, M, $\overline{\varepsilon}$, θ_2, ε_L, ζ, ε_{sh}, ε_{cr}, ε_{vecr}, σ_p, ε_H, ω_H, ε_{LH}, ζ_H) = (T, ε_{ve1}, ε_{ve2}, ε_R, M, $\overline{\varepsilon}$, θ_2, ε_L, ζ, ε_{sh}, ε_{cr}, ε_{vecr}, σ_p, ε_H, ω_H, ε_{LH}, ζ_{Hprev})	*Time dependent processes are assumed to begin at t = t_{TH} thus update counters and set variables up to this point*
3	if t = t_{TH} Set ε_{TH}	*Apply thermal strain at t = t_{TH}* *See Equation (5.12).*
4	See iterative solver algorithm below	*Compute updated beam configuration for thermal strain*
5	See time step algorithm below	*Simulate time dependent processes and compute updated beam configuration for each time step up until time of loading, t_0*
6	Δt = 0, $\Delta M = \frac{M_{ap}}{n_{step}}$ See iterative solver algorithm below	*Incrementally apply permanent moment and compute beam configurations throughout*
7	See time step algorithm below	*Simulate time dependent processes and compute updated beam configuration for each time step up for required length of time I.e. up to t_{final}*

5.3.2 Algorithm for Each Time Step

Table 5.3 – Algorithm controlling the implementation time-dependent processes

1	t, T, ε_{ve1}, ε_{ve2}, ε_p, ε_B, M, $\bar{\varepsilon}$, θ_2, ε_L, ζ, ε_{sh}, ε_{cr}, ε_{vecr}, σ_p, ε_H, ω_H, ε_{LH}, ζ_H	*Input all values from previous time step*
2	is = is + 1	*Update counters*
3	$t = t + \Delta t$, $T = T + \Delta T$	*Set conditional changes for time step*
4	See creep algorithm below	*Update creep strains*
5	See shrinkage algorithm below	*Update shrinkage strains*
6	See polymer algorithm below	*Update polymer state*
7	See iterative solver algorithm below	*Compute updated beam configuration*

5.3.3 Creep

The creep strain is a function of both time and stress, thus it is different for each beam layer. The algorithm outlined details how the creep strain is computed for a single layer and is therefore run in full for each layer.

Table 5.4 – Algorithm for creep functions

1	$\varepsilon_{prevcr} = \varepsilon_{cr}$	*Record current creep strains*
2	$\varepsilon_{cr} = 0$	*Reset ε_{cr} array to zeros*
3	if $(\varepsilon - \varepsilon_{sh} - \varepsilon_{TH} - \varepsilon_{prevcr}) > 0$ $\varepsilon_{fr} = \omega(\zeta) * (\varepsilon - \varepsilon_{sh} - \varepsilon_{TH} - \varepsilon_{prevcr})$ otherwise $\varepsilon_{fr} = 0$	*Compute ε_{fr} to take account of any tensile creep* *See Equation (5.10).*
4	$\varepsilon_{efc} = \varepsilon - \varepsilon_{sh} - \varepsilon_{TH} - \varepsilon_{fr}$	*Compute effective creep strain to be applied to creep model for current time step* *See Equation (5.9).*
5	for i = 2…4 $\varepsilon_{vec} = \varepsilon_{efc}\left(1 - e^{-\frac{\Delta t}{\tau_i}}\right) + \varepsilon_{vec_i}\left(e^{-\frac{\Delta t}{\tau_i}}\right)$ $\varepsilon_{cr} = \varepsilon_{cr} + \beta_{ci}\, \varepsilon_{veci}$	*Compute viscoelastic strain for each dashpot and updated creep strain for each layer* *See Equations (4.6) and (5.11).*
6	$\Delta\varepsilon_{cr} = \varepsilon_{cr} - \varepsilon_{prevcr}$	*Compute change in creep strain for time step*

5.3.4 Shrinkage

Determining the shrinkage strain, ε_{sh}, is the simplest process as the strain is purely time-dependent and as such is the same for each beam layer.

Table 5.5 – Algorithm for shrinkage function

1	$\Delta\varepsilon_{sh} = \varepsilon_{sh}(t) - \varepsilon_{sh}(t- \Delta t)$	*Compute change in shrinkage strain for time step*
2	$\varepsilon_{sh} = \varepsilon_{sh} + \Delta\varepsilon_{sh}$	*Update total shrinkage strain*

5.3.5 Polymer Functions

Table 5.6 – Algorithm for polymer functions

1	$\varepsilon_{ve1} = \varepsilon_R\left(1 - e^{-\frac{\Delta t}{\tau}}\right) + \varepsilon_{ve1_{prev}}\left(e^{-\frac{\Delta t}{\tau}}\right)$ $\varepsilon_{ve2} = \varepsilon_R\left(1 - e^{-\frac{\Delta t}{\tau(T)}}\right) + \varepsilon_{ve2_{prev}}\left(e^{-\frac{\Delta t}{\tau(T)}}\right)$	*Update viscoelastic strains* *See Equation (4.6)*

5.3.6 Iterative Solver

Table 5.7 – Algorithm for computing updated beam configuration

1	$\bar{\varepsilon}$, θ_2, ε_L, ζ, ε_{LH}, ζ_H, T, M, ΔM, σ_p, ε_{sh}, $\Delta\varepsilon_{sh}$, ε_{cr}, $\Delta\varepsilon_{cr}$, ε_{TH}, $\Delta\varepsilon_{TH}$, ε_H, ω_H, H, ε_{ve1}, ε_{ve2}, ε_R	*Inputs from time dependent processes and current beam configuration*
2	$\zeta_{prev} = \zeta$, $\zeta_{Hprev} = \zeta_H$, $\psi = 10^{20}$, $i_{sec} = 0$, $\sigma_{prev} = \sigma_p$	*Initialise previous damage array, convergence parameter and tangent/secant matrix selector parameter*
3	$L_R = L + \Delta L_{FPZ} + \Delta L_{nle}$ $\varepsilon_R = \frac{L_R - L_{pmin}}{L_{pmin}}$ $\sigma_p = \beta \cdot E_1 \cdot \varepsilon_R + (1-\beta) \cdot E_1 \cdot (\varepsilon_R - \varepsilon_{ve1}) + E_2(T) \cdot (\varepsilon_R - \varepsilon_{ve2}) - \alpha \cdot \left(E_1 + E_2(T)\right) \cdot (T - T_{ambient})$ $\Delta\sigma_p = \sigma_p - \sigma_{prev}$	*Update polymer stress for updated viscous strains and compute change in polymer stress* *See Equations (5.13) - (5.16), and (4.27) - (4.30).*
4	while ψ > 10-5	*Enter iterative loop*
5	$\Omega = \Omega_T(\bar{\varepsilon}, \theta_2, \zeta, \varepsilon_H, \omega_H, H, \zeta_H)$ $RHS = RHS\left(\Delta M, \Delta\sigma_p, \Delta\varepsilon_{sh}, \Delta\varepsilon_{cr}, \Delta\varepsilon_{TH}, \zeta, \varepsilon_H, \omega_H, H, \zeta_H, \bar{\varepsilon}, \theta_2\right)$	*Form stiffness matrix for nonlinear fracture zone and right hand side of equation*
6	$\begin{bmatrix} \Delta\bar{\varepsilon} \\ \Delta\theta_2 \end{bmatrix} = [\Omega]^{-1} * [RHS]$	*Solve system of equations*
7	$\bar{\varepsilon} = \bar{\varepsilon} + \Delta\bar{\varepsilon}$, $\theta_2 = \theta_2 + \Delta\theta_2$	*Add strain increments to current strain level*
8	$\varepsilon_L = \bar{\varepsilon} - 2\frac{\theta_2}{w_c} z_L - \varepsilon_{sh} - \varepsilon_{cr} - \varepsilon_{TH}$ $\zeta = \max\left(0.999\varepsilon_t, \varepsilon_L, \zeta_{prev}\right)$ $\varepsilon_{LH} = \varepsilon_L - \varepsilon_H$ $\zeta_H = \max\left(0.999\varepsilon_t, \varepsilon_{LH}, \zeta_{Hprev}\right)$	*Update layer data*
9	$\Psi_{prev} = \psi$ $\psi = RHS\left(M, \sigma_p, \varepsilon_{sh}, \varepsilon_{cr}, \varepsilon_{TH}, \zeta, \varepsilon_H, \omega_H, H, \zeta_H, \bar{\varepsilon}, \theta_2\right) - \Omega(\bar{\varepsilon}, \theta_2, \zeta, \varepsilon_H, \omega_H, H, \zeta_H)$	*Store previous convergence parameter, and compute current convergence.*
10	if $\psi - \Psi_{prev} > 0$ $i_{sec} = 1$	*Set tangent/secant matrix selector parameter*
11	if $\psi < 10^{-5}$ Break return ($\bar{\varepsilon}$, θ_2, ζ, σ_p, ζ_H) else continue iterative procedure below	*Evaluate convergence and break if converged*
12	RHS = ψ if isec = 0 $\Omega = \Omega_T(\bar{\varepsilon}, \theta_2, \zeta, \varepsilon_H, \omega_H, H, \zeta_H)$ else $\Omega = \Omega(\bar{\varepsilon}, \theta_2, \zeta, \varepsilon_H, \omega_H, H, \zeta_H)$	*Reform stiffness matrix for latest strains and damage parameters, RHS is the out of balance force from previous iteration*
13	while $\psi > 10^{-5}$ Repeat steps 6 – 13	*Continue iterative process from step 6 onwards*

5.4 Validations

The data from two experimental programs have been used to validate the numerical model. Further to this, an exercise comparing crack width predictions from the model with those calculated according to Eurocode 2 (BSI 2004) has been undertaken for a range of beams with the aim of better understanding the results output by the model.

5.4.1 Validation 1

This validation considered experimental data from Jefferson et al. (2010). This test series used hollow prismatic mortar beams with SMP tendons fixed within; the beam cross-sections were 25mm square with a central 10mm square void. These samples were first mechanically tested 4 days after casting with the polymer in its pre-activated state thus providing no resistance to the applied load. Next the samples were heated to 90°C and soaked at this temperature for 18 hours to activate the shrinkage process of the polymer tendons, they were then mechanically tested a second time 4 days later (8 days after casting) i.e. with the restrained activated polymer contributing to the load deflection behaviour. During both the 4 day and 8 day tests, the fracture-softening behaviour was recorded. With the exception of the healing parameter (H), the material properties of the mortar were determined from material tests carried out by Jefferson et al, and mean values of these are used in the analysis; the values of these parameters are given in Table 5.8. H has been set by experimental calibration with the 8 day test.

Table 5.8 - Material parameters for validation 1 (Jefferson et al. 2010)

	E kN/mm^2	E_p kN/mm^2	A_p mm^2	σ_{res} N/mm^2	w_c mm	f_c N/mm^2	f_t N/mm^2	H	G_f N/mm
Mean	24.8	6.0	20.7	33.8	5	19.5	2.0	0.005	0.025
CoV %	*1.6*	*2.5*	-	*2.3*	-	*8.3*	*7.3*	-	*11.7*

Note: f_c is taken as 0.85*f_{cu}, where f_{cu} was the strength obtained from 40mm cubes

A full description of the procedures involved in this experimental series can be found in the work of Jefferson et al. (2010).

Figure 5.7 shows the comparison between the experimental data and the model predictions using the material properties from Table 5.8, and it can be seen that the numerical predictions closely match the experimental data.

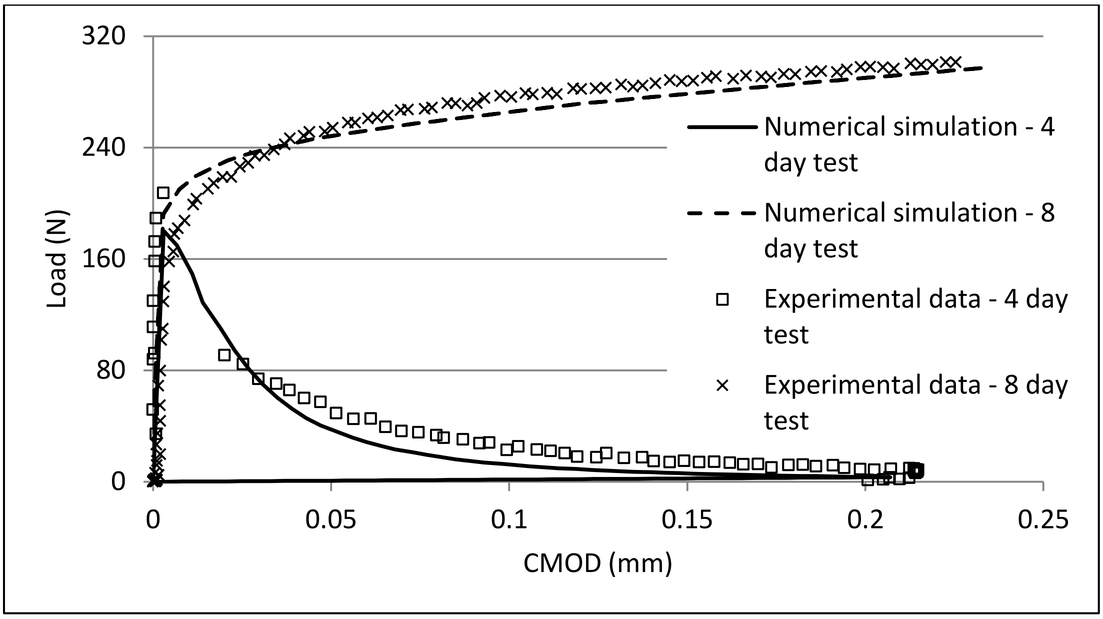

Figure 5.7 - Comparison between experimental data and numerical simulation predictions for validation 1

Close agreement is observed throughout the load-displacement curves for both test stages.

This validation is considered adequate to verify the numerical model's ability to predict the following to an adequate level for its intended purpose:

i. Fracture behaviour of a plain mortar beam (i.e. the cracking behaviour of mortar)
ii. Time-temperature interaction of the mortar beam and activated SMP tendon
iii. Re-fracture behaviour of the same beam subsequent to this activation and interaction

5.4.2 Validation 2

In this validation, the nonlinear time-dependent beam model was used to analyse 12 singly reinforced concrete specimens tested by Gilbert (2013). Over a period of 400 days the simply supported specimens were subjected to a constant sustained service load. A more detailed description of the tests and specimens can be found in the original work. The general material parameters and individual specimen parameters displayed in Table 5.9 and Table 5.10 respectively were used to predict the specimen's deflections; these are taken directly from the original publication.

Table 5.9 – General material parameters for validation 2

L (mm)	E_c (GPa)	f_c (MPa)	f_t (MPa)	E_s (GPa)	f_y (MPa)	Φ (400 days)	ε_{sh} (400 days)	T_1 (°C)	T_2 (°C)	w_c (mm)
3500	22.82	18.3	2.57	200	500	1.71	0.000825	10	0	100

Table 5.10 – Individual specimen parameters for validation 2

	Specimen	b	h	d	A_s	M_{ap}
		mm	mm	mm	mm^2	kNm
Beams	1a	250	348	300	400	24.90
	1b	250	348	300	400	17.00
	2a	250	333	300	400	24.80
	2b	250	333	300	400	16.80
	3a	250	333	300	600	34.60
	3b	250	333	300	600	20.80
Slabs	1a	400	161	130	226	6.81
	1b	400	161	130	226	5.28
	2a	400	161	130	339	9.87
	2b	400	161	130	339	6.81
	3a	400	161	130	452	11.40
	3b	400	161	130	452	8.34

A comparison of the predicted and measured 400 day deflections is displayed in Table 5.11. The predictions show good agreement with a mean percentage difference of 12.46 %. The standard deviation is 8.54 % which although large is considered within acceptable limits when taking into account the variability of concrete properties.

Table 5.11 – Validation 2 – Results

	Specimen	400 day deflection (mm)		% difference
		Measured	Simulated	
Beams	1a	12.1	11.7	3.31
	1b	7.4	8.5	14.86
	2a	12.4	11.8	4.84
	2b	7.9	8.7	10.13
	3a	13.3	12.6	5.26
	3b	7.9	8.7	10.13
Slabs	1a	25.1	31.1	23.90
	1b	19.9	26.2	31.66
	2a	29.8	33	10.74
	2b	21.9	26	18.72
	3a	32.5	32	1.54
	3b	22.9	26.2	14.41
		Mean		**12.46**
		Standard deviation		**8.54**

This agreement is considered to validate the numerical model's ability to take account of the time-dependent creep and shrinkage behaviour of the concrete, strains due to thermal contraction of the concrete, and the effects of cracking in both the elastic beam elements and the FPZ on the load-deflection relationship. Finally the constitutive model for reinforcement bars and the reinforcement-concrete interaction are considered valid as demonstrated by this close agreement.

5.4.3 Validation 3

Crack width predictions from the model and those calculated according to Eurocode 2 (BSI 2004) have also been compared. This comparison has been carried out for a range of different beam designs and sustained applied moments.

Information pertaining to the use of the model in simulating the behaviour of theoretical beams designed to Eurocode standards is discussed in detail in Chapter 6. The material properties used in the model and in the design of the beams, and the relevant partial factors for all materials are displayed in Table 6.4 and Table 6.5. The environmental conditions assumed for the functions relating to the creep, shrinkage, and thermal strains, and other model parameters can be seen in Table 6.6 and Table 6.7.

All beam designs have the same cross section of 250 mm x 400 mm which was selected arbitrarily. There is a limiting value (M_{bal}) of the moment of resistance (M_R) for any section to remain under-reinforced; this limit is discussed in more detail at the relevant point of Chapter 6. The proportion of the maximum moment utilised is determined by the area of steel provided up to the limiting area that results in M_R = M_{bal}. To ensure that this crack width prediction comparison considers a representative range of beam behaviour the utilisation of M_{bal} has been varied from 50 % up to 100 % in 10 % increments where the utilisation is given by (5.25).

$$utilisation = 100 \cdot \frac{M_R}{M_{bal}} \tag{5.25}$$

These utilisation factors, the resulting value of M_R, and the steel areas are shown in Table 5.12.

Table 5.12 – Beam designs for crack width prediction comparison

Beam ref	*Utilisation* (%)	M_R (kNm)	A_s (mm^2)
50	50	100	627
60	60	120	768
70	70	141	915
80	80	161	1070
90	90	181	1233
100	100	201	1407

For each of these beams, 50 year crack width predictions from the model were found for sustained applied moments ranging from 50 % - 80 % of M_R in 10 % increments.

This range of M_{bal} utilisation in the beam designs and M_R utilisation in the applied moments is considered to encompass the full range of relevant cracking behaviour.

Crack width calculations according to Eurocode 2 (BSI 2004) were also carried out for the same set of beams and applied moments, however obtaining a realistically comparable value is a little complicated. The Eurocode procedure for calculating crack widths can be seen in Appendix B; in this procedure the final crack width is given by the difference between the mean reinforcement strain (ε_{sm}), and mean concrete strain (ε_{cm}), multiplied by the maximum crack spacing ($S_{r,max}$), with $S_{r,max}$ given by the empirical formula of Equation (5.26).

$$S_{r,max} = 3.4c + \frac{0.425 k_1 k_2 \varphi}{\rho_{p,eff}} \tag{5.26}$$

in which c is the concrete cover to reinforcement, k_1 and k_2 are coefficients accounting for the bond properties of the reinforcement and nature of the strain distribution respectively, φ is the diameter of the bars, and $\rho_{p,eff}$ is the effective reinforcement ratio $A_s/A_{c,eff}$, in which A_s is the area of steel in the effective tension area of concrete ($A_{c,eff}$). The complication arises from the two dimensional nature of the model not taking any account of the transverse spacing of longitudinal bars in the crack width predictions. In contrast, the bar diameter in the Eurocode calculation has a significant effect. To ascertain the effect the bar diameter has on the Eurocode calculation, and how the model predictions compare, two Eurocode crack widths have been calculated for each beam, a maximum and a minimum. The minimum is calculated using a value of φ = 1, and the maximum using a value of φ that results in a single bar being sufficient to make up the whole steel area. These maximum φ values are shown in Table 5.13.

Table 5.13 – φ values used in calculating maximum EC crack widths

A_s (mm2)	627	768	915	1070	1233	1407
φ (mm)	14.13	15.64	17.07	18.46	19.81	21.16

The maximum, minimum, and resulting average crack widths calculated according to Eurocode 2 and corresponding model predictions are shown in Table 5.14. In Table 5.14, the percentage difference column is calculated with respect to the average Eurocode 2 value.

Table 5.14 – Crack width comparison results

Beam ref	M_{ult} Utilisation (%)	M_{ap} (kNm)	Crack widths (mm)				Percentage difference (%)
			Eurocode 2 - min	Eurocode 2 - max	Average	Model	
50	50	50.2	0.139	0.225	0.182	0.181	-0.55
	60	60.2	0.178	0.289	0.234	0.217	-7.07
	70	70.3	0.218	0.353	0.286	0.25	-12.43
	80	80.3	0.257	0.416	0.337	0.281	-16.49
60	50	60.2	0.145	0.227	0.186	0.189	1.61
	60	72.3	0.183	0.288	0.236	0.223	-5.31
	70	84.3	0.222	0.349	0.286	0.254	-11.03
	80	96.4	0.260	0.409	0.335	0.284	-15.10
70	50	70.3	0.148	0.227	0.188	0.194	3.47
	60	84.3	0.186	0.284	0.235	0.226	-3.83
	70	98.4	0.224	0.342	0.283	0.257	-9.19
	80	112	0.260	0.398	0.329	0.286	-13.07
80	50	80.3	0.150	0.224	0.187	0.198	5.88
	60	96.4	0.187	0.279	0.233	0.229	-1.72
	70	112	0.223	0.333	0.278	0.259	-6.83
	80	128	0.260	0.388	0.324	0.289	-10.80
90	50	90.3	0.150	0.219	0.185	0.201	8.94
	60	108	0.185	0.272	0.229	0.231	1.09
	70	126	0.222	0.325	0.274	0.262	-4.20
	80	145	0.260	0.380	0.320	0.293	-8.44
100	50	100	0.148	0.213	0.181	0.203	12.47
	60	120	0.184	0.264	0.224	0.233	4.02
	70	141	0.221	0.318	0.270	0.265	-1.67
	80	161	0.256	0.369	0.313	0.295	-5.60

These results show that the model always predicts a crack width somewhere between the minimum and maximum Eurocode predictions, which suggests that the model is useful as a crack width predictor. Furthermore if the model is being used to predict the difference in crack width for similar beams with and without the LatConX system the model can be relied upon to provide suitable quantitative comparisons.

5.5 Conclusions

- A numerical model for long-term simulation of reinforced concrete beams and its coupling with a thermomechanical transient model for SMPs has been described.
- The full model has first been validated by comparison with two experimental datasets, close agreement was observed throughout both comparisons.
- Further to this, the crack widths predicted by the model have been compared with those calculated according to Eurocode 2 (BSI 2004), and found to be in agreement for all cases considered.
- Based on the above, the model described is considered suitable for simulating the long-term behaviour of both standard reinforced concrete sections, and those including the LatConX system. Thus predictions regarding the long-term performance of the LatConX system, and related conclusions can be confidently drawn.

Chapter 6 – LatConX – Long-term Predictions

In this Chapter the models developed in Chapter 4 and Chapter 5 are used to investigate and predict the long-term behaviour of beams designed incorporating the LatConX system. The main aim of the Chapter is to compare these predictions with those for beams conforming to current Eurocode 2 (BSI 2004) specifications subjected to the same conditions; from these comparisons, the advantages and disadvantages of the LatConX system as a design solution for various applications are assessed.

The first section of the Chapter discusses the additional factors that need to be considered when designing a beam incorporating the LatConX system to those usually considered for standard reinforced concrete beams. From these considerations an appropriate construction sequence is suggested along with the ultimate limit state checks required during this sequence.

New design equations are derived which are effectively modified forms of the currently accepted design equations which now take the moment and axial contributions of an activated SMP tendon into account.

Finally these design equations are used to design several sets of beams for two parametric investigations. Both investigations seek to compare the performance of the LatConX beams with that of those designed according to current practice. Further to this, a cost analysis has been undertaken assessing the material costs of each beam and once again comparing these with those of a standard reinforced concrete beam.

6.1 Design Considerations

The first step towards gaining a realistic understanding of the LatConX system's long-term behaviour is to develop a design procedure for LatConX elements based on the existing principles governing the design of reinforced concrete structures. This will ensure compliance with the accepted constraints of reinforced concrete design principles, and thus that any predictions made regarding the economic or structural performance of the LatConX system are realistic.

The aim of designing a structural element is to avoid any limit state being reached during the element’s design life; there are two key principal limit states that are considered in all structures, the ultimate limit state (ULS), and the serviceability limit state (SLS). ULS is usually the more critical of these two for reinforced concrete structures (Mosley et al. 2012), consequently elements are most commonly designed to satisfy ULS requirements before checks on their SLS suitability are carried out. A similar approach will be adopted throughout the two studies undertaken within this chapter. ULS design equations for reinforced concrete beams incorporating SMP tendons will be developed and utilised in the design of a range of beams. The behaviour of these beams will then be simulated using the numerical model developed in Chapter 5; firstly under ULS conditions, to check that design calculations and model predictions are in agreement, and secondly under SLS conditions, to investigate the behaviour of the beams under sustained serviceability loading. This is slightly different to the usual approach to SLS as this process is an investigation into the behaviour as opposed to a design or a check.

The designs and investigations presented in this Chapter are not exhaustive; only the flexural requirements of a simply supported beam, and the impact of the inclusion of the LatConX system, are considered.

6.1.1 Ultimate Limit State (ULS) Design - Criteria and Load Cases

As stated above, the initial design of a structural element should ensure satisfaction of ULS requirements; this refers to a structure’s ability to withstand the actions for which it is intended with an adequate factor of safety against collapse (Mosley et al. 2012). According to Eurocode 2 (BSI 2004) the design value of actions on a structure at ULS (E_d) is given by Equation (6.1):

$$E_d = 1.35\ G_k + 1.5\ Q_k \tag{6.1}$$

in which G_k and Q_k are the total values of any permanent and variable actions for the load case considered respectively.

An important criterion in reinforced concrete design is that any flexural failure of an element is initiated through yielding of the tension reinforcement, ensuring a ductile failure (i.e an under-reinforced concrete beam).

The alternative to this would be failure initiation through concrete crushing; this is likely to result in a potentially dangerous, sudden brittle failure of the concrete in compression. A ductile failure is ensured by limiting two design values; the neutral axis depth at failure, and the area of tension steel provided. Eurocode 2 (BSI 2004) Clause 5.6.3 sets the limiting value for the neutral axis depth as $x_u/d < 0.45$ for concrete strength classes less than or equal to C50/60. The limiting moment of resistance for any section (M_{bal}) is that which theoretically results in failure of the section through steel yielding and concrete crushing simultaneously; it is therefore the maximum safe moment of resistance for any given section. M_{bal} is given by Equation (6.2).

$$M_{bal} = 0.167 f_{ck} b d^2 \tag{6.2}$$

in which 0.167 is a factor taking account of the combination of the neutral axis depth, a simplification relating to the depth of the concrete stress block ($s = 0.8x$ in which s is the depth of the concrete stress block), and the partial factors relevant to the characteristic compressive strength of concrete; f_{ck} is the characteristic compressive strength of concrete, b is the width of the section, and d is the depth of the section. The value of M_{bal} must exceed that of the design moment M_d otherwise the section size must be increased to allow the design of an under-reinforced section. Adherence to these criteria ensures that the maximum moment capacity of the steel is less than that of the concrete, and thus a ductile failure through steel yielding. The area of tension steel required is determined from equation (6.3).

$$A_s = \frac{M_d}{0.87 f_{yk} z} \tag{6.3}$$

The need to ensure under-reinforcement of a section means that polymer tendons cannot simply be added to the cross section of a pre-designed beam, as this may render the section over-reinforced upon activation. Hence the design equations must be modified to account for the activated stress contribution of any polymer to the cross sectional behaviour.

The implications of the considerable difference in moment resistance provided by the polymer tendons pre- and post-activation (due to the large stress change) will need to be considered in any design process. As the maximum moment resistance of a beam will not be available until activation it seems logical to limit the applied moment until this time, hence it is suggested that activation should take place after the permanent actions are present but before any variable actions are applied. The implications of this approach will need to be assessed on a case by case basis to ensure the tension steel provided is sufficient to resist the ULS moment from permanent actions.

A final design consideration stems from the “active” nature of the moment resistance provided by the polymer tendons. Unlike standard reinforcement, which remains unstressed until a moment is applied to the beam, any eccentric activated polymer tendons will apply a hogging moment to the beam. The hogging moment due to activated polymer action is given by Equation (6.4).

$$M_p = A_p z_p \sigma_p \gamma_{p,unfav} \tag{6.4}$$

where A_p is the area of polymer, z_p is the polymer eccentricity, σ_p is the shrinkage stress of the polymer, and $\gamma_{p,unfav}$ is a factor that Eurocode 2 (BSI 2004) recommends the use of in situations where the actions due to prestressing are unfavourable. The recommended value for $\gamma_{p,unfav}$ is 1.3 given in Clause 2.4.2.2.

This hogging moment will have the most onerous effect on a beam when applied moments are at a minimum. The minimum applicable applied moment after polymer activation is that due to permanent actions, which in the majority of cases will exceed M_p. Further to this, at least two bars will be required at the top of any reinforced concrete beam to give the cage stability. In all beams studied in this Chapter two 16 mm diameter bars have been used in the top face (A_s' = 402 mm^2). The most onerous polymer moment for these top bars to resist will be for the beam with the largest polymer force; this is the polymer force in the "Poly Max" beam described in the second parametric study of Section 6.6 below. Making use of Equation (6.4), M_p for this beam is found to be 218 kNm, giving a resultant moment after the unfactored permanent moment (Table 6.3) is removed of 52.4 kNm. M_R for a section with b = 350 mm, d = 547 mm, and A_s = 402 mm^2 (top steel is tension steel in this case) is 93 kNm, thus the two 16 mm diameter bars provide sufficient top reinforcement to resist the worst case polymer moment expected during construction of any of the beams presented in the parametric studies that follow. In the calculations above, the axial contribution of the SMP tendon has been ignored for simplicity; this is a conservative approach as the compressive force applied by the SMP tendon would increase the hogging capacity of the beam and is thus deemed an acceptable simplification.

Taking the above considerations into account, the recommended construction sequence for a LatConX structure, and the way in which this sequence is simulated by the model is described in Table 6.1.

Table 6.1 - Construction sequence and resulting model considerations

Time from t_0 (days)	Real life event	Model event	Relevant algorithms/Equations
0-3	Concrete is curing	No functions active	NA
3	Concrete is considered solid	Thermal strain applied	Equation (5.12)
3-5	Time-dependent processes active	Creep, shrinkage, and polymer functions are active, and resulting changes in beam configurations are computed for each incremental time step.	Table 5.3 - Table 5.7
5	Formwork removed	Permanent moment applied	Table 5.7
5-6	Time-dependent processes active	Creep, shrinkage, and polymer functions are active, and resulting changes in beam configurations are computed for each incremental time step.	Table 5.3 - Table 5.7
6-7	Polymer tendons activated	Time-temperature path incorporating a one hour soak time is applied to the beam model. Creep, shrinkage, and polymer functions are active throughout, and resulting changes in beam configurations are computed for each incremental time step.	Table 5.3 - Table 5.7
7	Structure is considered ready for full loading	Variable moment applied	Table 5.7
7-3650 (ten years)	Time-dependent processes active	Creep, shrinkage, and polymer functions are active, and resulting changes in beam configurations are computed for each incremental time step.	Table 5.3 - Table 5.7

6.1.2 Serviceability Limit State (SLS) Investigations - Criteria and Load Cases

As mentioned earlier, a reinforced concrete element that has been designed and deemed adequate to satisfy ULS requirements should also be checked for compliance with SLS requirements. According to (Mosley et al. 2012), the key SLS criteria to check are:

- Deflections should not be large enough to affect the appearance or efficiency of any part of the structure, or adversely impact upon the comfort of the building's users.
- Cracking should be limited so that any local damage caused does not affect the appearance efficiency or durability of the structure.
- The structure must be sufficiently durable to adequately last for the duration of its proposed life while being subject to its exposure conditions.

As the LatConX system has been designed with crack size limitation and/or closure as a primary objective this will be used as the performance indicator in the SLS investigation throughout this Chapter.

Eurocode 2 (BSI 2004) Clause 7.3 sets out the serviceability requirements relating to crack widths, with Table 7.1N recommending a value of 0.3 mm under the quasi-permanent action combination as the maximum permissible crack width. The design value of the total quasi-permanent action is shown in Equation (6.5).

$$E_d = G_k + \Psi_2 Q_k \tag{6.5}$$

in which Ψ_2 is the quasi-permanent load factor selected in conjunction with the category of loading applied according to Eurocode 1 (BSI 2002) Table 6.1 and Eurocode 0 (BSI 2006b) Table A1.1.

The procedure for calculating the maximum crack width according to Eurocode 2 (BSI 2004) is summarised in Appendix B. This procedure would normally be used to check a beam's compliance with the maximum permissible crack width restriction. However the procedures for calculating crack widths in reinforced concrete and prestressed concrete are different and no direct guidance is given as to how they should be combined in situations such as those investigated in this thesis. Therefore the model developed in Chapter 5 will be relied upon for the prediction of the long-term crack widths of all beams.

A benefit of this use of the model for crack width prediction is that the full construction sequence will be simulated. This will give accurate predictions as to the effects of the interactions of all applied actions, and behaviour phenomena of the different materials through the full life of the structural element, thus allowing easy observation of the expected crack development with time as well as the effects of polymer activation. The construction sequence simulated is that described in the ULS considerations section above, and shown in the flow chart of Table 6.1.

6.2 Parametric Consistencies

To ensure that the results of the different studies and their respective beam designs can be reasonably compared several properties and parameters relating to the beam designs and simulations have been set and kept constant throughout the two studies presented in this Chapter.

6.2.1 Design Scenario

An externally exposed, cast insitu reinforced concrete beam exposed to loading in accordance with category C2 from Table 6.2 in Eurocode 1 has been selected. Table 6.1 defines this loading as “Areas where people may congregate with fixed seats e.g. churches, theatres or cinemas” (BSI 2002). This is considered a relatively standard application for a reinforced concrete beam. A supported floor of width 6 m, slab thickness of 0.2 m, and an additional 0.05 m of screed have been assumed, with the applied actions derived from these. The design criteria, and design moments (SLS and ULS) for all designs are displayed in Table 6.2 and Table 6.3.

Table 6.2 – Design criteria

Design life (years)	Exposure class	Span (m)	Concrete class	Cover (mm)
50	XC3	6	C30/37	35

Table 6.3 – Design moments and their derivation

	Unfactored UDL (kN/m)	**Unfactored moment (kNm)**	**Factors**		**Factored moments**	
			SLS	**ULS**	**SLS (kNm)**	**ULS (kNm)**
Permanent	36.8	165.6	1.0	1.35	165.6	223.6
Variable	20.0	90.0	0.6	1.5	54.0	135.0
Total applied moments					**SLS**	**ULS**
					219.6	358.6

6.2.2 Material Properties and Factors

In the parametric studies that follow, characteristic values were used for the material strengths in the design equations as is standard practice. However in the model simulations mean values were used as the material strengths.

Characteristic values are defined as the strength values that 95 % of all material samples will exceed, therefore their use in the design of structural elements ensures a conservative approach. However, considering this definition, it is unlikely that all materials will have strength values corresponding to the characteristic values in a real situation. In the simulation of the behaviour of a composite material such as reinforced concrete, the relative differences between the individual material properties are expected to have a significant impact on the simulation results. Thus it is important that as far as possible, the values used are those likely to exist concurrently for the different materials. It is for this reason that mean values have been used in the model simulations throughout this chapter as they are by definition those most likely to occur.

The characteristic material properties used for all designs, and corresponding mean values used in the model simulations are those shown in Table 6.4.

Table 6.4 – Characteristic and mean material strength values

	f_c (MPa)	f_t (MPa)	f_y (Reinforcement steel) (MPa)	f_y (prestressing steel) (MPa)
Characteristic	30	NA	500	1468
Mean	38	2.9	580	1689

The implications of using different values for the model simulations to those used in the design equations differ depending on which limit state is considered. At ULS, the moment capacity of a beam predicted by the model is expected to increase considerably from the design moment as the design equations are heavily reliant on the values used for the material strengths. At SLS, the use of mean values is not expected to affect the suitability of the crack width predictions. Inspection of the Eurocode 2 (BSI 2004) procedure for the calculation of crack widths (See appendix B) reveals that the only material properties required are the mean tensile strength of the concrete and the Young's modulus of the steel and concrete, all of which are unchanged in the model simulations, thus at SLS, the crack width predictions of the model are expected to be close to those from Eurocode 2 (BSI 2004).

The partial material factors for the polymer (γ_p), steel (γ_s), and concrete (γ_c), and an additional factor (α_{cc}) allowing for long-term effects in the concrete are shown in Table 6.5; with the exception of γ_p, all values are taken from Table 2.1N of Eurocode 2 and Clause 3.1.6 of the UK National Annex to Eurocode 2 (BSI 2004). The partial factor γ_p has been taken as 1.15, the partial factor appropriate for prestressing materials.

Table 6.5 – Material factors applied to characteristic materials properties in design process

γ_p	γ_s	α_{cc}	γ_c
1.15	1.15	0.85	1.5

6.2.3 Model Simulations

6.2.3.1 Simplifications

There are two minor simplifications that have been utilised in all model simulations.

The first of these is that the steel and polymer areas used are exactly those required for precise satisfaction of the design equations, they are not rounded up to an area provided by the appropriate number of bars of a certain diameter. This approach has been taken with the intention of providing quantitative predictions for the effects of varying areas of polymer and steel, thus, for this purpose it is preferred to assume that these areas are continuous rather than discrete variables.

The second simplification, implemented with similar reasoning to the first, is that the polymer tendons and steel reinforcement are always located at the same effective depth (d) with no consideration made for the available width for a single layer of bars/tendons. Clearly this is not realistic for all of the beam designs, however for the purpose of these studies a constant value of d was deemed more important than meticulous consideration of the reinforcement detailing.

6.2.3.2 Parameters

Consistent environmental conditions for the creep, shrinkage, and thermal functions used in the model have been set; these are displayed in Table 6.6.

Table 6.6 – Environmental conditions for model functions relating to creep, shrinkage, and thermal strains

Thermal			Shrinkage and creep	
T_1 (°C)	T_2 (°C)	α_c	RH (%)	t_s (days)
28	0	12×10^{-6}	80	3

Further to these, the other model parameters which remain constant in all simulations are summarised in Table 6.7.

Table 6.7 – Constant model parameters for all simulations

E_c (GPa)	E_s (GPa)	α_c	α_p	u_0 (mm)	w_c (mm)
33	200	12.0×10^{-6}	15.8×10^{-6}	0.25	100

Unless otherwise stated, the material properties relating to the LTMx2 polymer constitutive model are those given in Table 4.4.

6.3 Derivation of Design Equations

The equations for the design of under-reinforced concrete beams containing both steel and activated SMP will now be developed.

Prior to activation, the addition of any polymer tendons is considered to have a negligible effect on the behaviour of a reinforced concrete beam, accordingly the design equations developed herein are only relevant post-activation of the polymer. The current Eurocode 2 (BSI 2004) approach to ULS design can be adopted for any consideration of a beam prior to activation; indeed, if the value for σ_p is taken as 0 in the equations developed below, the ULS design will exactly follow Eurocode 2.

The expressions for axial and moment equilibrium in a cross section containing both steel reinforcement and activated polymer are given by Equation (6.6) and (6.7) respectively, where moments have been taken about the mid-height of the section. Additional polymer stress due to strain changes induced by mechanical loading has been ignored in these expressions. This is considered a reasonable simplification due to the low Young's modulus of the polymer relative to steel.

$$\frac{\sigma_p}{\gamma_p} A_p + \frac{f_{yk}}{\gamma_s} A_s = 0.8 \frac{\alpha_{cc} f_{ck}}{\gamma_c} bx \tag{6.6}$$

$$M_{ap} = \left(\frac{\sigma_p}{\gamma_p} A_p + \frac{f_{yk}}{\gamma_s} A_s\right)\left(d - \frac{h}{2}\right) + 0.8 \frac{\alpha_{cc} f_{ck}}{\gamma_c} bx \left(\frac{h}{2} - 0.4x\right) \tag{6.7}$$

Introducing the values for γ_p, γ_s, α_{cc}, and γ_c shown in Table 6.5, rearranging Equation (6.6), and substituting into Equation (6.7) yields a quadratic in x:

$$0 = 0.181 f_{ck} bx^2 - 0.453 f_{ck} bdx + M_{ap} \tag{6.8}$$

Solution of this via the quadratic formula (shown in (6.9)) yields the depth of the neutral axis for any applied moment.

$$x = \frac{-B - \sqrt{B^2 - 4AC}}{2A} \tag{6.9}$$

in which:

$$A = 0.181 f_{ck} b \qquad B = -0.453 f_{ck} bd \qquad C = M_{ap}$$

with a limit of $x \leq 0.45d$ applied in accordance with Eurocode 2 Clause 5.6.3 (BSI 2004).

Making use of this x value, with a further rearrangement of Equation (6.6) the required area of steel for a set polymer area can be found; this is shown in Equation (6.10).

$$A_s = \frac{0.521 f_{ck} bx - \sigma_p A_p}{f_{yk}} \tag{6.10}$$

6.4 Cost Analysis

One potential benefit of the proposed LatConX system is the possibility for a reduction in the amount of reinforcement steel required without compromising a structure’s compliance with Eurocode 2 (BSI 2004) requirements. To analyse the extent of any cost reduction stemming from this reduction in reinforcing steel, a cost analysis has been undertaken on the beams designed throughout this Chapter; the results of this are presented at the relevant points in the forthcoming sections. The material costs and other properties required to convert these costs into useable values are displayed in Table 6.8 along with references for the data source in each case.

Table 6.8 – Material costs and relevant properties used in cost analysis

Material	Concrete	Steel		Polymer
Details	Grade C30 – 20mm aggregate	High yield steel, bent bars, ϕ = 25mm	Strands of prestressing wire to BS 5896	Polypropylene/PET – raw material
Unit	m^3	Tonne	Tonne	Tonne
Unit cost	£ 89.8	£ 620	£ 423	£ 604 (+ 10 %)
Density	NA	78 kN/m^3	78 kN/m^3	6.4 kN/m^3
Reference	(Davis Langdon LLP 2012)	(Davis Langdon LLP 2012) and Eurocode 1 Table A.4 (BSI 2002)	(http://www.alibaba.com 2014)	(http://www.alibaba.com 2014)

Some of the unit costs displayed in Table 6.8 were only available in US$, these costs have been converted to GBP (£) using an exchange rate of 0.6045 GBP (£) to the US$ (http://www.xe.com/ 2014).

As shown in Table 6.8, an additional 10 % has been added to the raw material cost for the polymer material; this is an estimate to account for the manufacturing process required.

At points during the studies presented in this Chapter steel reinforcement with non-standard yield stresses are used, the costs for these have been assumed equal to that for the high yield steel shown in Table 6.8.

6.5 Parametric Study 1

In the first study, each beam has been designed so that its ultimate moment of resistance is precisely adequate to resist the ULS moment shown in Table 6.3. In each set of beams the first beam is designed according to current Eurocode 2 procedures, i.e. using just steel as the means of moment resistance. In the remaining beams, the area of polymer provided is increased from 0.5 % of the effective concrete area ($A_{ef} = b \times d$), in 0.5 % increments, until the maximum polymer area is reached. The maximum polymer area is reached when either the total area of steel and polymer exceed the 4 % limit Eurocode 2 Clause 9.2.1.1 (BSI 2004), or the increase in polymer area results in the steel area reducing below that required to resist the ULS permanent moment.

6.5.1 σ_p = 40 MPa, f_{yk} = 500 MPa

Other members of the same research group as the author have carried out further work into polymeric materials specifically designed for the purpose of the LatConX system since the research contained in Chapter 3 was conducted, thus higher shrinkage stresses have been achieved. The maximum shrinkage stress achieved at the time of writing this thesis was approximately 40 MPa, this will therefore be used as the polymer stress for the first set of beam designs in this study.

A section size of 350 mm x 550 mm was selected and confirmed sufficient for an under-reinforced beam to resist the total ULS moment. From here, the designs shown in Table 6.9 were produced using the designated polymer areas, and Equations (6.8) and (6.10).

Table 6.9 – Beam designs for f_{yk} = 500 MPa, σ_p = 40 MPa

Beam ref	b (mm)	d (mm)	A_p (mm^2)	A_s (mm^2)	ρ (%)
EC2	350	497	0	1948	1.1
Poly 0.5	350	497	865	1879	1.6
Poly 1.0	350	497	1731	1810	2.0
Poly 1.5	350	497	2596	1741	2.5
Poly 2.0	350	497	3462	1671	3.0
Poly 2.5	350	497	4327	1602	3.4
Poly 3.0	350	497	5192	1533	3.9

For this section size a minimum steel area of 1135 mm^2 is required to resist the ULS permanent moment, thus all designs are adequate for this condition.

The creep calibration and resulting model parameters for these designs are shown in Figure 6.1 and Table 6.10 respectively.

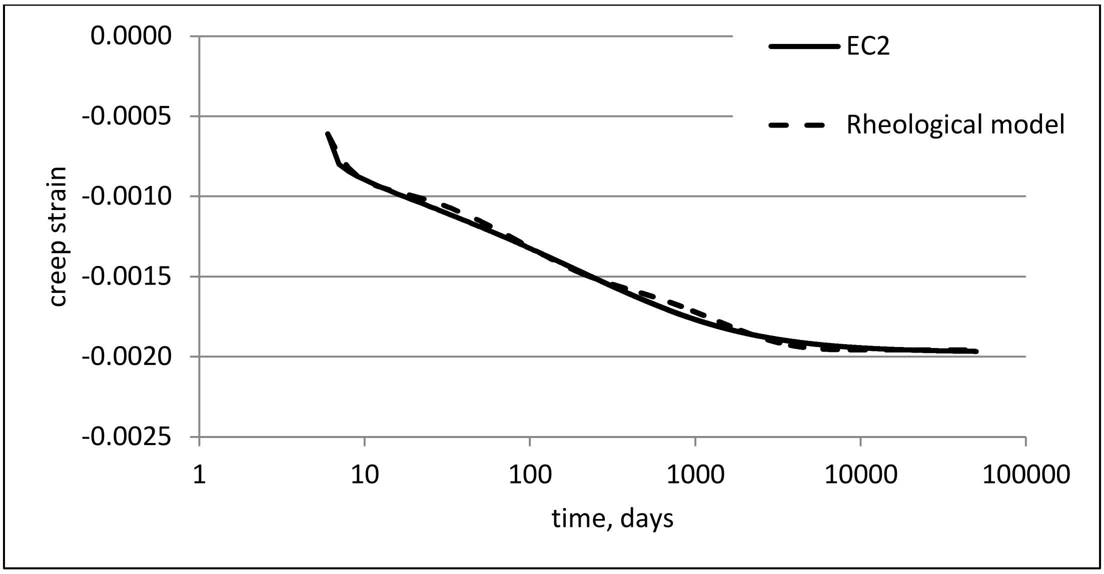

Figure 6.1 - Creep calibration for concrete cross section of 350 mm x 550 mm

Table 6.10 – Creep model parameters for concrete cross section of 350 mm x 550 mm

Arm number	1	2	3	4
β_c	0.311	0.336	0.253	0.1
τ_c (days)	NA	1	50	1000

6.5.1.1 ULS Behaviour

Figure 6.2 shows the predicted moment curvature relationships for each of the beams throughout the proposed construction sequence as described in Table 6.1, although after activation the beams are loaded beyond the total ULS moment to demonstrate their failure behaviour.

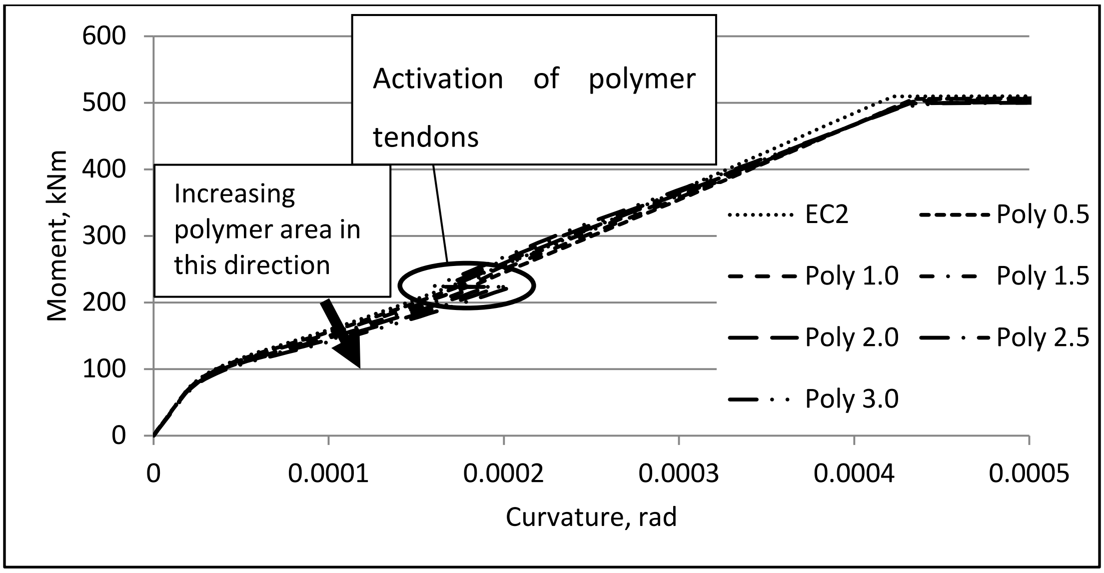

Figure 6.2 – ULS simulation results for beams designed with f_{yk} = 500 MPa and σ_p = 40 MPa

As would be expected, up to approximately 60 kNm the moment curvature relationship is linear and almost identical for all beams, from here the concrete begins to crack and the behaviour of the different beams diverges a little. The sections appear to be fully cracked once the applied moment reaches approximately 110 kNm at which point the relationships becomes linear again, with the gradient of each line representing the flexural stiffness of each beam. The stiffness of the beams decreases as the polymer area increases, this is due to the corresponding decrease in steel area. This decreasing stiffness with increasing polymer area causes the Eurocode beam to display the smallest curvature for any applied moment up to the ULS permanent moment of 223.6 kNm.

There are two reasons for this proportionality. Firstly and more significantly, it is the result of the ratio of Young's moduli for the reinforcing steel and polymer (0.03) being lower than the ratio of the stresses used in the design calculations i.e. steel yield stress and polymer shrinkage stress (0.08). As the polymer area increases the steel area decreases according to the stress ratio thus maintaining an unchanged moment of resistance, whereas the stiffness of the beam is a function of the Young's moduli ratio and therefore reduces with increasing polymer area. Secondly, the change in strain applied to the steel by any increase in curvature is larger than that applied to the polymer tendons, since the latter are unbonded.

At this point the polymer is activated; causing the step reduction in curvature with no change in applied moment observable in Figure 6.2. As the polymer area increases, the size of this step in curvature also increases.

The applied moment is then increased until failure occurs; this is defined as the point at which the curvature increases significantly with no corresponding increase in applied moment. As the moment increases up to the point of failure, the relationships are once again linear with the flexural stiffness of a beam proportional to the area of reinforcing steel provided. The moment, and curvature at failure is very similar for all beams, the maximum failure moment is approximately 510 kNm for the EC2 beam, whilst the minimum is approximately 494 kNm for the Poly 3.0 beam. Generally, as the polymer area increases, the failure moment exhibits a slight decrease; this is the case despite the beams having all been designed for the same ULS moment. There are two reasons for the variation. The first is the use of mean values instead of characteristic values for the material properties and omission of partial factors in the model predictions. This has an effect because the ratio of steel yield stress to polymer shrinkage stress governs the relationship between the areas of polymer and steel provided, this ratio increases when mean values are used. Thus the area of steel would also need to increase for the failure moment to remain unchanged. The second reason for the variation in failure moments is the simplification within the design equations that any stress contributions from mechanical strains applied to the polymer are ignored.

6.5.1.2 SLS Behaviour

Figure 6.3 shows the predicted long-term behaviour for each of the beams as a result of the construction sequence described in Table 6.1. The applied moments at each stage are those calculated using quasi permanent factors i.e. the SLS moments from Table 6.3. These predictions have been plotted using a logarithmic scale for the time axis to allow clearer observation of the early age behaviour.

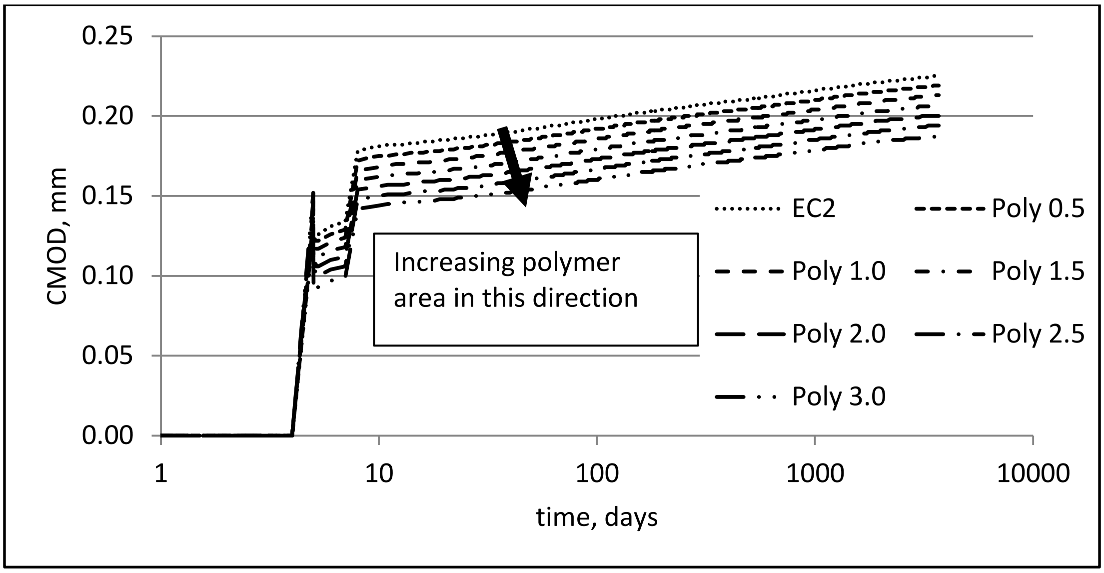

Figure 6.3 - SLS simulation results for beams designed with f_{yk} = 500 MPa and σ_p = 40 MPa

Upon application of the permanent moment, cracking first occurs; the size of this initial crack increases with increasing polymer area from approximately 0.13 mm for the EC2 beam, to approximately 0.15 mm for the Poly 3.0 beam. This increase is due to the decreasing area of steel with increasing area of polymer, which is at this stage unactivated, thus providing a negligible contribution towards the prevention of cracking. The polymer tendons are then activated giving a reduction in crack widths; the magnitude of this reduction increases with increasing area of polymer. From this point, crack widths continue to increase at a similar rate in all beams due to the effects of creep and shrinkage of the concrete, and relaxation of the polymer stress, until the quasi-permanent variable moment is applied at which point all cracks are seen to grow by a similar amount, approximately 0.05 mm. Finally the crack widths for all beams continue to grow logarithmically at similar rates.

The predicted ten year crack widths decrease with increasing polymer area according to what appears to be a linear relationship; the predicted crack width for the EC2 beam is 0.23 mm, this reduces by approximately 0.007 mm or 2.7 % for each incremental increase in polymer area. The crack width reduction for the Poly 3.0 beam is approximately 0.04 mm or 17 %.

The simulations presented above demonstrate that beams utilising a combination of shrinkable SMPs tendons with a shrinkage stress of 40 MPa, and reinforcing steel can be conveniently designed to conform to Eurocode 2 (BSI 2004) requirements. It has also been shown that the long-term crack widths expected in these beams can be reduced by up to 17 % when compared with beams designed with reinforcing steel alone.

6.5.2 σ_p = 100 MPa, f_{yk} = 500 MPa

Having demonstrated the potential capabilities of a LatConX beam using the currently available polymer shrinkage stress, an identical study will now be presented however with the polymer shrinkage stress increased to 100 MPa. This is considered to be a realistically attainable shrinkage stress according to Long and Ward (Long and Ward 1991) given the correct material properties and drawing conditions.

The applied moments and neutral axis limitations are unchanged, thus the same section size of 350 mm x 550 mm is adequate. Using the same designated polymer areas and Equations (6.8) and (6.10) as before the designs in Table 6.11 were established.

Table 6.11 - Beam designs for f_{yk} = 500 MPa, σ_p = 100 MPa

Beam ref	b (mm)	d (mm)	A_p (mm^2)	A_s (mm^2)	ρ (%)
EC2	350	497	0	1948	1.1
Poly 0.5	350	497	865	1775	1.5
Poly 1.0	350	497	1731	1602	1.9
Poly 1.5	350	497	2596	1429	2.3
Poly 2.0	350	497	3462	1256	2.7
Poly 2.5	350	497	4327	1083	3.1
Poly 3.0	350	497	5192	910	3.5
Poly 3.5	350	497	6058	737	3.9

As the polymer area for each beam is set, these have not changed from the previous designs shown in Table 6.9; however due to the increased shrinkage stress, the reduction in the area of reinforcing steel for each increase in polymer area is greater. This results in a lower maximum polymer area for an acceptable design due to the limitation imposed by the requirement that the reinforcing steel alone be adequate to resist the permanent ULS moment. As in the previous set of designs the minimum steel area is 1135 mm^2, therefore only the designs with a polymer area of 2 % or less are acceptable. In a genuine design scenario the polymer area could be increased slightly to reduce the steel area to precisely 1135 mm^2 however for the purpose of the parametric study undertaken here this has not been considered.

6.5.2.1 ULS Behaviour

The moment-curvature relationships for the relevant beams from Table 6.11 can be observed in Figure 6.4.

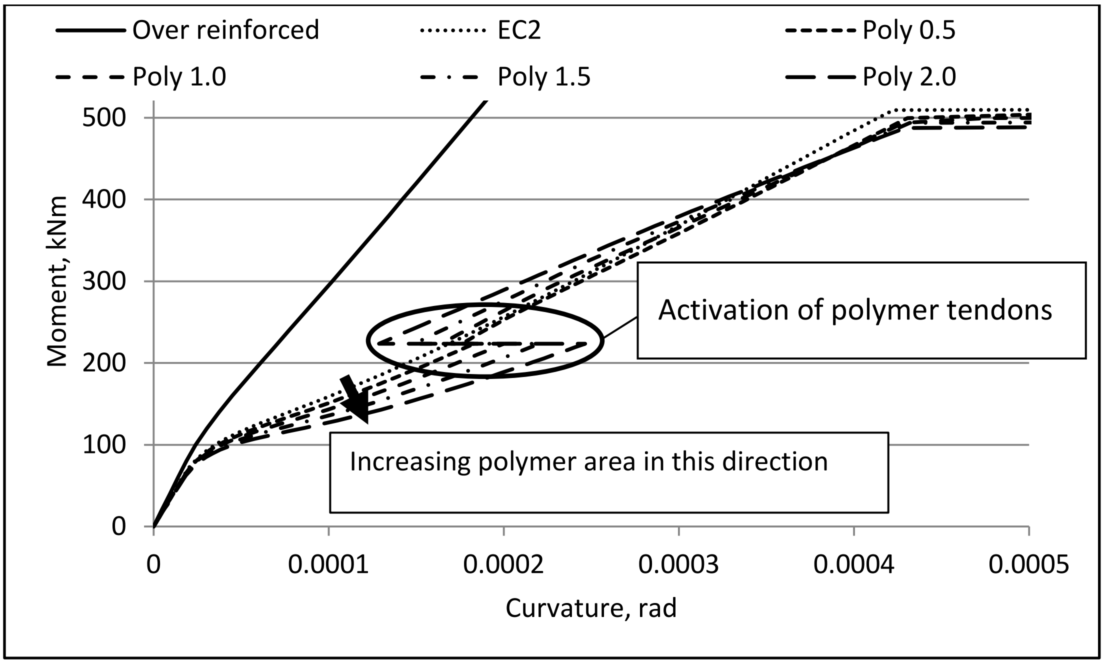

Figure 6.4 - ULS simulation results for beams designed with f_{yk} = 500 MPa and σ_p = 100 MPa

Similar trends to those described in detail for the ULS results of the beams designed with a polymer shrinkage stress of 40 MPa (Figure 6.2) can be clearly seen. However due to the increased ratio of the polymer shrinkage stress to reinforcing steel yield stress (0.2), and therefore greater reduction in the area of reinforcing steel for each incremental increase in polymer area the reduction in stiffness for each increase in polymer area is larger, this is true for the behaviour both before and after polymer activation.

6.5.2.2 SLS Behaviour

As with the ULS behaviour, the SLS predictions displayed in Figure 6.5 show similar trends to those observed for the beams designed with a polymer shrinkage stress of 40 MPa (Figure 6.3).

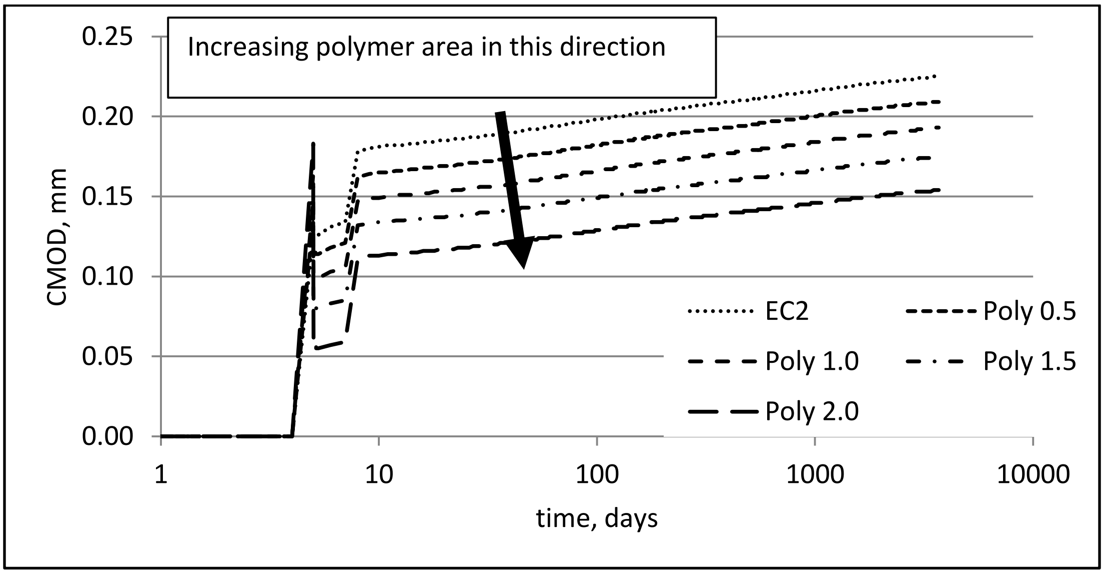

Figure 6.5 - SLS simulation results for beams designed with f_{yk} = 500 MPa and σ_p = 100 MPa

Once again ten year crack widths are reduced, with the size of the reduction increasing as the polymer area increases. In the Poly 2.0 beam, a reduction of 32 % is observed. This is a significant increase on the maximum reduction of 17 % achieved in the set of beams using a polymer shrinkage stress of 40 MPa.

The predictions presented above suggest that if a shrinkage stress of 100 MPa can be achieved for the polymer tendons then the LatConX system will be capable of significantly reducing long-term crack widths in reinforced concrete members, while at the same time reducing the amount of reinforcing steel required and replacing it with relatively inexpensive polymer material.

6.5.3 σ_p = 100 MPa, f_{yk} = 1468 MPa

Having shown that the LatConX system is capable of limiting crack widths in reinforced concrete beams complying with Eurocode 2 (BSI 2004) some further potential applications for the system will now be investigated. One such application worth closer inspection is the idea of utilising the higher maximum stress of prestressing wire (f_{yk} = 1468 MPa) ((BSI 2012)), instead of high yield reinforcing steel (f_{yk} = 500 MPa) to satisfy the ULS requirements with a substantially reduced steel area. Steel of this type cannot usually be used because it has the same Young's modulus as high yield reinforcing steel, thus the substantially reduced area results in an equally substantial reduction in flexural stiffness, and hence very large crack widths and a failure of SLS requirements. As it has now been shown that the LatConX system can reduce long-term crack widths significantly, it is suggested that a combination of Bridon prestressing wire with the LatConX system will be capable of conforming to both ULS and SLS requirements. If this hypothesis proves correct, it is anticipated that the reduced areas of steel will result in significant savings in the material cost of the beams compared to those designed using the current methods.

A similar parametric study to those carried out for high yield steel above will now be undertaken for this case.

6.5.3.1 Modifications to Design Criteria

Due to the differing stress-strain behaviour between reinforcing steel and prestressing steel some alterations to the design criteria are required. Both steel types have the same Young's modulus; however the yield stress of prestressing steel is significantly higher than reinforcing steel. The benefit of this is that a smaller area of steel can be used to provide the same tensile force (and therefore moment of resistance) at yield. However the increased yield stress with an unchanged Young's modulus results in an increased yield strain, therefore in order to maintain a ductile failure the limiting depth of the neutral axis must be modified.

For concrete class ≤ C50/60 at ULS the maximum compressive strain is ε_{cu2} = 0.0035 (Eurocode 2 - Table 3.1 - (BSI 2004)). The yield strain for prestressing wire is calculated as shown in equation (6.11).

$$\varepsilon_{yk} = \frac{F_{p0.1}}{EA\gamma_s} \tag{6.11}$$

in which $F_{p0.1}$ is the characteristic 0.1 % proof force, A is the cross-sectional area, and E is the modulus of elasticity, all of which are taken from BS 5896:2012 (BSI 2012); and γ_s is the partial factor for steel taken as 1.15. Thus ε_{yk} = 0.0064.

Assuming that plane sections remain plane and that there is strain compatibility between the steel and concrete, the relationship between the steel and concrete strains (ε_s and ε_c respectively) and the neutral axis depth can be written as:

$$\frac{d-x}{x} = \frac{\varepsilon_s}{\varepsilon_c} \tag{6.12}$$

Rearranging Equation (6.12) and substituting ε_{yk} and ε_{cu2} for the steel and concrete strains gives the maximum neutral axis depth for an under-reinforced beam:

$$x = \frac{d}{1+\frac{\varepsilon_{yk}}{\varepsilon_{cu2}}} \quad \therefore x = 0.35d \tag{6.13}$$

In accordance with Eurocode practice this should be further limited (Mosley et al. 2012), in this case to a value of $x \leq 0.3d$. This is to allow for factors such as strain hardening of the steel, and ensure adequate rotation of plastic hinges and thus moment redistribution.

A section size of 350 mm x 600 mm was selected and confirmed sufficient for a beam complying with these modified neutral axis limitations to resist the total ULS moment shown in Table 6.3. From here, the designs shown in Table 6.12 were produced using the designated polymer areas shown and Equations (6.8) and (6.10).

Table 6.12 - Beam designs for f_{yk} = 1468 MPa, σ_p = 100 MPa

Beam ref	b (mm)	d (mm)	A_p (mm^2)	A_s (mm^2)	ρ (%)
EC2	350	547	0	577	0.3
Poly 0.5	350	547	961	511	0.8
Poly 1.0	350	547	1921	446	1.2
Poly 1.5	350	547	2882	380	1.7
Poly 2.0	350	547	3843	315	2.2

Since the polymer area for each beam is set to the fixed values used in the previous designs (Table 6.9 and Table 6.11); however due to the increased steel yield stress, the steel area required for each design is reduced. The minimum steel area to resist the permanent ULS moment is now 342 mm^2, therefore any design with a polymer area greater than 1.5 % is not acceptable. As with the beam designs with f_{yk} = 500 MPa and σ_p = 100 MPa, in a genuine design scenario the polymer area could be increased slightly to reduce the steel area to precisely 342 mm^2 however for the purpose of the parametric study undertaken here this has not been considered.

The creep calibration and resulting parameters for this section are shown in Figure 6.6 and Table 6.13 respectively.

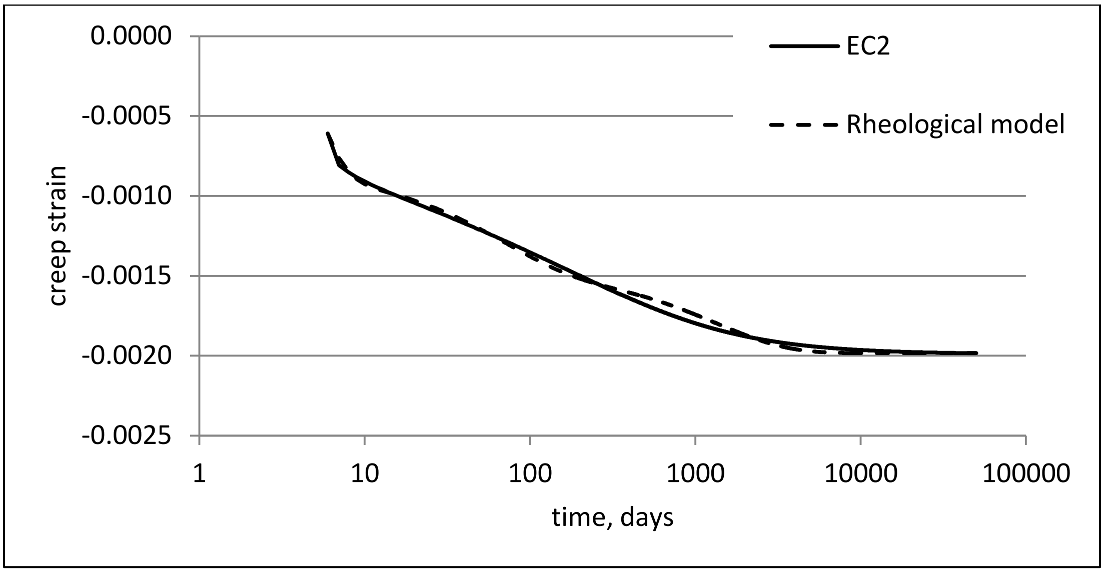

Figure 6.6 - Creep calibration for concrete cross section of 350 mm x 550 mm

Table 6.13 - Creep model parameters for concrete cross section of 350 mm x 550 mm

Arm number	1	2	3	4
β_c	0.307	0.343	0.250	0.1
τ_c (days)	NA	0.8	40	1000

6.5.3.2 ULS Behaviour

The moment-curvature relationships for the relevant beams from Table 6.12 are shown in Figure 6.7. Once again, the behaviour and trends are similar to those displayed in the previous ULS simulations (See Figure 6.2 and Figure 6.4) however due to the further reduced steel areas the reduction in stiffness for each increase in the area of polymer is more notable.

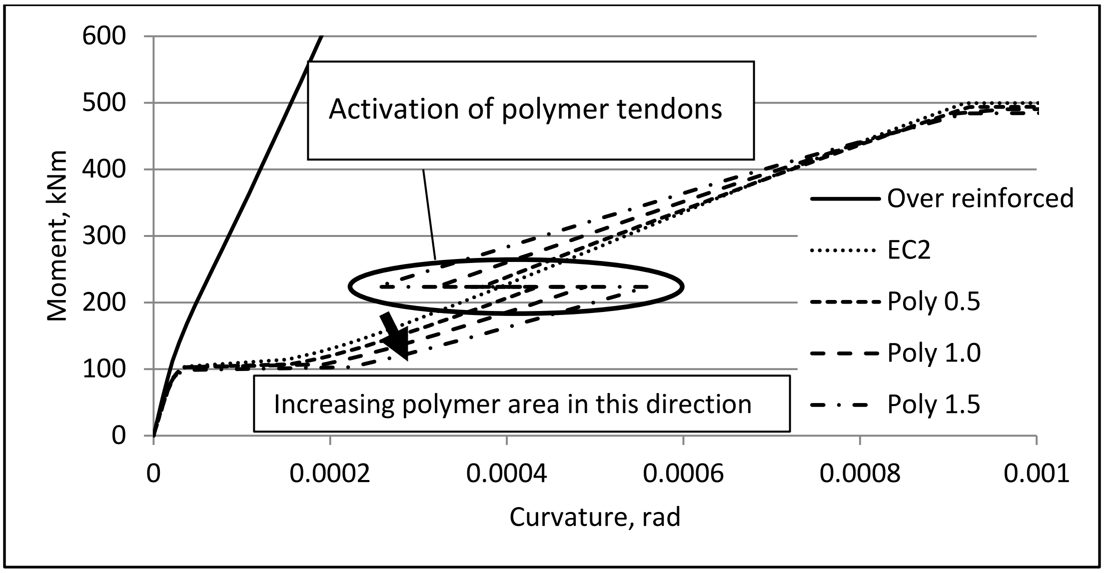

Figure 6.7 - ULS simulation results for beams designed with f_{yk} = 1468 MPa and σ_p = 100 MPa

6.5.3.3 SLS Behaviour

Once again, as with the ULS behaviour, the SLS predictions displayed in Figure 6.8 show similar trends to those observed in Figure 6.3, and Figure 6.5; however as expected the crack widths are significantly increased due to the substantial reduction in steel area for each beam.

The 10 year crack width for the EC2 beam containing no polymer is now approximately 0.47 mm compared to the 0.23 mm predicted previously, an increase of 104 %. As before, as the polymer area increases the crack widths are reduced with the beam containing the largest area of polymer (Poly 1.5) having a crack width of 0.30 mm, an increase of 33.8 % on that of the previous EC2 beams, however the reduction from 0.47 mm is an encouraging finding, suggesting that beams designed in this way may be capable of satisfying Eurocode 2 requirements (BSI 2004), depending on the precise design scenario. One possible limitation on the use of these beams is the increase in the required section size due to the decrease in neutral axis depth, rendering this an unlikely solution for any application with a space constraint on the section size.

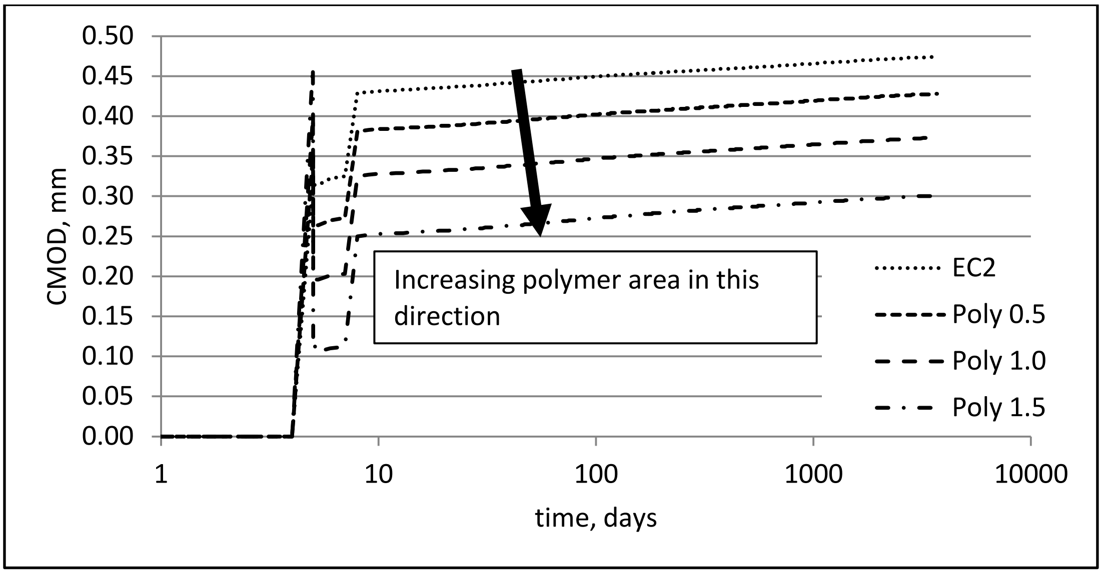

Figure 6.8 - SLS simulation results for beams designed with f_{yk} = 1468 MPa and σ_p = 100 MPa

6.5.4 Study 1 – Cost analysis

A cost analysis has been undertaken for the three sets of beams designed, assessed, and discussed in this study. A summary of the material cost, and predicted 10 year crack width for each beam design in Table 6.9, Table 6.11, and Table 6.12 is shown in Table 6.14. The values shown in the “percentage change in cost” and “percentage change in 10 year crack width” columns are calculated with respect to the EC2 beam designed using high yield steel reinforcement.

Table 6.14 – Summary of SLS results and cost analysis for study 1

		Material			Total cost	% change in cost	Crack width	% change in crack width
		Concrete	Steel	Polymer				
Beam ref	f_{yk} = 500, σ_p = 40							
EC2	Area	190552	1948	0	£159.92	0.0	0.23	0.0
	Cost	£102.67	£57.25	£0.00				
Poly 0.5	Area	189756	1879	865	£159.71	-0.1	0.22	-2.7
	Cost	£102.24	£55.22	£2.25				
Poly 1.0	Area	188959	1810	1731	£159.51	-0.3	0.21	-5.3
	Cost	£101.81	£53.19	£4.51				
Poly 1.5	Area	188163	1741	2596	£159.30	-0.4	0.21	-8.0
	Cost	£101.38	£51.17	£6.76				
Poly 2.0	Area	187367	1671	3462	£159.07	-0.5	0.20	-11.1
	Cost	£100.95	£49.11	£9.01				
Poly 2.5	Area	186571	1602	4327	£158.87	-0.7	0.19	-13.8
	Cost	£100.52	£47.08	£11.26				
Poly 3.0	Area	185775	1533	5192	£158.66	-0.8	0.19	-16.9
	Cost	£100.10	£45.05	£13.51				
Beam ref	f_{yk} = 500, σ_p = 100							
EC2	Area	190552	1948	0	£159.92	0.0	0.23	0.0
	Cost	£102.67	£57.25	£0.00				
Poly 0.5	Area	189860	1775	865	£156.71	-2.0	0.21	-7.1
	Cost	£102.30	£52.16	£2.25				
Poly 1.0	Area	189167	1602	1731	£153.51	-4.0	0.19	-14.2
	Cost	£101.92	£47.08	£4.51				
Poly 1.5	Area	188475	1429	2596	£150.30	-6.0	0.18	-22.2
	Cost	£101.55	£42.00	£6.76				
Poly 2.0	Area	187782	1256	3462	£147.10	-8.0	0.15	-31.6
	Cost	£101.18	£36.91	£9.01				
Beam ref	f_{yk} = 1468, σ_p = 100							
EC2	Area	209423	577	0	£124.41	-22.2	0.47	110.7
	Cost	£112.84	£11.57	£0.00				
Poly 0.5	Area	208624	511	865	£124.91	-21.9	0.43	90.2
	Cost	£112.41	£10.25	£2.25				
Poly 1.0	Area	207823	446	1731	£125.43	-21.6	0.37	65.8
	Cost	£111.98	£8.95	£4.51				
Poly 1.5	Area	207024	380	2596	£125.92	-21.3	0.30	33.8
	Cost	£111.54	£7.62	£6.76				

An examination of Table 6.14 shows that for both beam sets designed with standard high yield steel, the material cost reduces as the area of polymer increases; this is the result of the decrease in steel area which is considerably more expensive than the polymer that replaces it. The cost decrease is only marginal in the beams with a polymer shrinkage stress of 40 MPa, the maximum decrease being 0.8 %. However in the beams designed using a shrinkage stress of 100 MPa the Poly 2.0 beam shows a significant cost reduction of 8 %. These cost reductions, coupled with the reductions in crack widths previously discussed demonstrate that the LatConX system is capable of delivering an improved design solution, both in terms of economic and structural performance.

For the set of beams designed using the higher yield stress of prestressing wire, the cost reductions are even more significant due to the further reduced steel areas required. All beams are at least 21.3 % cheaper than the high yield steel Eurocode equivalent. A slight difference in this beam set to the two that use standard high yield steel is that as the polymer area increases, the beam cost also increases very slightly. This is because the steel area only reduces by a small amount for each relatively large increase in polymer thus the increase in polymer cost outstrips the decrease in steel cost; this effect is only very slight though at 0.9 % for the beam with the largest polymer area. As discussed previously the crack widths for these beams are larger than the high yield steel equivalents, however similar designs may provide a useful means for reducing material costs in applications where crack widths are not critical for the durability of the structure i.e. applications where crack width limitations are only in place for aesthetic reasons. (Exposure classes X0 and XC1 - Table 7.1N in Eurocode 2 (BSI 2004)).

All findings presented so far; both those relating to crack widths and to cost variations; suggest that wherever possible, for the maximum benefit to be gained from the LatConX system, the minimum steel area required to resist the ULS permanent moment along with an area of polymer that is at least sufficient to resist the ULS variable moment should be provided.

Depending on the application it may be beneficial to provide more polymer than the minimum required to resist the ULS variable moment, this will be investigated and discussed in the next parametric study.

6.6 Parametric Study 2

A second parametric study has also been conducted with the aim of investigating the effects of varying two further properties of the designs.

The first of these is the proportion of a beam's balancing moment (M_{bal}) that is utilised. Based on the assumption that an idealised rectangular concrete stress block with a depth equal to 0.8x is applicable, the maximum moment of resistance for a section to remain under-reinforced is given by Equation (6.14), which is a more general version of (6.2) suitable for use with any value of x_{lim}.

$$M_{bal} = 0.8 \frac{f_{ck}\alpha_{cc}}{\gamma_c} b x_{lim} \cdot (d - 0.4 x_{lim}) \tag{6.14}$$

in which x_{lim} is the limiting value of x for an under-reinforced section. All beams in the previous study were designed so that their ultimate moments of resistance (M_R) were precisely equal to the ULS moment, this resulted in $M_R < M_{bal}$ for all beams. Usually this would be an appropriate approach to design as this minimises the amount of steel used and therefore the costs; however as the polymer material used in the LatConX system is significantly cheaper than steel it is interesting to assess both the performance and cost implications of increasing the area of polymer provided up to the limiting area that results in $M_R = M_{bal}$. Based on the observations of the previous study, these increases in polymer areas are expected to result in further reductions in 10 year crack widths at minimal additional cost.

Another observation taken from the previous study was that a beam combining both steel with an increased yield stress and the LatConX system will be capable of satisfying both the SLS and ULS requirements of Eurocode 2 (BSI 2004) at a reduced material cost compared to the current RC design procedures. However the minimum crack width observed for beams designed using steel with a yield stress of 1468 MPa was 0.30mm, as this is on the limit of the Eurocode requirements the performance of beams designed with intermediate yield stresses will also be investigated in this study. Thus in this second parametric study 5 sets of beams have been designed with the steel yield stress varying from 500 MPa up to 1468 MPa in 250 MPa increments.

As with the prestressing steel used in the previous study, each different yield stress will require a different limiting value for the neutral axis depth to be calculated. This is done using Equation (6.13); the results of this process are shown in Table 6.15.

Table 6.15 – Yield stress and strain values, and resulting x_{lim} values for parametric study 2

f_{yk} (MPa)	500	750	1000	1250	1468
ε_{yk}	0.0022	0.0033	0.0043	0.0054	0.0064
x_{lim}	0.45d	0.38d	0.33d	0.30d	0.30d

From Table 6.15 it can be seen that the neutral axis depth limit decreases as the yield stress increases, this results in the minimum section size for an under-reinforced beam increasing as a result of the relationship shown in Equation (6.14). However in order to keep the results of the study comparable a section size that allows all beams to remain under-reinforced while carrying the ULS moment has been chosen, as the minimum value of x_{lim} is that for f_{yk} = 1468 MPa the section required is the same as that for the set of beams using this yield stress in the previous study: 350 mm x 600 mm. The creep parameters for this are unchanged and are shown in Table 6.13.

For each yield stress, 6 beams have been designed. The first one (EC2) uses only steel reinforcement with no polymer, the steel area is designed to be that required to resist the total ULS moment. In the other 5 designs the steel area is reduced to the minimum amount required to resist the permanent ULS moment, as this maximises the permissible polymer area. The minimum required polymer area is that required to resist the applied variable moment, this is found by rearranging Equation (6.10) and substituting the area of steel provided; this gives the area of polymer in the Poly min beams. The maximum permissible polymer area is governed by either the total ρ value relating to the tension steel and polymer combined which should not exceed 4 % of the effective concrete area, or the area that results in $M_R = M_{bal}$, whichever is the lesser; this is the area of polymer in the

Poly max beams. The amount of polymer provided in the 3 intermediate beams is simply interpolated between these maximum and minimum areas i.e. the area of Polymer provided in a Poly 25 beam is that given by Equation (6.15) etc.

$$A_{p,25} = A_{p,min} + 0.25\left(A_{p,max} - A_{p,min}\right) \tag{6.15}$$

All beam designs for this study are displayed in Table 6.16.

The CMOD vs time plots for the beam designs shown in Table 6.16 show the same trends as those observed in Figure 6.3, Figure 6.5, and Figure 6.8 only with differing values throughout, thus for reasons of conciseness the plots have been omitted from the main body of this thesis, they are however included in Appendix C. Instead, only the final 10 year crack widths predicted are displayed in Table 6.17 and Table 6.18 along with the cost analysis information.

Table 6.16 – All beam designs for study 2

Beam ref	b (mm)	d (mm)	A_p (mm^2)	A_s (mm^2)	ρ (%)
f_{yk} = 500					
EC2	350	547	0	1693	0.9
Poly min	350	547	3446	1004	2.3
Poly 25	350	547	4255	1004	2.7
Poly 50	350	547	5064	1004	3.2
Poly 75	350	547	5873	1004	3.6
Poly max	350	547	6682	1004	4.0
f_{yk} = 750					
EC2	350	547	0	1129	0.4
Poly min	350	547	3446	669	2.1
Poly 25	350	547	4185	669	2.5
Poly 50	350	547	4924	669	2.9
Poly 75	350	547	5662	669	3.3
Poly max	350	547	6401	669	3.7
f_{yk} = 1000					
EC2	350	547	0	847	0.3
Poly min	350	547	3446	502	2.1
Poly 25	350	547	3809	502	2.2
Poly 50	350	547	4172	502	2.4
Poly 75	350	547	4535	502	2.6
Poly max	350	547	4898	502	2.8
f_{yk} = 1250					
EC2	350	547	0	677	0.2
Poly min	350	547	3446	402	2.0
Poly 25	350	547	3584	402	2.1
Poly 50	350	547	3722	402	2.1
Poly 75	350	547	3859	402	2.2
Poly max	350	547	3997	402	2.3
f_{yk} = 1468					
EC2	350	547	0	577	0.2
Poly min	350	547	3446	342	2.0
Poly 25	350	547	3584	342	2.0
Poly 50	350	547	3722	342	2.1
Poly 75	350	547	3859	342	2.2
Poly max	350	547	3997	342	2.3

Table 6.17 – Summary of SLS results and cost analysis for study 2

		Material			Total cost	% change in cost	Crack width	% change in crack width
		Concrete	Steel	Polymer				
Beam ref	f_{yk} = 500							
EC2	Area	208307	1693	0	£161.99	0.0	0.21	0.0
	Cost	£112.24	£49.75	£0.00				
Poly min	Area	205550	1004	3446	£149.23	-7.9	0.13	-37.0
	Cost	£110.75	£29.51	£8.97				
Poly 25	Area	204741	1004	4255	£150.90	-6.8	0.10	-55.0
	Cost	£110.31	£29.51	£11.07				
Poly 50	Area	203932	1004	5064	£152.56	-5.8	0.06	-73.0
	Cost	£109.88	£29.51	£13.18				
Poly 75	Area	203123	1004	5873	£154.23	-4.8	0.03	-88.2
	Cost	£109.44	£29.51	£15.29				
Poly max	Area	202314	1004	6682	£155.90	-3.8	0.02	-92.9
	Cost	£109.01	£29.51	£17.39				
Beam ref	f_{yk} = 750							
EC2	Area	208871	1129	0	£145.72	-10.0	0.28	33.6
	Cost	£112.54	£33.18	£0.00				
Poly min	Area	205885	669	3446	£139.56	-13.8	0.17	-21.3
	Cost	£110.93	£19.66	£8.97				
Poly 25	Area	205146	669	4185	£141.09	-12.9	0.11	-46.4
	Cost	£110.53	£19.66	£10.89				
Poly 50	Area	204407	669	4924	£142.61	-12.0	0.06	-70.6
	Cost	£110.13	£19.66	£12.82				
Poly 75	Area	203669	669	5662	£144.13	-11.0	0.02	-89.1
	Cost	£109.74	£19.66	£14.74				
Poly max	Area	202930	669	6401	£145.66	-10.1	0.01	-94.8
	Cost	£109.34	£19.66	£16.66				
Beam ref	f_{yk} = 1000							
EC2	Area	209153	847	0	£137.58	-15.1	0.35	67.3
	Cost	£112.69	£24.89	£0.00				
Poly min	Area	206052	502	3446	£134.74	-16.8	0.20	-6.6
	Cost	£111.02	£14.75	£8.97				
Poly 25	Area	205689	502	3809	£135.49	-16.4	0.16	-23.2
	Cost	£110.83	£14.75	£9.91				
Poly 50	Area	205326	502	4172	£136.24	-15.9	0.13	-39.8
	Cost	£110.63	£14.75	£10.86				
Poly 75	Area	204963	502	4535	£136.99	-15.4	0.09	-55.5
	Cost	£110.43	£14.75	£11.80				
Poly max	Area	204600	502	4898	£137.74	-15.0	0.06	-70.6
	Cost	£110.24	£14.75	£12.75				

Table 6.18 - Summary of SLS results and cost analysis for study 2 (cont'd)

		Material			Total cost	% change in cost	Crack width	% change in crack width
		Concrete	Steel	Polymer				
Beam ref	f_{yk} = 1250							
EC2	Area	209323	677	0	£132.68	-18.1	0.42	100.5
	Cost	£112.78	£19.90	£0.00				
Poly min	Area	206152	402	3446	£131.86	-18.6	0.23	7.1
	Cost	£111.07	£11.81	£8.97				
Poly 25	Area	206014	402	3584	£132.14	-18.4	0.21	-0.9
	Cost	£111.00	£11.81	£9.33				
Poly 50	Area	205876	402	3722	£132.43	-18.2	0.19	-8.5
	Cost	£110.93	£11.81	£9.69				
Poly 75	Area	205739	402	3859	£132.71	-18.1	0.18	-16.6
	Cost	£110.85	£11.81	£10.04				
Poly max	Area	205601	402	3997	£133.00	-17.9	0.16	-24.2
	Cost	£110.78	£11.81	£10.40				
Beam ref	f_{yk} = 1468							
EC2	Area	209423	577	0	£124.41	-23.2	0.48	129.4
	Cost	£112.84	£11.57	£0.00				
Poly min	Area	206212	342	3446	£126.94	-21.6	0.25	18.5
	Cost	£111.11	£6.86	£8.97				
Poly 25	Area	206074	342	3584	£127.22	-21.5	0.23	9.5
	Cost	£111.03	£6.86	£9.33				
Poly 50	Area	205936	342	3722	£127.51	-21.3	0.21	0.5
	Cost	£110.96	£6.86	£9.69				
Poly 75	Area	205799	342	3859	£127.79	-21.1	0.19	-8.5
	Cost	£110.88	£6.86	£10.04				
Poly max	Area	205661	342	3997	£128.07	-20.9	0.17	-17.5
	Cost	£110.81	£6.86	£10.40				

The crack width vs cost trends from Table 6.17 and Table 6.18 for each yields stress have been summarised for easier viewing in Figure 6.9.

In keeping with earlier observations, the crack widths reduce with increasing area of polymer and increase with increasing yield strain. More significantly, these results go further towards demonstrating the LatConX system's potential for both reducing material costs and improving structural performance. The greatest crack width reduction is found in the beam set designed using a steel yield stress of 750 MPa, and is of course that of the beam with the largest polymer area in which the 10 year crack width is 0.01 mm, a reduction of 94.8 %

from the standard Eurocode 2 beam. The minimum crack width not occurring in the beam set with the minimum yield stress might seem contrary to expectations, however closer inspection of the beam designs in Table 6.16 reveals an explanation. The maximum polymer area in the beam set with f_{yk} = 500 MPa is limited by the ρ value due to the larger steel areas required at the reduced yield stress, whereas the maximum polymer area in all other beam sets is limited by M_{bal}. This suggests that an optimum yield stress for crack width limitation may lie between 500 MPa and 750 MPa; however the exact value is likely to vary depending on the nature of the design scenario considered. This optimum value would be that which results in both the ρ and M_{bal} limits being met by the same area of supplied polymer. This would result in the maximisation of the flexural stiffness of the beam without over-reinforcement; concurrently, yield stress would be at a minimum, thus decreasing the initial crack width as previously discussed.

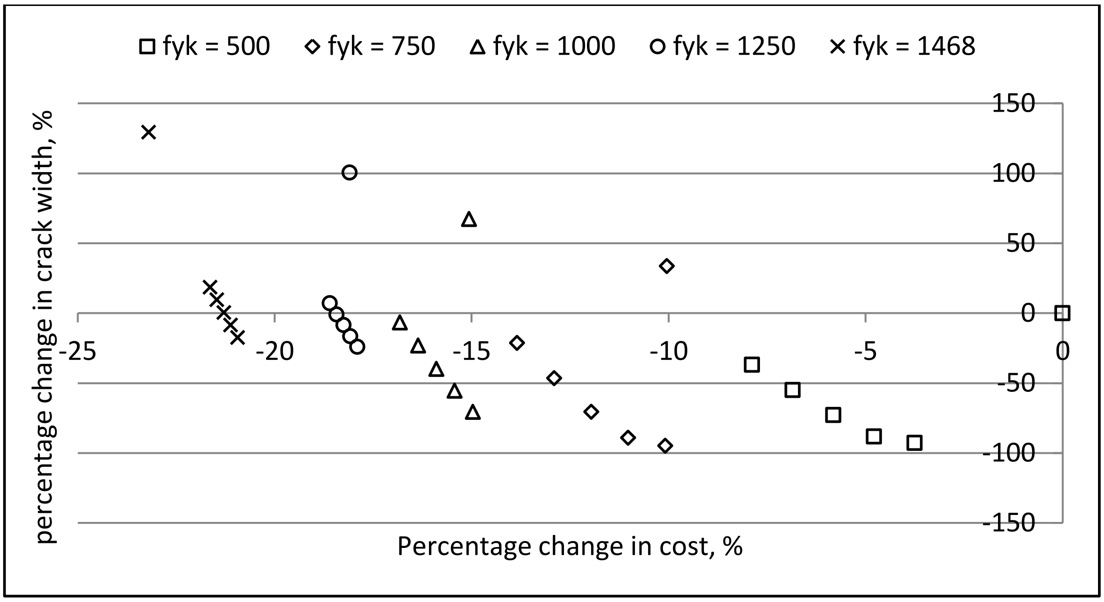

Figure 6.9 – Crack width vs cost trends for varying steel yield stresses

For the beams with maximum polymer areas in the beam sets with yield stresses of 500 MPa, 750 MPa, and 1000 MPa, cracking is extremely limited at less than 0.1 mm in each case. This is a result of the decreased yield strain and resulting increased maximum neutral axis depth giving an increased value of M_{bal} and hence more residual moment capacity allowing a larger polymer area. The lower yield stresses also mean that larger areas of steel are provided, thus increasing flexural stiffness and reducing the initial crack width. If such a degree of crack limitation is not required then an alternative capability for the system might be in applications requiring more standard crack limitation of 0.3 mm however with reduced section dimensions, particularly depth. This dimensional reduction may be more marked if higher classes of concrete are considered as this will increase the value of $\mathrm{M_{bal}}$ and thus allow the inclusion of a higher area of polymer without a beam becoming over-reinforced.

Finally considering the set of beams designed with the highest yield stress, significant reductions are once again seen in the material cost of each beam. Further to this the 10 year crack widths for both the Poly 75 and Poly max beams are now reduced below that of the original Eurocode beam by 8.5 % and 17.5 % respectively; with these reductions coming at a decreased material costs of 21.1 % and 20.9 % respectively. This demonstrates that the LatConX system will be capable of providing designs that conform to all Eurocode 2 (BSI 2004) requirements at significantly reduced material costs.

6.7 Sensitivity Studies

Some sensitivity studies have been undertaken to ascertain which factors, if any, have a significant effect on the predictions of the model. Initially the poly max beam presented in Table 6.16 with a steel yield strength of 750 MPa was studied to see which parameters the model's predictions were most sensitive to.

The parameters investigated were the creep strain, shrinkage strain, and polymer relaxation. Initial results revealed that the influence of both the creep and shrinkage strain on the ten year crack width was negligible, with a 10 % increase in either of these strains resulting in less than a 0.1 % decrease in the percentage change in crack width (i.e. the system is 0.1 % less effective at closing cracks). The polymer relaxation was increased from the 3.7 % calibrated in Chapter 4 (see β_{1a} Table 4.4) to 10 %, this is considered to be a highly pessimistic value for the relaxation as it is a factor of 2.7 higher than the relaxation plateau observed in the experiments of Chapter 3. This increased relaxation caused the final crack width to increase from 0.011 mm to 0.018 mm. This is an increase of 64 % which may seem excessively large, however if put into the context of the effectiveness of the system at closing cracks, a crack reduction of 91.4 % is still achieved, suggesting that even if pessimistic material behaviour for the polymer is assumed the system will still be highly effective.

These results suggest that variations in the behaviour of the polymer will have a larger influence on the effectiveness of the system than variation in the concrete behaviour. For this reason the polymer relaxation sensitivity study was extended to include all five of the poly max beams presented in Table 6.16; the results of this are displayed in Table 6.19.

Table 6.19 - Summary of polymer relaxation sensitivity study

Beam	Baseline (3.7% Relaxation)		10% Relaxation	
	Crack width (mm)	% change in crack width	Crack width (mm)	% change in crack width
Poly max 500	0.015	92.9	0.020	90.5
Poly max 750	0.011	94.8	0.018	91.4
Poly max 1000	0.062	70.5	0.091	56.7
Poly max 1250	0.160	23.8	0.191	9.0
Poly max 1468	0.174	17.1	0.210	0.0

From Table 6.19 it can be seen that all beams except Poly max 1468 continue to show a reduction in crack width even with the pessimistic polymer properties described above. Encouragingly the Poly max 500 and Poly max 750 beams which showed the most significant reductions in crack width continue to show similarly large reductions of 90.5 % and 91.4 % respectively. The author would like to reiterate that this is considered to be a highly pessimistic scenario thus it is encouraging that significant reductions in crack width are still predicted.

6.8 Conclusions

- It has been demonstrated that beams incorporating the LatConX system can be designed to conform to Eurocode 2 (BSI 2004) requirements at both the serviceability and ultimate limit states.
- The variable moment capacity before and after polymer activation means that a specific construction sequence is required. First the beam and slab should be cast with the required steel bars and unactivated polymer tendons. The polymer tendons should then be activated before the application of any variable actions.
- From this sequence, the key design considerations are as follows:
    - The moment of resistance due to the steel alone must at least be sufficient for the permanent actions.
    - The moment of resistance due to the steel and polymer must at least be sufficient for the total of the permanent and variable actions.
    - The moment of resistance due to the steel and polymer must not result in $M_R > M_{bal}$.
    - The total area of steel and polymer must not cause ρ to exceed 4 %.
- In the first parametric study, the raw findings were:
    - In beams designed assuming a shrinkage stress of 40 MPa and yield stress of 500 MPa, the 10 year crack width was reduced by up to 17 %; the concurrent reduction in cost was minor at 0.8 %.
    - In beams designed assuming a shrinkage stress of 100 MPa and yield stress of 500 MPa 10 year crack width was reduced by up to 32 %; and the concurrent reduction in cost was 8 %.
    - In beams designed assuming a shrinkage stress of 100 MPa and yield stress of 1468 MPa 10 year crack width increased by 34 %; however the concurrent reduction in cost was significant at 21 %.
- In the second parametric study, the raw findings were:

  - The ten year crack width was reduced by up to 95 % in the case of the beam designed with a yield stress of 750 MPa and the maximum polymer area.
  - The most significant reduction in cost while achieving a ten year crack width no larger than that of the original Eurocode 2 beam was 21 % for the beam designed using a yield stress of 1468 MPa and a polymer area of 75 % of the maximum.
- The key conclusion of this Chapter is that if beams are designed appropriately, incorporation of the LatConX system can improve the performance of a design solution in one or more of three key areas:
  - Cracks can be significantly limited
  - Cost can be reduced by reducing steel area
  - Section dimensions can be reduced
- Owing to the large number of factors that can be varied in the design considerations of reinforced concrete, and the additional factors relating to the LatConX system, only a limited number of overarching suggestions for future work are proffered here. The following would seem to be interesting investigations to pursue:
  - The possibility of reducing section dimensions while still satisfying SLS requirements of Eurocode 2 (BSI 2004), particularly in conjunction with beams designed using a higher class of concrete than the C30/37 used throughout this Chapter.
  - A wider range of design scenario, i.e. by varying span/permanent actions/variable actions/concrete class.
  - The behaviour of beams designed and detailed in full, i.e. without the simplifications outlined in 6.2.3.1.

Chapter 7 – Conclusions and Further Work

This Chapter brings together the conclusions drawn from the research work reported in this thesis and recommends appropriate future work for continued development of the LatConX system. For more specific conclusions the reader is referred to the individual conclusions section at the end of each of Chapters 3 – 6.

A list of specific research objectives were described on page 7 of Chapter 1. The research presented in this thesis, and summarised below, has been undertaken with the aim of satisfying these objectives and has led to the following conclusions:

a) An experimental programme was undertaken to investigate the long-term stress relaxation behaviour of the PET material proposed for use in the LatConX system. The observed stress relaxation was limited in all tests, further confirming pre-drawn PET as a suitable material for use in the LatConX system. More specifically, the experimental programme yielded the following conclusions:
    i. Early stress loss to relaxation (over the first 4 - 10 days) ranged from 1.5 % to 4.3 % of the initially applied stress; the average stress loss was 3.6 %.
    ii. Specimens were observed to relax to an average stress of 95.5 % of the initially applied stress over approximately 95 days.

b) Two new transient thermomechanical models were developed for the restrained shrinkage behaviour of pre-drawn PET and subsequent long-term relaxation behaviour. Both of these models were found to be capable of simulating the experimental behaviour observed in Chapter 3 if correctly calibrated. The LTMx2 model, differentiated from the LTMx1 model by its additional Maxwell element, was deemed to be the superior of the two owing to its ability to simulate a broader range of material behaviour with a single calibration and only one set of material parameters.

c) A numerical model in the form of a layered beam model for long-term simulation of reinforced concrete beams has been developed and coupled with the LTMx2 polymer constitutive model. This coupled model has been validated by comparison with two experimental datasets and a range of code based crack width predictions to confirm its reliability and consistency in accurately simulating a range of physical behaviour. Based on this, the model has been deemed suitable for simulating the long-term behaviour of both standard reinforced concrete sections and those containing the LatConX system.

d) A design procedure for reinforced concrete beams incorporating the LatConX system has been described including both a proposed construction sequence and the derivation of modified design equations. This procedure has been demonstrated to be appropriate for the design of beams conforming to Eurocode requirements at both serviceability and ultimate limit states. Within this procedure the requirements for an acceptable design were as follows:
    i. The moment of resistance due to the steel alone must at least be sufficient for the permanent actions.
    ii. The moment of resistance due to the steel and polymer must at least be sufficient for the total of the permanent and variable actions.
    iii. The combination of the effect of the steel and the activated polymer must not result in the section becoming over-reinforced. More specifically, the moment of resistance (M_R) for any section must not exceed the limiting value (M_{bal}).
    iv. The total area of steel and polymer must not cause ρ to exceed 4 %.

e) Two parametric studies have been presented, encompassing an in-depth comparison of the structural performance of reinforced concrete elements with and without the incorporation of the LatConX system; all beams were designed to conform to Eurocode requirements. These studies used ten year crack width predictions from the layered beam model as the indicator of structural performance. Several design parameters were varied including the restrained shrinkage stress of the polymer, the yield stress of the steel, the concrete cross sectional dimensions, and the areas of steel and polymer provided. These studies revealed a number of findings which are described in detail in the conclusions section of Chapter 6. There were two key conclusions relating to structural performance:

   i. The predicted crack width could be significantly limited - a 95 % reduction from a Eurocode design was achieved for the scenario considered.
   ii. Alternatively the section dimensions could be reduced from those required for a standard reinforced concrete beam to conform to Eurocode requirements.

f) Cost analyses were undertaken on all beams designed for the two parametric studies, again the conclusions of Chapter 6 should be referred to for a detailed summary of findings however key results were:

   i. Costs were reduced for all beams designed, the magnitude of this reduction varied significantly depending on the concurrent polymer and concrete areas, and design parameters imposed.
   ii. Increasing the yield stress of the steel allowed greater cost reductions while maintaining acceptable crack width predictions according to Eurocode requirements. This approach gave a reduction in cost of up to 21 %.

As the literature review in Chapter 2 revealed, self-healing cementitious materials have the potential to improve the durability and design life of concrete structures significantly. This will in turn reduce the environmental impact of the cement and concrete industry by reducing global cement demand and reduce the whole life cost of concrete structures by reducing the need for inspection, maintenance, and repairs.

The LatConX system has been shown to have the potential to significantly reduce crack widths in reinforced concrete elements. It is anticipated that this demonstrated crack closure capability combined with an effective healing agent such as cyanoacrylate may result in significant mechanical strength regain of the cementitious matrix, accompanied by a reduction in permeability. It is recommended that the healing agent is delivered via a vascular network of some type after activation of the SMP tendons; this way leakage out of the initially large cracks will be eliminated allowing the healing/sealing agent to be supplied when crack widths are at a minimum. The combination of reduced crack widths and permeability, and increased mechanical strength is expected to significantly improve the durability and design life of concrete structures.

Further development of this system will require work in a number of areas. The production of an appropriate SMP with both an increased shrinkage stress and increased size is vital for the success of the LatConX system. This polymer must be capable of a shrinkage stress of 100 MPa for the work presented in this thesis to be relevant, if this is not achievable then similar parametric studies to those presented in Chapter 6 will be required to gauge the potential of the system. The final polymer material must also be resistant to an alkali environment, and conveniently mass-producible. It would also be optimum for the final polymer material to be activated by some other means such as an electric current or magnetic field.

The numerical model presented in Chapter 5 could be developed in two different ways. Firstly a full consideration of the hydration processes and associated early age behaviour could be included. This would allow an investigation into the effect of varying the time of applied loads, particularly any compressive force from polymer tendons activated at relatively early ages. Secondly the model could be extended to three-dimensions which would allow a more comprehensive investigation of the behaviour of individual elements and complete structures incorporating the LatConX system. The simplest approach to this is likely to involve coupling the LTMx2 polymer model with an existing finite element modelling system for concrete, e.g. LUSAS.

Experimentally it is important to subject the system to circumstances similar to those expected in a real world application. This should include increasing the size of the test specimen, including reinforcement and polymer designed according to the equations presented in Chapter 6, using a self-healing agent, and applying a sustained load throughout the duration of the test.

Bibliography

Abdel-Bary, E. 2003. *Handbook of Plastic Films*. iSmithers Rapra Publishing.

Abd-Elmoaty, M. 2011. Self-Healing of Polymer Modified Concrete. *Alexandria Engineering Journal* 50(2), pp. 171–78.

Abrahamson, E.R., Lake, M.S., Munshi, N.A., and Gall, K. 2003. Shape Memory Mechanics of an Elastic Memory Composite Resin. *Journal of Intelligent Materials Systems and Structures* 14 (10), pp. 623–32.

Abu Al-Rub, R.K. and Darabi, M.K. 2012. A Thermodynamic Framework for Constitutive Modeling of Time- and Rate-Dependent Materials. Part I: Theory. *International Journal of Plasticity* 34, pp. 61–92.

ACI Committee 548. 2009. *Guide for the Use of Polymers in Concrete*. Farmington Hills, Mich.: American Concrete Institute.

Aflaki, S. and Hajikarimi, P. 2012. Implementing Viscoelastic Rheological Methods to Evaluate Low Temperature Performance of Modified Asphalt Binders. *Construction and Building Materials* 36, pp. 110–18

Agopyan, V., Savastano, H., John, V.M., and Cincotto, M.A. 2005. Developments on Vegetable Fibre–cement Based Materials in São Paulo, Brazil: An Overview. *Cement and Concrete Composites*, Natural fibre reinforced cement composites, 27 (5), pp. 527–36.

Ahn, T.H. and Kishi, T. 2009. The Effect of Geo-Materials on the Autogenous Healing Behavior of Cracked Concrete. In: *Concrete Repair, Rehabilitation and Retrofitting II*, Cape Town, 24-26 November, 2008. pp. 125–26.

Alam, M.S., Youssef, M.A., and Nehdi, M. 2008. Analytical Prediction of the Seismic Behaviour of Superelastic Shape Memory Alloy Reinforced Concrete Elements. *Engineering Structures* 30(12), pp. 3399–3411.

Aldea, C.M., Song, W.J., Popovics, J.S., and Shah, S.P. 2000. Extent of Healing of Cracked Normal Strength Concrete. *Journal of Materials in Civil Engineering* 12(1), pp. 92–96.

Alibaba Group. 2014. [Online] Available at: http://www.alibaba.com [Accessed: 2 September 2014]

Almagableh, A., Raju Mantena, P., and Alostaz, A. 2010. Creep and Stress Relaxation Modeling of Vinyl Ester Nanocomposites Reinforced by Nanoclay and Graphite Platelets. *Journal of Applied Polymer Science* 115(3), pp. 1635–41.

American Concrete Institute (ACI). 1982. Prediction of Creep, Shrinkage, and Temperature Effects in Concrete Structures. *ACI Committee* 209.

Argon, A.S. 1973. A Theory for the Low-Temperature Plastic Deformation of Glassy Polymers. *Philosophical Magazine* 28(4), pp. 839–65.

AZOM. 2003. Polyethylene Terephthalate Polyester (PET, PETP) - Properties and Applications. [Online] Available at: http://www.azom.com/article.aspx?ArticleID=2047 [Accessed: 27 September 2014].

Bakis, C.E., Nanni, A., Terosky, J.A., and Koehler, S.W. 2001. Self-Monitoring, Pseudo-Ductile, Hybrid FRP Reinforcement Rods for Concrete Applications. *Composites Science and Technology* 61(6), pp. 815–23.

Bamforth, P.B. 2007. *Early-Age Thermal Crack Control in Concrete*. CIRIA.

Bank, L.C. 2006. *Composites for Construction: Structural Design with FRP Materials*. New Jersey: John Wiley & Sons.

Bank, L.C. 2013. Progressive Failure and Ductility of FRP Composites for Construction: Review. *Journal of Composites for Construction* 17(3), pp. 406–19.

Barbero, E.J., Greco, F., and Lonetti, P. 2005. Continuum Damage-Healing Mechanics with Application to Self-Healing Composites. *International Journal of Damage Mechanics* 14(1), pp. 51–81.

Barot, G. and Rao, I.J. 2006. Constitutive Modeling of the Mechanics Associated with Crystallizable Shape Memory Polymers. *Zeitschrift Für Angewandte Mathematik Und Physik* 57(4), pp. 652–81.

Barot, G., Rao, I.J., and Rajagopal, K.R. 2008. A Thermodynamic Framework for the Modeling of Crystallizable Shape Memory Polymers. *International Journal of Engineering Science* 46(4), pp. 325–51.

Baschek, G. and Hartwig, G. 1998. Parameters Influencing the Thermal Expansion of Polymers and Fibre Composites. *Cryogenics* 38(1), pp. 99–103.

Bažant, Z.P. and Oh, B.H. 1983. Crack band theory for fracture of concrete. *Materials and Structures* 16, pp. 155-177.

Bažant, Z.P. and Prasannan, S. 1989. Solidification Theory for Concrete Creep I. Formulation. *Journal of Engineering Mechanics* 115(8), pp. 1691–1703.

Bažant, Z.P. and Baweja, S. 1995. Creep and Shrinkage Prediction Model for Analysis and Design of Concrete Structures- Model B3. *Materials and Structures* 28(6), pp. 357–65.

Bažant, Z.P., Hauggaard, A.B., Baweja, S., and Ulm, F.J. 1997. Microprestress-Solidification Theory for Concrete Creep. I: Aging and Drying Effects. *Journal of Engineering Mechanics* 123(11), pp. 1188–94.

Bažant, Z.P. 2001. Prediction of Concrete Creep and Shrinkage: Past, Present and Future. *Nuclear Engineering and Design* 203(1), pp. 27–38.

BBC. 2012. Key Test for Re-Healable Concrete [Online] Available at: http://www.bbc.co.uk/news/science-environment-20121303 [Accessed: 18 September 2014].

Beeby, A.W. and Scott, R.H. (2005) Cracking and deformation of axially reinforced members subjected to pure tension. *Magazine of Concrete Research* 57(10), pp. 611-21

Behl, M. and Lendlein, A. 2007. Shape-Memory Polymers. *Materials Today* 10(4), pp. 20–28.

Portland Cement Association. 'Bendable Concrete' Replaces Bridge Expansion Joints. [Online] Available at: http://www.cement.org/for-concrete-books-learning/concrete-technology/concrete-construction/engineered-cementitious-composite-link-slabs [Accessed: 18 September 2014].

Bhattacharyya, A. and Tobushi, H. 2000. Analysis of the Isothermal Mechanical Response of a Shape Memory Polymer Rheological Model. *Polymer Engineering & Science* 40(12), pp. 2498–2510.

Bhushan, B. 2000. *Mechanics and Reliability of Flexible Magnetic Media - 2nd Edition*. New York: Springer.

Brandt, A.M. 2008. Fibre Reinforced Cement-Based (FRC) Composites after over 40 Years of Development in Building and Civil Engineering. In: *Composite Structures*, Fourteenth International Conference on Composite Structures ICCS14, 86(1–3), pp. 3–9.

Brandt, W.W. 1959. Model Calculation of the Temperature Dependence of Small Molecule Diffusion in High Polymers. *The Journal of Physical Chemistry* 63(7), pp. 1080–85.

British Standard Institution. 2002. *BS EN 1991-1-1:2002 Eurocode 1: Actions on Structures - Part 1-1: General Actions - Densities, Self-Weight, Imposed Loads for Buildings*. London, UK: BSI.

British Standard Institution. 2004. *BS EN 1992-1-1:2004 Eurocode 2: Design of Concrete Structures - Part 1-1: General Rules and Rules for Buildings*. London, UK: BSI.

British Standard Institution. 2006a. *BS EN 14889-1:2006 Fibres for Concrete. Steel Fibres. Definitions, Specifications and Conformity*. London, UK: BSI.

British Standard Institution. 2006b. *BS EN 14889-2:2006 Fibres for Concrete. Polymer Fibres. Definitions, Specifications and Conformity*. London, UK: BSI.

British Standard Institution. 2012. *BS 5896:2012 High Tensile Steel Wire and Strand for the Prestressing of Concrete. Specification*. London, UK: BSI.

Buckley, C.P. and Jones, D.C. 1995. Glass-Rubber Constitutive Model for Amorphous Polymers near the Glass Transition. *Polymer* 36(17), pp. 3301–12.

CEB-FIP. 2010. *CEB-FIP Model Code for Concrete Structures 2010: Design Code*. London: Thomas Telford.

Chandran, P. and Jabarin, S. 1993a. Biaxial Orientation of Poly(ethylene Terephthalate). Part I: Nature of the Stress-Strain Curves. *Advances in Polymer Technology* 12(2), pp. 119–32.

Chandran, P. and Jabarin, S. 1993b. Biaxial Orientation of Poly(ethylene Terephthalate). Part II: The Strain-Hardening Parameter. *Advances in Polymer Technology* 12(2), pp. 133–51.

Chandran, P. and Jabarin, S. 1993c. Biaxial Orientation of Poly(ethylene Terephthalate). Part III: Comparative Structure and Property Changes Resulting from Simultaneous and Sequential Orientation. *Advances in Polymer Technology* 12(2), pp. 153–65.

Chen, A.C.T. and Chen, W.F. 1975. Constitutive Relations for Concrete. *ASCE J Eng Mech Div* 101(4), pp. 465–81.

Chen, W.F. 2007. *Plasticity in Reinforced Concrete*. Florida: J. Ross Publishing Classics.

Cheremisinoff, N.P. 1989. *Handbook of Polymer Science and Technology*. New York: Marcel Dekker Inc.

Cicekli, U., Voyiadjis, G.Z., and Abu Al-Rub, R.K. 2007. A Plasticity and Anisotropic Damage Model for Plain Concrete. *International Journal of Plasticity*. 23(10–11), pp. 1874–1900.

Clarke, J.L. 2003. *Alternative Materials for the Reinforcement and Prestressing of Concrete*. London: CRC Press.

Clear, C.A. 1985. *Effects of Autogenous Healing Upon the Leakage of Water Through Cracks in Concrete.* Technical Report - Cement and Concrete Association.

Comi, C. 2001. A Non-Local Model with Tension and Compression Damage Mechanisms. *European Journal of Mechanics - A/Solids* 20(1), pp. 1–22.

Comi, C., and Perego, U. 2001. Fracture Energy Based Bi-Dissipative Damage Model for Concrete. *International Journal of Solids and Structures* 38(36-37), pp. 6427–54.

Contrafatto, L. and Cuomo, N. 2006. A Framework of Elastic-Plastic Damaging Model for Concrete under Multiaxial Stress States. *International Journal of Plasticity* 22(12), pp. 2272–2300.

Currie, R.J. and Crammond, N.J. 1994. Assessment of Existing High Alumina Cement Construction in the UK. *Proceedings of the Institution of Civil Engineers: Structures and Buildings* 104(1), pp. 83–92.

Daniels, C.A. 1989. *Polymers: Structure and Properties*. CRC Press.

Darabi, M.K., Abu Al-Rub, R.K., and Little, D.N. 2012. A Continuum Damage Mechanics Framework for Modeling Micro-Damage Healing. *International Journal of Solids and Structures* 49(3–4), pp. 492–513.

Davidovits, J. 1994. Global Warming Impact on the Cement and Aggregates Industries. *World Resource Review* 6(2), pp. 263–78.

Davidovits, J. 2010. Geopolymer Cement for Mitigation of Global Warming. *Geopolymer Institute*. www.geopolymer.org/applications/global-warming.

Davis Langdon LLP. 2012. *Spon's Civil Engineering and Highway Works Price Book 2013*. London: Taylor & Francis.

Debenedetti, P.G. and Stillinger, F.H. 2001. Supercooled Liquids and the Glass Transition. *Nature* 410(6825) pp. 259–67.

Dejonghe, P., De Belie, N., Steuperaert, S., and Snoeck, D. 2011. The Behaviour of Suberabsorbing Polymers as a Sealing Agent in Concrete: Absorption Kinetics, Degradation and Water Permeability. In *3rd International Conference on Self-Healing Materials*. Bath, United Kingdom, 27 - 29 June 2011.

Deng, Z., Li, Q., and Sun, H. 2006. Behavior of Concrete Beam with Embedded Shape Memory Alloy Wires. *Engineering Structures* 28(12), pp. 1691–97.

Department of Trade and Industry. 2001. *Foresight: Constructing the Future*. London: Crown Copyright.

Department of Trade and Industry. 2014. *Construction Statistics Annual Report*. London: TSO.

Desmorat, R., Gatuingt, F., and Ragueneau, F. 2007. Nonlocal Anisotropic Damage Model and Related Computational Aspects for Quasi-Brittle Materials. *Engineering Fracture Mechanics* 74(10), pp. 1539–60.

Dismore, P.F. and Statton, W.O. 1964. Chain Folding in Oriented 66-Nylon Fibers. *Journal of Polymer Science Part B: Polymer Letters* 2(12), pp. 1113–16.

Doolittle, A.K. 1951. Studies in Newtonian Flow. II. the Dependence of the Viscosity of Liquids on Free-Space. *Journal of Applied Physics* 22(12), pp. 1471–75.

Dragon, A., Halm, D., and Désoyer, T. 2000. Anisotropic Damage in Quasi-Brittle Solids: Modelling, Computational Issues and Applications. *Computer Methods in Applied Mechanics and Engineering* 183(3-4), pp. 331–52.

Dry, C. 1994. Matrix Cracking Repair and Filling Using Active and Passive Modes for Smart Timed Release of Chemicals from Fibers into Cement Matrices. *Smart Materials and Structures* 3(2), pp. 118–23.

Dry, C., and McMillan, W. 1996. Three-Part Methylmethacrylate Adhesive System as an Internal Delivery System for Smart Responsive Concrete. *Smart Materials and Structures* 5(3), pp. 297–300.

Dunn, S.C. 2010. Novel Self-Healing Shape Memory Polymer-Cementitious System. PhD Thesis, Cardiff University.

Dunn, S.C., Jefferson, A.D., Lark, R.J., and Isaacs, B. 2011. Shrinkage Behavior of Poly(ethylene Terephthalate) for a New Cementitious-Shrinkable Polymer Material System. *Journal of Applied Polymer Science* 120(5), pp. 2516–26.

Dusunceli, N. and Colak, O.U. 2008. Modelling Effects of Degree of Crystallinity on Mechanical Behavior of Semicrystalline Polymers. *International Journal of Plasticity* 24(7), pp. 1224–42.

Duxson, P., Provis, J.L., Lukey, G.C., and van Deventer, J.S.J. 2007. The Role of Inorganic Polymer Technology in the Development of ‘green Concrete’. *Cement and Concrete Research* 37(12), pp. 1590–97.

Edvardsen, C. 1999. Water Permeability and Autogenous Healing of Cracks in Concrete. *ACI Materials Journal* 96(4), pp. 448–54.

El-Tawil, S. and Ortega-Rosales, J. 2004. Prestressing Concrete Using Shape Memory Alloy Tendons. *ACI Structural Journal* 101(6), pp. 846–51.

Encyclopedia Britannica. 2014. *Polyethylene Terephthalate (PET or PETE) (chemical Compound)* [Online]. Available at: http://www.britannica.com/EBchecked/topic/468536/polyethylene-terephthalate-PET-or-PETE [Accessed: September 27 2014].

Etse, G. and Willam, K. 1994. Fracture Energy Formulation for Inelastic Behavior of Plain Concrete. *Journal of Engineering Mechanics* 120(9), pp. 1983–2011.

European Cement Association. 2013. *Activity Report 2013*. Brussels: CEMBUREAU.

Eyring, H. 1936. Viscosity, Plasticity, and Diffusion as Examples of Absolute Reaction Rates. *The Journal of Chemical Physics* 4(4), pp. 283–91.

Faria, R., Oliver, J., and Cervera, M. 1998. A Strain-Based Plastic Viscous-Damage Model for Massive Concrete Structures. *International Journal of Solids and Structures* 35(14), pp. 1533–58.

Feenstra, P.H. and De Borst, R. 1995. A Plasticity Model and Algorithm for Mode-I Cracking in Concrete. *International Journal for Numerical Methods in Engineering* 38(15), pp. 2509–29.

Feist, C. and Hofstetter, G. 2006. An Embedded Strong Discontinuity Model for Cracking of Plain Concrete. *Computer Methods in Applied Mechanics and Engineering*, Computational Modelling of Concrete, 195(52), pp. 7115–38.

Findley, W.N. and Kasif, O. 1976. *Creep and Relaxation of Nonlinear Viscoelastic Materials: With an Introduction to Linear Viscoelasticity*. Dover Publications.

Foresight Smart Materials Taskforce. 2004. *Smart Materials for the 21st Century*. London: The Institute of Materials, Minerals & Mining.

Fox Jr, T.G. and Flory, P.J. 1950. Second-Order Transition Temperatures and Related Properties of Polystyrene. I. Influence of Molecular Weight. *Journal of Applied Physics* 21(6), pp. 581–91.

Freyermuth, C.L. 2001. Life-Cycle Cost Analysis for Large Segmental Bridges. *Concrete International* 23(2), pp.89-95.

Garcia, A., Schlangen, E., and van de Ven, M. 2010. Two Ways of Closing Cracks on Asphalt Concrete Pavements: Microcapsules and Induction Heating. *Key Engineering Materials* 417–418, pp. 417-418.

Gardner, N.J. and Lockman, M.J. 2002. Design Provisions for Drying Shrinkage and Creep of Normal-Strength Concrete. *ACI Materials Journal* 99(1), pp. 111–12.

Gartner, E. 2004. Industrially Interesting Approaches to ‘low-CO2’ Cements. *Cement and Concrete Research* 34(9) pp. 1489–98.

Gilbert, R.I. 2013. Time-Dependent Stiffness of Cracked Reinforced and Composite Concrete Slabs. In *Procedia Engineering*, 57, pp. 19–34.

Giry, C., Dufour, F., and Mazars, J. 2011. Stress-Based Nonlocal Damage Model. *International Journal of Solids and Structures* 48(25-26), pp. 3431–43.

Glanville, W.H. 1931. *The Permeability of Portland Cement Concrete*. H. M. Stationery Office [printed by Harrison and sons, Limited].

Global Association of Manufacturers of Polyester Film. 2014. *Polyester Film Manufacturing and Technology* [Online]. Available at: http://www.ampef.com/technology.html [Accessed: 27 September].

Goel, R., Kumar, R., and Paul, D.K. 2007. Comparative Study of Various Creep and Shrinkage Prediction Models for Concrete. *Journal of Materials in Civil Engineering* 19(3), pp. 249–60.

Goodfellow. 2014. *Polyethylene Terephthalate (Polyester, PET, PETP) Material Information* [Online]. Available at: http://www.goodfellow.com/E/Polyethylene-terephthalate.html.

Granger, S., Loukili, A., Pijaudier-Cabot, G., and Chanvillard, G. 2007. Experimental Characterization of the Self-Healing of Cracks in an Ultra High Performance Cementitious Material: Mechanical Tests and Acoustic Emission Analysis. *Cement and Concrete Research* 37(4), pp. 519–27.

Grassl, P. and Jirásek, M. 2006. Damage-Plastic Model for Concrete Failure. *International Journal of Solids and Structures* 43(22-23), pp. 7166–96.

Grassl, P., Lundgren, K., and Gylltoft, K. 2002. Concrete in Compression: A Plasticity Theory with a Novel Hardening Law. *International Journal of Solids and Structures* 39(20), pp. 5205–23.

Guiu, F. and Pratt, P.L. 1964. Stress Relaxation and the Plastic Deformation of Solids. *Physica Status Solidi (b)* 6(1), pp. 111–20.

Gupta, V.B., Radhakrishnan, J., and Sett, S.K. 1994. Effect of Processing History on Shrinkage Stress in Axially Oriented Poly(ethylene Terephthalate) Fibres and Films. *Polymer* 35(12), pp. 2560–67.

Halsey, G., White, H.J., and Eyring, H. 1945. Mechanical Properties of Textiles, I. *Textile Research Journal* 15(9), pp. 295–311.

Harris, H., Somboonsong, W., and Ko, F. 1998. New Ductile Hybrid FRP Reinforcing Bar for Concrete Structures. *Journal of Composites for Construction* 2(1), pp. 28–37.

Häussler-Combe, U. and Hartig, J. 2008. Formulation and Numerical Implementation of a Constitutive Law for Concrete with Strain-Based Damage and Plasticity. *International Journal of Non-Linear Mechanics* 43(5), pp. 399–415.

Haward, R.N. and Thackray, G. 1968. The Use of a Mathematical Model to Describe Isothermal Stress-Strain Curves in Glassy Thermoplastics. *Proceedings of the Royal Society of London. Series A. Mathematical and Physical Sciences* 302(1471), pp. 453–72.

Haworth, B., Dong, Z.W., and Davidson, P. 1993. Characterisation of Shrinkage in Oriented PET Films and Containers by Thermomechanical Analysis (TMA). *Polymer International* 32(3), pp. 325–35.

Hayashi, S., Tasaka, Y., and Akita, Y. 2004. Development of Smart Polymer Materials and Its Various Applications. *Mitsubishi Juko Giho* 41(1), pp. 62–64.

Hazelwood, T., Jefferson, A.D., Lark, R.J., and Gardner, D.R. 2014. Long-Term Stress Relaxation Behavior of Predrawn Poly(ethylene Terephthalate). *Journal of Applied Polymer Science* 131(23).

Hearn, N. 1998. Self-Sealing, Autogenous Healing and Continued Hydration: What Is the Difference? *Materials and Structures* 31(8), pp. 563–67.

Hendrik, G. Van Oss. 2005. *Background Facts and Issues Concerning Cement and Cement Data*. US Dept. of the Interior & US Geological Survey.

Huang, H. and Ye, G. 2011. Application of Sodium Silicate Solution as Self-Healing Agent in Cementitious Materials. In *Proceedings of International RILEM Conference on Advances in Construction Materials Through Science and Engineering.* Hong Kong, 5-7 September, 2011. Bagneaux: RILEM Publications, pp. 530-536.

Hota, G. and Liang, R. 2011. Advanced Fiber Reinforced Polymer Composites for Sustainable Civil Infrastructures. In *Proceedings of the International Symposium on Innovation & Sustainability of Structures in Civil Engineering*. Xiamen, 2011.

Hyde, G.W. and Smith, W.J. 1889. Results of Experiments Made to Determine the Permeability of Cements and Cement Mortars. *Journal of the Franklin Institute* 128(3), pp. 199–207.

Idiart, A.E. 2009. Coupled Analysis of Degradation Processes in Concrete Specimens at the Meso-Scale. PhD Thesis, Barcelona: Universitat Politecnica De Catalunya.

International Life Sciences Institute Europe 2000. *Packaging Materials - 1. Polyethylene Terephthalate (PET) for Food Packaging Applications*. Brussels, Belgium: ILSI Europe.

Independent Chemical Information Service. 2007. *Polyethylene Terephthalate (PET) Production and Manufacturing Process* [Online]. Available at: http://www.icis.com/resources/news/2007/11/06/9076427/polyethylene-terephthalate-pet-production-and-manufacturing-process/ [Accessed: 27 September 2014].

International Energy Agency, World Business Council for Sustainable Development, and Organisation for Economic Co-operation and Development. 2009. *Cement Technology Roadmap 2009 Carbon Emissions Reductions up to 2050.* Paris, France; Conches-Geneva, Switzerland: OECD, IEA, WBCSD.

Isaacs, B., Lark, R.J., Jefferson, A.D., Davies, R., and Dunn, S.C. 2013. Crack Healing of Cementitious Materials Using Shrinkable Polymer Tendons. *Structural Concrete* 14(2), pp. 138–47.

Jefferson, A.D. 2003. Craft - a plastic-damage-contact model for concrete. I. Model theory and thermodynamic considerations. *International Journal of Solids and Structures* 40 pp. 5973-5999.

Jefferson, A.D., Joseph, C., Lark, R.J., Isaacs, B, Dunn, S.C., and Weager, B. 2010. A New System for Crack Closure of Cementitious Materials Using Shrinkable Polymers. *Cement and Concrete Research* 40(5), pp. 795–801.

Jefferson, A.D. 2010. Finite Element Material Models for Concrete. In: *Proceedings of The Tenth International Conference on Computational Structures Technology*. Valencia, 14-17 September 2010. Civil-Comp Press

Jefferson, A.D., Tenchev, R., Chitez, A., Mihai, I., Coles, G., Lyons, P., and Ou, J.. 2014. Finite Element Crack Width Computations with a Thermo-Hygro-Mechanical-Hydration Model for Concrete Structures. *European Journal of Environmental and Civil Engineering 18(7), pp. 793-813.*

Jirásek, M. and Zimmermann, T. 1998. Rotating Crack Model with Transition to Scalar Damage. *Journal of Engineering Mechanics* 124(3), pp. 277–84.

Jo, B.W., Park, S.K., and Park, J.C. 2008. Mechanical Properties of Polymer Concrete Made with Recycled PET and Recycled Concrete Aggregates. *Construction and Building Materials* 22(12), pp. 2281–91.

Jonkers, H.M. 2007. Self Healing Concrete: A Biological Approach. In *Self Healing Materials - An Alternative Approach to 20 Centuries of Material Science*, 195–204. Dordrecht, the Netherlands: Springer.

Jonkers, H.M. 2011. Bacteria-Based Self-Healing Concrete. *Heron* 56(1-2), pp. 5–16.

Jonkers, H.M. and Schlangen, E. 2009. Towards a Sustainable Bacterially-Mediated Self Healing Concrete. In *2nd International Conference on Self-Healing Materials*. Chicago, Illinois, 28 June-1 July 2009, pp. 1-4.

Joseph, C. 2008. Experimental and Numerical Study of the Fracture and Self-Healing of Cementitious Materials. PhD Thesis, Cardiff University.

Joseph, C., Jefferson, A.D., Isaacs, B., Lark, R.J., and Gardner, D. 2010. Experimental Investigation of Adhesive-Based Self-Healing of Cementitious Materials. *Magazine of Concrete Research* 62(11), pp. 831–43.

Kardon, J.B. 1997. Polymer-Modified Concrete: Review. *Journal of Materials in Civil Engineering* 9(2), pp. 85–92.

Kennett, S. 2009. *Green Cement: An Industry Revolution?* [Online] Available at: http://www.building.co.uk/green-cement-an-industry-revolution?/3133227.article [Accessed: 13 September 2014]

Kenplas Industry Limited. 2010. *What Is PET (PolyEthylene Terephthalate)?* [Online] Available at: www.kenplas.com. http://www.kenplas.com/project/pet/ [Accessed: 27 September 2014]

Khonakdar, H.A., Morshedian, J., Mehrabzadeh, M., and Wagenknecht, U. 2003. Thermal and Shrinkage Behaviour of Stretched Peroxide-Crosslinked High-Density Polyethylene. *European Polymer Journal* 39(8), pp. 1729–34.

Kim, J.S. and Schlangen, E. 2011. Self-Healing in ECC Stimulated by SAP under Flexural Cyclic Load. In *Proceedings of 3rd International Conference on Self Healing Materials, Bath, UK*, 27–29 June 2011.

Klompen, E.T.J. 2005. *Mechanical properties of solid polymers: constitutive modelling of long and short term behaviour*. PhD Thesis, Technische Universiteit Eindhoven.

Krajcinovic, D. and Fonseka, G.U. 1981. Continuous Damage Theory of Brittle Materials - 1. General Theory. *Journal of Applied Mechanics, Transactions ASME* 48(4), pp. 809–15.

Kuang, Y. and Ou, J. 2008a. Self-Repairing Performance of Concrete Beams Strengthened Using Superelastic SMA Wires in Combination with Adhesives Released from Hollow Fibers. *Smart Materials and Structures* 17(2).

Kuang, Y. and Ou, J. 2008b. Passive Smart Self-Repairing Concrete Beams by Using Shape Memory Alloy Wires and Fibers Containing Adhesives. *Journal of Central South University of Technology (English Edition)* 15(3), pp. 411–17.

Kupfer, H.B. and Gerstle, K.H. 1973. Behavior of Concrete Under Biaxial Stresses. *ASCE Journal of the Engineering Mechanics Division* 99(EM4), pp. 853–66.

Lee, H.X.D., Wong, H.S., and Buenfeld, N.R. 2010. Potential of Superabsorbent Polymer for Self-Sealing Cracks in Concrete. *Advances in Applied Ceramics* 109(5), pp. 296–302.

Lee, J. and Fenves, G.L. 1998. Plastic-Damage Model for Cyclic Loading of Concrete Structures. *Journal of Engineering Mechanics* 124(8), pp. 892–900.

Lees, J.M. and Burgoyne, C.J. 1999. Experimental Study of Influence of Bond on Flexural Behavior of Concrete Beams Pretensioned with Aramid Fiber Reinforced Plastics. *ACI Structural Journal* 96(3), pp. 377–85.

Lees, J.M. and Burgoyne, C.J. 2000. Analysis of Concrete Beams with Partially Bonded Composite Reinforcement. *ACI Structural Journal* 97(2), pp. 252–58.

Lemaître, J. 2005. *Engineering Damage Mechanics: Ductile, Creep, Fatigue and Brittle Failures*. Berlin ; New York: Springer.

Lemaitre, J. and Chaboche, J.L. 1990. *Mechanics of Solid Materials*. Cambridge University Press.

Lendlein, A. and Kelch, S. 2002. Shape-Memory Polymers. *Angewandte Chemie - International Edition* 41(12), pp. 2035–57.

Li, L., Li, Q., and Zhang, F. 2007. Behavior of Smart Concrete Beams with Embedded Shape Memory Alloy Bundles. *Journal of Intelligent Material Systems and Structures* 18(10), pp. 1003–14.

Liu, C., Qin, H., and Mather, P.T. 2007. Review of Progress in Shape-Memory Polymers. *Journal of Materials Chemistry* 17(16), pp. 1543–58.

Liu, Q., Schlangen, E., van de Ven, M., van Bochove, G., and van Montfort, J. 2012. *Predicting the Performance of the Induction Healing Porous Asphalt Test Section*. Vol. 4. RILEM Bookseries.

Liu, Y., Gall, K., Dunn, M.L., Greenberg, A.R., and Diani, J. 2006. Thermomechanics of Shape Memory Polymers: Uniaxial Experiments and Constitutive Modeling. *International Journal of Plasticity* 22(2), pp. 279–313.

Li, V.C., Lepech, M., Wang, S., Weimann, M., and Keoleian, G. 2004. Development of Green Engineered Cementitious Composites for Sustainable Infrastructure Systems. In: *Proc., Int'l Workshop on Sustainable Development and Concrete Technology*. Beijing, China, 20-21 May, 2004.

Li, V.C., Lim, Y.M., and Chan, Y.W. 1998. Feasibility Study of a Passive Smart Self-Healing Cementitious Composite. *Composites Part B: Engineering* 29(6), pp. 819–27.

Long, S.D. and Ward, I.M. 1991. Shrinkage Force Studies of Oriented Polyethylene Terephthalate. *Journal of Applied Polymer Science* 42(7), pp. 1921–29.

Lothenbach, B., Schrivener, K., and Hooton, R.D. 2011. Supplementary Cementitious Materials. *Cement and Concrete Research* 41(12), pp. 1244–56.

Lubliner, J., Oliver, J., Oller, S., and Oñate, E. 1989. A Plastic-Damage Model for Concrete. *International Journal of Solids and Structures* 25(3), pp. 299–326.

Maji, A.K. and Negret, I. 1998. Smart Prestressing with Shape-Memory Alloy. *Journal of Engineering Mechanics* 124(10), pp. 1121–28.

Marfia, S., Rinaldi, Z., and Sacco, E. 2004. Softening Behavior of Reinforced Concrete Beams under Cyclic Loading. *International Journal of Solids and Structures* 41(11-12), pp. 3293–3316.

Mazars, J. 1986. A Description of Micro- and Macroscale Damage of Concrete Structures. *Engineering Fracture Mechanics* 25(5-6), pp. 729–37.

McCrum, N.G., Buckley, C.P., and Bucknall, C.B. 1997. *Principles of Polymer Engineering*. Oxford: Oxford University Press.

McGavin, G. and Guerin, G. 2002. Real-Time Seismic Damping and Frequency Control of Steel Structures Using Nitinol Wire. In: *Proceedings of SPIE 4696 - Smart Structures and Materials 2002: Smart Systems for Bridges, Structures, and Highways. San Diego, 17 March 2002.*

McLeod, R.S. 2005. Ordinary Portland Cement. *Building for a Future Magazine*.

Mergheim, J. and Steinmann, P. 2013. Phenomenological Modelling of Self-Healing Polymers Based on Integrated Healing Agents. *Computational Mechanics* 52(3), pp. 681–92.

Miao, S., Wang, M.L., and Schreyer, H.L. 1995. Constitutive Models for Healing of Materials with Application to Compaction of Crushed Rock Salt. *Journal of Engineering Mechanics* 121(10), pp. 1122–29.

Mihai, I. 2012. Micromechanical Constitutive Models for Cementitious Composite Materials. PhD Thesis, Cardiff University.

Mihashi, H., Kaneko, Y., Nishiwaki, T., and Otsuka, K. 2000. Fundamental Study on Development of Intelligent Concrete Characterized by Self-Healing Capability for Strength. *Transactions of the Japan Concrete Institute* 22, pp. 441–50.

Mody, R., Lofgren, E.A., and Jabarin, S.A. 2001. Shrinkage Behavior of Oriented Poly(ethylene Terephthalate). *Journal of Plastic Film and Sheeting* 17(2), pp. 152–63.

Morshedian, J., Khonakdar, H.A., and Rasouli, S. 2005. Modeling of Shape Memory Induction and Recovery in Heat-Shrinkable Polymers. *Macromolecular Theory and Simulations* 14(7), pp. 428–34.

Moser, K., Bergamini, A., Christen, R., and Czaderski, C. 2005. Feasibility of Concrete Prestressed by Shape Memory Alloy Short Fibers. *Materials and Structures/Materiaux et Constructions* 38(279), pp. 593–600.

Mosley, W.H., Bungey, J.H., and Hulse,R. 2012. *Reinforced Concrete Design to Eurocode 2*. New York: Palgrave Macmillan.

National Association for PET Container Resources (NAPCOR). *What Is PET?* [Online] Available at: http://www.napcor.com/PET/whatispet.html [Accessed: 27 September 2014]

Neville, A. 2002. Autogenous Healing: a Concrete Miracle? *Concrete International* 24(11), pp. 76-82.

Neville, A.M. 1996. *Properties of Concrete*. 4th ed. New York: Wiley.

Ngo, D. and Scordelis, A.C. 1967. Finite Element Analysis of Reinforced Concrete Beams. *ACI Journal Proceedings* 64(3), pp. 152-163.

Nguyen, G.D. 2008. A Thermodynamic Approach to Non-Local Damage Modelling of Concrete. *International Journal of Solids and Structures* 45(7–8), pp. 1918–34.

Ochi, T., Okubo, S., and Fukui, K. 2007. Development of Recycled PET Fiber and Its Application as Concrete-Reinforcing Fiber. *Cement and Concrete Composites* 29(6), pp. 448–55.

O'Connell, P.A. and McKenna, G.B. 1999. Arrhenius-Type Temperature Dependence of the Segmental Relaxation below Tg. *The Journal of Chemical Physics* 110(22), pp. 11054–60.

Ortiz, M. 1985. A Constitutive Theory for the Inelastic Behavior of Concrete. *Mechanics of Materials* 4(1), pp. 67–93.

Otsuka, K. and Kakeshita, T. 2002. Science and Technology of Shape-Memory Alloys: New Developments. *MRS Bulletin* 27(2), pp. 91–98.

Pacheco-Torgal, F. and Jalali, S. 2011. Cementitious Building Materials Reinforced with Vegetable Fibres: A Review. *Construction and Building Materials*, Composite Materials and Adhesive Bonding Technology, 25(2), pp. 575–81.

Pakula, T. and Trznadel, M. 1985. Thermally Stimulated Shrinkage Forces in Oriented Polymers: 1. Temperature Dependence. *Polymer* 26(7), pp. 1011–18.

Papa, E. and Taliercio, A. 1996. Anisotropic Damage Model for the Multiaxial Static and Fatigue Behaviour of Plain Concrete. *Engineering Fracture Mechanics* 55(2), pp. 163–79.

Patel, R., Kinney, F., and Schumacher, G. 2012. Green Concrete Using 100 % Fly Ash Based Hydraulic Binder. In *International Concrete Sustainability Conference.* Seattle, USA, 7 - 10 May 2012.

Patoor, E., Lagoudas, D.C., Entchev, P.B., Brinson, L.C., and Gao, X. 2006. Shape Memory Alloys, Part I: General Properties and Modeling of Single Crystals. *Mechanics of Materials* 38(5-6), pp. 391–429.

Pearce, F. 1997. The Concrete Jungle Overheats. *New Scientist* 2091, pp. 14.

Peltier, M. 2010. Smart Concrete. [Online] Available at: http://www.archdaily.com/62357/smart-concrete-michelle-pelletier/ [Accessed: September 18 2014]

Peterlin, A. 1971. Chain Scission and Plastic Deformation in the Strained Crystalline Polymer. *Journal of Polymer Science Part C: Polymer Symposia* 32(1), pp. 297–317.

Prevorsek, D.C., Tirpak, G.A., Harget, P.J., and Reimschuessel, A.C. 1974. Effects of Thermal Contraction on Structure and Properties of PET Fibers. *Journal of Macromolecular Science, Part B* 9(4), pp. 733–59.

Qian, S., Zhou, J., de Rooij, M.R., Schlangen, E., Gard, W., and van de Kuilen, J.W. 2009. Self-Healing Cementitious Composites under Bending Loads. In *Second International Conference on Self-Healing Materials*. Chicago, Illinois.

Qian, S.Z., Zhou, J., and Schlangen, E. 2010. Influence of Curing Condition and Precracking Time on the Self-Healing Behavior of Engineered Cementitious Composites. *Cement and Concrete Composites* 32(9), pp. 686–93.

Qi, H.J., Nguyen, T.D., Castro, F., Yakacki, C.M., and Shandas, R. 2008. Finite Deformation Thermo-Mechanical Behavior of Thermally Induced Shape Memory Polymers. *Journal of the Mechanics and Physics of Solids* 56(5), pp. 1730–51.

Ramachandran, S.K., Ramakrishnan, V., and Bang, S.S. 2001. Remediation of Concrete Using Micro-Organisms. *ACI Materials Journal* 98(1), pp. 3–9.

Ramakrishnan, V., Zellers, R., and Patnaik, A.K. 2007. Plastic Shrinkage Reduction Potential of a New High Tenacity Monofilament Polypropylene Fiber. In *International Conference on Recent Advances in Concrete*. American Concrete Institute.

Ramm, W. and Biscoping, M. 1998. Autogenous Healing and Reinforcement Corrosion of Water-Penetrated Separation Cracks in Reinforced Concrete. *Nuclear Engineering and Design* 179(2), pp. 191–200.

Rashid, Y.R. 1968. Ultimate Strength Analysis of Prestressed Concrete Pressure Vessels. *Nuclear Engineering and Design* 7(4), pp. 334–44.

Rebeiz, K.S. 1995. Time-Temperature Properties of Polymer Concrete Using Recycled PET. *Cement and Concrete Composites* 17(2), pp. 119–24.

Reinhardt, H.W. and Jooss, M. 2003. Permeability and Self-Healing of Cracked Concrete as a Function of Temperature and Crack Width. *Cement and Concrete Research* 33(7), pp. 981–85.

Richardson, M.G. 2002. *Fundamentals of Durable Reinforced Concrete*. Modern Concrete Technology 12. London ; New York: Spon Press.

RILEM. 2013. *Self-Healing Phenomena in Cement-Based Materials: State-of-the-Art Report of Rilem Technical Committee 221-SHC: Self-Healing Phenomena in Cement-Based Materials*. 1st ed. RILEM 11. New York: Springer.

Romualdi, J.P. and Batson, G.B. 1963. Mechanics of Crack Arrest in Concrete. *Journal of the Engineering Mechanics Division* 89(3), pp. 147–68.

Romualdi, J.P. and Mandel, J.A. 1964. Tensile Strength of Concrete Affected by Uniformly Distributed and Closely Spaced Short Lengths of Wire Reinforcement. *American Concrete Institute* 61(6), pp. 657–72.

Saiidi, M.S., Sadrossadat-Zadeh, M., Ayoub, C., and Itani, A. 2007. Pilot Study of Behavior of Concrete Beams Reinforced with Shape Memory Alloys. *Journal of Materials in Civil Engineering* 19(6), pp. 454–61.

Salari, M.R., Saeb, S., Willam, K.J., Patchet, S.J., and Carrasco, R.C. 2004. A Coupled Elastoplastic Damage Model for Geomaterials. *Computer Methods in Applied Mechanics and Engineering* 193(27-29), pp. 2625–43.

Sangadji, S. and Schlangen, E. 2013. Mimicking Bone Healing Process to Self Repair Concrete Structure Novel Approach Using Porous Network Concrete. In: *Procedia Engineering*, The 2nd International Conference on Rehabilitation and Maintenance in Civil Engineering (ICRMCE), 54, pp. 315–26.

Schimmel, E.C. and Remmers, J.J.C. 2006. *Development of a Constitutive Model for Self-Healing Materials*. Delft: Delft Aerospace Computational Science.

Schlangen, E. and Sangadji, S. 2013. Addressing Infrastructure Durability and Sustainability by Self Healing Mechanisms - Recent Advances in Self Healing Concrete and Asphalt. In: Proceedings of The 2nd International Conference on Rehabilitation and Maintenance in Civil Engineering (ICRMCE).

Schmets, A.J.M. 2004. Self-Healing: An Emerging Property for New Materials. *Leonardo Times* 8(4), pp. 16-18.

Schneider, M., Romer, M., Tschudin, M., and Bolio, H. 2011. Sustainable Cement Production—Present and Future. *Cement and Concrete Research* 41(7), pp. 642–50.

Sellier, A. and Bary, B. 2002. Coupled Damage Tensors and Weakest Link Theory for the Description of Crack Induced Anisotropy in Concrete. *Engineering Fracture Mechanics* 69(17), pp. 1925–39.

Sharma, S.K. and Misra, A. 1987. The Effect of Stretching Conditions on Properties of Amorphous Polyethylene Terephthalate Film. *Journal of Applied Polymer Science* 34(6), pp. 2231–47.

Sharp, S.R. and Clemeña, G.G. 2004. State of the-Art Survey of Advanced Materials and Their Potential Application in Highway Infrastructure. Charlottesville: Virginia Transportation Research Council. pp 1-41.

Sherby, O.D. and Dorn, J.E. 1958. Anelastic Creep of Polymethyl Methacrylate. *Journal of the Mechanics and Physics of Solids* 6(2), pp. 145–62.

Shrestha, K.C., Araki, Y., Nagae, T., Koetaka, Y., Suzuki, Y., Omori, T., Sutou, Y., Kainuma, R., and Ishida, K. 2013. Feasibility of Cu-Al-Mn Superelastic Alloy Bars as Reinforcement Elements in Concrete Beams. *Smart Materials and Structures* 22(2), pp. 025025.

Simo, J.C. and Hughes, T.J.R. 1998. *Computational Inelasticity*. New York, USA: Springer-Verlag.

Sisomphon, K. and Copuroglu, O. 2011. Self Healing Mortars by Using Different Cementitious Materials. In *International Conference on Advances in Construction Materials through Science and Engineering*. Hong Kong, China.

Snoeck, D., Van Tittelboom, K., De Belie, N., Steuperaert, S., and Dubruel, P. 2012. The Use of Superabsorbent Polymers as a Crack Sealing and Crack Healing Mechanism in Cementitious Materials. In *Concrete Repair, Rehabilitation and Retrofitting III - Proceedings of the 3rd International Conference on Concrete Repair, Rehabilitation and Retrofitting*, ICCRRR. Cape Town, South Africa, 3-5 September, 2012. London: CRC Press, pp. 152–57.

Song, G., Ma, N., and Li, H.N. 2006. Applications of Shape Memory Alloys in Civil Structures. *Engineering Structures* 28(9), pp. 1266–74.

Sperling, L.H. 2005. *Introduction to Physical Polymer Science*. New Jersey: John Wiley & Sons.

Struik, L.C.E. 1976. Physical Aging in Amorphous Glassy Polymers. *Annals of the New York Academy of Sciences* 279(1), pp. 78–85.

Sweeney, J., Shiritaki, H., Unwin, A.P., and Ward, I.M. 1999. Application of a Necking Criterion to PET Fibers in Tension. *Journal of Applied Polymer Science* 74(14), pp. 3331–41.

Tao, X. and Phillips, V.D. 2005. A Simplified Isotropic Damage Model for Concrete under Bi-Axial Stress States. *Cement and Concrete Composites* 27(6), pp. 716–26.

Taylor, M., Tam, C., and Gielen, D. 2005. Energy Efficiency and CO2 Emissions from the Global Cement Industry. *Energy Technology Policy Division*.

Ter Heide, N. and Schlangen, E. 2007. Self-Healing of Early Age Cracks in Concrete. In *First International Conference on Self Healing Materials.* Dordrecht: Springer.

Thao, T.D.P., Johnson, T.J.S., Tong, Q.S., and Dai, P.S. 2009. Implementation of Self-Healing in Concrete – Proof of Concept. *The IES Journal Part A: Civil & Structural Engineering* 2(2), pp. 116–25.

The Highways Agency. 1987. *BD 28/87 Early Thermal Cracking of Concrete*.

Tobushi, H., Hashimoto, T., Hayashi, S., and Yamada, E. 1997. Thermomechanical Constitutive Modeling in Shape Memory Polymer of Polyurethane Series. *Journal of Intelligent Material Systems and Structures* 8(8), pp. 711–18.

Tobushi, H., Okumura, K., Hayashi, S., and Ito, N. 2001. Thermomechanical Constitutive Model of Shape Memory Polymer. *Mechanics of Materials* 33(10), pp. 545–54.

UNEP. 2010. Greening Cement Production Has a Big Role to Play in Reducing Greenhouse Gas Emissions. *UNEP Global Environmental Alert Service*.

Van Breugel, K. 2007. Is There a Market for Self-Healing Cement-Based Materials? In *First International Conference on Self Healing Materials*. Noordwijk aan Zee, The Netherlands: Springer.

van Breugel, K. 2009. Self Healing Concepts in Civil Engineering for Sustainable Solutions: Potential and Constraints. In *2nd International Conference on Self-Healing Materials*. Chicago.

Vander Werf, P. 2012. Cement for Severe Environments. *Concrete Construction - World of Concrete* 57(2), pp. 28–30.

van der Zwaag. 2007. *Self Healing Materials an Alternative Approach to 20 Centuries of Materials Science*. Dordrecht: Springer.

Van Deventer, J.S.J., Provis, J.L., and Duxson, P. 2012. Technical and Commercial Progress in the Adoption of Geopolymer Cement. *Minerals Engineering*, Sustainability through Resource Conservation and Recycling, 29(March), pp. 89–104.

Van Tittelboom, K. and De Belie, N. 2013. Self-Healing in Cementitious Materials-a Review. *Materials* 6(6), pp. 2182–2217.

Van Tittelboom, K., De Belie, N., Van Loo, D., and Jacobs, P. 2011. Self-Healing Efficiency of Cementitious Materials Containing Tubular Capsules Filled with Healing Agent. *Cement and Concrete Composites* 33(4), pp. 497–505.

Van Tittelboom, K., Gruyaert, E., Rahier, H., and De Belie, N. 2012. Influence of Mix Composition on the Extent of Autogenous Crack Healing by Continued Hydration or Calcium Carbonate Formation. *Construction and Building Materials* 37(December), pp. 349–59.

Volk, B. and Whitley, K. 2005. Characterization of Shape Memory Polymers [Online]. Langley, Virginia: *NASA Langley Research Centre.* Available at: http://smart.tamu.edu/presentations/presentationfiles/researchpresentations/brentreport.pdf [Accessed: 19 May 2015].

Voyiadjis, G.Z., Shojaei, A., and Li, G. 2011. A Thermodynamic Consistent Damage and Healing Model for Self Healing Materials. *International Journal of Plasticity* 27(7), pp. 1025–44.

Voyiadjis, G.Z., Taqieddin, Z.N., and Kattan, P.I. 2008. Anisotropic Damage–plasticity Model for Concrete. *International Journal of Plasticity* 24(10), pp. 1946–65.

Wang, J., Van Tittelboom, K., and Verstraete, W. 2012. Use of Silica Gel or Polyurethane Immobilized Bacteria for Self-Healing Concrete. *Construction and Building Materials* 26(1), pp. 532–40.

Wang, L.F., Kuo, J.F., and Chen, C.Y. 1995. Viscoelasticity and Stability of Nylon 66 Langmuir Films. *European Polymer Journal* 31(8), pp. 769–73.

Wang, X., Xing, F., Zhang, M., Han, N., and Qian, Z. 2013. Experimental Study on Cementitious Composites Embedded with Organic Microcapsules. *Materials* 6(9), pp. 4064–81.

Ward, I.M. 1983. *Mechanical Properties of Solid Polymers*. Wiley.

Ward, I.M. and Sweeney, J. 2004. *An Introduction to the Mechanical Properties of Solid Polymers*. Chichester, West Sussex, England: Wiley.

Wayman, C.M. and Ōtsuka, K. 1999. *Shape Memory Materials*. Cambridge; New York: Cambridge University Press.

Wendner, R., Hubler, M.H., and Bažant, Z.P. 2013. The B4 Model for Multi-Decade Creep and Shrinkage Prediction. In: *Proceedings of Ninth International Conference on Creep, Shrinkage, and Durability Mechanics (CONCREEP-9).* Cambridge, Massachusetts 22-25 September 2013. Virginia: American Society of Civil Engineers pp. 429–36.

White, S.R., Sottos, N.R., Geubelle, P.H., Moore, J.S., Kessler, M.R., Sriram, S.R., Brown, E.N., and Viswanathan, S. 2001. Autonomic Healing of Polymer Composites. *Nature* 409(6822), pp. 794–97.

William, K.J. and Warnke, E.P. 1975. Constitutive Models for Triaxial Behavior of Concrete. *Proc. Int. Assoc. Bridge Struct.* Engrg (Report 19), pp. 1–30.

Williams, M.L., Landel, R.F., and Ferry, J.D. 1955. The Temperature Dependence of Relaxation Mechanisms in Amorphous Polymers and Other Glass-Forming Liquids. *Journal of the American Chemical Society* 77(14), pp. 3701–7.

Worrell, E., Price, L., Martin, N., Hendriks, C., and Meida, L.O. 2001. Carbon Dioxide Emissions from the Global Cement Industry. *Annual Review of Energy and the Environment* 26 (1), pp. 303–29.

Wu, M. 2012. A Review: Self-Healing in Cementitious Materials and Engineered Cementitious Composite as a Self-Healing Material. *Construction and Building Materials* 28(1), pp. 571–83.

Wu, Y.F., Zhou, Y.W., and He, X.Q. 2010. Performance-Based Optimal Design of Compression-Yielding FRP-Reinforced Concrete Beams. *Composite Structures* 93(1), pp. 113–23.

XE - The World's Trusted Currency Authority. 2014 [Online] Available at: http://www.xe.com/ [Accessed: 2 September 2014].

Yang, Y., Lepech, M.D., Yang, E.H., and Li, V.C. 2009. Autogenous Healing of Engineered Cementitious Composites under Wet-Dry Cycles. *Cement and Concrete Research* 39(5), pp. 382–90.

Yang, Y., Yang, E.H., and Li, V.C. 2011. Autogenous Healing of Engineered Cementitious Composites at Early Age. *Cement and Concrete Research* 41(2), pp. 176–83.

Yang, Z., Hollar, J., He, X., and Shi, X. 2011. A Self-Healing Cementitious Composite Using Oil Core/silica Gel Shell Microcapsules. *Cement and Concrete Composites* 33(4), pp. 506–12.

Zollo, R.F. 1997. Fiber-Reinforced Concrete: An Overview after 30 Years of Development. *Cement and Concrete Composites* 19(2), pp. 107–22.

Appendix A: Determination of Creep and Shrinkage Strain in Accordance with Eurocodes

The Eurocodes state that creep and shrinkage are dependent on “the ambient humidity, the dimensions of the element, and the composition of the concrete”. Creep is also further affected by the age of the concrete at first loading, and the duration and magnitude of the loading”.

A.1 Creep Strain

The creep deformation, $\varepsilon_{cc}(\infty,t_0)$, at time t=∞ for a constant compressive stress, σ_c, applied at the concrete age t_0 is given by:

$$\varepsilon(\infty, t_0) = \varphi(\infty, t_0) \cdot (\sigma_c/E_c) \qquad \text{A.1q}$$

Where E_c is the tangent modulus taken as 1.05 E_{cm}, and φ is the creep coefficient. If great accuracy is not required, and the concrete is not subjected to a compressive stress greater than 0.45 f_{ck} at the time of first loading, the creep coefficient can be taken from Figure A.1.

If a more precise measure of the creep deformation is required then the following set of equations is used to calculate the creep coefficient at a time t, $\varphi(t, t_0)$.

$$\varphi(t, t_0) = \varphi_0 \cdot \beta_c(t, t_0) \qquad \text{A.2}$$

In which the notional creep coefficient, φ_0, is estimated as:

$$\varphi_0 = \varphi_{RH} \cdot \beta(f_{cm}) \cdot \beta(t_0) \qquad \text{A.3}$$

φ_{RH}, is a factor accounting for the effects of relative humidity on the notional creep coefficient:

$$\varphi_{RH} = 1 + \frac{1 - RH/100}{0.1 \cdot \sqrt[3]{h_0}} \text{ for } f_{cm} \leq 35MPa \tag{A.4}$$

$$\varphi_{RH} = \left[1 + \frac{1 - RH/100}{0.1 \cdot \sqrt[3]{h_0}} \cdot \alpha_1\right] \cdot \alpha_2 \text{ for } f_{cm} > 35MPa \tag{A.5}$$

RH is the relative humidity of the ambient environment in %, f_{cm} is the mean compressive strength of the concrete at the age of 28 days, and h_0 is the notional size of the member in mm given by Equation A.6.

$$h_0 = \frac{2A_c}{u} \tag{A.6}$$

In which A_c is the cross sectional area, and u is the perimeter of the member in contact with the atmosphere.

$\beta(f_{cm})$ and $\beta(t_0)$ are factors which allow for the effect of concrete strength on the notional creep coefficient, and the effect of concrete age at loading on the notional creep coefficient respectively:

$$\beta(f_{cm}) = \frac{16.8}{\sqrt{f_{cm}}} \tag{A.7}$$

$$\beta(t_o) = \frac{1}{(0.1 + {t_0}^{0.2})} \tag{A.8}$$

$\beta_c(t, t_0)$ is a coefficient which describes the development of creep with time elapsed from loading and is estimated using Equation A.9.

$$\beta_c(t, t_o) = \left[\frac{(t - t_o)}{\beta_H + t - t_0}\right]^{0.3} \qquad \text{A.9}$$

In which t is the age of concrete in days at the moment considered, t_o is the age of concrete at loading in days, and β_H is a coefficient related to the effects of the relative humidity, RH, and the notional member size, h_0.

$$\beta_H = 1.5[1 + (0.012\, RH)^{18}]h_0 + 250 \leq 1500 \text{ for } f_{cm} \leq 35MPa \qquad \text{A.10}$$

$$\beta_H = 1.5[1 + (0.012\, RH)^{18}]h_0 + 250\, \alpha_3 \leq 1500\, \alpha_3 \text{ for } f_{cm} > 35MPa \qquad \text{A.11}$$

Finally; α_1, α_2, and α_3 are coefficients which consider the influence of the concrete strength:

$$\alpha_1 = \left[\frac{35}{f_{cm}}\right]^{0.7} \quad \alpha_2 = \left[\frac{35}{f_{cm}}\right]^{0.2} \quad \alpha_3 = \left[\frac{35}{f_{cm}}\right]^{0.5} \qquad \text{A.12}$$

Appendix A: Determination of Creep and Shrinkage Strain in Accordance with Eurocodes

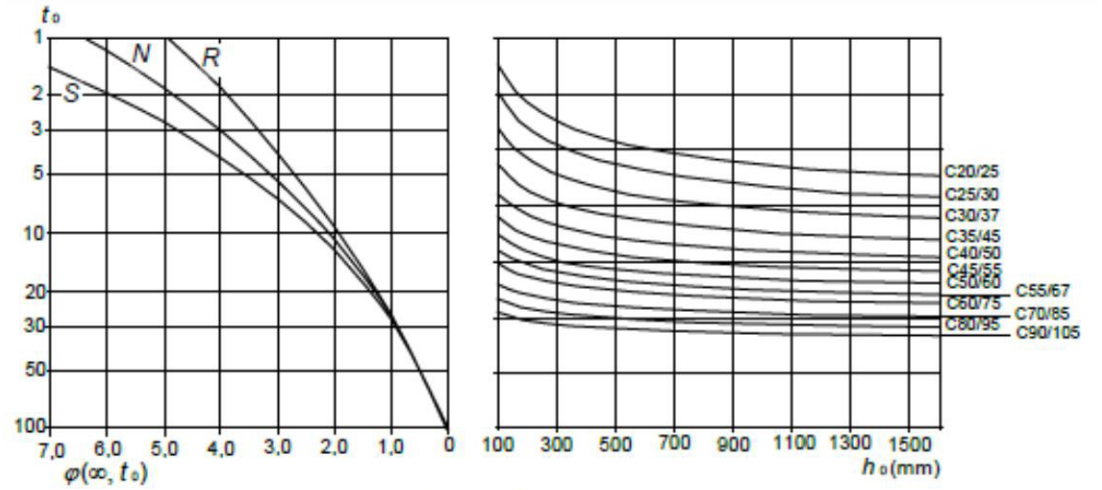

a) inside conditions - RH = 50%

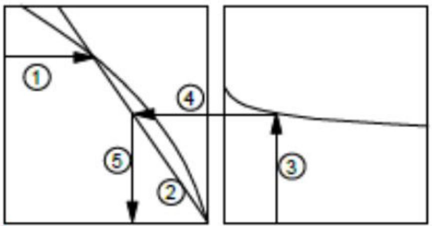

Note:
- intersection point between lines 4 and 5 can also be above point 1
- for t_0 > 100 it is sufficiently accurate to assume t_0 = 100 (and use the tangent line)

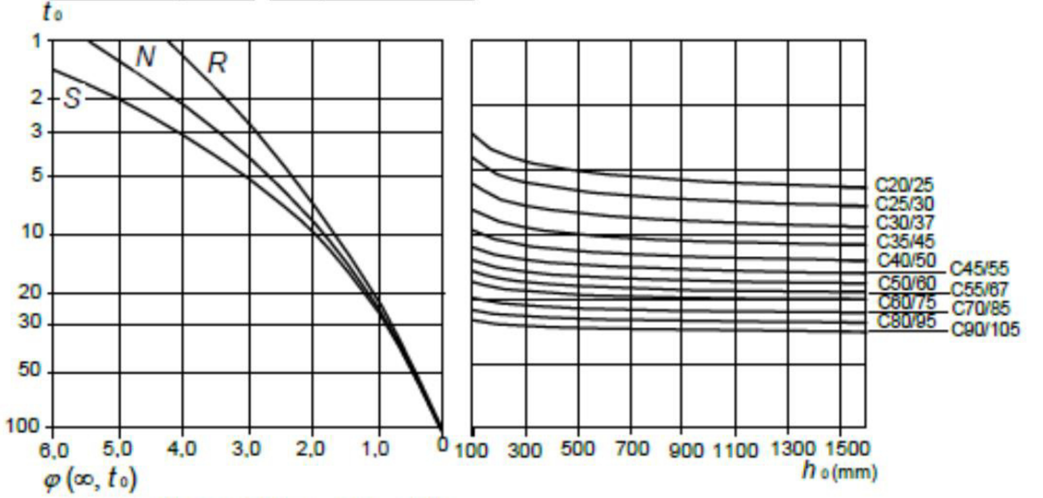

b) outside conditions - RH = 80%

Figure A.1 - Method for determining the creep coefficient $\varphi(\infty, t_0)$ for concrete under normal environmental conditions

A.2 Shrinkage Strain

Total shrinkage strain, ε_{cs}, is the sum of two components; the drying shrinkage strain, ε_{cd}, and the autogenous shrinkage strain, ε_{ca}; hence the value of the total shrinkage strain is given by:

$$\varepsilon_{cs} = \varepsilon_{cd} + \varepsilon_{ca} \qquad \text{A.13}$$

The drying shrinkage strain at any point in time is calculated using Equation A.14

$$\varepsilon_{cd}(t) = \beta_{ds}(t, t_s) \cdot k_h \cdot \varepsilon_{cd,0} \qquad \text{A.14}$$

Where k_h is a coefficient depending on the notional size h_0, and β_{ds} is given by:

$$\beta_{ds}(t, t_s) = \frac{(t - t_s)}{(t - t_s) + 0.04\sqrt{{h_0}^3}} \qquad \text{A.15}$$

Finally, $\varepsilon_{cd,0}$ is the basic drying shrinkage strain, calculated from Equation A.16.

$$\varepsilon_{cd,0} = 0.85\left[(220 + 110 \cdot \alpha_{ds1}) \cdot exp\left(-\alpha_{ds2} \cdot \frac{f_{cm}}{f_{cmo}}\right)\right] \cdot 10^{-6} \cdot \beta_{RH} \qquad \text{A.16}$$

$$\beta_{RH} = 1.55\left[1 - {\frac{RH}{RH_0}}^3\right] \qquad \text{A.17}$$

In which f_{cm} is the mean compressive stress, f_{cmo} = 10 MPa, α_{ds1} and α_{ds2} are coefficients which depend on the cement type, RH is the relative humidity, and RH_0 = 100 %.

The autogenous shrinkage strain at any point in time is calculated using the following:

$$\varepsilon_{ca}(t) = \beta_{as}(t)\varepsilon_{ca}(\infty) \qquad \text{A.18}$$

In which;

$$\varepsilon_{ca}(\infty) = 2.5(f_{ck} - 10)10^{-6} \qquad \text{A.19}$$

and;

$$\beta_{as}(t) = 1 - exp(-0.2t^{0.5}) \qquad \text{A.20}$$

Appendix B: Calculation of Maximum Crack Width in Accordance with Eurocodes

The Eurocodes give the following expression for the calculation of the maximum expected crack width:

$$w_k = S_{r,max}(\varepsilon_{sm} - \varepsilon_{cm}) \tag{B.1}$$

In which $S_{r,max}$ is the maximum crack spacing, ε_{sm} is the mean strain in the reinforcement under the relevant load combination, and ε_{cm} is the mean strain in the concrete between cracks; all of which are calculated from the following expressions:

$$S_{r,max} = k_3 c + k_1 k_2 k_4 \varphi / \rho_{p,eff} \tag{B.2}$$

In which φ is the bar diameter, c is the cover to the longitudinal reinforcement, and k_1, and k_2 are coefficients taking account of the bond properties of the bars, and the strain distribution respectively. $\rho_{p,eff}$ for a member without prestressing steel is the ratio $A_s/A_{c,eff}$. The values of k_3, and $k_4$are taken from a country's National Annex; recommended values are 3.4 and 0.425 respectively.

$$(\varepsilon_{sm} - \varepsilon_{cm}) = \frac{\sigma_s - k_t \dfrac{f_{ct,eff}}{\rho_{p,eff}}\left(1 + \alpha_e \rho_{p,eff}\right)}{E_s} \geq 0.6\frac{\sigma_s}{E_s} \tag{B.3}$$

Where σ_s is the stress in the tension reinforcement assuming a fully cracked section, k_t is a factor accounting for the duration of the applied load, $f_{ct,eff}$ is the characteristic effective tensile strength of the concrete, and α_e is the ratio E_s/E_{cm}.

Appendix C: SLS simulation results for Parametric Study 2 in Chapter 6

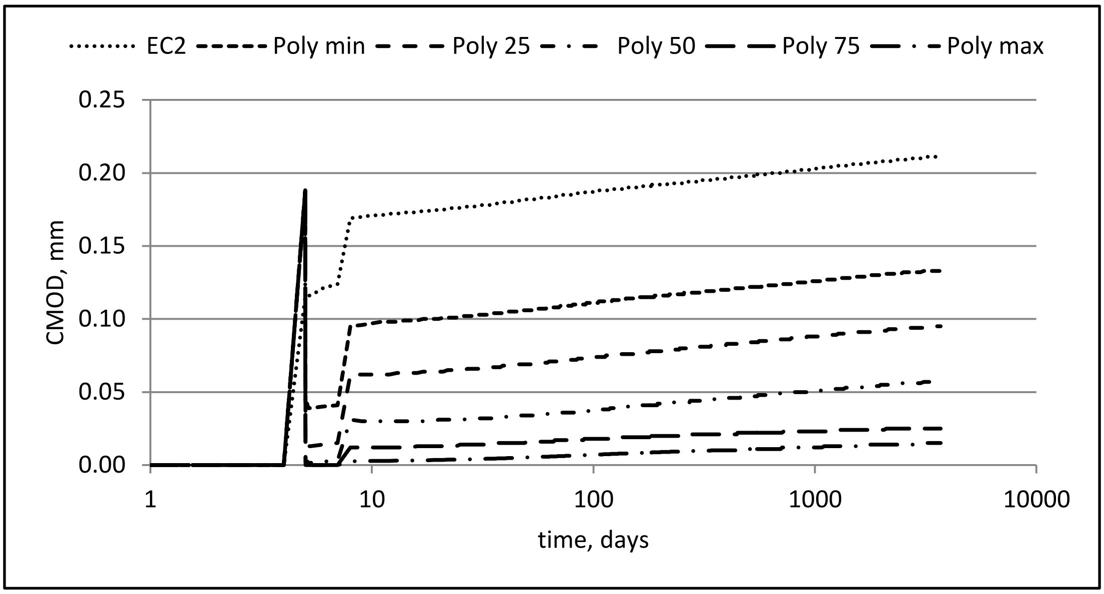

Figure C.1 - SLS simulation results for beams designed with f_{yk} = 500 MPa

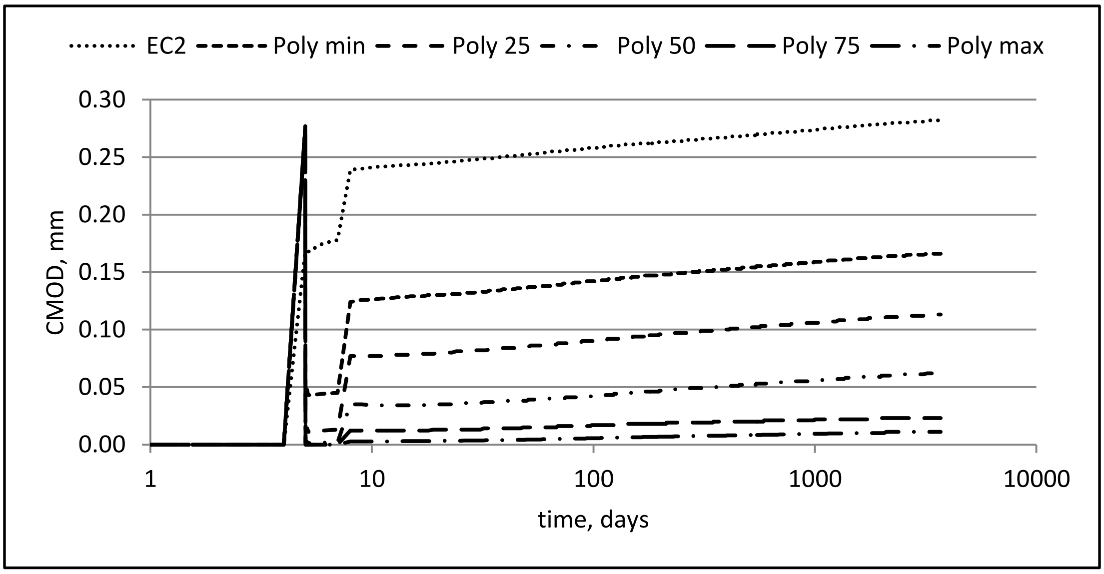

Figure C.2 - SLS simulation results for beams designed with f_{yk} = 750 MPa

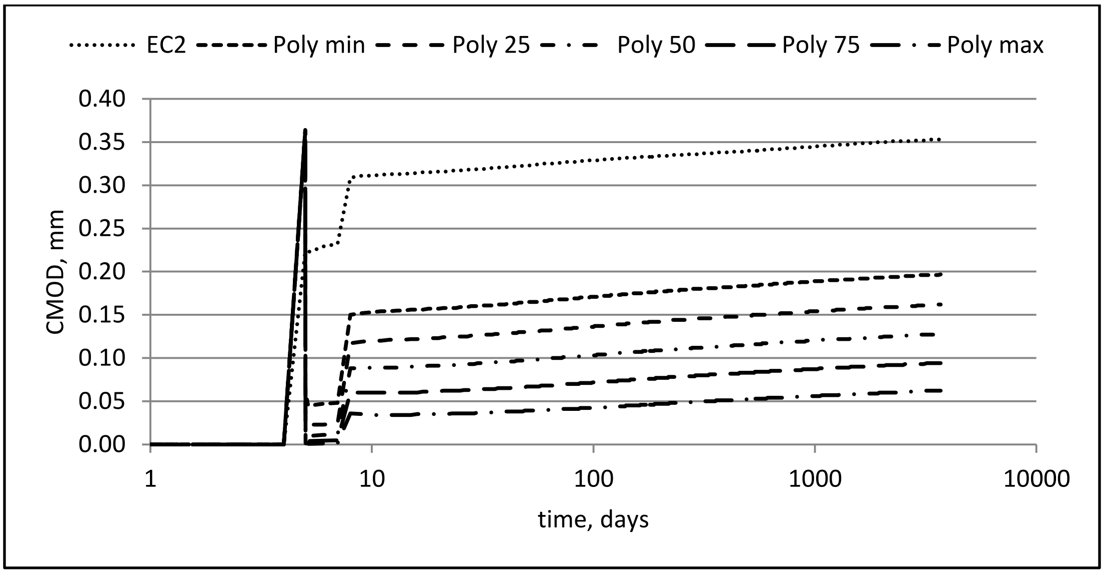

Figure C.3- SLS simulation results for beams designed with $\mathrm{f_{yk}}$ = 1000 MPa

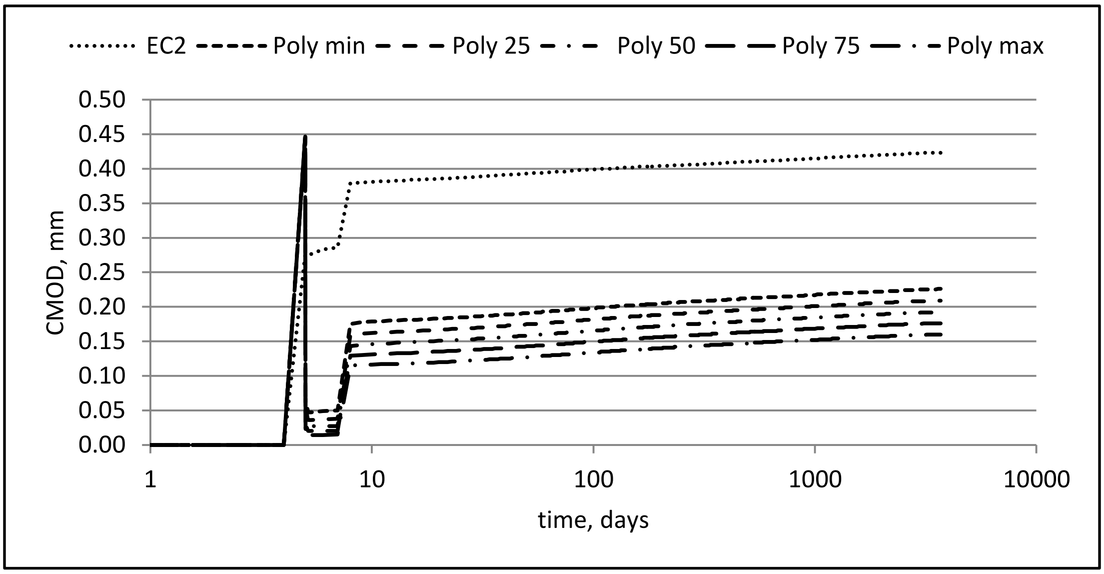

Figure C.4 - SLS simulation results for beams designed with $\mathrm{f_{yk}}$ = 1250 MPa

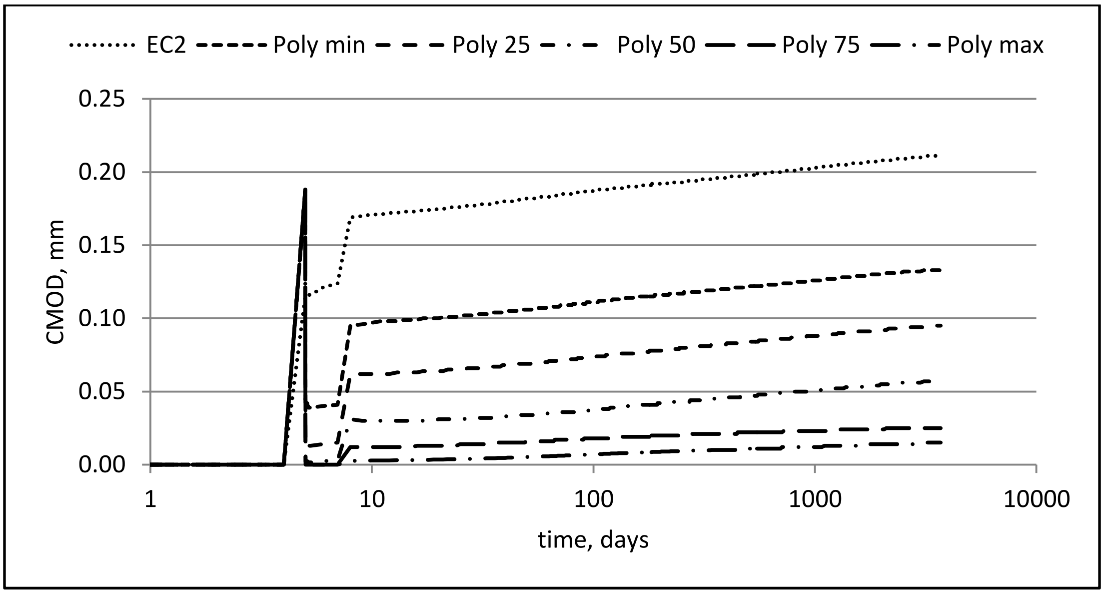

Figure C.5 - SLS simulation results for beams designed with f_{yk} = 1468 MPa